_____

Peptide microarray fabrication by laser-based in situ synthesis

and utilization for infectious disease research

_____

Inaugural-Dissertation

to obtain the academic degree

Doctor rerum naturalium (Dr. rer. nat.)

Submitted to Fachbereich Biologie, Chemie, Pharmazie

of Freie Universität Berlin

by

Jasmin Heidepriem

Berlin, 2022

The presented work was carried out under the supervision of Dr. Felix. F. Löffler and Prof. Dr. Peter H. Seeberger from January 2019 until September 2022 in the Department of Biomolecular Systems at the Max Planck Institute of Colloids and Interfaces in Potsdam. This work was supervised by Prof. Dr. Beate Koksch from the Institute of Chemistry and Biochemistry of Freie Universität Berlin.

1st Reviewer: Prof. Dr. Beate Koksch (Freie Universität Berlin)

2nd Reviewer: PD Dr. Harald Seitz (Fraunhofer-Institut für Zelltherapie und Immunologie)

Date of Defense: 26.06.2023

Declaration of authorship

Herewith I certify that I have prepared and written my thesis with the title "Peptide microarray fabrication by laser-based in situ synthesis and utilization for infectious disease research" independently and that I have not used any sources and aids other than those indicated by me. My own contribution and the contribution of other authors is depicted for each included publication. The here presented dissertation was not submitted in any other doctorate degree procedure before.

Jasmin Heidepriem

Date and Signature:

Acknowledgements

First, I would like to thank the Max Planck Institut of Colloids and Interfaces and the Department of Biology, Chemistry, and Pharmacy of Freie Universität Berlin for supporting my doctoral thesis. I would like to thank Prof. Dr. Beate Koksch and Dr. Harald Seitz for the supervision of my dissertation. Furthermore, I thank Harald for bringing me to the Science Park in Potsdam Golm.

In addition, I would like to thank Prof. Dr. Peter H. Seeberger and the Biomolecular Systems Department for the excellent working environment.

I would like to thank Dr. Felix F. Löffler for encouraging me to start as a PhD student in his group and for all the support during this time. Working together in various collaboration projects was very exciting. In particular, I would like to express my appreciation for the collaboration with Dr. Christine Dahlke, Dr. Verena Krähling, and Dr. Anahita Fathi. Also, all the other collaboration partners not mentioned here should feel addressed.

I would like to especially thank Grigori Paris for the joint work on a laborious but fantastic project. I want to express my sincere thanks to Grigori for all his support. The "**much more**" will make me smile again and again.

I am very grateful for the scientific support of Alexandra Tsouka, Marco Mende, Sandra M. Pinzón Martín, and Chandrahdish Gosh. I am even more grateful for their friendship.

I would like to thank my colleagues from the Synthetic Array Technologies group for their support and the pleasant environment. Furthermore, I would like to thank Celina Lindner and Dominik Bierbaum for their great work in our group.

I am very grateful that the spin coater and the robot did not let me down (too often) throughout the years.

For their scientific support and their time for discussions, I would like to thank Dr. F. Ralf Bischoff, Dr. Anette Jacob, and Dr. Daniela S. Mattes.

I would like to thank the pleasant Lager team: Jürgen Wiggert, Henry Liebner, Robert Gaebel, and Andrè-Patrick Ottenhus. Not only do they do a great job, but they also are such nice people.

I would like to thank Klaus Bienert, Eva Settels, and Katrin Sellrie for their technical support, as well as the team of the IT-Service for their help.

Finally, I would like to thank the Max Planck Society for the MPG-FhG cooperation grant "Glyco3Display" and the Federal Ministry of Education and Research for the BMBF grant 13XP5050A.

Publications

*Paris, G., *Heidepriem, J., (*shared first authorship) Tsouka, A., Liu, Y., Mattes, D. S., Pinzón Martín, S., Dallabernardina, P., Mende, M., Lindner, C., Wawrzinek, R., Rademacher, C., Seeberger, P. H., Breitling, F., Bischoff, F. R., Wolf, T., Loeffler, F. F. (2022). Automated Laser-Transfer Synthesis of High-Density Microarrays for Infectious Disease Screening. *Advanced Materials*, 34, 2200359.

Fathi, A., Dahlke, C., Krähling, V., Kupke, A., Okba, N., Raadsen, M. P., Heidepriem, J., Müller, M. A., Paris, G., Lassen, S., Klüver, M., Volz, A., Koch, T., Ly, M. L., Friedrich, M., Fux, R., Tscherne, A., Kalodimou, G., Schmiedel, S., Corman, V. M., Hesterkamp, T., Drosten, C., Loeffler, F. F., Haagmans, B. L., Sutter, G., Becker, S., Addo, M. M. (2022). Increased neutralization and IgG epitope identification after MVA-MERS-S booster vaccination against Middle East respiratory syndrome. *Nature Communications*, 13(1), 4182.

Tsouka, A., Hoetzel, K., Mende, M., Heidepriem, J., Paris, G., Eickelmann, S., Seeberger, P. H., Lepenies, B., & Loeffler, F. F. (2021). Probing Multivalent Carbohydrate-Protein Interactions With On-Chip Synthesized Glycopeptides Using Different Functionalized Surfaces. *Frontiers in Chemistry*, 9, 766932.

*Heidepriem, J., *Dahlke, C., (*shared first authorship) Kobbe, R., Santer, R., Koch, T., Fathi, A., Seco, B. M. S., Ly, M. L., Schmiedel, S., Schwinge, D., Serna, S., Sellrie, K., Reichardt, N.-C., Seeberger, P. H., Addo, M. M., Loeffler, F. F., on behalf of the ID-UKE COVID-19 Study Group (2021). Longitudinal Development of Antibody Responses in COVID-19 Patients of Different Severity with ELISA, Peptide, and Glycan Arrays: An Immunological Case Series. *Pathogens*, 10(4), 438.

Heiss, K., Heidepriem, J., Fischer, N., Weber, L. K., Dahlke, C., Jaenisch, T., & Loeffler, F. F. (2020). Rapid Response to Pandemic Threats: Immunogenic Epitope Detection of Pandemic Pathogens for Diagnostics and Vaccine Development Using Peptide Microarrays. *Journal of Proteome Research*, 19(11), 4339-4354.

Mende, M., Tsouka, A., Heidepriem, J., Paris, G., Mattes, D. S., Eickelmann, S., Bordoni, V., Wawrzinek, R., Fuchsberger, F. F., Seeberger, P. H., Rademacher, C., Delbianco, M., Mallagaray, A., & Loeffler, F. F. (2020). On-Chip Neo-Glycopeptide Synthesis for Multivalent Glycan Presentation. *Chemistry - A European Journal*, 26(44), 9954-9963.

*Heidepriem, J., *Krähling, V., (*shared first authorship) Dahlke, C., Wolf, T., Klein, F., Addo, M. M., Becker, S., & Loeffler, F. F. (2020). Epitopes of Naturally Acquired and Vaccine-Induced Anti-Ebola Virus Glycoprotein Antibodies in Single Amino Acid Resolution. *Biotechnology Journal*, 15(9), e2000069.

Paris, G., Klinkusch, A., Heidepriem, J., Tsouka, A., Zhang, J., Mende, M., Mattes, D. S., Mager, D., Riegler, H., Eickelmann, S., & Loeffler, F. F. (2020). Laser-induced forward transfer of soft material nanolayers with millisecond pulses shows contact-based material deposition. *Applied Surface Science*, 508, 144973.

Paris, G., Heidepriem, J., Tsouka, A., Mende, M., Eickelmann, S., Loeffler, F. F., (2019). Automated laser-assisted synthesis of microarrays for infectious disease research. *Proceedings SPIE,* 10875, Microfluidics, BioMEMS, and Medical Microsystems XVII, 108750C.

Eickelmann, S., Tsouka, A., Heidepriem, J., Paris, G., Zhang, J., Molinari, V., Mende, M., Loeffler, F. F. (2019). A Low-cost laser-based nano-3d polymer printer for rapid surface patterning and chemical synthesis of peptide and glycan microarrays. *Advanced Materials Technologies,* 4 (11), 1900503.

Fühner, V., Heine, P. A., Helmsing, S., Goy, S., Heidepriem, J., Loeffler, F. F., Dübel, S., Gerhard, R., & Hust, M. (2018). Development of Neutralizing and Non-neutralizing Antibodies Targeting Known and Novel Epitopes of TcdB of *Clostridioides difficile*. *Frontiers in Microbiology*, 9, 2908.

Abstract

Due to the circulation of infectious diseases and the emergence of new pathogens, fundamental research, as well as the development of vaccines are of utmost importance. Peptide microarrays (PMAs) can facilitate the investigation of an immune response to an antigen by detecting linear B cell epitopes. They consist of a miniaturized spot pattern containing different peptide sequences. These reproduce all potential linear epitopes of a protein, usually as a map of overlapping peptides. Therefore, PMAs allow for high-throughput screening in a fast manner. To show their versatility, PMAs were applied for the detection of linear B cell epitopes elicited by infectious pathogens or a vaccine-delivered antigen. First, PMAs of the Ebola virus spike glycoprotein were used to analyze the development of antibodies, recognizing linear peptide epitopes, in vaccine recipients and an Ebola virus disease survivor. Second, PMAs covering the SARS-CoV-2 coronavirus proteome were used to identify epitopes. The antibodies elicited by patients with COVID-19 disease were studied during the course of the disease. Today, commercially available PMAs do either lack peptide sequence flexibility and/or a high peptide density. Thus, the price per analyzed sample is high and therefore, reducing the usage of PMAs. Hence, the combinatorial laser-induced forward transfer (cLIFT) technology was developed for the fabrication of high-density PMAs. Thereby, a polymer and an amino acid are transferred via laser irradiation from a donor to an acceptor in a spot pattern. Together with intermittent chemical processing, this laser-based technique can be used to in situ synthesize microarrays. With the implementation of an automated synthesizer and optimal synthesis parameters, it was possible to produce up to 20-residue peptides with controlled spot size. Finally, a full combinatorial synthesis of overlapping 15-mer peptides containing the Ebola virus proteome with 4444 and 10 000 spots per cm^2 was performed. The antibody binding was compared to a commercial peptide microarray containing the same peptides of the spike glycoprotein. The results revealed an excellent quality up to a density of 4444 spots per cm^2. Moreover, the flexibility of this method allows the exchange of building blocks and thus, enables the synthesis of other molecules.

Kurzfassung

Angesichts der Verbreitung von Infektionskrankheiten und dem Auftreten neuer Krankheitserreger sind Grundlagenforschung und die Entwicklung von Impfstoffen von größter Bedeutung. Peptid-Microarrays (PMAs) können die Untersuchung einer Immunantwort auf ein Antigen durch den Nachweis linearer B-Zell-Epitope erleichtern. Sie bestehen aus einem miniaturisierten Spotmuster, welches verschiedene Peptidsequenzen enthält. Diese bilden alle potentiellen linearen Epitope eines Proteins ab, in der Regel als überlappende Peptide. Daher ermöglichen PMAs schnelle Hochdurchsatz-Untersuchungen. Um ihre Vielseitigkeit zu zeigen, wurden PMAs für den Nachweis linearer B-Zelle-Epitope eingesetzt, die durch infektiöse Erreger oder durch ein Impfstoff-verabreichtes Antigen ausgelöst wurden. Zuerst wurden PMAs des Ebolavirus Spike-Glykoproteins verwendet, um die Entwicklung von Antikörpern, welche lineare Peptidepitope erkennen, in Geimpften und einem Überlebenden der Ebolavirus-Erkrankung zu analysieren. Zweitens wurden PMAs, die das Proteom des Coronavirus SARS-CoV-2 umfassen, zur Identifizierung von Epitopen eingesetzt. Somit konnten die gebildeten Antikörper von Patienten mit der COVID-19-Erkrankung im Verlauf der Erkrankung untersucht werden. Heutzutage, mangelt es kommerziell erhältlichen PMAs entweder an Peptidsequenzflexibilität und/oder an hoher Peptiddichte. Dadurch ist der Preis pro analysierter Probe hoch und schränkt somit die Anwendung von PMAs ein. Daher wurde der kombinatorische Laser-induzierte Vorwärtstransfer (cLIFT) zur Herstellung von PMAs mit hoher Dichte entwickelt. Dabei werden Spots, die ein Polymer und eine Aminosäure enthalten, von einem Donator auf einen Akzeptor übertragen, um ein Spotmuster zu erzeugen. Zusammen mit intermittierenden chemischen Schritten kann diese Laser-basierte Technik zur in situ Synthese von Microarrays verwendet werden. Mit der Einführung einer automatisierten Synthesemaschine und optimaler Syntheseparameter war es möglich Peptide mit bis zu 20 Aminosäuren und kontrollierter Spotgröße herzustellen. Schließlich wurde eine vollständig kombinatorische Synthese von überlappenden 15-mer Peptiden, die das Proteom des Ebolavirus umfassen, mit 4444 und 10 000 Spots pro cm^2 durchgeführt. Die Antikörperbindung wurde mit einem kommerziellen Peptid-Microarray verglichen, der die gleichen Peptide des Spike-Glykoproteins enthält. Die Ergebnisse zeigten eine hervorragende Qualität bis zu einer Dichte von 4444 Spots pro cm^2. Darüber hinaus ermöglicht die Flexibilität dieser Methode den Austausch von Bausteinen und damit die Synthese anderer Moleküle.

Table of Contents

List of abbreviations and acronyms

AA	amino acid
ACE2	angiotensin-converting enzyme 2
AEU	arbitrary enzyme-linked immunosorbent assay units
AFU	arbitrary fluorescence units
APC	antigen-presenting cell
BA	blister-actuated
BCR	B cell receptor
Boc	tert-butyloxycarbonyl group
C	constant
CD	cluster of differentiation
CDR	complementarity determining region
cLIFT	combinatorial laser-induced forward transfer
CMOS	complementary metal oxide semiconductor
COVID-19	coronavirus disease 2019
cryo EM	cryogenic electron microscopy
CuAAC	copper(I)-catalyzed azide-alkyne cycloaddition
D	diversity
DCC	N,N'-dicyclohexylcarbodiimide
DIC	N,N'-diisopropylcarbodiimide
DMF	N,N-dimethylformamide
DMSO	dimethyl sulfoxide
DRC	Democratic Republic of the Congo
DRL	dynamic release layer
EBOV	Ebola virus
ELISA	enzyme-linked immunosorbent assay

EVD	Ebola virus disease
Fab	fragment antigen-binding
Fc	fragment crystallizable
Fmoc	fluorenylmethoxycarbonly
GP	glycoprotein
HF	hydrofluoric acid
HLA	human leukocyte antigen
HOBt	*N*-hydroxybenzotriazole
Ig	immunoglobulin
J	joining
LIFT	laser-induced forward transfer
MA	microarray
MALDI-MS	matrix-assisted laser desorption/ionization mass spectrometry
MAPLE DW	matrix-assisted pulsed-laser evaporation direct write
MERS	Middle East respiratory syndrome
MHC	major histocompatibility complex
MMA	methyl methacrylate
NHS	*N*-hydroxysuccinimide
OD	optical density
OtBu	*tert*-butyl ester
Pbf	2,2,4,6,7-pentamethyldihydrobenzofuran-5-sulfonyl
PCR	polymerase chain reaction
PEGMA	poly(ethylene glycol) methacrylate
PfpOH	pentafluorophenol
pfu	plaque-forming units
PG	protecting group

PMA	peptide microarray
RBD	receptor-binding domain
rVSV-ZEBOV	recombinant vesicular stomatitis virus-Zaire ebolavirus
S1	subunit 1
SARS-CoV-2	severe acute respiratory syndrome coronavirus 2
S GP	spike glycoprotein
tBu	*tert*-butyl ether
TCR	T cell receptor
TFA	trifluoroacetic acid
Trt	triphenylmethyl
V	variable

1. Introduction

Molecules interact in different ways with attractive and repulsive forces influencing their interaction. For most protein functions, interactions with ligands, nucleic acids or other proteins are necessary. Transient or long-lived binding is mostly formed through noncovalent interactions, e.g., hydrophobic effects, hydrogen bonding and electrostatic interaction [1]. Hence, fundamental understanding of protein interaction will help to unravel biological processes of healthy cells and diseases. Consequently, understanding processes, such as antibody-antigen binding, can be applied for advanced applications, such as vaccine development and drug discovery. As an example, many pathogens are invading the body via binding to specific host cell receptors. The severe acute respiratory syndrome coronavirus 2 (SARS-CoV-2) utilizes the spike protein receptor-binding domain (RBD) for binding to the human receptor angiotensin-converting enzyme 2 (ACE2). While the SARS-CoV-2 mutated during the past years, it developed different variants. Due to structural changes of the spike protein, the viral binding affinity to the ACE2 of these variants differ, which is a main factor in viral transmissibility and for vaccine effectiveness [2].

Since the invention of the microscope, tissues and microorganisms can be visualized and studied. This allowed Louis Pasteur and Robert Koch to discover the relationship between pathogens and diseases in the 19th century. Today, molecular analysis is the most important method for the medical diagnosis of infectious diseases. During the COVID-19 pandemic two common diagnostic assays have been used intensively. First, the polymerase chain reaction (PCR) test to identify the viral RNA. Second, the antigen test, a lateral flow immunoassay, detecting SARS-CoV-2 antigens. Analyzing antigens of a pathogen can be used to identify a disease or to analyze the quantity of an encountered antigen. The enzyme-linked immunosorbent assay (ELISA) is used to analyze binding of antibodies to a corresponding antigen. Multiple analyses can be performed in 96-well plates or with even higher density to allow for higher throughput. In this way, many binding events can be investigated at the same time. Moreover, microarrays (MAs) can be utilized to screen a large number of molecular interactions in parallel and provide a platform for high-throughput screening in biology. Nowadays, MAs are not yet applied widely in diagnostics, because their production is still expensive and needs special equipment, which is not available in every laboratory. However, they have a great potential in the field of biomarker identification and epitope mapping. Furthermore, they can be used to study antibody response during the course of a disease or after vaccination. In this work, peptide microarrays (PMAs) were applied to investigate antibody development against peptide epitopes. Moreover, an automated laser-based technology was developed for the fabrication of high-density PMAs.

1.1 From amino acids to protein structure

Proteins are biopolymers, which play an important role in most cellular activities. Their function, ranging from structural elements to catalysts (enzymes) of metabolic reactions, is closely related to their structure. In eukaryotes, a large variety of proteins occurs and they are all built from a linear chain of amino acids (AAs). The 21 proteinogenic alpha-AAs are used during eukaryotic translation. They include the 20 canonical AAs (see Figure 1), which are encoded by nucleotide triplets in the genetic code, as wells as the rare selenocysteine [3]. These monomers have a common core structure: an amino group, a carboxyl group, a hydrogen atom, and a specific side chain group connected to a central alpha C-atom. The functional side chain groups lead to different physicochemical properties of each AA.
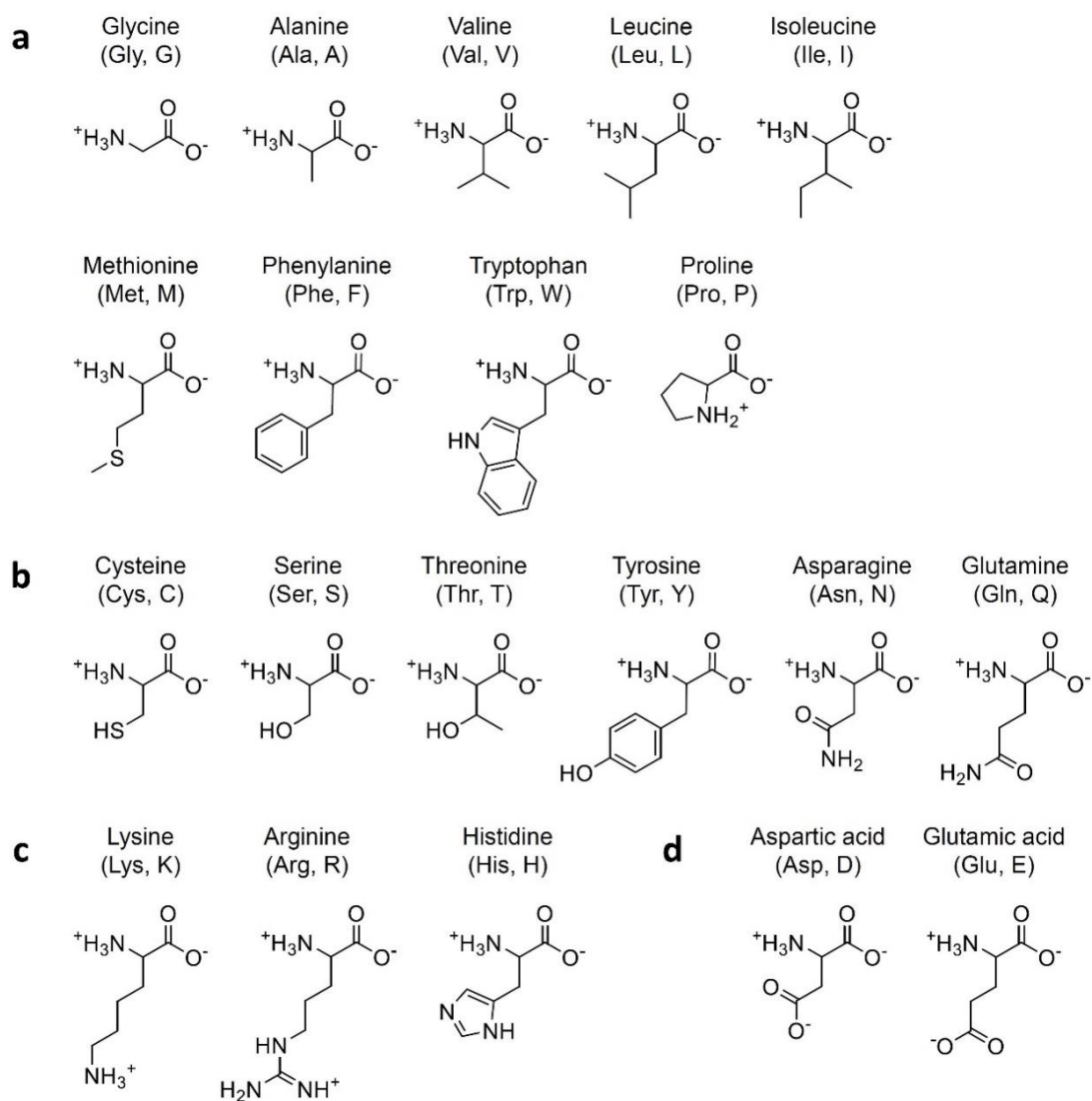

Figure 1: The 20 canonical AAs that are encoded by the nucleotide triplets of the universal genetic code. Grouped into a) hydrophobic AAs, b) polar AAs, c) positively charged AAs, and d) negatively charged AAs [4].

The condensation reaction of two AAs leads to the formation of a dipeptide. Long peptides are called polypeptides or proteins. The amino group of one AA and the carboxyl group of another AA react to form a peptide bond undergoing a condensation reaction. The C-N peptide bond has a double bond character (see Figure 2b). Moreover, rotation about the peptide bond (C-N and C=O) is restricted. Only the bonds between the alpha C and the carbonyl C of the fist AA, as well as the bond between the NH and the alpha C atom of the second AA can rotate [4]. That is causing the peptide bond to be planar (see Figure 2a) [4].
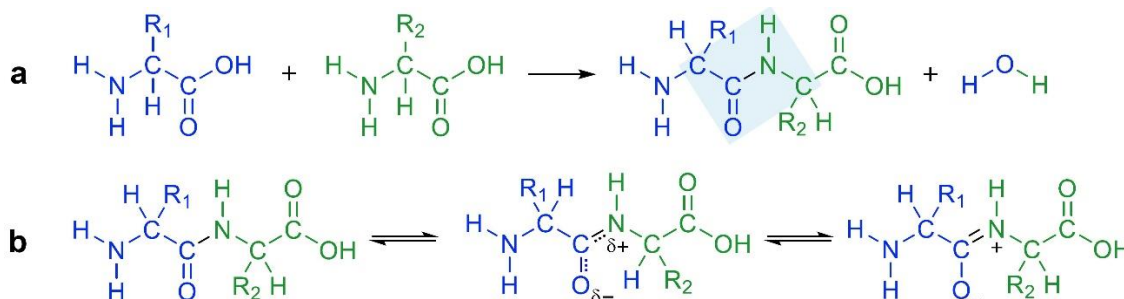

Figure 2: Characteristics of the peptide bond a) Condensation reaction of two AAs forming a dipeptide with a planar peptide bond. b) Double bond character of the peptide bond due to partial negative charge of carbonyl oxygen and partial positive charge on the amide nitrogen.

The peptide or protein chain starts with the N-terminus (amino terminus) and ends with the C-terminus (carboxyl terminus). Once the AAs grow into a polypeptide chain, the sequence forms a local conformation, which is called the secondary structure of a protein. This three-dimensional conformation is a result of hydrogen bond interactions between the amide (N-H) and the carbonyl (C=O) in the peptide backbone [4]. The two major secondary structures of proteins are the α-helix and the β-sheet (see Figure 3). The α-helix structure results from a hydrogen bond between the C=O of an AA to the N-H four AAs ahead of it [4, 5]. Within this helical turn, the side chain groups are pointing out of the helix. The second structure postulated by Pauling and Corey is the β-sheet [5]. It consists of at least two or more stretched polypeptide β-strands, which are held together by hydrogen bonding of adjacent strands [5]. Other structures, e.g., turns and loops, enable the polypeptide chain to reverse its direction and join different secondary structure elements (see Figure 3). Parts of the protein that are missing a higher order structure are called random coil. The overall folding of the whole protein is responsible for its tertiary structure. This three-dimensional shape is highly connected to the protein function, which is usually only gained when the polypeptide is folded. Proteins, soluble in water, have a core built of mainly hydrophobic AAs, and a hydrophilic surface due to more polar AAs. Mainly the hydrophobic interactions between the inner core AAs are inducing a globular tertiary structure of these proteins. Furthermore, hydrogen bonds between polar side chains and ionic interactions of side chains with positive or negative charges help to form the tertiary structure [4]. Additionally, disulfide bridges, covalent bonds between two cysteine
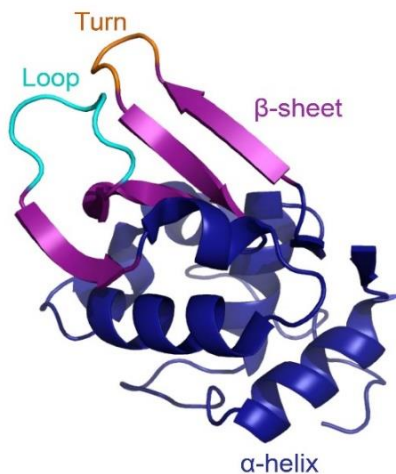
Figure 3: Three-dimensional structure of human lysozyme (pdb 133l) with highlighted secondary structure motifs [6] illustrated with PyMol.

residues, stabilize the protein folding. The counterpart of globular proteins are fibrous proteins, which are long filaments that are insoluble in water. Some proteins exert their function only when two or more subunits, which are each a polypeptide chain, form a complex quaternary structure. The interacting polypeptide chains can have the same or different sequences (homomeric or heteromeric). The protein diversity can be additionally enhanced via post-translational modifications, such as hydroxylation, phosphorylation or glycosylation at certain AAs. For example, hydroxyproline is present in collagen, the most abundant structural protein in humans [7]. Moreover, glycosylation is a common modification of proteins. The monosaccharides and the glycosidic linkages, which differ between organisms, create a great variety of glycans. Besides their role for biological functions, such as cellular interaction and recognition, glycans influence the folding and the half-life of a protein [8]. The two well-known forms of protein glycosylation are N-glycans and O-glycans. N-glycans are attached to the functional side chain of asparagine via N-glycosidic bond and O-glycans are bound to the protein via serine or threonine residues by O-glycosidic bond [8].

1.2 The human immune system

Our body is constantly challenged by environmental stress. Pathogens, e.g., viruses, bacteria, fungi, and parasites, are able to trigger an infection. Therefore, efficient defense mechanisms are necessary to combat diseases. Our immune system protects us from these threats by utilizing different proteins, cells, and organs, and can be divided into two main parts: the innate and the adaptive immune system. Organs and tissues, which play an important role within the immune system include the skin, spleen, lymph nodes and lymph vessels, thymus and bone marrow [9]. The blood is filtered in the spleen and lymph fluid is filtered in the lymph nodes. Both organs contain immune cells. Leukocytes (white blood cells) travel through our body inside the blood stream, the lymphatic system, or inside tissues to search for foreign (pathogens) or altered cells (cancer). As all types of blood cells, leukocytes differentiate from hematopoietic stem cells found in the bone marrow [9]. In most cases, the innate and the adaptive immune system function together in a complex interaction to fight diseases. We are born with a complex innate immune system, which immediately attacks invading pathogens. It comprises of physical barriers, such as skin and saliva,

4

antimicrobial proteins, the complement system, and immune cells, such as macrophages and natural killer cells. The adaptive immune system develops over a person's life due to contact with pathogens or vaccines and creates a memory to encountered antigens.

1.2.1 The role of B cells and T cells for the adaptive immune system

The interaction between B cells (bone marrow–derived) and T cells (thymus-derived) plays a very important role for the adaptive immunity. They react to new antigens and create a memory to respond efficiently to repeating infections. B cells, T cells, and natural killer cells are found in the lymph, and therefore called lymphocytes. T cells are produced in the bone marrow and their maturation occurs in the thymus. The production of B cells takes place in the bone marrow and their activation occurs in the spleen and lymph nodes [9, 10]. They are specialized to develop into antibody-producing cells after antigen contact. On the one hand, B cells can recognize soluble antigens originating from microorganisms, and on the other hand, they recognize captured antigens presented by dendritic cells or macrophages [11, 12]. B cells bind extracellular antigens, with their B cell receptor (BCR). Then, the BCR-antigen complex will be internalized and degraded into antigen fractions [10]. The internalization of the BCR-antigen-complex occurs in endosomes (endocytosis) or in phagosomes (phagocytosis) in case of large antigens [13, 14]. The degradation of a protein antigen into peptides with the help of proteases takes place after the endosome or phagosome fuses with a lysosome [13-15]. Inside the antigen-processing compartment (endolysosome or phagolysosome), the peptides are loaded onto the major histocompatibility complex (MHC) molecules class II [10, 15]. Subsequently, the MCH II-peptide complex will be presented on the B cell surface. Presentation of antigens is used to activate T helper cells, which bind to the MHC II-peptide complex with their T cell receptor (TCR) [15]. After binding of the TCR to the MHC-II-peptide complex, the T helper cell releases cytokines and expresses additional surface proteins binding to corresponding B cell surface proteins (see Figure 4) [16]. Consequently, the interaction between the T helper cell and the B cell promotes the survival, proliferation and differentiation of B cells into plasma cells [16, 17]. These differentiated B cells can secrete different isotypes of immunoglobulins; also known as antibodies. Secreted antibodies and BCRs are composed of the same immunoglobulin (Ig). Surface bound BCR comprises of additional domains, such as a transmembrane domain [9]. The variable region of an BCR or an antibody that bind the antigen are identical for the same B cell clone but differ between B cells. Next to B cells, also dendritic cells and macrophages present antigens to the T helper cells via MHC II molecules. These three cells are the professional antigen-presenting cells (APCs) of the immune system [18].
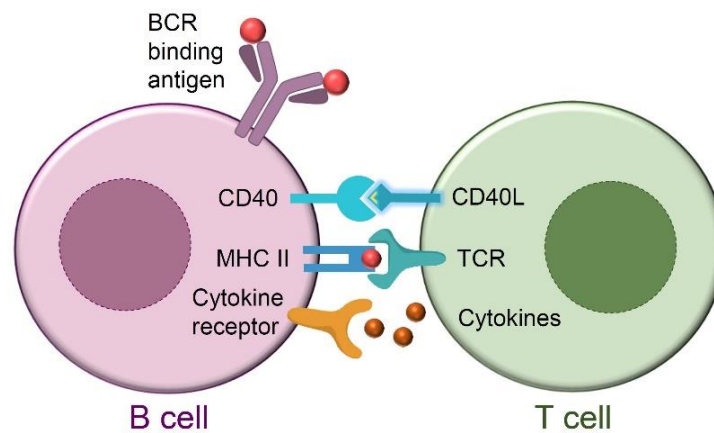
Figure 4: Interaction of B cell and T cell. The BCR captures an antigen. After internalization and degradation, the antigen is presented on the MHC II molecule to a T cell. The TCR binds the presented antigen. Then, the T cell expresses more surface proteins, such as CD40L and cytokines to promote B cell proliferation and differentiation.

If solely an antigen is activating a B cell without T cell stimulation, it will differentiate into a short-lived, proliferating antibody-secreting plasmablast and secrete mostly IgM, an early weak-affinity antibody. Microbial lipopolysaccharides antigens can induce this activation pathway [9]. However, the stimulation by T cells is leading to the differentiation of B cells into long-lived, non-proliferating antibody-secreting plasma cells and the production of more variable antibody isotypes [9, 19]. Next to the differentiation of B cells into plasmablasts or plasma cells, another important evolution for long-lived immunity is the development of memory B cells. Multiple programming events, such as repeated antigen contact and T helper cell stimulation are necessary to generate memory B cells and memory plasma cells [17]. For vaccine strategies, effective B cell memory is a desired outcome. Repeated vaccinations are a way to ensure the development of high-affinity antibodies and memory B and T cells.

Unlike B cells, T cells only recognize antigens, which are presented by MHC molecules. T cells are grouped according to their function and are distinguished by expression of surface marker proteins; cluster of differentiation (CD). The two dominant types are T helper cells (CD4+) and cytotoxic T cells (CD8+). Endogenous antigens are presented on the cell surface if a virus or bacterium infected it, or if the cell suffers from a serious mutation (tumor growth) [9]. Endogenous antigens can be bound to the MHC I molecules and brought to the cell surface to be presented to cytotoxic T cells (see Table 1) [9]. All nucleated cells have MHC I molecules on their surface [9, 20]. Consequently, cytotoxic T cells can kill infected cells or tumor cells. Exogenous antigens are released from pathogens or are present on their surface without penetrating the host cell. These antigens are often captured and engulfed by APCs, which present the antigen via MHC II molecules to trigger other immune cells to recognize the infection [9]. T helper cells can bind to the MHC II-antigen complex and activate other immune cells, such as B cells and macrophages, to clear the pathogen (see Table 1) [9]. Between the interface of a T cell and an antigen-presenting cell (APC) a highly

organized and dynamic immunologic synapse is formed [10, 21]. After the first contact between MHC II-peptide complex and TCR, more cell surface proteins interact to form a stable interface [21]. The cell contact area is used for interaction and information flow between the cells after antigen contact. An immunological synapse is formed between an APC and a lymphocyte (B/T cell) and involves cytoskeleton reorganization and cell-surface receptor enrichment for cell polarization [10, 21].

Table 1: Different T cell types recognize presented antigens of different origin.

Cell type	Cluster of differentiation	Activation via	Antigen processing
T helper cell	CD4	Antigen-presenting cells (MHC II-peptide complex)	Exogenous antigens (bacteria, virus)
Cytotoxic T cell	CD8	Infected and abnormal cells (MHC I-peptide complex)	Endogenous antigens (intracellular pathogens, cancer cell)

Activated antigen-specific T cells expand and differentiate into effector T cells to help clearing an infection. Afterwards, the majority of T cells die by apoptosis [22]. A fraction of primed T cells persists as long-lived memory T cells and can quickly protect the body in case of recurrent infection [23, 24].

Both MHC I and II bind the peptide in a groove of the three-dimensional protein structure [25-27]. However, the structure of the binding grooves differ between the two types. The MHC I groove is closed and binds short peptides (9 to 11 AA residues), whereas the MHC II groove is having a more open conformation enabeling longer peptides (9 to 22 AA residues) to interact [27]. The core peptide is bound in the MHC II groove and additional AA residues of longer peptides extend outsite the groove [25-27]. The allelic variation of the MHC genes between humans causes small structural differences in the MHC peptide-binding groove [20]. Thereby the genetic variability influences the repertoire of peptides presented [20]. The different MHC variants are expressed from the human leukocyte antigens (HLAs) gene complex, which are the most polymorphic genetic region in humans [28]. Next to the genetic polymorphism, factors, such as protease and chaperone activity for the antigen digestion, explain small differences in MHC antigen presentation resulting in individual T cells antigen recognition [20, 28].

1.2.2 Antibody structure, function and mechanisms for structural variety

A plasma cell can secrete thousands of antibodies per second. The 150 kDa big protein consists of four polypeptide chains: two identical heavy and two identical light chains. Disulfide bridges connect the two heavy chains and each light chain to the heavy chain. Each polypeptide chain has

a constant and a variable (V) region. The two identical antigen-binding sites consist of the variable regions of the heavy chain (VH) and of the light chain (VL) and determine the antigen binding property of each antibody (see Figure 5).
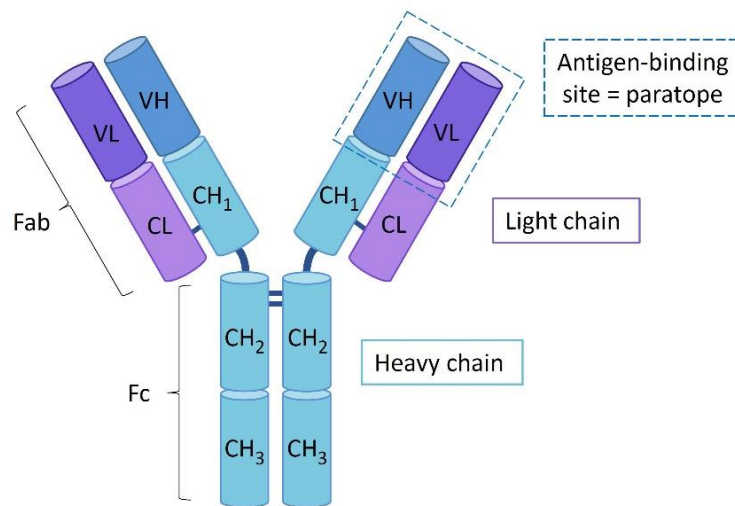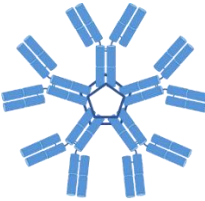

Figure 5: Immunoglobulin G (IgG) structure divided into fragment crystallizable (Fc) and fragment antigen-binding (Fab). Each (purple) light chain (L) consists of a constant region (CL) and a variable region (VL). Each (blue) heavy chain (H) consisting of several constant domains (CH$_1$, CH$_2$, CH$_3$) and a variable region (VH). Disulfide bonds join the two (blue) heavy chains together and each (purple) light chains is joined to the heavy chain.

The three variable segments in the light and the heavy chain (VH and VL) contain hypervariable loops and framework regions [9]. The β-sheet framework regions have a smaller AA variability than the hypervariable loops, also known as complementarity determining regions (CDRs) [29]. The six CDRs (three in VH and three in VL) are the most variable region of an antibody and define its antigen-binding site (i.e. paratope) [9]. The antibody binds the antigen by forming a pocket between the AAs of the CDRs, which are complementary in size, shape and charge to the ones in the antigen [30]. The Fab fragment surface topographies form different structures, such as cavities, grooves, or are more planar [29]. There are nine forms of heavy chain constant regions, which determine the different immunoglobulin classes or isotypes: IgA, IgD, IgE, IgG, and IgM (see Table 2 and Table 3) [9]. Furthermore, there are four subclasses of IgG and two subclasses of IgA. Often, IgA and IgM occur as multimers (see Table 2). The dimeric IgA and the pentameric IgM are linked by a joining (J) chain and disulfide bonds [9]. IgG is the most abundant isotype in the human blood and lymph fluid (systemic immune system), whereas dimeric IgA is prevalent in the gastrointestinal and respiratory tract (mucosal immune system) [9]. Dimeric secretory IgA is complexed with the secretory component, which is a glycoprotein necessary for the epithelial cell transport of dimeric IgA into the lumen of organs, such as nose, gut, or bronchia [31]. In contrast, in the blood mainly monomeric IgA is present [9].

Table 2: Antibody classes and multimers.

Immunoglobulin isotypes / classes				
IgA1,2	IgD	IgE	IgG1-4	IgM
Constant region heavy chain form				
α1, α2	δ	ε	γ1-4	μ
Monomeric IgA, IgD, IgE, IgG		Dimeric IgA		Pentameric IgM

A key function of antibodies is the neutralization of pathogens by blocking their surface or their released toxins due to binding with the variable region [32]. A very effective protection is accomplished, if the antibody neutralizes surface proteins of the pathogen, which are needed to infect the host cell. The larger heavy chain is bearing the constant region, which plays a role for immunity beyond antigen binding. In contrast to the variable region, the Fc fragment determines the effector function of an antibody depending on the isotype. In this way, the antibody cannot only block an antigen, but also label an antigen for other immune cells. Activation of the complement system or recruitment of other immune cells, such as phagocytes or natural killer cells are typical effector functions [32]. Immune cells that can engulf a microorganism in a process called phagocytosis have Fc receptors for binding to the constant region of an antibody [32]. The phagocytosis is enhanced, when antibodies label a pathogen. The process of antibody mediated phagocytosis is called opsonization [9].

A large amount of different BCRs, antibodies and TCRs is required to ensure selective and specific binding to a diverse range of antigens. Every human has a broad repertoire of antibodies. They are the soluble form of the BCR. A great diversity of the receptors and antibodies is created with genetic mechanisms. First, the variety of TCR and BCR is accomplished via rearranging gene segments encoding for the antigen-binding variable region [33-35]. The assembly of gene segments in B cells for diverse antibody production is known as somatic recombination or V(D)J recombination and will be explained in the following based on Murphy et al. [9]. The antibody´s heavy and light chain contain each a variable region (VH and VL) and a constant region (CH and CL). There are two types of light chains (κ and λ) and one heavy chain, which are organized in distinct gene loci [9]. The corresponding genes of the variable regions are composed of multiple different gene segments. These gene segments encode different sequences and need to be assembled to form a complete template for the variable regions. The variable region of an Ig heavy chain contains multiple variable (V), diversity (D), and joining (J) gene segments (see Table 3). The variable region of an Ig light chain contains multiple V and J gene segments (see Table 3). During the recombination process, one V, D (only in the heavy chain) and J gene segment are assembled stepwise creating the complete gene. The constant (C) region of the heavy chain is determined later during DNA rearrangement of Ig class switching. The random selection of one of multiple gene segments enable unique variable regions of each antibody [9]. Consequently, the large number of randomly assembled genes for the antigen-binding sites empowers the recognition of many

Table 3: Number of gene segments to assemble to the full gene of the variable regions in the light and the heavy chain of immunoglobulins. This table is based on Figure 5.2 in chapter 5 of [9].

Segment	Light chain		Heavy chain
	κ	λ	H
Variable (V)	34 - 38	29 - 33	38 - 46
Diversity (D)	0	0	23
Joining (J)	5	4 - 5	6
Constant (C)	1	4 - 5	9

different antigens. Next, a junctional diversity between different segments arises from addition or subtraction of nucleotides during segment joining [33].

Upon antigen contact in form of natural pathogens or vaccination, B cells differentiate into antibody-producing plasmablasts, plasma cells, or memory B cells. The differentiation is supported by T cells. B cell maturation takes place in the germinal center, which is formed during immune response in the lymph nodes. The special structure is seeded by antigen-stimulated B and T cells and is an important site for B cell proliferation and cell death [36]. Important processes during B cell maturation and antibody production are immunoglobulin affinity maturation and class switching. First, point mutations (somatic hypermutation) in the variable region increase the diversity and affinity of antibodies after an initial antigen contact [9, 33]. Interestingly, only one enzyme is responsible for the whole mechanism of hypermutation. The activation-induced cytidine deamidase is converting the DNA base cytosine to uracil by catalyzing deamination resulting in different mutation mechanisms [37]. The constant change of the variable region of an antibody is crucial during infections with changing antigen structures. Secondly, only the B cells with high antibody affinity for the antigen receive survival signals from T helper cells (clonal selection) [9]. The two affinity maturation processes raise the diversity of antibodies and their binding capacity to the antigen [9, 17]. Lastly, immunoglobulin class or isotype switching refers to the change of antibody isotype, which is produced by a plasma cell after pathogen contact. It takes place after V(D)J recombination and affinity maturation of a B cell clone, when the variable region of the immunoglobulin is fully mature. The BCR during B cell maturation is a monomeric IgM or IgD and can change to different isotypes, such as IgA, IgG or IgE [9, 32]. Only the constant region of the heavy chain will be changed irreversibly during class switching. Gene fragments of the full-length heavy chain constant region will be recombined out with the help of enzymes resulting in expression of only one of nine possible isotypes of secreted antibody (see Table 32 and Table 3) [9]. The specific Fc region is important for determining the antibody´s effector function [38]. The gene segment for the μ heavy chain are adjacent to the VDJ genes and therefore expressed first [9]. Hence, IgM is the first immunoglobulin isotype, which is produced during B cell maturation. The antibody isotype, which will be produced after class switching, is highly dependent on the type of cytokine secreted by T helper cells in the interaction with B cells after antigen contact [9].

1.2.3 Epitope definition & epitope mapping

The small fraction of an antigen, which is bound by the antibody, BCR or TCR, is called epitope. The mostly encountered antigens are proteins, but also polysaccharides can act as antigen. Solvent-exposed regions in the antigen can be recognized by B cells or antibodies whereas T cells recognize antigen fractions displayed by antigen-presenting cells via MHC molecules (see Table 1). Therefore, the recognition of T cell epitopes is dependent on the digested antigen as well as the expressed MHC molecules. Due to an identical antigen-binding site of the BCR and the Fab fragment of the secreted antibody, the B cell and the antibody epitope of one B cell clone are the same. Therefore, B cell epitopes can be identified by analyzing the binding of antibodies to an antigen region after immune response. Commonly, B cell epitopes can be classified into linear and conformational epitopes. A linear protein epitope is a sequence of consecutive AAs, whereas a conformational epitope constitutes distant AAs, which come into close proximity due to protein folding. Furthermore, B cell epitopes can be categorized as continuous (sequential) or discontinuous epitopes. However, there is no clear separation between these definitions (see Figure 6).
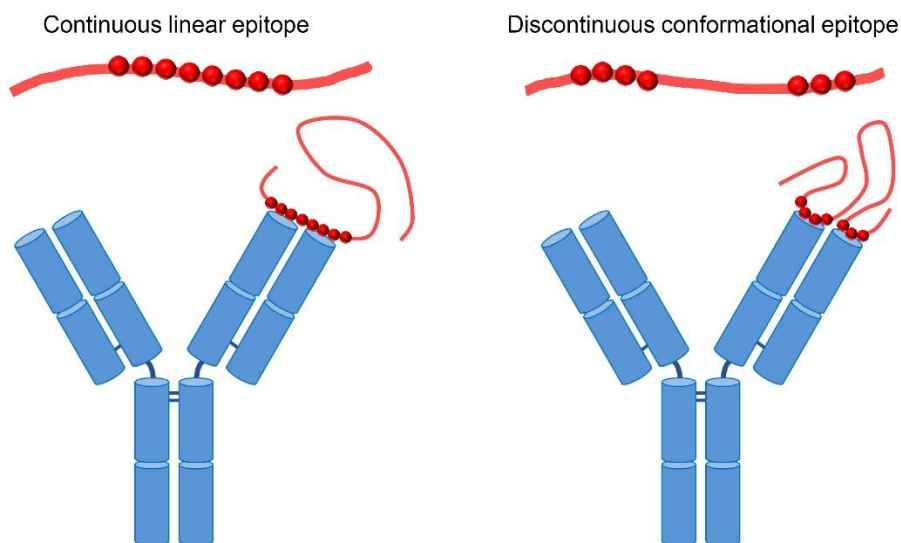

Figure 6: B cell epitopes can be linear or conformational. They are recognized by the BCR or the antibody paratope. Conformational epitopes are more abundant due to protein folding.

It is difficult to determine, whether all consecutive AAs (continuous) in a stretch of a linear epitope are included in binding or if some AAs within the stretch do not take an active part in the binding (discontinuous). This could be assessed performing substitution analyses of AAs. Usually, linear epitopes can also be bound in the denatured form of the protein. Therefore, peptides can be used to display linear epitopes. However, peptides outside the stabilizing tertiary protein structure usually form only random coiled or low level of α-helix conformation [39]. Moreover, also linear or continuous epitopes can be part of a folded protein structure. It was evaluated that approximately

90% of B cell epitopes are conformational or at least part of a higher-order structure [40-42]. The less frequent linear epitopes have the potential to replace a whole antigen, making linear epitope identification or prediction relevant for vaccine development and monoclonal antibody production. Today only few peptide vaccine candidates mad it to clinical trials, e.g., one against influenza [43]. More complex vaccines, which are composed of inactivated or attenuated pathogens, can effectively stimulate B cell and T cell responses, which is challenging to be induced with peptide-based vaccines.

Epitope mapping is the identification of an epitope bound by an antibody. Analysis of B cell epitopes is the most commonly used method, because antibodies can be easily obtained from blood and do not require cell cultivation. A prerequisite for epitope mapping is the identification of an antigen. This can be performed with ELISA, where the antigen is coated on a surface. An antibody of interest or antibody containing sample (blood serum) is incubated with the immobilized antigen. Afterwards, the binding antibody is detected with a secondary antibody, which is conjugated with an enzyme that can catalyze a detectable reaction of a substrate. This results in the development of a color with an intensity correlating with the amount of enzyme-conjugated secondary antibody binding.

Several methods for detailed epitope identification have evolved and are usually applied to characterize monoclonal antibodies. At first, structural biology approaches can be applied to visualize the epitope. Therefore, the antibody has to be co-crystallized with the antigen, followed by X-ray diffraction and structural analysis, to gain detailed information on the epitope and paratope interaction. This method enables determining a molecular structure at high resolution, which allows for detailed analysis of the interacting AA residues of epitope and paratope. However, it is time-consuming and does not give evidence which AAs of the epitope contribute the most to the recognition [44]. For linear epitopes, it is often seen that not all AAs in the peptide sequence have the same importance for the paratope binding and can be even substituted by others. An other technique is the cryogenic electron microscopy (cryo EM) assisted by single particle analysis. The structural analysis of antibody-antigen interactions with cyro EM usually has a lower resolution than crystallography. Though, the techniqe is faster and does not need a high amount of crystallized material for the measurement.

With mutagenesis, DNA mutations are engineered to the gene of interest, to produce mutant antigens. The effect of the protein mutation on its ability to be recognized by the antibody can be examined to determine the epitope. Loss of binding indicates that the mutated AA is crucial for the antibody-antigen interaction. In alanine scanning mutagenesis, every AA residue in the protein sequence is subsequently replaced by alanine and an alanine residue in the original sequence is replaced by glycine [45]. This method is fairly simple but laborious due to the expression and purification of all mutated proteins [44].

In phage or yeast display, foreign DNA of interest is inserted into the microorganism´s gene for a surface protein, which will lead to the expression of the foreign protein or peptide on the surface [46]. The different variants of phages or yeasts can then be tested in binding assays, such as ELISA, with subsequnt gene isolation and analysis. On the one hand, the technique can be used to express different versions of antigens, which can be studied in binding assays with immobilized antibodies to capture high-affinity antigens [46]. On the other hand, the phage or yeast can be used for expression of different antibodies or antibody fragments for an reverse approach with immobilized antigen [47]. The technique is powerful, but demands a lot of expertise and repeated cycles of binding, isolating and amplifying phages to obtain higher-affinity binders.

A peptide microarray (PMA) comprises a miniaturized spot pattern of different peptide sequences, which originate from a protein. Most frequently, a protein sequence or even a full proteome is cut in silico into overlapping peptides, which can have a different offset (see Figure 7). As an example, 15-mer peptides with 14 overlapping residues have an offset of one AA or 15-mer peptides with 13 overlapping residues have an offset of two AAs. These differences can result in varying detailed analysis of the antibody binding. Similar to the ELISA method, the sample can be incubated on the array surface after a blocking step. The peptide-binders (e.g., antibodies) are usually detected by a secondary antibody, which is conjugated with a fluorescent dye (see Figure 7). The readout is performed with a fluorescence scanner. PMAs are most commonly used to analyze B cell epitopes with antibodies from serum samples. However, they can be applied to investigate other protein-protein-interactions [48]. Furthermore, they can be applied to perform substitution analysis of AAs within a peptide epitope, to detect the AA residues taking an active part in binding [49, 50]. PMAs allow for high-throughput screening in a fast and simple manner. However, they can only be used to analyze linear B cell epitopes.
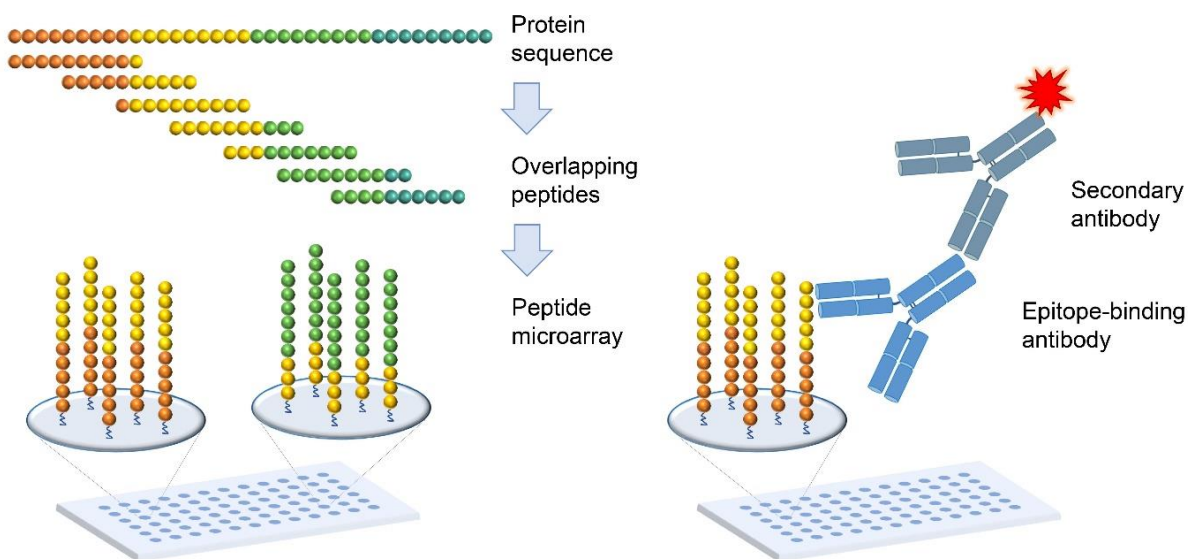
Figure 7: PMA fabrication and linear epitope mapping. Left: Overlapping peptides are obtained from the protein sequence. Each spot of the microarray contains many peptides of the same sequence. Right: The antibody of interest or an antibody containing sample is incubated on the peptide microarray. The binding antibody is detected with a secondary antibody, which is conjugated with a fluorescent dye.

1.3 Microarrays

A microarray (MA) is a solid support, most commonly a glass slide, which has many different molecules attached to its surface in a miniaturized pattern. MAs aim to increase the number of parallel analyses of molecular interactions between a sample and the molecules attached to the array. Furthermore, the parallel screening is reducing the necessary amount of sample for incubation. A major goal of MA production is to increase the number of molecules placed in a certain area. The spot-to-spot distance (i.e. spot pitch) specifies the distance between the centers of two neighboring spots and is therefore determining the density of distinct spots per area.

For MA fabrication, two main technologies can be distinguished: The first is the pre-synthesis or extraction of molecules with subsequent deposition onto the surface and binding. For deposition of pre-synthesized molecules, mostly printing (i.e. spotting) of molecules in aqueous solution with the help of a spotting robot is used. The second technology is the in situ synthesis. With this approach, many different molecules are synthesized at the same time in small amounts directly on the MA surface. Compared to spotting of single pre-synthesized molecules, the simultaneous synthesis requires less material and time and is therefore ideal for MA production. Particularly for the production of up to thousands of different molecules, only the in situ technology for synthesis is feasible. However, a direct verification of every biooligomer structure can only be executed with chemical analysis of pre-synthesized molecules. For both main production technologies, the molecules can either be covalently or non-covalently attached to the MA surface, which functions

as solid support. Most of the time, a covalent linkage is preferred. Depending on the available functional moieties of the biomolecules, the introduced functional groups on the MA surface for the covalent attachment vary. The glass surface can be directly modified for the introduction of functional groups or it can carry an additional network of polymer for a three-dimensional presentation of functional groups (see Figure 8). Non-covalent immobilization can be carried out via adsorption of the biomolecule on the solid support or by introducing hydrophobic lipid-linkers [51] or complementary DNA linkers [52].
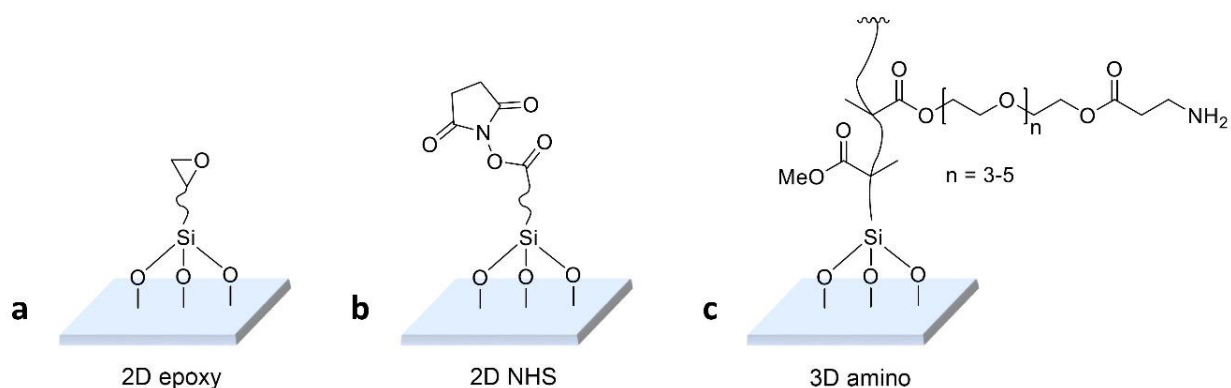

Figure 8: Examples of MA glass slide functionalization. a) Two-dimensional functionalization with epoxy group. b) Two-dimensional functionalization with *N*-hydroxysuccinimide (NHS) ester. c) Polymer functionalization with poly(ethylene glycol) methacrylate (PEGMA) and methyl methacrylate (MMA) and β-alanine for three-dimensional amino group presentation (PEPperPRINT slide).

Different biomolecules can be immobilized on a microarray. DNA MAs are used for gene expression level measurement, but are now replaced by next generation sequencing techniques [53]. Protein microarrays can utilize specific antibodies to capture target proteins in a sample mixture [54]. Furthermore, protein arrays can display purified proteins to study protein function (e.g., protein-protein interaction, binding of other biomolecules) or to determine the presence of post-translational modifications [55]. Reverse-phase protein arrays use cell lysate to immobilize all expressed proteins of a tissue, cell or body fluid to detect a target protein or protein modification [56, 57]. They can be used to analyze protein phosphorylation as marker of pathway activity [56] or to compare protein expression under different conditions [58]. PMAs as well as glycan microarrays are often utilized to perform epitope mapping for infectious disease research and vaccine development [59, 60]. The relatively robust chemical synthesis of peptides enabled the development of different PMA fabrication technologies.

1.3.1 Peptide microarray fabrication

One of the first techniques for PMA fabrication was developed by Geysen et al. in 1984 [61]. The peptides were synthesized on polyethylene pins (solid support) and presented in an ELISA plate format for the identification of linear epitopes. The array-based approach was later also known as

Pepscan. Following this development, other methods for PMA fabrication were devised. Today, PMAs are widely used for the identification of linear epitopes among thousands of overlapping peptides, thus they are utile to screen for biomarkers [59]. Furthermore, they are applied to analyze antibody responses during infectious diseases or after vaccination [62, 63]. This can assist to compare the strength of a triggered antibody production against epitopes over time. Moreover, PMAs can be used to determine substrate specificity of enzymes [64]. For high-throughput screening, in situ synthesis of peptides allows for the generation of thousands of different peptides at the same time. Different technologies have been developed for the in situ synthesis of peptides and most of them will be explained in the following chapters (1.3.1.2 – 1.3.1.5). The foundation of PMA fabrication is the solid-phase peptide synthesis (SPPS) developed by Merrifield.

1.3.1.1 Solid-phase peptide synthesis

A pioneer in the field of automated synthesis of biopolymers, Merrifield, introduced the SPPS on a resin in 1963 [65] and further developed a machine for automated SPPS [66]. To overcome the limits of polypeptide synthesis, Merrifield linked the protected AA, growing into the peptide, to a solid support. Thus, he replaced time-consuming purification of the intermediates by simple washing steps. The SPPS applies repetitive cycles of activation, coupling, and deprotection of protected AAs and allows for high polypeptide synthesis yield (see Figure 7). The synthesis of peptides is carried out from C-terminus to N-terminus, which needs to be protected during coupling reaction to prevent reaction between AAs. Therefore, the α-amino group is protected by a temporary protecting group (PG), which should be easily removable before each coupling step. A permanent PG is protecting the functional groups of the AA side chain and it should be stable throughout the whole synthesis. For solid-phase synthesis, it is favored in most cases to remove the permanent PGs simultaneously with the peptide liberation from the resin. Therefore, a sophisticated system of temporary and permanent PGs and linkage to the solid support is necessary. The first requirement for Merrifield´s SPPS was a polymer, which is insoluble in used solvents, carrying a functional group for the reaction with the first AA and having a porous structure in the swollen state to allow for easy penetration [65]. Next, he investigated suitable conditions for deprotection, AA coupling and acetylation of unreacted amine groups. Lastly, the covalent linkage of the growing peptide to the solid polymer particles (resin) needed to be stable during the process but cleaved again after the synthesis to release the peptide. During the automation process, Merrfield changed the carbobenzoxy PG for the tert-butyloxycarbonyl group (Boc) for the α-amino groups (see Figure 8), thereby the removal became easier and the deprotection resulted in less partial cleavage of the peptide from the resin [66]. Furthermore, he was able to synthesize an nonapeptide carrying benzyl side chain PGs, which were deprotected simultaneously with cleavage

from the resin. Due to this achievements the first long polypeptides, such as insulin could be produced afterwards [67].
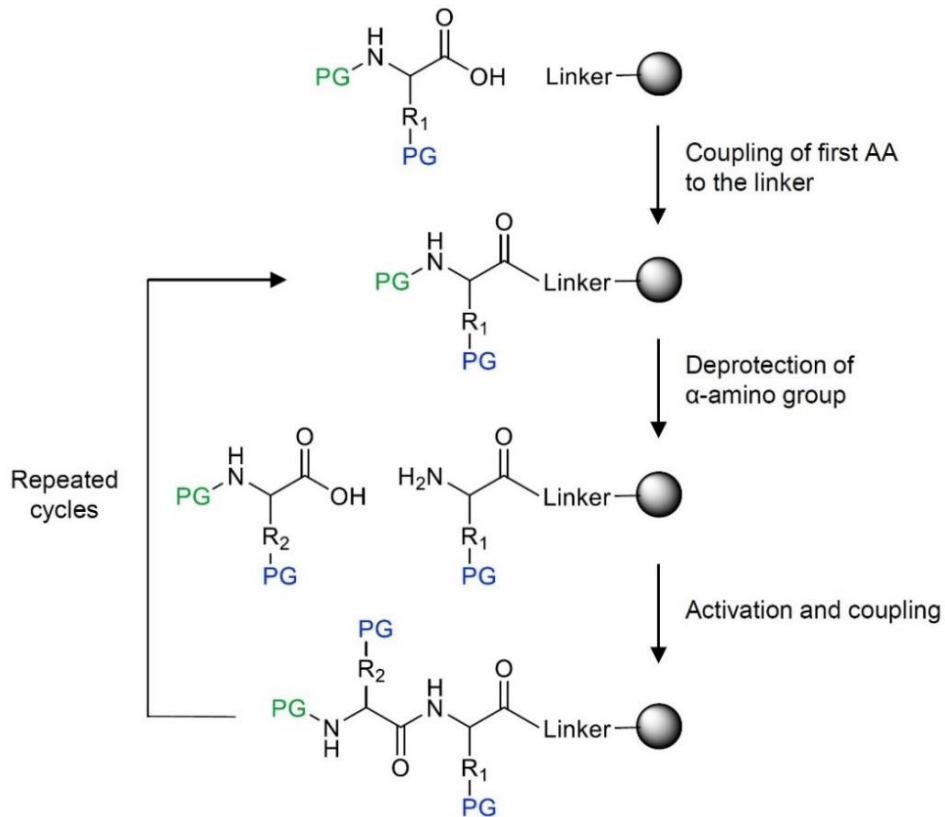

Figure 7: Basic principle of the SPPS. The first AA protected with a (green) temporary PG and a (blue) permanent PG is activated and coupled to a functionalized resin via the carboxyl group. Next, the (green) temporary PG is removed from the α-amino group to allow the next AA to couple. The consecutive steps are followed by washing. The steps are repeated until the desired peptide sequence. After the synthesis, the different (blue) permanent PGs are removed with concomitant peptide cleavage from the resin depending on the strategy and linker.

Consequently, automated solid-phase synthesis of other biooligomer classes, such as oligonucleotides [68] and oligosaccharides [69], apply an equivalent principle of repetitive cycles.

The use of Boc as temporary PG for the α-amino group became the first common SPPS strategy. It is cleaved under acidic conditions generally using trifluoroacetic acid (TFA). The side chain PGs are stable under TFA conditions, but cleaved during peptide release from resin [70]. For release of the final peptide from the resin, hydrofluoric acid (HF) is most commonly used, but the harsh conditions require special equipment and safe handling [70].

Moreover, the fluorenylmethoxycarbonly (Fmoc) group was introduced as temporary PG for the α-amino group (see Figure 8), to overcome the constant use of corrosive TFA, which was causing unwanted partial removal of acid-labile side chain PGs as well as peptide cleavage from the resin [70]. The orthogonal Fmoc PG is labile to bases, particularly secondary amines, leading to the advantageous absence of acid during the peptide elongation steps. For Fmoc deprotection, 20%

of piperidine in *N,N*-dimethylformamide (DMF) is widely used and does not cause any loss of the permanent side chain PGs.
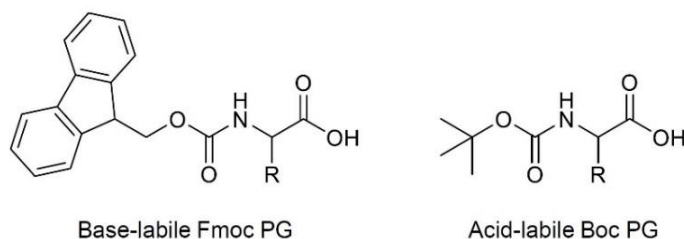

Base-labile Fmoc PG   Acid-labile Boc PG

Figure 8: The α-amino group of an AA protected by either base-labile fluorenylmethoxycarbonly (Fmoc) or acid-labile tert-butyloxycarbonyl group (Boc).

The Fmoc PG was proposed by Carpino and Han in 1972 for solution chemistry [71], but was explored later to be a suitable invention for SPPS [72]. The non-volatile dibenzofulvene produced during Fmoc cleavage could undergo unwanted reactions, such as polymerization in solution peptide synthesis. This problem could be avoided during Fmoc SPPS, where it was simply washed away [72, 73]. Furthermore, the UV absorption properties of the dibenzofulvene can be used to quantify the coupling reaction success [72, 73]. For the AA coupling reaction the α-carboxyl group has to be activated (see Figure 9). For example, *N,N'*-dicyclohexylcarbodiimide (DCC) or *N,N'*-diisopropylcarbodiimide (DIC) are used for activation in combination with *N*-hydroxybenzotriazole (HOBt) or pentafluorophenol (PfpOH) to obtain an active ester (benzotriazole or pentafluorophenyl ester). The active esters can either be pre-generated or formed in situ.
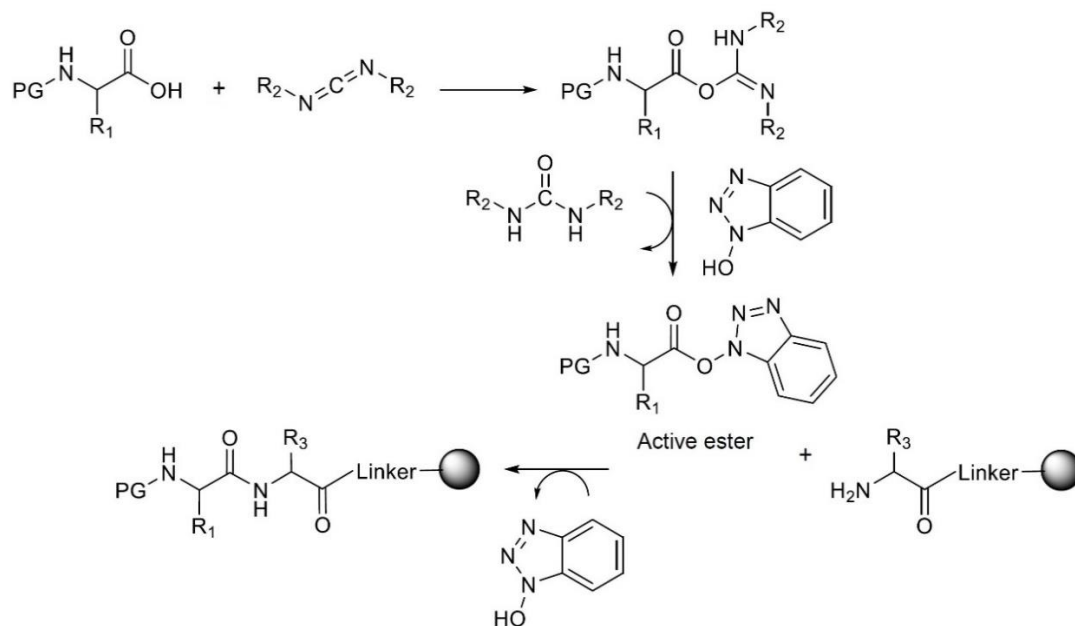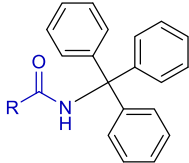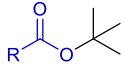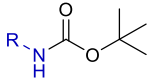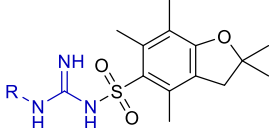

Figure 9: AA carboxyl group activation with carbodiimide and HOBt for the formation of an active ester followed by C-terminal coupling to a free α-amino group of the AA/peptide immobilized to the resin.

Due to the use of the base-labile temporary PG, it is possible to use more sensitive acid-labile side chain PGs (see Table 4) for Fmoc SPPS and avoid the harsh conditions for their removal. For side

chain deprotection different concentrations of TFA depending on the permanent PG need to be applied. During the acidic deprotection of the side chain groups, reactive electrophilic carbocations are generated, which have to be quenched to prevent side reactions with the AA´s functional groups, e.g. Tyr, Trp, Cys, and Met [70, 72]. Therefore, nucleophilic scavengers, such as water and triisopropylsilane are added to the TFA. At the same time as the removal of permanent protecting groups, the linkage between peptide and resin is cleaved. Linkers for Fmoc SPPS are designed to release the peptide upon TFA treatment with α-carboxyl group as acid or amide [72]. After cleavage from the resin, the volatile TFA can also be readily removed.

Table 4: Standard acid-labile permanent PGs for Fmoc SPPS for global peptide deprotection with TFA [73]. For triphenylmethyl a structural example for Asn or Gln is shown.

Amino acid	Side chain permanent PG	Structure
Asn, Gln, Cys, His	Triphenylmethyl (Trt)	
Asp, Glu	*tert*-butyl ester (OtBu)	
Ser, Thr, Tyr	*tert*-butyl ether (tBu)	
Lys, Trp	*tert*-butyloxycarbonyl (Boc)	
Arg	2,2,4,6,7-pentamethyldihydrobenzofuran-5-sulfonyl (Pbf)	

The advantage of Fmoc SPPS is the orthogonal PG strategy allowing for the replacement of frequent TFA use and replacement of HF by TFA for final deprotection and peptide release. The absence of special equipment in Fmoc SPPS is leading to easy automation and accordingly broader application. However, the Fmoc SPPS also has some drawbacks in comparison to the Boc approach. Aspartimide formation is the most serious side reaction occurring in Fmoc SPPS. Aspartic acid can undergo a base-catalyzed cyclization with the next AA´s amine [72, 73]. Furthermore, cysteine and histidine are prone to racemization during coupling, but it can be reduced using DIC activation and active ester formation [73]. Sequence dependent (hydrophobic peptides) poor solubility of peptides or aggregation caused during formation of secondary structures in longer peptides are further limitations of Fmoc SPPS [73].

1.3.1.2 Liquid-based in situ synthesis of microarrays

For liquid-based synthesis of PMAs, the AAs are transferred in solution to the solid support to react in a specific area of the array. For different techniques, the approach of liquid transport as well as suitable surface properties of the synthesis substrate vary. A milestone in PMA history was the development of the SPOT synthesis by Frank in 1992. Inspired by the Pepscan or multipin method of Geysen et al. in 1984, Frank combined the principle of Fmoc SPPS and in situ synthesis to produce peptides in parallel on a cellulose membrane [74]. In this method, AA containing solutions are pipetted to distinct spots on a cellulose membrane sheet, which takes up the reagent solution (see Figure 10). For the coupling reaction, the cellulose membrane is functionalized with β-alanine to display free amino groups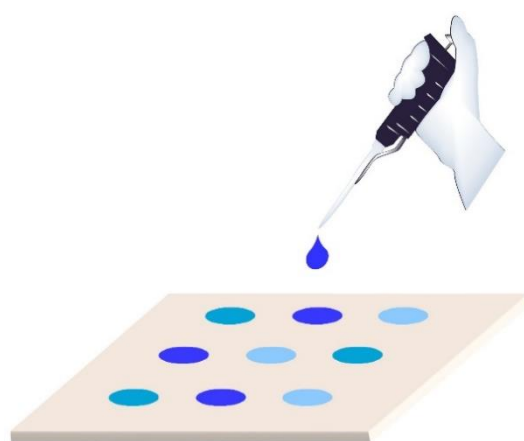. The spotting and coupling reactions are carried out with low volatile solvents. Afterwards, the entire membrane is washed and treated with reagents (e.g., for deprotection). Starting from manually dispensed solutions, the method was later extended by spotting robots for automated liquid delivery [75]. To trace the coupling reaction, bromophenol blue can be applied to indicate free amino groups with blue color and complete coupling with a change to yellow [74]. This staining technique helps to determine parameters, which enable high reaction yields (e.g., reaction time, AA concentration, necessity of re-spotting). The final

Figure 10: Manual spotting onto cellulose membrane for SPOT synthesis.

peptides can directly be used for antibody binding assays or are cleaved from the cellulose membrane. Even if the SPOT synthesis is not as miniaturized as other in situ synthesis approaches, it was adopted by many researchers, because it is easy to perform, inexpensive and allows for a reliable custom peptide synthesis in parallel [75]. The diffusion of the solution inside the porous membrane limits the spot density. Using a spotting robot, the peptide spots can have a size of 1 mm and a spot pitch of 2 mm, resulting in only 25 spots per cm^2 [76]. Such macroarrays need a high amount of sample for incubation. A further development of the SPOT synthesis is the use of a special membrane, which can be solubilized during TFA side chain deprotection without liberation of the peptide from the cellulose (CelluSpot by Intavis Peptide Science) [76]. Then, the peptide-cellulose conjugates can be diluted and spotted with smaller spot pitch onto a glass slide [76]. This process facilitates the production of several MA copies from one SPOT synthesis, resulting in an overall more material-efficient production and allowing for screening of several samples needing less volume.

For the production of MAs with liquid-based synthesis on slides, an omnipresent challenge is the development of suitable surface wettability properties. The synthesis surface needs to match the used solvents to reduce spreading of the building block solution on the array surface. At the same time, the surface has to enable the interactions for the biological assay afterwards. Hydrophobic patterning of the surface is a possibility to prevent liquid spreading due to high wettability and therefore allows for distinct spots. However, if the wettability of the solvent is low (large contact angle of droplet on the surface), the droplet might move uncontrollably in case of small disturbances. Therefore, an optimum contact angle is required to pin droplets to defined areas. Another strategy is the introduction of an alternating pattern, e.g. hydrophilic-hydrophobic patterning of the surface to form liquid wetting/repellent areas. Applying this strategy, in 2019, Benz et al. enabled a combination of solution-based in situ synthesis and subsequent biological screening [77]. They applied an extensively modified glass slide to create a low surface tension liquid slide to facilitate stable solvent droplets. They deposited the droplets, which contain the different building blocks for the synthesis of lipidoids in dimethyl sulfoxide (DMSO), manually onto two slides. To allow a reaction to take place, the two slides were brought into contact in a sandwich format for reagent mixing. For biological applications, the group created high surface tension liquid slides, which were used for aqueous solutions containing DNA plasmids. The slide with aqueous droplets was applied to the slide containing lipidoids in the sandwich format to build lipoplexes (lipid carriers for DNA) for cell transfection. This work employs a high-throughput chemical synthesis and applies it to a biological application in one sophisticated procedure. However, the slides need specialized modification and the solvent handling is not automated resulting in a laborious procedure [77]. Furthermore, DMSO is the only solvent, which Benz et al. proved to be suitable for the chemical reactions due to its relatively high surface tension.

Developing a suitable surface with optimal wettability for liquid-based synthesis was implemented by Li et al. in 2021 [78]. They generated an amphiphilic surface coating for glass slides to form droplets of solvents (DMF, DMSO, and sulfolane) with an enhanced contact angle and inhibited droplet motion. They fabricated slides with a chitosan hydrogel coating bearing amino groups for peptide synthesis as well as hydroxyl groups to couple lipids to adjust the wettability to organic solvents. After Fmoc SPPS, the lipids can be hydrolyzed from the chitosan coating to create a hydrophilic surface for biological assays. For liquid-based syntheses, a spotting robot was used. It should be noted that only a part of the surface functionalization is used to introduce amino groups for peptide synthesis, which is reducing the loading capacity of the solid support [78]. A drawback of this technique is the inhomogeneous spot shape of the presented PMAs, which may result in problems during automated spot intensity analysis.

There are other specialized techniques, which can generate high-density (> 10 000 spots per cm^2) MAs. In 2016, the work of Hirtz et al. showed the patterning of graphene using microchannel

cantilever spotting and dip-pen nanolithography [79]. The pretreated graphene was functionalized by copper(I)-catalyzed azide-alkyne cycloaddition (CuAAC) also known as "click-reaction" to immobilize molecules. The reaction was demonstrated with biotin azide detected with labeled streptavidin. On the one hand, the group used microchannel cantilever spotting, which enables contact-driven deposition of tiny (~130 femtoliter) droplets (~8 µm diameter) due to liquid flow by capillary forces. These droplets can serve as reaction vessels for the click-reaction. On the other hand, they prepared a pattern in the low micrometer range with 500 – 700 nm line width using dip-pen nanolithography [79].

Atwater and Mattes et al. applied the microchannel cantilever spotting in 2018 not only for single deposition of biomolecules, but also to synthesize 9-mer peptides in situ on a functionalized glass slide with a spot pitch of 40 µm (62 500 spots per cm^2) [80]. They produced HA (influenza hemagglutinin AA 98-106) and Flag (artificial epitope) peptides using Fmoc SPPS and stained the array directly after synthesis with corresponding labeled antibodies, proving this technique can produce high-density PMAs. One challenge is the spot alignment, which was overcome by marking the spot area with a high-power laser, followed by camera position alignment. Furthermore, the spot patterns for each building block needed further subdivision into smaller subpatterns to allow for a spot pitch below 50 µm. Additionally to the individual spotting of each AA, the charging of the microchannel cantilever with the respective AA resulted in a time consuming process. A feasible strategy would include multiple microchannel cantilevers to hold all required building blocks needed for the synthesis and a procedure without subpatterning [80]. To sum up, microchannel cantilever spotting and dip-pen nanolithography enable very small spot-to-spot distances but are much too slow and laborious to apply them for PMA production.

1.3.1.3 Photolithographic in situ synthesis of microarrays

In 1991, Fodor et al. invented the photolithographic in situ synthesis and produced a PMA with 40 000 spots per cm^2 [81]. The technique uses building blocks protected with photolabile PGs, which are removed in distinct areas by light irradiation to enable the next building block coupling in this position. The selected areas are addressed by lithographic masks, which cover parts of the array from the ultraviolet (UV) light, which is used for deprotection. The deprotected areas can undergo coupling reaction with one building block at a time. Since only parts of the array are deprotected, the chemical building blocks can be applied to the whole surface [81]. Nevertheless, in case of 20 different monomers, the process is very time-consuming. In contrast to PMA production, the process is more suited for oligonucleotide synthesis, due to the limited amount of only four monomers needed. As a result, one of the first commercially available microarrays (MAs) were DNA MAs produced by the company Affymetrix.

In 1999, Singh-Gasson et al. fabricated oligonucleotide MAs with virtually generated masks by digital micromirror devices, to overcome the high costs of many consumed photolithographic masks [82]. This technique was later applied for SPPS for the synthesis of high-density PMAs in 2013 by Hansen et al. [83]. The according method for PMA synthesis was described by Buus et al. 2012 [84]. Here, the AAs with photolabile PGs are deprotected in relevant areas under a UV light irradiation pattern using a digital mirror device (see Figure 11). Then, the deprotected locations are extended by one of 20 different Fmoc-protected AAs. This process is repeated until all defined areas are coupled with the desired AA. After finishing the peptide elongation cycle, the Fmoc groups are deprotected and replaced with the photolabile PGs [84]. Shin et al. 2010 used an approach for automated photolithographic PMA synthesis with all 20 different AAs protected with a photolabile PG as well as a digital micromirror device [85].
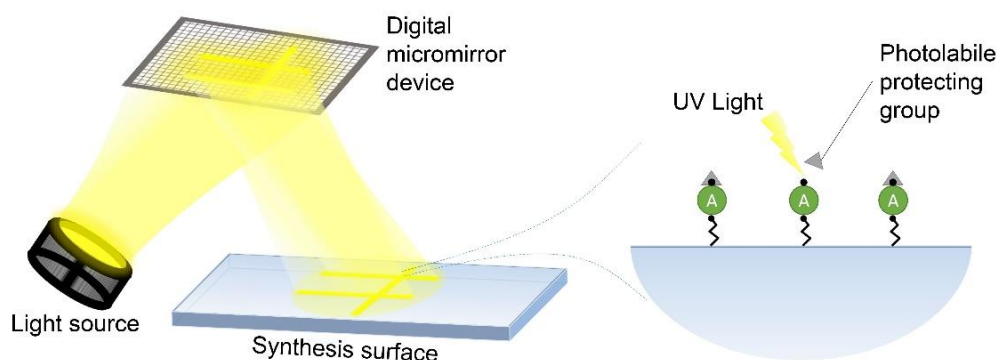

Figure 11: Photolithographic synthesis using digital micromirror devices. The photolabile PGs are deprotected under UV light irradiation in defined areas to allow coupling of the next monomer. This figure is recreated from https://doi.org/10.1021/acs.jproteome.0c00484 [86]. Permission for reuse granted by ACS Publications.

The removal of photolabile PGs can be of low efficiency and consequently hampers high yield peptide synthesis [87, 88]. Another strategy for light-induced deprotection, is the formation of photogenerated acids, to remove the acid-labile Boc PG. Therefore, the targeted area on the MA is filled with a photogenerated acid precursor, which will form an acid when irradiated with visible light by a digital mirror projector [89]. In 2014, Legutki et al. synthesized 660 000 peptides per cm^2 on silicon wafers [90]. They used photogenerated acid formation by UV light irradiation in distinct areas of the MA with the help of lithographic masks for Boc SPPS. Photogenerated acid diffusion has to be avoided and after deprotection, the generated acid has to be removed from the microarray without contaminating neighboring areas. In the same way as in Fodor et al., the procedure of Legutki et al. is time consuming because many lithographic deprotection and coupling steps have to be performed for the PMA synthesis [90].

1.3.1.4 Particle-based in situ synthesis of microarrays

The particle-based synthesis employs a matrix material, most commonly a polymer, which is solid at room temperature to imbed the AA inside a particle. The particles can be deposited in different ways on the solid support to create the array pattern. Each building block is embedded in particles leading to different particle types, which have to be deposited sequentially in specific patterns. Solid materials do not face the issue of spreading or evaporation on the surface. It can be advantageous to structure a MA with solid particles instead of spotting tiny liquid droplets. After structuring the surface with all building blocks, the entire solid support is heated up for the coupling reaction. At higher temperature, the polymer portion of the particles reaches its glass transition point and turns from the solid to a viscous liquid state. This allows the embedded AAs to diffuse and bind to a local area on the solid support, which carries functional groups. The polymer not only functions as a "solid solvent" for the structuring of the surface but also shields the building blocks from degradation. The repetition of particle deposition, coupling reaction, washing and deprotection of the entire solid support is allowing the synthesis of PMAs. Several methods apply this concept and use different techniques for particle deposition.

In 2007, Beyer et al. showed the synthesis of 40 000 spots per cm^2 on a complementary metal oxide semiconductor (CMOS) microchip [91]. A high voltage can be applied to these chips to generate a particle-attracting electric field. This is used to "switch on" selected pixels, which will attract the particles from an aerosol. For the peptide synthesis, Fmoc-protected AA with OPfp-activated carboxyl group are mixed with polymer to form solid particles in an air jet mill. A charged particle aerosol is transported to the functionalized microchip in an airflow created by an aerosol generator. The process is sequentially repeated with all types of particles with embedded AA to adhere them to the microchip before inducing the coupling reaction via melting all the particles at once. The group used their method to synthesize the well-known HA and Flag peptides for detection with corresponding antibodies [91]. On the one hand, a drawback of this technique is the high cost and the fragile surface of the CMOS microchip. On the other hand, particle contaminations between pixels occur. This problem was addressed using smaller particle sizes and an advanced aerosol generator in the work of Loeffler et al. 2012 for the synthesis of many different peptides [92].

In 2008, Stadler et al. used the particle-based approach and utilized a modified color laser printer for deposition with 20 printing units for each type of AA toner particle containing Fmoc-protected AA with OPfp-activated carboxyl group [93]. The printing of AA toner particles is based on the standard xerography printing process. The organic photoconductor drum inside the printing unit is evenly charged. When the drum is irradiated with light at specific positions, it becomes locally discharged. Subsequently, the charged AA toner particles adhere in these discharged areas of the drum. Finally, an electric field is applied to the solid support to attract the delivered AA particles. As

described before, the particles comprise a polymer, which is solid at room temperature to imbed the AA in a defined particle size. The particles additionally require additives, such as a charge transfer agent and silica powder, to enable xerographic processing. Moreover, the polymer is protecting the AAs from decay under ambient conditions for several weeks. After printing all AAs, heating induces simultaneous coupling by melting the polymer (see Figure 12). Excess material is washed away and the whole solid support is deprotected in order to repeat the cycle [93]. PEPperPRINT GmbH commercialized the technique, but it can produce only about 500 – 1000 peptides per cm^2.

Maerkle et al. 2014 reached a small spot pitch by first spreading a layer of particles with embedded AA onto the MA surface and then gluing them as small spots with a laser pulse [94]. The production of small particles and the creation of a homogeneous layer on the solid support are complex. The introduction of a laser into the in situ synthesis of PMAs will be illustrated in the next chapter 1.3.1.5 Laser-based in situ synthesis of microarrays.
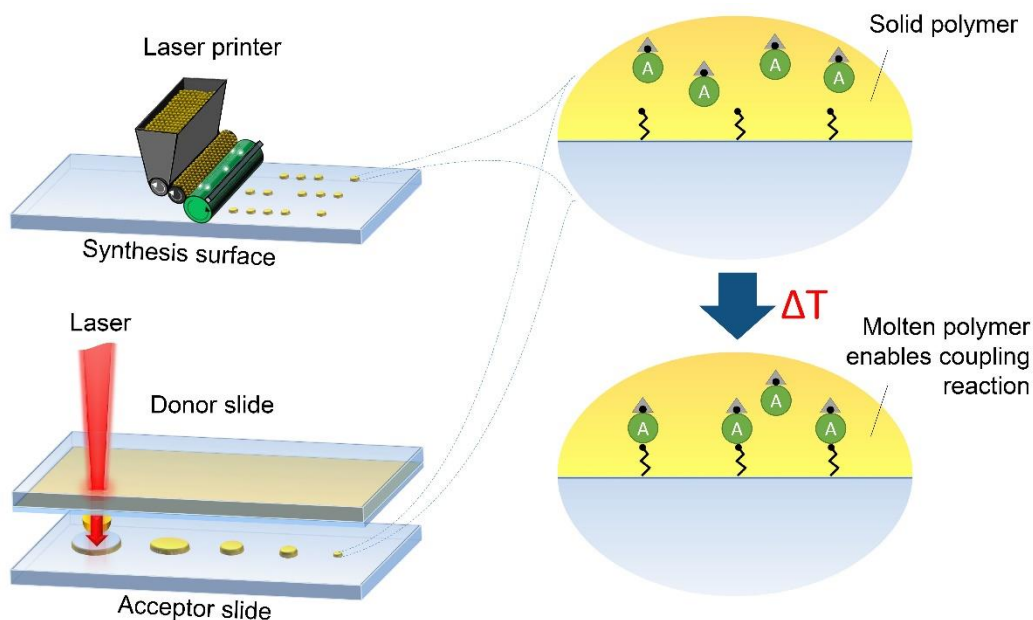

Figure 12: Particle-based synthesis using printer and laser-based synthesis for material transfer. Both processes imbed the AA inside polymer, either in form of a particle or in form of a thin material film. This figure is recreated from https://doi.org/10.1021/acs.jproteome.0c00484 [86]. Permission for reuse granted by ACS Publications.

A disadvantage of most particle-based syntheses, besides xerographic printing, is that excess particles on the solid support are not recycled causing a material-costly process. Furthermore, a contamination-free material deposition with aerosols is difficult. Only the xerographic printing approach is saving material and uses an advanced technology for particle deposition.

1.3.1.5 Laser-based in situ synthesis of microarrays

In general, the term laser-induced forward transfer (LIFT) is used to describe a transfer of material from a donor film to a material receiving substrate (i.e. acceptor slide) by laser irradiation. The donor slide bearing the material film has to come in contact or at least in close proximity to the acceptor slide for material deposition. The printing technique can transfer solid materials as well as liquids without using a nozzle [95]. Different mechanisms of transfers and donor slide composition have been described and some of them will be mentioned below.

Bohandy et al. used the concept of LIFT in 1986 for the transfer of metals, such as copper, from a film on a transparent substrate to a silicon substrate (see Figure 13a) [96]. The high energy laser induces heat to the metal coating leading to melting and vaporization resulting in material ejection [95, 97]. Next to the printing of solid metal films, matrix-assisted pulsed-laser evaporation direct write (MAPLE DW) was developed by Piqué et al. in 1999 [98]. For MAPLE DW, the material of interest is mixed with a gel of photo-sensitive polymer, which will vaporize under laser irradiation resulting in the transfer (see Figure 13b) [95, 98]. This technique allowed the transfer of embedded powders from a uniform coating to different acceptor substrates [98]. Later the principle of MAPLE DW was applied to liquids. Here the donor slides carries a liquid film, which stays in this phase during the LIFT process [95]. Upon laser irradiation, a high-pressure cavitation bubble is formed inside the liquid film generating a thin long jet (see Figure 13c) [99, 100]. The liquid jet reaches the acceptor slide and forms a droplet [100]. It has been demonstrated that even cells can be printed with LIFT from high viscosity liquids [101, 102]. Another addition to LIFT for more sensitive or transparent materials is a dynamic release layer (DRL) [103]. Therefore, an absorbing sacrificial layer, which can be a metal [104] or triazene polymer [105], is coated between the donor slide and the solid material of interest. In DLR LIFT, the material of interest is protected from arising heat and the sacrificial layer vaporizes or decomposes fully or partially upon laser irradiation enabling the ejection of material (see Figure 13d) [95]. The next mechanism for liquid (ink) transfer is blister-actuated (BA) LIFT. It has the potential to shield sensitive compounds due to a polymer layer absorbing most of the laser irradiation [95]. For BA LIFT, a solid absorbing polymer layer (often polyimide), which is thicker in comparison to other sacrificial layer of DRL LIFT, is attached to the donor slide as intermediate before the liquid material of interest (see Figure 13e) [95]. In contrast to the dynamic release layer LIFT, this polymer layer is not vaporized, instead a blister is formed between the glass slide and the polymer layer [95]. Upon laser irradiation, the trapped gas expands into a rapidly growing blister and causes deformation of the polymer layer resulting in material transfer as described for LIFT of liquids [95]. With the invariant absorbing polymer layer, only one laser wavelength is needed and the material of interest does not need to be absorbent. In

contrast, for DRL LIFT techniques, the wavelength of the laser needs to be suitable for each specific absorbing sacrificial layer [95].
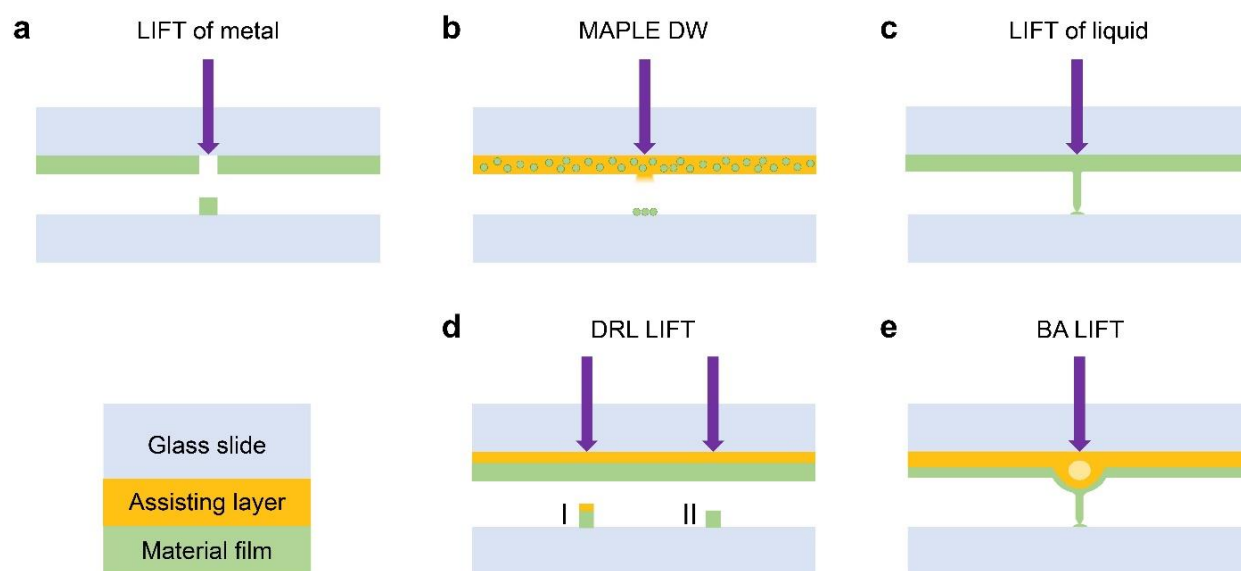

Figure 13: Different mechanisms of LIFT and donor slide composition with material transfer from donor slide (top) to acceptor slide (bottom) upon laser irradiation (purple arrow). a) LIFT of a solid metal film b) MAPLE DW with particles embedded in polymer layer, which is vaporized c) LIFT of liquid material transfer via jet formation d) DRL LIFT of solid material with I) additional transfer of sacrificial layer and II) without contamination e) BA LIFT with solid polymer layer and liquid material transfer via jet formation.

In 2016, Loeffler et al. used the combinatorial laser-induced forward transfer (cLIFT) for the synthesis of the HA and Flag peptides [106]. The approach can be applied for combinatorial synthesis due to the locally defined laser irradiation and exchangeable donor slides, which each contain an AA. A functionalized glass slide serves as acceptor during the solid-phase synthesis and can be directly utilized as MA for biological assays. For the donor slide preparation, a light-absorbing polyimide foil is attached to a microscopic glass slide. Then, a mixture of polymer and Fmoc-protected AA with OPfp-activated carboxyl group in fast evaporating solvent is spin coated to create a thin material film of polymer and embedded AA on the donor slide [106] (see Figure 16). For the transfer of small spots from the dried material film to the acceptor slide, millisecond laser pulses are employed. After transfer of all AA-containing spots, the entire acceptor slide is heated up for melting the polymer and to allow coupling (see Figure 12). Afterwards, polymer and uncoupled AAs are washed away [106]. The cLIFT approach was also utilized by Mattes et al. in 2018 to stack multiple layers of reagents, such as monomers and activators, embedded in polymer spots [107]. Then, the activation and reaction of monomers to the functionalized surface was initiated by heat-induced diffusion between the layers [107]. However, this procedure was leading to lower synthetic success than the synthesis with building blocks, which are pre-activated. The PMA production with cLIFT by Loeffler et al. was only a proof of concept. There, only two different
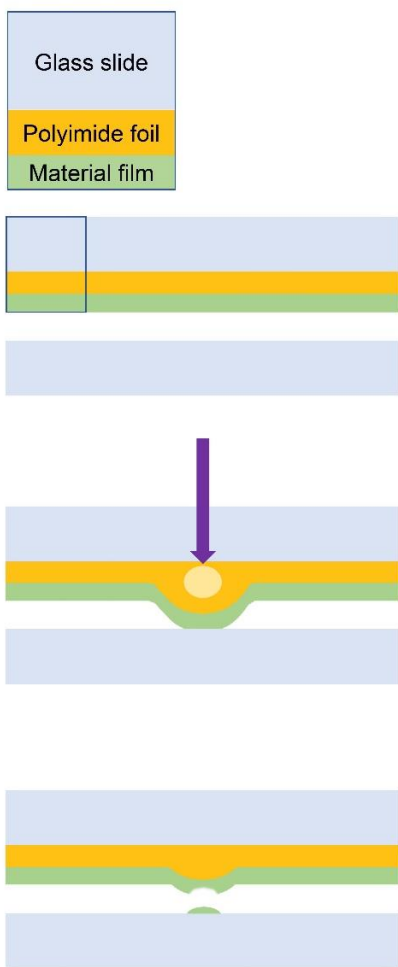
Figure 14: Scheme of cLIFT with blister formation upon laser irradiation (purple arrow) and contact-based material transfer from donor slide (top) to acceptor slide (bottom).

AA containing donor slides at a time and overall seven different AAs were used, limiting the synthesis to 64 different 9-mer peptides. The process lacked thorough investigation of the material deposition process and verification that all 20 AAs can be transferred by laser deposition to achieve a full combinatorial PMA production. During laser irradiation, the polyimide expands due to a heat-induced deformation and a blister forms between the glass slide and the polyimide foil resulting in a contact between material film of the donor and acceptor slide (see Figure 14) [108]. After the laser irradiation, the polyimide foil relaxes and the material film detaches while some material will deposit on the acceptor slide [108]. After the transfer, some deformation of the polyimide foil persists. Furthermore, the donor slide can be reused for several transfers of material to the functionalized acceptor slide, because the transferred spot, (below 20 nm high [108]) is less high than the material film (several hundred nm high [109]). Eickelmann and Moon et al. 2022 showed the influence of the polymer structure and surface wettability on the transferred polymer spots during cLIFT [110]. They found that the spots of different polymers vary in diameter and height after the contact-based transfer on glass. In addition, they show that the acceptor slide surface wettability is influencing the polymer spot morphology and proposed that the softened or melted polymer film will be influenced by adhesion and dewetting after the contact [110].

Abstract

Current methods for epitope mapping are laborious and demand special equipment or expertise. Peptide microarrays (PMAs) are used to detect linear B cell epitopes in a simple and fast manner. Commonly, technologies for PMA fabrication lack in spot density and/or the possibility to synthesize thousands of different sequences in parallel. In this work, PMAs should be used to screen serum antibodies of Ebola virus vaccine recipients and patients with a COVID-19 infection. Furthermore, a potential fabrication of high-density PMAs applying a laser-based in situ synthesis should be investigated.

In a first project, the antibody response after vaccination or after natural infection with the Ebola virus should be examined. The Ebola virus repeatedly causes severe epidemics with very high mortality rates. Therefore, the rVSV-ZEBOV vaccine was developed and extensive clinical trials were conducted. An Ebola virus ELISA and PAMs with overlapping peptides of the spike glycoprotein will be used to identify the antibody level and the linear B cell epitopes. It is of high interest, if the same epitopes are recognized in multiple individuals and if they overlap with already detected epitopes in the literature. Furthermore, a possible influence of the vaccine dose on the antibody response might be determined.

In a second project, the antibody response to SARS-CoV-2 should be investigated. Since COVID-19 is a novel viral disease, the immunogenicity of the viral antigens needed to be investigated. Sera of COVID-19 patients, who donated serum at different time points after onset of symptoms, should be screened for linear epitopes of the SARS-CoV-2 proteome with PMAs. Additionally, the sera will be analyzed using ELISA and glycan MAs. It could be important to analyze, if the level of different antibody classes and the number of detected epitopes vary over time of disease progression. It should be determined if the severity of symptoms might correlate with the antibody response of patients.

In the final project, a full combinatorial in situ synthesis of PMAs utilizing the cLIFT method should be developed. The automated cLIFT might be an attractive alternative for the flexible fabrication of high-density PMAs and other molecules in the array format. For the generation of PMAs, lasing parameters for the spot deposition with different spot sizes and spot pitches will be determined. For a straightforward spot analysis, the stained spots should have a homogenous and round morphology and a reproducible spot diameter. Then, the synthesis procedure should be optimized towards high AA coupling yield. Furthermore, the stability and reusability of the donor slides will be analyzed. The initially optimized synthesis parameters will be evaluated with peptide test syntheses and antibody staining. Finally, these optimizations should allow for the fabrication of 15-mer peptides covering the whole Ebola virus proteome with a high spot density.

3. Publish+ed work

3.1 Epitopes of Natural and Vaccine-Induced Anti-Ebola Virus Glycoprotein Antibodies in Single Amino Acid Resolution

J. Heidepriem, V. Krähling, C. Dahlke, T. Wolf, F. Klein, M. M. Addo, S. Becker, F. F. Loeffler

Author Contributions

J. Heidepriem and V. Krähling contributed equally to this work. J. Heidepriem developed the peptide array content and performed all microarray related experiments and data analysis. V. Krähling performed the ELISA experiments. C. Dahlke, V. Krähling, S. Becker, and M. M. Addo performed and supervised all vaccine trial related experiments, T. Wolf collected the survivor sample and F. Klein provided the monoclonal antibody 3T0331. F. F. Loeffler supervised the microarray experiments and analysis. S. Becker, M. M. Addo, and F. F. Loeffler supervised the project. All authors wrote and revised the manuscript.

Rationale and summary of this publication

The Ebola virus (EBOV) is one of the most threatening pathogens, causing the Ebola virus disease (EVD). EVD outbreaks in the last years have been caused be the Zaire EBOV subtype and had very high fatality rates [111]. The largest EVD outbreaks took place in West Africa from 2014 – 2016 and the Democratic Republic of the Congo (DRC) from 2018 – 2020 [111]. The EBOV is transmitted from fruit bats or non-human primates to the human population and spreads through direct contact with body fluids [111]. The dominant antigen of the EBOV is the spike glycoprotein (GP), which mediates binding to various host cell receptors for viral entry [112]. It is the only antigen on the EBOV surface and therefore, the major target for therapeutics and vaccines. The recombinant vesicular stomatitis virus-Zaire ebolavirus (rVSV-ZEBOV) vaccine uses a recombinant replication-competent viral vector, which expresses the GP. The experimental vaccine proved safe and protective in a study in Guinea 2015 [113, 114]. The Ebola Zaire Vaccine, Live (Tradename ERVEBO) was approved in EU and US in December 2019, and was already used to help controlling the outbreaks in Guinea and the DRC [115].

For this study, we received serum samples of a phase 1 vaccination trial with rVSV-ZEBOV in Europe (NCT02283099). The volunteers received one dose with different numbers of viral particles measured in plaque-forming units (pfu). The serum samples were collected on different time points after vaccination (see Table 5). Additionally we tested the serum from an EVD survivor. The study aimed to analyze and compare the antibody response against EBOV GP after a natural infection with EBOV or after vaccination. We performed ELISA using inactivated viral particles to detect EBOV-specific antibodies. This assay can detect IgG against different EBOV antigens with intact three-dimensional conformation [116].

Table 5: Vaccine recipients and EVD survivor information and signal of ELISA EBOV-specific IgG presented in optical density (OD) and normalized arbitrary ELISA units (AEU). Serum for the EVD survivor was collected two month later for the ELISA than for the PMA. Table copied from [117].

Sample	Vaccine dose (pfu)	Day of serum collection after vaccination	ELISA OD (450 – 630 nm)	Arbitrary ELISA units
1	2×10^7	28	0.811	4156
2	3×10^5	28	0.826	3874
3	3×10^5	56	1.220	6233
4	3×10^5	56	0.928	4483
5	2×10^7	56	0.428	1703
6	3×10^6	180	0.446	1424
7	2×10^7	180	0.802	3190
Survivor	n. a.	n. a.	3.565	22737

The ELISA detected antibodies in all vaccine recipients against the GP with signal intensities, which did not to correlate with the vaccine dose or day of serum collection. Because the EVD survivor has IgG against different viral antigens, the signal was much stronger. Furthermore, we compared the naturally acquired and the vaccine-induced antibody response to linear epitopes of the GP. Therefore, we applied PMAs, which carry 15-mer peptides of the EBOV GP with an overlap of 14 AAs (one AA offset). We detected linear IgG and IgM epitopes in the GP for all vaccine recipients, except for sample #6 (see Figure 15). We detected a broader IgM response with several overlapping epitopes in similar regions of the GP for different samples. For samples #5 and #6 we observed low ELISA signals and also only weak responses to the linear peptides on the PMAs. Some vaccine recipients responded to the same antigen regions in the mucin-like domain with IgG and IgM (see Figure *15*). The EVD survivor showed more diverse binding to linear epitopes in the GP1 domain, which is important for host receptor binding (see Figure *15*). In some regions of the GP, the response of the EVD survivor and the vaccine recipients revealed overlapping linear epitopes. For the analyzed samples, the vaccine dose or day of serum collection could not be correlated with the number of detected epitopes.
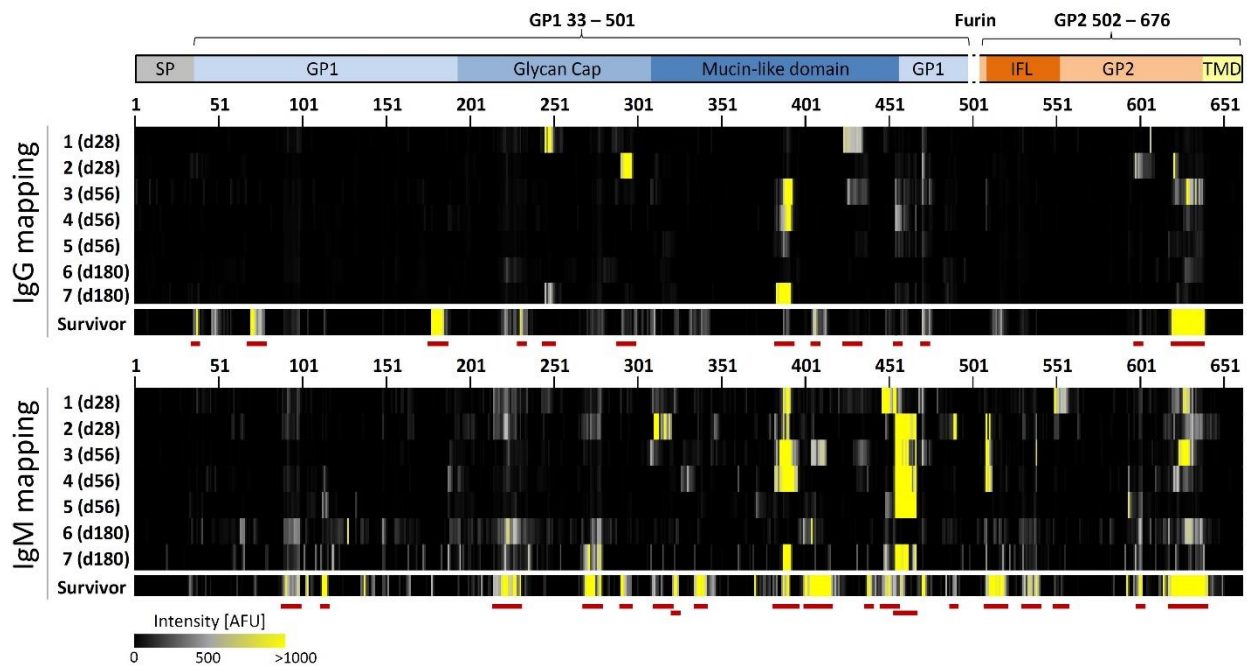
Figure 15: Fluorescence signals (AFU) of the GP peptide microarray shown as heat map with IgG and IgM response. The GP domains are visualized on top (SP: signal peptide; IFL: internal fusion loop; TMD: transmembrane domain; and furin cleavage site). Linear epitopes of are highlighted with a red line below the heat map. Data originate from [117].

Moreover, the linear epitope (AA 491–506) of a neutralizing monoclonal antibody was identified in the furin cleavage site, confirming the previously determined antigen-binding region by X-ray crystallography [118]. In conclusion, we compared the epitopes analyzed in our study with published epitopes of EVD survivors [119] and another experimental vaccine [120]. Multiple epitopes of EVD survivors in the published literature overlapped with our detected epitopes of the EVD survivor and vaccine-induced IgG epitopes (see Figure 2 in the published article).

The study showed that PMAs can support determining the antibody response in vaccine development. PMAs are useful to analyze antibody isotype development over time and to detect common linear epitopes found in several individuals in an easy and fast manner. However, the epitope analysis could have significantly benefited from more samples included in the study.

Epitopes of Naturally Acquired and Vaccine-Induced Anti-Ebola Virus Glycoprotein Antibodies in Single Amino Acid Resolution

Jasmin Heidepriem, Verena Krähling, Christine Dahlke, Timo Wolf, Florian Klein, Marylyn M. Addo,* Stephan Becker,* and Felix F. Loeffler*

The Ebola virus (EBOV) can cause severe infections in humans, leading to a fatal outcome in a high percentage of cases. Neutralizing antibodies against the EBOV surface glycoprotein (GP) can prevent infections, demonstrating a straightforward way for an efficient vaccination strategy. Meanwhile, many different anti-EBOV antibodies have been identified, whereas the exact binding epitopes are often unknown. Here, the analysis of serum samples from an EBOV vaccine trial with the recombinant vesicular stomatitis virus-Zaire ebolavirus (rVSV-ZEBOV) and an Ebola virus disease survivor, using high-density peptide arrays, is presented. In this proof-of-principle study, distinct IgG and IgM antibodies binding to different epitopes of EBOV GP is detected: By mapping the whole GP as overlapping peptide fragments, new epitopes and confirmed epitopes from the literature are found. Furthermore, the highly selective binding epitope of a neutralizing monoclonal anti-EBOV GP antibody could be validated. This shows that peptide arrays can be a valuable tool to study the humoral immune response to vaccines in patients and to support Ebola vaccine development.

1. Introduction

The Ebola virus (EBOV) is, due to its high fatality rate of 50% on average, one of the most threatening pathogens in our society.[1] The 2014–2016 outbreak of EBOV in West Africa was the largest since the virus discovery and the outbreak in the Democratic Republic of Congo is still ongoing since 2018 with the current overall case fatality ratio of 67%.[2] Both are caused by the Zaire ebolavirus species.[1] Thus, several passive and active immunotherapies against EBOV infection are currently under development. Few monoclonal antibodies (mAbs) for passive immunization have been shown to alleviate the Ebola virus disease (EVD).[3–8] Active immunotherapy has some advantages over passive. The currently most promising approach in EVD prevention is the recombinant vesicular stomatitis

J. Heidepriem, Dr. F. F. Loeffler
Max Planck Institute of Colloids and Interfaces
Department of Biomolecular Systems
Potsdam 14476, Germany
E-mail: felix.loeffler@mpikg.mpg.de

Dr. V. Krähling, Prof. S. Becker
Institute of Virology, Faculty of Medicine
Philipps University Marburg
Marburg 35043, Germany
E-mail: becker@staff.uni-marburg.de

Dr. V. Krähling, Prof. S. Becker
German Center for Infection Research
partner site Gießen-Marburg-Langen
Marburg 35043, Germany

Dr. C. Dahlke, Prof. M. M. Addo
Division of Infectious Diseases, First Department of Medicine
University Medical Center Hamburg-Eppendorf
Hamburg 20246, Germany
E-mail: m.addo@uke.de

Dr. C. Dahlke, Prof. M. M. Addo
Department of Clinical Immunology of Infectious Diseases
Bernhard Nocht Institute for Tropical Medicine
Hamburg 20359, Germany

Dr. C. Dahlke, Prof. M. M. Addo
German Center for Infection Research
Partner Site Hamburg-Lübeck-Borstel-Riems
Hamburg 20359, Germany

Dr. T. Wolf
Department of Medicine, Infectious Diseases Unit
Goethe University Hospital
Frankfurt 60590, Germany

Prof. F. Klein
Laboratory of Experimental Immunology
Institute of Virology
University of Cologne
Faculty of Medicine and University Hospital of Cologne
Cologne 50931, Germany

**ADVANCED
SCIENCE NEWS**
www.advancedsciencenews.com

**Biotechnology
Journal**
www.biotechnology-journal.com

virus-Zaire ebolavirus (rVSV-ZEBOV) vaccine, based on the rVSV, carrying the EBOV glycoprotein (GP).[1] The rVSV-ZEBOV recently received conditional market authorization and, thereby, represents the world's first licensed Ebola virus vaccine. Operational research during the current Democratic Republic of Congo outbreak revealed 97.5% efficacy for the prevention of EVD.[9] The surface protein of EBOV, the GP, is the target of neutralizing antibodies. It is cleaved by the enzyme furin into two subunits, GP1 and GP2. The cleavage products GP1 and GP2 are connected through a disulfide linkage between Cys53 and Cys609 and are inserted in the viral membrane as a trimeric complex, which mediates the entry into host cells.[10–13] GP1 contains receptor-binding regions, the glycan cap, and the mucin-like domain.[11] After the uptake of the virus by the cell, cathepsins remove the glycan cap and the mucin-like domain, leading to the exposure of the receptor-binding region.[14–16] GP2 serves as the membrane fusion subunit and contains the internal fusion loop, two heptad repeats, and the transmembrane domain.[11] In addition to the surface bound GP, there are two other gene products of the *GP* gene, resulting from stuttering of the polymerase at the editing site of GP: the secreted (soluble) glycoprotein (sGP) and the small secreted glycoprotein. With ≈70%, sGP is the main gene product.[17] It is highly secreted from infected cells and detected in the serum of EBOV-infected hosts.[18] The secreted form shares the first 295 residues with the surface GP,[12] which therefore may decoy antibodies and help the virus to escape the immune response.[19–22]

To develop new vaccines, it is important to identify those epitopes, which are targeted by protective antibodies in humans. For this purpose, peptide microarrays[23] can be used to rapidly study antibody interactions (e.g., mAbs or serum samples) with a large number of linear epitopes, which can be screened by simple incubation and fluorescence scan analysis. Advances in technology development, which for example rely on the patterning of co-polymers for the synthesis of biomolecules,[24] make the rapid production of peptide microarrays feasible.[25–27] High-density peptide microarrays have been used for the development of diagnostic biomarkers, for example, in Malaria, Zika virus, and Chagas disease,[28–30] as well as in the analysis of therapeutic antibodies against *C. difficile*.[31] Additionally, epitopes recognized by antibodies elicited after vaccination against infectious diseases, such as Tuberculosis, Malaria, and Tetanus, can be identified.[32–34]

Here, we report the use of high-density peptide arrays to exactly map the epitopes of naturally acquired antibodies against EBOV GP from volunteers, vaccinated with rVSV-ZEBOV, and one survivor of EVD. Our results show that many distinct epitopes are targeted by the humoral immune response. Generally,

Prof. F. Klein
Center for Molecular Medicine Cologne (CMMC)
University of Cologne
Faculty of Medicine
Cologne 50931, Germany
Prof. F. Klein
German Center for Infection Research
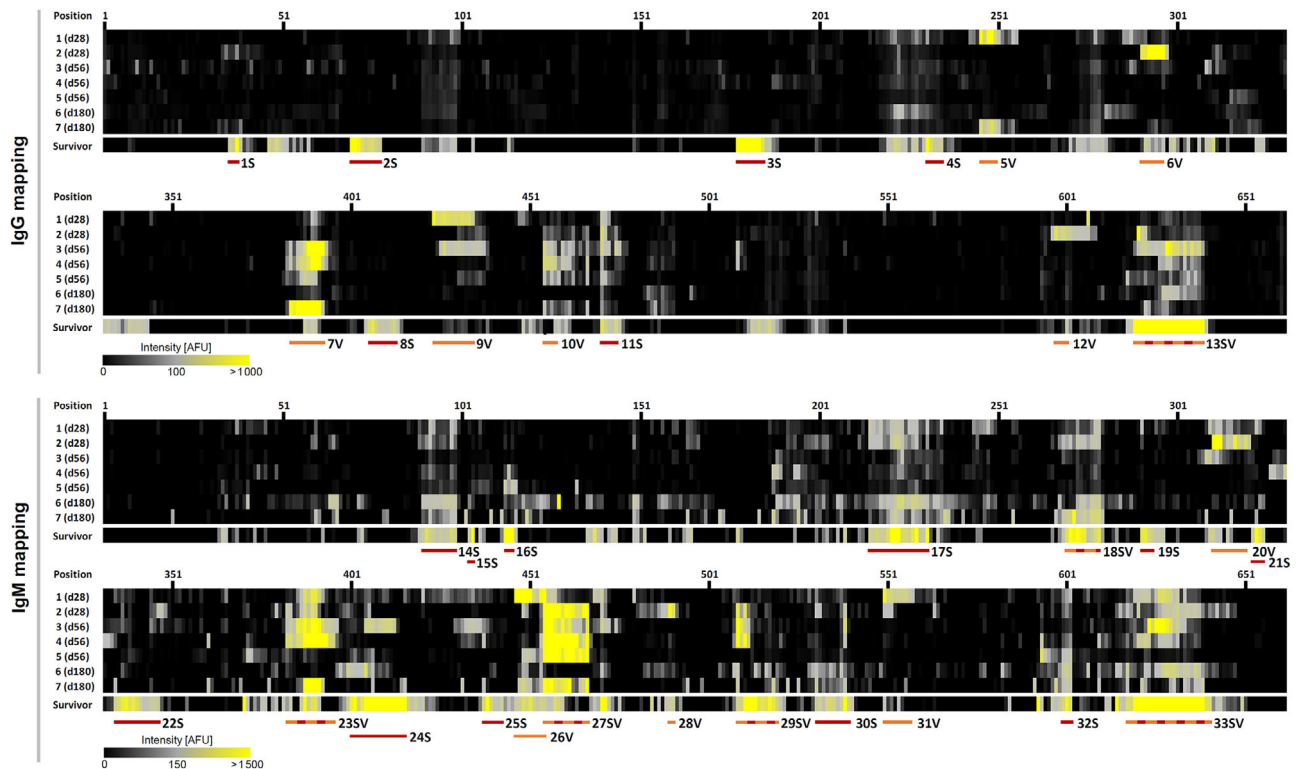partner site Bonn-Cologne
Cologne 50931, Germany

Table 1. Patient and vaccine recipient information.

Sample	Vaccine dose [pfu][a]	Day of serum collection after vaccination	ELISA OD[b] (450–630 nm)	Arbitrary ELISA units[b]
1	2×10^7	28	0.811	4156
2	3×10^5	28	0.826	3874
3	3×10^5	56	1.220	6233
4	3×10^5	56	0.928	4483
5	2×10^7	56	0.428	1703
6	3×10^6	180	0.446	1424
7	2×10^7	180	0.802	3190
Survivor[c]	n.a.	n.a.	3.565	22 737

[a] plaque forming units (pfu); [b] ELISA data, representing the total sample-specific EBOV-binding antibodies (IgG) in optical density (OD) and normalized arbitrary ELISA units (AEU); [c] Sample was collected 2 months later than the survivor serum sample, which was analyzed with the peptide array.

we could identify many distinct epitopes in the EBOV GP, with significant differences as well as overlaps in EBOV vaccine recipients in comparison to EVD infection.

2. Results

2.1. Enzyme-Linked Immunosorbent Assay to Detect EBOV-Specific Antibodies

We analyzed the sera from seven vaccines with rVSV-ZEBOV expressing EBOV GP, one EVD survivor from 2014,[35] and one neutralizing monoclonal antibody (mAb) 3T0331.[36] The sera from volunteers, once vaccinated with rVSV-ZEBOV, were collected on days 28 ($n = 2$), 56 ($n = 3$), and 180 ($n = 2$) after vaccination. Each sample is from a different vaccine recipient, at different time points after vaccination, using different vaccine doses (**Table 1**).

First, we performed an Enzyme-linked immunosorbent assay (ELISA) to test the samples for EBOV-specific antibodies.[37] Microtiter plates were coated with inactivated whole EBOV particles. Thus, in this assay, all antibodies against EBOV proteins were detected, resulting in a generally much stronger signal in the survivor sample (as shown in [37]), since the survivor has developed antibodies against several EBOV proteins (GP, NP, VP40). Therefore, a direct comparison of survivor and vaccines is not possible. Nevertheless, the investigated serum samples of vaccines were all positive for anti-GP antibodies.

2.2. Epitope Mapping Using Peptide Microarrays

Then, we mapped the amino acid (AA) sequence of the EBOV GP (676 AA, National Center for Biotechnology Information [NCBI] accession number AAG40168.1) as 662 overlapping 15-mer peptide fragments with a lateral shift of one AA (14 AA overlap). With this information, we obtained nine high-density peptide microarrays (PEPperPRINT GmbH, Germany), displaying these 662 peptides as spot duplicates.

**ADVANCED
SCIENCE NEWS**
www.advancedsciencenews.com

**Biotechnology
Journal**
www.biotechnology-journal.com

Figure 1. Peptide microarray data shown as a heat map (top: IgG response, bottom: IgM response). The EBOV GP (676 AA) was mapped as 662 spots of 15-mer peptides with a lateral shift of one AA. Sera from seven rVSV-ZEBOV-GP vaccines (numbered) and one EVD survivor were analyzed on separate microarrays. The vaccines are listed with the day of serum collection after vaccination. The defined epitopes are named by their origin from vaccines (V, in orange), survivor (S, in red) or both (SV, in orange and red). The identified peptide epitopes are summarized in Table 2.

Next, we performed the peptide microarray experiments. The peptide arrays were incubated with the eight diluted sera or the respective mAb, followed by incubation with fluorescently labeled secondary antibodies against human IgG and IgM (see Experimental Section). The obtained fluorescence scans were analyzed regarding the intensity of the peptides and visualized as a heat map (**Figure 1**). The IgG response shows a more specific binding pattern (less noise) than the IgM response, which reflects the higher specificity of IgGs. A binding epitope is defined by at least two neighboring peptide binders (one AA offset in the EBOV-GP) above certain intensity thresholds. For the IgG response, we defined the initial threshold as 500 arbitrary fluorescence units (AFU). The end of the epitope is defined, when the intensity of neighboring peptide(s) is below 250 AFU. For the IgM response, the initial intensity threshold for an epitope is 750 AFU and 375 AFU for the neighboring peptide(s). The identified peptide epitopes are summarized in **Table 2**.

Some of the epitopes in the IgG and IgM response show significant overlap (Figure 1). Furthermore, some epitopes are IgM specific, but do not induce a strong binding for IgG, especially in the day 28 patient samples. Comparing the antibody responses from the vaccines, we see differential responses. As we would expect, we observe the tendency that IgG epitopes show higher intensities in the sera of days 56 and 180 after vaccination, whereas in the earlier serum samples (day 28 and 56), the IgM response is higher. We did not observe a vaccine dose dependent (pfu) antibody response, but more samples should be analyzed to validate

this. However, we observed a qualitative correlation between the arbitrary ELISA units of the vaccine recipients and the arbitrary fluorescence intensity of the epitopes. For example, vaccine recipients 5 and 6 show the lowest signals in ELISA, as well as a low number of epitopes with lower fluorescence intensity.

The number of epitopes found in the vaccines sera within the N-terminal half of the EBOV-GP is low and not homogeneous. Some epitopes can be found in the IgG and IgM response of the survivor, with almost no overlap to the vaccines samples. Yet, for the following C-terminal half, several epitopes (IgG: 13SV; IgM: 23SV, 27SV, 29SV, 33SV) are recognized by antibodies of the survivor and the vaccines. Our strict selection criterion might have caused us to miss some shared epitopes (e.g., 11S), where weaker signals are present in both, the survivor and the vaccines.

The IgG epitope mapping of the potently neutralizing mAb 3T0331 indicated one position within the EBOV GP at position 491–506 with the AA sequence GLITGGRRTRREAIVN.[36]

Furthermore, we compared the epitopes found by us with published GP epitopes from EVD survivors, which were analyzed with ELISA (Becquart et al.), and from vaccinated individuals (prime/boost vaccination with chimpanzee adenovirus 3 encoding EBOV GP (ChAD3) and modified vaccinia virus Ankara encoding the GP of different filoviruses and the nucleoprotein of Tai forest ebolavirus), analyzed with yeast surface peptide-display assay (Rijal et al.). The epitopes are illustrated within the domains of the GP protein sequence (**Figure 2**A).[38,39] Additionally, we

Table 2. Amino acid position and sequence of the GP epitopes of IgG and IgM aligned from top to bottom according to GP amino acid position (see Figure 1).

	IgG			IgM	
Epitope	Position	Sequence	Epitope	Position	Sequence
1S [a]	36–52	GVIHNSTLQVSDVDKLV	14S	90–113	SGVPPKVVNYEAGEWAENCYNLEI
2S	70–92	LEGNGVATDVPSATKRWGFRSGV	15S	103–118	EWAENCYNLEIKKPDG
3S	178–199	EGVVAFLILPQAKKDFFSSHPL	16S	113–129	IKKPDGSECLPAAPDGI
4S	231–249	EYLFEVDNLTYVQLESRFT	17S	215–245	STTIRYQATGFGTNETEYLFEVDNLTYVQLE
5 V [b]	246–265	SRFTPQFLLQLNETIYTSG	18SV	270–293	TGKLIWKVNPEIDTTIGEWAFWET
6V	291–312	WETKKNLTRKIRSEELSFTVV	19S	291–308	WETKKNLTRKIRSEELSF
			20V	311–334	VSNGAKNISGQSPARTSSDPGTNT
			21S	322–339	SPARTSSDPGTNTTTEDH
			22S	335–361	TTEDHKIMASENSSAMVQVHSQGREAA
7V	384–407	PDNSTHNTPVYKLDISEATQVEQH	23SV	383–410	GPDNSTHNTPVYKLDISEATQVEQHHRR
8S	406–427	QHHRRTDNDSTASDTPSATTAA	24S	400–433	EATQVEQHHRRTDNDSTASDTPSATTAAGPPKAE
9V	424–449	TTAAGPPKAENTNTSKSTDFLDPATT	25S	438–457	SKSTDFLDPATTTSPQNHSE
10V	455–473	HSETAGNNNTHHQDTGEE	26V	447–469	ATTTSPQNHSETAGNNNTHHQDT
11S	471–489	EESASSGKLGLITNTIAGV	27SV	455–481	HSETAGNNNTHHQDTGEESASSGKLGL
			28V	490–505	AGLITGGRRTRREAIV
			29SV	509–534	PKCNPNLHYWTTQDEGAAIGLAWIPY
			30S	531–554	WIPYFGPAAEGIYIEGLMHNQDGL
			31V	550–571	NQDGLICGLRQLANETTQALQL
12V	598–616	GGTCHILGPDCCIEPHDW	32S	600–616	TCHILGPDCCIEPHDWT
13SV [c]	620–653	TDKIDQIIHDFVDKTLPDQGDNDNWWTGWRQWIP	33SV	618–655	NITDKIDQIIHDFVDKTLPDQGDNDNWWTGWRQWIPAG

[a] The defined epitopes, named by their origin from survivor (S); [b] vaccine recipients (V); [c] or both (SV).

mapped and highlighted our found IgG epitopes on the 3D structure of the GP (Figure 2B–D).

Compared to the seven epitopes (1A–7A) from Becquart et al.,[38] five epitopes coincide with our defined IgG epitopes from the survivor and vaccines. In fact, four of these (1A, 3A, 6A, 7A) overlap with the antibody response of our survivor sample (1S, 4S, 8S, 11S). Rijal et al.,[39] defined three rather large epitopes (1B–3B), of various lengths. The first (1B) overlaps with one epitope of the survivor (3S), the second (2B) includes one survivor epitope (4S) and one epitope of a vaccine (5 V), and the third (3B) has a small overlay of 2 amino acids with one vaccine epitope (6 V).

3. Discussion

Peptide microarrays are a useful high-throughput platform for epitope mapping. With our approach, we identified the epitopes of the acquired IgG and IgM response in parallel against EBOV GP from rVSV-ZEBOV vaccine recipients and one survivor of EVD. For the first time, we used overlapping peptides to map the EBOV GP with an offset of one amino acid to determine the exact position and length of the epitopes. Furthermore, for the first time, we followed the development of isotype switch in rVSV-ZEBOV vaccine recipients at different time points after vaccination with this approach, which will help to investigate vaccination boost strategies.

The mAb 3T0331, which is a potently neutralizing anti-GP antibody, binds to a peptide on the microarray at the position AA491–506 in the GP, which correlates well with the determined binding site from Ehrhardt et al.[36] They have determined a binding of the N-terminal GP2 and parts of GP1 with main interactions to Val505 and Glu502, but not to Gln508. Thus, peptide microarrays can be readily used to identify the antigen binding sites of mAbs or antibodies found in more complex samples like sera with high precision.

Recently, the Viral Hemorrhagic Fever Immunotherapeutic Consortium screened a global collection of 168 monoclonal antibodies against EBOV GP.[40] Although being a landmark contribution to the EBOV field, the workflow is highly labor-intensive: To determine the binding domain of the mAbs within the GP, they first performed ELISA to detect antibody binding to different forms of the GP antigen, followed by imaging the complexation of the mAb Fab fragments with GP using electron microscopy. For in depth evaluation of the bound epitope, they performed alanine scanning mutagenesis to create point mutated antigens and characterize the essential epitope residues for mAb binding. They could cluster the mAbs into the respective epitope classes of GP base, glycan cap, fusion loop, GP1 head, GP1/2, HR2, mucin-like domain, and unknown binding. Similarly, Rijal et al.,[39] isolated 82 antibodies from plasmablasts or B cells from 11 vaccines with ChAD3 EBOV after day 7 and 28. A cocktail of four of these antibodies targeting the glycan cap, the receptor binding region, and the base, was protective in guinea pigs when given at day 3 after EBOV infection. They performed
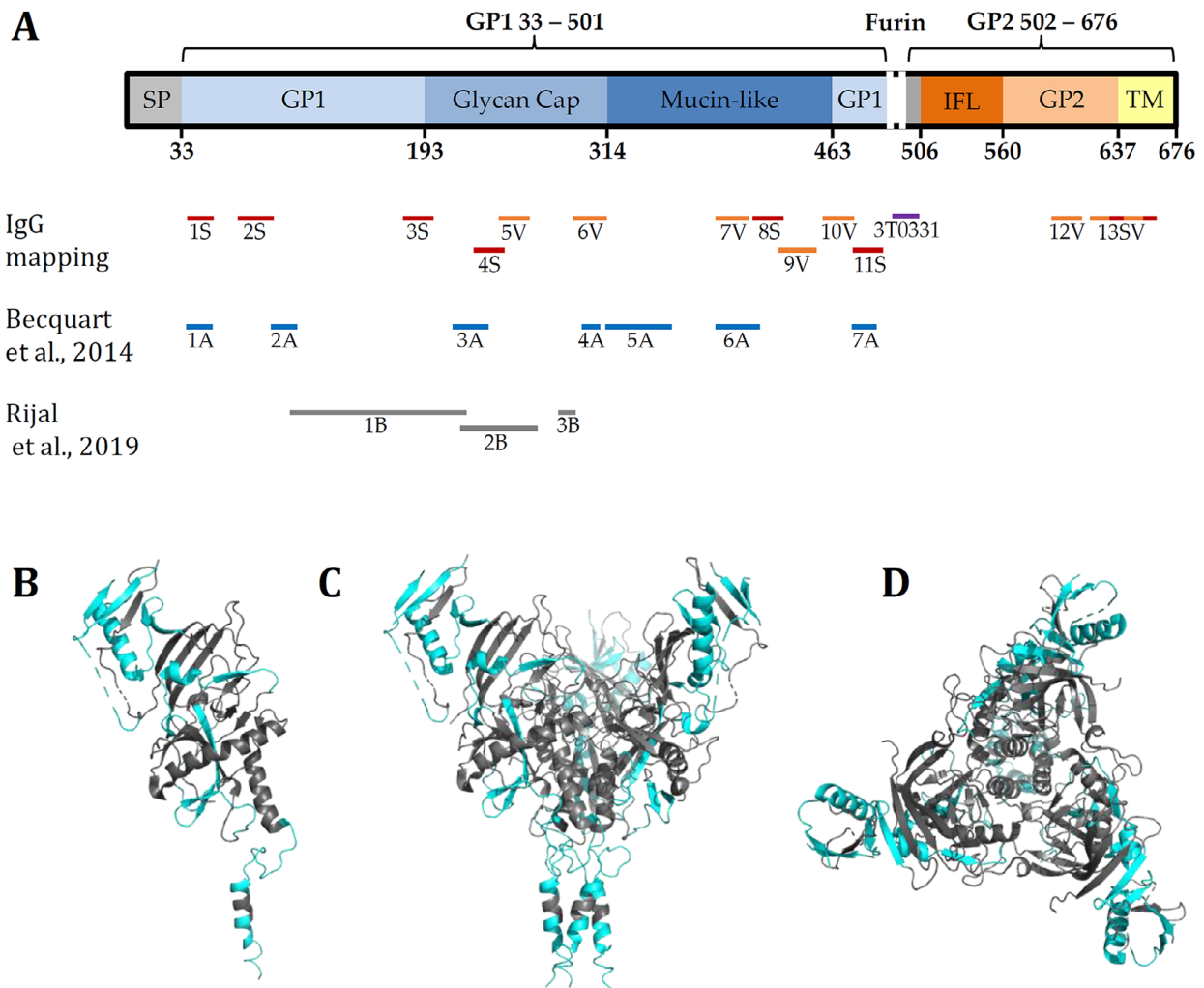
**ADVANCED
SCIENCE NEWS**
www.advancedsciencenews.com

**Biotechnology
Journal**
www.biotechnology-journal.com

Figure 2. Epitopes of the EBOV GP. A) Comparison of the immunogenic epitopes of the EBOV GP. The herein presented IgG epitopes (S/V) compared to epitopes published in Bequart et al.,[38] (A) and Rijal et al.,[39] (B); for details, also see Tables S2 and S3, Supporting Information. Structural domains of the envelope glycoprotein (GP) from Saphire et al.:[40] SP: signal peptide; mucin-like: mucin-like domain; IFL: internal fusion loop, TM: transmembrane domain. 3D view of the (incomplete) EBOV GP structure with the herein identified IgG epitopes (vaccines and survivor) highlighted in cyan (generated with PyMOL from Protein Data Bank[41] file 5jq3[42]—Crystal structure of Ebola glycoprotein). B) Side view of GP monomer C) side view of GP trimer D) Top view of GP trimer. For more details on missing sequences, see Table S4, Supporting Information .

a yeast surface peptide-display assay to identify the GP epitopes bound by these mAbs. The advantage of this display technology is the possibility to identify longer and conformational epitopes, but it lacks precise amino acid resolution. P. Becquart et al.,[38] identified linear B cell epitopes of GP by ELISA of synthetic 15-mer peptides with an overlap of 11 amino acids. First, they screened two pools of different sera from EVD survivors and identified 19 peptides, which were recognized by IgG. Then, they used these peptides for further epitope mapping of 21 survivor sera. The drawback of this approach is the lower resolution of only 11 amino acids overlap, which might cause false negative results. In addition, pooling of sera makes it impossible to distinguish individual antibody responses.

Thus, peptide microarrays can offer an attractive and rapid alternative to the afore mentioned cost- and labor-intensive methods and still provide high-resolution epitope mapping. This

screening platform has advantages, such as reduced laboratory efforts due to parallel screenings, minimal demand of sample volumes and its ability to be used for diverse samples. For in-depth analysis of essential amino acids within the epitope sequences, amino acid substitution analysis can be performed.[43] This may help to elucidate the crucial amino acids for vaccine development. To investigate a possible dose dependent response, more samples and different time points need to be analyzed. The applied peptide arrays also have their limitations, since they contain exclusively linear peptides and cannot identify antibodies that bind conformational or discontinuous epitopes.

We show that peptide arrays can be a versatile tool for highly precise epitope identification of a large number of mAbs or different antibody classes in sera of patients or vaccine recipients. Therefore, peptide arrays are useful in vaccine development

**ADVANCED
SCIENCE NEWS**

www.advancedsciencenews.com

**Biotechnology
Journal**

www.biotechnology-journal.com

to reduce laboratory efforts and minimize demand of sample volumes.

4. Experimental Section

rVSV-ZEBOV Vaccines: Serum samples of rVSV-ZEBOV vaccinated volunteers were obtained from an open-label, dose-escalation phase 1 trial performed in Hamburg (ClinicalTrials.gov; NCT02283099). Volunteers were vaccinated once with rVSV-ZEBOV-GP with a dose of 3×10^5, 3×10^6, or 2×10^7 pfu. Sera were collected on day 28, 56, 180 after vaccination.[44,45] The protocol was approved by the Institutional Review Board of the University Medical Center Hamburg-Eppendorf, Germany.

ELISA Analysis: ELISA was performed as described by Krähling et al.[37] Briefly, microtiter plates coated with EBOV or mock antigen, were washed three times with PBST (0.1% (v/v) Tween 20 in phosphate-buffered saline) and then blocked with PBS containing 5% milk powder. Washing procedure was repeated three times with PBST. Human sera/plasma and controls were diluted 1:200 in PBST containing 1% milk powder and allowed to react with the antigens. After washing plates three times with PBST, polyclonal HRP-coupled antibodies and TMB substrate and stop solution were used for detection. The optical density (OD) was determined at 450–630 nm using an automated spectrophotometer. Each control and serum were analyzed in duplicate, and mean OD value of each sample on mock antigen is subtracted from OD value on EBOV antigen to obtain corrected OD values. To calculate arbitrary ELISA units (AEU), the straight line equation of the standard curve on each plate is determined by linear regression analysis. Positive samples had an AEU of 1000 and higher, and negative samples were set to 500 AEU.

Generation of Peptide Microarrays: For the epitope mapping of patient sera with peptide microarrays, the Ebola virus glycoprotein, obtained from NCBI (AAG40168.1, 676 amino acids, https://www.ncbi.nlm.nih.gov/protein/11761750) was used. The GP sequence was cut in silico into 662 overlapping 15-mer peptide fragments, with an overlap of 14 amino acids between two neighboring peptides. These sequences were ordered as custom peptide arrays from PEPperPRINT GmbH (Heidelberg, Germany). Each microarray contained five copies of the Ebola GP array displayed as 15-mer peptide duplicate spots (2×662 individual spots per array).

Incubation and Analysis of Peptide Microarrays: Before incubation of the serum samples, the arrays were pre-swollen for 15 min with 300 µL PBST (0.05% [v/v]) at room temperature and orbital shaking with 150 rpm. To avoid unspecific binding of the serum antibodies, the arrays were blocked with blocking buffer (MB-070, Rockland Immunochemicals Inc., Limerick, USA) for 30 min, 150 rpm, room temperature. After short washing with PBST, 200 µL of the mAb 3T0031 diluted to 0.01 mg mL^{-1} and sera diluted 1:500 in staining buffer (10% [v/v] blocking buffer in PBST) were incubated overnight, 150 rpm, at 4 °C. To remove unbound serum components, the arrays were shortly washed three times with PBST. The human serum antibodies were detected with fluorescently labeled secondary antibodies: 0.5 mg mL^{-1} Anti-Human IgG-Fc Fragment cross-adsorbed DyLight 680 conjugated (A80-304D6, Bethyl Laboratories, Montgomery, USA), 1.0 mg mL^{-1} Human IgM (mu chain) Antibody DyLight 800 conjugated (609-145-007, Rockland Immunochemicals Inc., Limerick, USA) and 1.0 mg mL^{-1} anti-HA-peptide antibody (RT028, Bio X Cell, New Hampshire, USA) labeled with Lightning-Link Rapid Dylight 680 (327-0010, Innova Biosciences Ltd., Cambridge, United Kingdom). Therefore, the secondary antibodies were diluted 1:2000 in staining buffer and applied to the microarrays for 30 min, 150 rpm, room temperature. To remove unbound secondary antibodies, the arrays were shortly washed three times with PBST. Finally, the arrays were dipped in 1 mM Tris HCl pH 7.4 and dried in a jet of air. To monitor unspecific binding of the secondary antibodies (Anti-Human IgG 680, Anti-human IgM 800), the arrays were pre-stained and scanned before incubation with the samples using the same method. The arrays were scanned and fluorescence signals were detected at 700 nm and 800 nm with an Odyssey Scanner (LI-COR Biotechnology Inc., Lincoln, Nebraska, USA). Analysis of the scans was performed using PepSlide Analyzer software (SICASYS Software GmbH, Heidelberg, Germany).

Supporting Information

Supporting Information is available from the Wiley Online Library or from the author.

Conflict of Interest

F.F.L. is named on a patent for the production of microarrays. All other authors declare no conflict of interest. The funders had no role in the design of the study, in the collection, analyses, or interpretation of data, in the writing of the manuscript, or in the decision to publish the results.

Author Contributions

J.H. and V.K. contributed equally to this work. J.H. developed the peptide array content and performed all microarray related experiments and data analysis. V.K. performed the ELISA experiments. C.D., V.K., S.B., and M.M.A. performed and supervised all vaccine trial related experiments, T.W. collected the survivor sample and F.K. provided the monoclonal antibody 3T0331. F.F.L. supervised the microarray experiments and analysis. S.B., M.A., and F.F.L. supervised the project. All authors wrote and revised the manuscript.

Keywords

Ebola virus, epitope mapping, human sera, neutralizing antibodies, recombinant vesicular stomatitis virus-Zaire ebolavirus

[1] World Health Organization, Ebola Virus Disease, https://www.who.int/news-room/fact-sheets/detail/ebola-virus-disease (accessed: December 2019).

[2] World Health Organization, Ebola Virus Disease–Democratic Republic of the Congo, https://www.who.int/csr/don/14-november-2019-ebola-drc/en/ (accessed: December 2019).

[3] P. I. W. Group, P. I. I. S. T. Multi-National, R. T. Davey, Jr., L. Dodd, M. A. Proschan, J. Neaton, J. Neuhaus Nordwall, J. S. Koopmeiners, J. Beigel, J. Tierney, H. C. Lane, A. S. Fauci, M. B. F. Massaquoi, F. Sahr, D. Malvy, *N. Engl. J. Med.* **2016**, *375*, 1448.

[4] D. Corti, J. Misasi, S. Mulangu, D. A. Stanley, M. Kanekiyo, S. Wollen, A. Ploquin, N. A. Doria-Rose, R. P. Staupe, M. Bailey, W. Shi, M.

**ADVANCED
SCIENCE NEWS**

www.advancedsciencenews.com

**Biotechnology
Journal**

www.biotechnology-journal.com

Choe, H. Marcus, E. A. Thompson, A. Cagigi, C. Silacci, B. Fernandez-Rodriguez, L. Perez, F. Sallusto, F. Vanzetta, G. Agatic, E. Cameroni, N. Kisalu, I. Gordon, J. E. Ledgerwood, J. R. Mascola, B. S. Graham, J. J. Muyembe-Tamfun, J. C. Trefry, A. Lanzavecchia, et al., *Science* **2016**, *351*, 1339.

[5] M. R. Gaudinski, E. E. Coates, L. Novik, A. Widge, K. V. Houser, E. Burch, L. A. Holman, I. J. Gordon, G. L. Chen, C. Carter, M. Nason, S. Sitar, G. Yamshchikov, N. Berkowitz, C. Andrews, S. Vazquez, C. Laurencot, J. Misasi, F. Arnold, K. Carlton, H. Lawlor, J. Gall, R. T. Bailer, A. McDermott, E. Capparelli, R. A. Koup, J. R. Mascola, B. S. Graham, N. J. Sullivan, J. E. Ledgerwood, et al., *Lancet* **2019**, *393*, 889.

[6] K. E. Pascal, D. Dudgeon, J. C. Trefry, M. Anantpadma, Y. Sakurai, C. D. Murin, H. L. Turner, J. Fairhurst, M. Torres, A. Rafique, Y. Yan, A. Badithe, K. Yu, T. Potocky, S. L. Bixler, T. B. Chance, W. D. Pratt, F. D. Rossi, J. D. Shamblin, S. E. Wollen, J. M. Zelko, R. Carrion, Jr., G. Worwa, H. M. Staples, D. Burakov, R. Babb, G. Chen, J. Martin, T. T. Huang, K. Erlandson, et al., *J. Infect. Dis.* **2018**, *218*, S612.

[7] S. Sivapalasingam, M. Kamal, R. Slim, R. Hosain, W. Shao, R. Stoltz, J. Yen, L. G. Pologe, Y. Cao, M. Partridge, G. Sumner, L. Lipsich, *Lancet Infect. Dis.* **2018**, *18*, 884.

[8] S. Mulangu, L. E. Dodd, R. T. Davey, Jr., O. Tshiani Mbaya, M. Proschan, D. Mukadi, M. Lusakibanza Manzo, D. Nzolo, A. Tshomba Oloma, A. Ibanda, R. Ali, S. Coulibaly, A. C. Levine, R. Grais, J. Diaz, H. C. Lane, J. J. Muyembe-Tamfun, P. W. Group, P. C. S. Team, B. Sivahera, M. Camara, R. Kojan, R. Walker, B. Dighero-Kemp, H. Cao, P. Mukumbayi, P. Mbala-Kingebeni, S. Ahuka, S. Albert, T. Bonnett, et al., *N. Engl. J. Med.* **2019**.

[9] European Medicines Agency, Ervebo, https://www.ema.europa.eu/en/medicines/human/summaries-opinion/ervebo (accessed: December 2019).

[10] S. A. Jeffers, D. A. Sanders, A. Sanchez, *J. Virol.* **2002**, *76*, 12463.

[11] J. E. Lee, M. L. Fusco, A. J. Hessell, W. B. Oswald, D. R. Burton, E. O. Saphire, *Nature* **2008**, *454*, 177.

[12] A. Sanchez, Z. Y. Yang, L. Xu, G. J. Nabel, T. Crews, C. J. Peters, *J. Virol.* **1998**, *72*, 6442.

[13] V. E. Volchkov, H. Feldmann, V. A. Volchkova, H. D. Klenk, *Proc. Natl. Acad. Sci. USA* **1998**, *95*, 5762.

[14] K. Chandran, N. J. Sullivan, U. Felbor, S. P. Whelan, J. M. Cunningham, *Science* **2005**, *308*, 1643.

[15] K. Schornberg, S. Matsuyama, K. Kabsch, S. Delos, A. Bouton, J. White, *J. Virol.* **2006**, *80*, 4174.

[16] E. H. Miller, G. Obernosterer, M. Raaben, A. S. Herbert, M. S. Deffieu, A. Krishnan, E. Ndungo, R. G. Sandesara, J. E. Carette, A. I. Kuehne, G. Ruthel, S. R. Pfeffer, J. M. Dye, S. P. Whelan, T. R. Brummelkamp, K. Chandran, *EMBO J.* **2012**, *31*, 1947.

[17] W. Zhu, L. Banadyga, K. Emeterio, G. Wong, X. Qiu, *Viruses* **2019**, *11*, 999.

[18] A. Sanchez, S. G. Trappier, B. W. Mahy, C. J. Peters, S. T. Nichol, *Proc. Natl. Acad. Sci. USA* **1996**, *93*, 3602.

[19] H. Ito, S. Watanabe, A. Takada, Y. Kawaoka, *J. Virol.* **2001**, *75*, 1576.

[20] J. A. Wilson, M. Hevey, R. Bakken, S. Guest, M. Bray, A. L. Schmaljohn, M. K. Hart, *Science* **2000**, *287*, 1664.

[21] G. S. Mohan, W. Li, L. Ye, R. W. Compans, C. Yang, *PLoS Pathog.* **2012**, *8*, e1003065.

[22] P. A. Ilinykh, X. Shen, A. I. Flyak, N. Kuzmina, T. G. Ksiazek, J. E. Crowe, Jr., A. Bukreyev, *J. Virol.* **2016**, *90*, 3890.

[23] L. C. Szymczak, H. Y. Kuo, M. Mrksich, *Anal. Chem.* **2018**, *90*, 266.

[24] V. Stadler, T. Felgenhauer, M. Beyer, S. Fernandez, K. Leibe, S. Guttler, M. Groning, K. Konig, G. Torralba, M. Hausmann, V. Lindenstruth, A. Nesterov, I. Block, R. Pipkorn, A. Poustka, F. R. Bischoff, F. Breitling, *Angew. Chem., Int. Ed.* **2008**, *47*, 7132.

[25] F. F. Loeffler, T. C. Foertsch, R. Popov, D. S. Mattes, M. Schlageter, M. Sedlmayr, B. Ridder, F.-X. Dang, C. von Bojničić-Kninski, L. K. Weber,

A. Fischer, J. Greifenstein, V. Bykovskaya, I. Buliev, F. R. Bischoff, L. Hahn, M. A. R. Meier, S. Bräse, A. K. Powell, T. S. Balaban, F. Breitling, A. Nesterov-Mueller, *Nat. Commun.* **2016**, *7*, 11844.

[26] S. Eickelmann, A. Tsouka, J. Heidepriem, G. Paris, J. Zhang, V. Molinari, M. Mende, F. F. Loeffler, *Adv. Mater. Technol.* **2019**, *4*, 1900503.

[27] D. S. Mattes, B. Streit, D. R. Bhandari, J. Greifenstein, T. C. Foertsch, S. W. Munch, B. Ridder, V. B.-K. C, A. Nesterov-Mueller, B. Spengler, U. Schepers, S. Brase, F. F. Loeffler, F. Breitling, *Macromol. Rapid Commun.* **2019**, *40*, 1800533.

[28] T. Jaenisch, K. Heiss, N. Fischer, C. Geiger, F. R. Bischoff, G. Moldenhauer, L. Rychlewski, A. Sie, B. Coulibaly, P. H. Seeberger, L. S. Wyrwicz, F. Breitling, F. F. Loeffler, *Mol. Cell. Proteomics* **2019**, *18*, 642.

[29] N. Mishra, A. Caciula, A. Price, R. Thakkar, J. Ng, L. V. Chauhan, K. Jain, X. Che, D. A. Espinosa, M. Montoya Cruz, A. Balmaseda, E. H. Sullivan, J. J. Patel, R. G. Jarman, J. L. Rakeman, C. T. Egan, C. Reusken, M. P. G. Koopmans, E. Harris, R. Tokarz, T. Briese, W. I. Lipkin, *mBio* **2018**, *9*, e00095.

[30] S. J. Carmona, M. Nielsen, C. Schafer-Nielsen, J. Mucci, J. Altcheh, V. Balouz, V. Tekiel, A. C. Frasch, O. Campetella, C. A. Buscaglia, F. Agüero, *Mol. Cell. Proteomics* **2015**, *14*, 1871.

[31] V. Fühner, P. A. Heine, S. Helmsing, S. Goy, J. Heidepriem, F. F. Loeffler, S. Dubel, R. Gerhard, M. Hust, *Front. Microb.* **2018**, *9*, 2908.

[32] D. Valentini, M. Rao, L. Rane, S. Rahman, R. Axelsson-Robertson, R. Heuchel, M. Lohr, D. Hoft, S. Brighenti, A. Zumla, M. Maeurer, *Int. J. Infect. Dis.* **2017**, *56*, 140.

[33] J. Tan, B. K. Sack, D. Oyen, I. Zenklusen, L. Piccoli, S. Barbieri, M. Foglierini, C. S. Fregni, J. Marcandalli, S. Jongo, S. Abdulla, L. Perez, G. Corradin, L. Varani, F. Sallusto, B. K. L. Sim, S. L. Hoffman, S. H. I. Kappe, C. Daubenberger, I. A. Wilson, A. Lanzavecchia, *Nat. Med.* **2018**, *24*, 401.

[34] A. Palermo, L. K. Weber, S. Rentschler, A. Isse, M. Sedlmayr, K. Herbster, V. List, J. Hubbuch, F. F. Löffler, A. Nesterov-Müller, F. Breitling, *Biotechnol. J.* **2017**, *12*, 1700197.

[35] T. Wolf, G. Kann, S. Becker, C. Stephan, H. R. Brodt, P. de Leuw, T. Grunewald, T. Vogl, V. A. Kempf, O. T. Keppler, K. Zacharowski, *Lancet* **2015**, *385*, 1428.

[36] S. A. Ehrhardt, M. Zehner, V. Krahling, H. Cohen-Dvashi, C. Kreer, N. Elad, H. Gruell, M. S. Ercanoglu, P. Schommers, L. Gieselmann, R. Eggeling, C. Dahlke, T. Wolf, N. Pfeifer, M. M. Addo, R. Diskin, S. Becker, F. Klein, *Nat. Med.* **2019**, *25*, 1589.

[37] V. Krähling, D. Becker, C. Rohde, M. Eickmann, Y. Eroğlu, A. Herwig, R. Kerber, K. Kowalski, J. Vergara-Alert, S. Becker, the European Mobile Laboratory consortium, *Med. Microbiol. Immunol.* **2016**, *205*, 173.

[38] P. Becquart, T. Mahlakoiv, D. Nkoghe, E. M. Leroy, *PLoS One* **2014**, *9*, e96360.

[39] P. Rijal, S. C. Elias, S. R. Machado, J. L. Xiao, L. Schimanski, V. O'Dowd, T. Baker, E. Barry, S. C. Mendelsohn, C. J. Cherry, J. Jin, G. M. Labbe, F. R. Donnellan, T. Rampling, S. Dowall, E. Rayner, S. Findlay-Wilson, M. Carroll, J. Guo, X. N. Xu, K. Y. A. Huang, A. Takada, G. Burgess, D. McMillan, A. Popplewell, D. J. Lightwood, S. J. Draper, A. R. Townsend, *Cell Rep.* **2019**, *27*, 172.

[40] E. O. Saphire, S. L. Schendel, M. L. Fusco, K. Gangavarapu, B. M. Gunn, A. Z. Wec, P. J. Halfmann, J. M. Brannan, A. S. Herbert, X. G. Qiu, K. Wagh, S. He, E. E. Giorgi, J. Theiler, K. B. J. Pommert, T. B. Krause, H. L. Turner, C. D. Murin, J. Pallesen, E. Davidson, R. Ahmed, M. J. Aman, A. Bukreyev, D. R. Burton, J. E. Crowe, C. W. Davis, G. Georgiou, F. Krammer, C. A. Kyratsous, J. R. Lai, et al., *Cell* **2018**, *174*, 938.

[41] H. M. Berman, J. Westbrook, Z. Feng, G. Gilliland, T. N. Bhat, H. Weissig, I. N. Shindyalov, P. E. Bourne, *Nucleic Acids Res.* **2000**, *28*, 235.

[42] Y. G. Zhao, J. S. Ren, K. Harlos, D. M. Jones, A. Zeltina, T. A. Bowden, R. Padilla-Parra, E. E. Fry, D. I. Stuart, *Nature* **2016**, *535*, 169.

**ADVANCED
SCIENCE NEWS**

www.advancedsciencenews.com

**Biotechnology
Journal**

www.biotechnology-journal.com

[43] L. K. Weber, A. Palermo, J. Kugler, O. Armant, A. Isse, S. Rentschler, T. Jaenisch, J. Hubbuch, S. Dubel, A. Nesterov-Mueller, F. Breitling, F. F. Loeffler, *J. Immunol. Methods* **2017**, *443*, 45.

[44] S. T. Agnandji, A. Huttner, M. E. Zinser, P. Njuguna, C. Dahlke, J. F. Fernandes, S. Yerly, J. A. Dayer, V. Kraehling, R. Kasonta, A. A. Adegnika, M. Altfeld, F. Auderset, E. B. Bache, N. Biedenkopf, S. Borregaard, J. S. Brosnahan, R. Burrow, C. Combescure, J. Desmeules, M. Eickmann, S. K. Fehling, A. Finckh, A. R. Goncalves, M. P. Grobusch, J. Hooper, A. Jambrecina, A. L. Kabwende, G. Kaya, D. Kimani, et al., *N. Engl. J. Med.* **2016**, *374*, 1647.

[45] C. Dahlke, R. Kasonta, S. Lunemann, V. Krahling, M. E. Zinser, N. Biedenkopf, S. K. Fehling, M. L. Ly, A. Rechtien, H. C. Stubbe, F. Olearo, S. Borregaard, A. Jambrecina, F. Stahl, T. Strecker, M. Eickmann, M. Lutgehetmann, M. Spohn, S. Schmiedel, A. W. Lohse, S. Becker, M. M. Addo, V. Consortium, *EBioMedicine* **2017**, *19*, 107.

Supporting Information

Epitopes of naturally acquired and vaccine-induced anti-Ebola virus glycoprotein antibodies in single amino acid resolution

Jasmin Heidepriem [1,‡], Verena Krähling [2,3,‡], Christine Dahlke [4,5,6], Timo Wolf [7], Florian Klein [8,9,10], Marylyn M. Addo [4,5,6,*], Stephan Becker [2,3,*], and Felix F. Loeffler [1,*]

[1] Max Planck Institute of Colloids and Interfaces, Department of Biomolecular Systems, Am Muehlenberg 1, 14476 Potsdam, Germany

[2] Institute of Virology, Faculty of Medicine, Philipps University Marburg, Marburg, Germany

[3] German Center for Infection Research, partner site Gießen-Marburg-Langen, Marburg, Germany

[4] Division of Infectious Diseases, First Department of Medicine, University Medical Center Hamburg-Eppendorf, Hamburg, Germany

[5] Department of Clinical Immunology of Infectious Diseases, Bernhard Nocht Institute for Tropical Medicine, Hamburg, Germany

[6] German Center for Infection Research, Partner Site Hamburg-Lübeck-Borstel-Riems, Hamburg, Germany

[7] Department of Medicine, Infectious Diseases Unit, Goethe University Hospital, Frankfurt/Main, Germany

[8] Laboratory of Experimental Immunology, Institute of Virology, University of Cologne, Faculty of Medicine and University Hospital of Cologne, Cologne, Germany

[9] Center for Molecular Medicine Cologne (CMMC), University of Cologne, Faculty of Medicine, Cologne, Germany

[10] German Center for Infection Research, partner site Bonn-Cologne, Cologne, Germany

[‡] These authors contributed equally

Supporting Information Table 4. Amino acids of the EBOV GP shown in the structure. Protein Data Bank [43] file 5jq3 [44] – Crystal structure of Ebola glycoprotein.

Resolved	Missing	Affected IgG epitopes
	1 - 31	
32 - 195		
	196 - 210	3S 178 - 199
211 - 284		
	285, 286	
287 - 293		
	294 - 301	6V 291 - 312
302 - 310		
	311 - 469	7V 384 – 407
		8S 406 – 427
		9V 424 – 449
		10V 455 - 473
470 – 478 (unknown)		
	479 - 501	11S 471 – 489
502 - 631		
	632 - 676	13SV 620 – 653

3.2 Longitudinal Development of Antibody Responses in COVID-19 Patients of Different Severity with ELISA, Peptide, and Glycan Arrays: An Immunological Case Series

Pathogens **2021**, *10(4)*, 438

Author contributions

Rationale and summary of this publication

responses starting from symptom onset and following disease progression. The infection was confirmed by PCR, but there is uncertainty about the exact time of infection. In detail, sera of patients have been analyzed with ELISA of spike glycoprotein subunit 1 (S1), PMAs covering the whole SARS-CoV-2 proteome (Wuhan strain, reference genome MN908947.3) with 15-mer peptides with an overlap of 13 AAs, and glycan arrays with 135 different structures. Four patients donated serum after symptom onset, and two patients donated serum on three days (see Table *6*). The negative control was donated from patient #3 180 days before COVID-19 infection.

Table 6: Patient and serum sample information; samples analyzed with peptide and glycan microarrays. Table copied from [123].

Sample	Patient ID	Gender	Age	Symptoms	Hospitalized	Day of serum collection after onset of symptoms
1						d6
2	#1	Male	64	Moderate	Yes	d10
3						d22
4						d3
5	#2	Female	62	Mild	No	d15
6						d24
7						d-180
8	#3	Male	37	Mild	No	d4
9						d11
10	#4	Female	23	Mild	No	d12

The S1 ELISA detected IgA, IgG and IgM levels of patient #1, #2, and #3 during disease progression and also before infection (#3 day -180). The antibody development in patient #1 with moderate symptoms was increasing over time for all immunoglobulin classes. The measured IgA level of patient #2 peaked on day 15 and decreased on day 24. The IgG signal of patient #2 was increasing over time. In patient #3 only a positive signal for IgA with a peak on day 11 was observed with S1-specific ELISA. With the proteome PMAs, well defined signals could be obtained for IgA and IgG responses (see Figure 16). Here, the 99.9th percentile fluorescence intensity of IgA and IgG bound peptides detected with the negative control (#3 day -180) was defined the threshold. Patient #1 with moderate symptoms developed an increasing number of IgA and IgG peptide epitopes above the threshold over time (see Figure 16). In contrast, patient #2 with mild symptoms showed a decrease for most IgA and IgG peptide epitopes during disease progression. On day three, most peptides were detected above the threshold for patient #2 (see Figure 16). Patient #3 showed the highest IgA signals on day 4 after symptom onset and a low level of IgG against peptides (see Figure 16). The response to SARS-CoV-2 derived peptides was early peaking and decreasing over time in the two patients with mild symptoms (#2 and #3). In contrast, the IgA and IgG response of patient #1 with moderate symptoms was increasing over time.
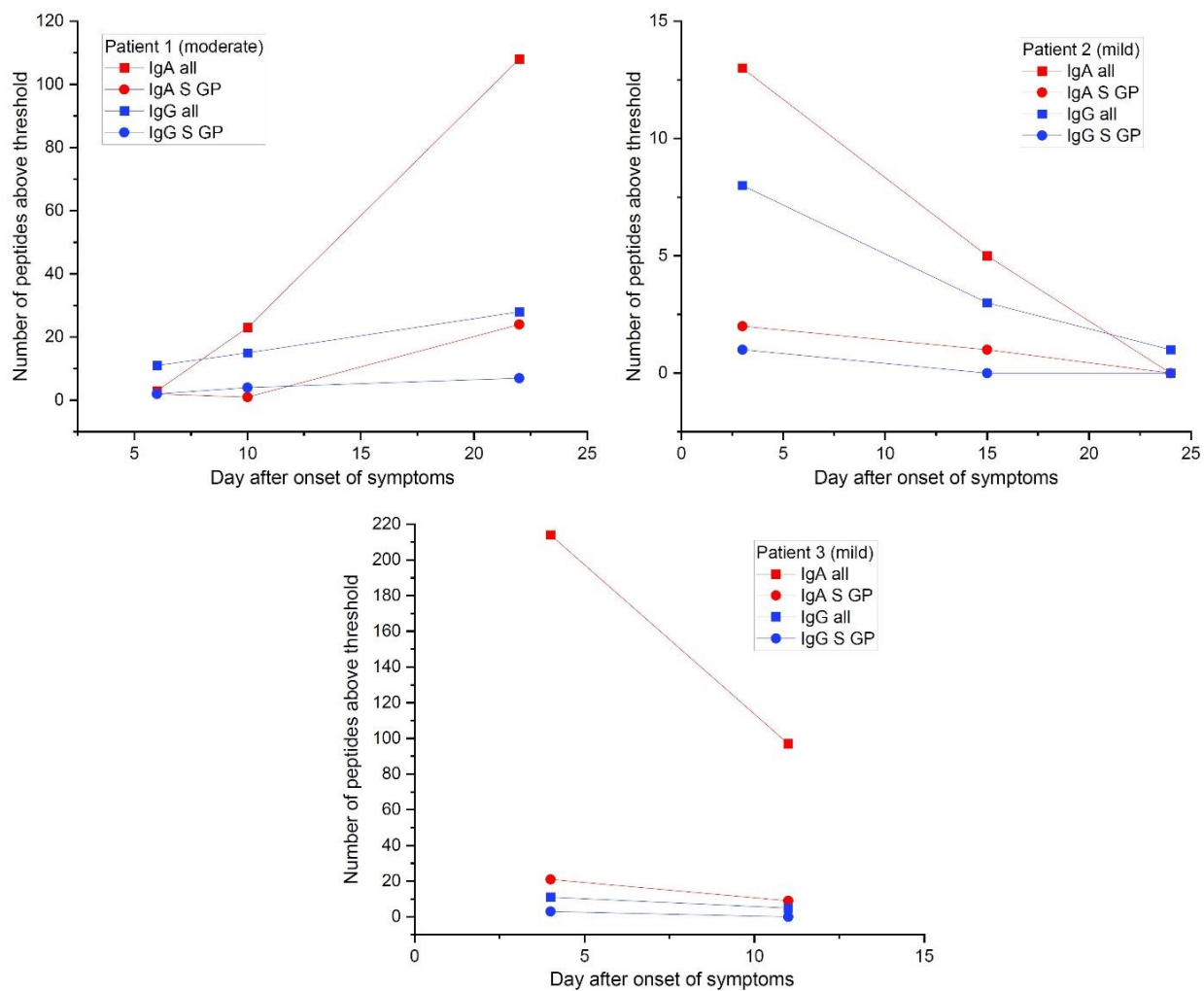
Figure 16: Number of peptides above fluorescence intensity threshold detected by IgA and IgG on different days after symptom onset detected with SARS-CoV-2 proteome PMAs. Data originate from [123].

Overall, a higher number of IgA than IgG reactive peptides was detected, which was also observed by others, when screening patient's antibody responses against receptor-binding domain (RBD) [124]. Many positive peptides from non-structural proteins were detected, which were later shown to be likely enhanced from cross-reactions to proteins from other coronavirus infections [125]. Epitopes of the spike glycoprotein (S GP) could be detected in all patients with IgA and IgG following the same trend as the patient´s overall antibody response over time to SARS-CoV-2 derived peptides (see Figure 16). Patient #2 showed a lower number of detected epitopes than patient #1 and #3 (see Figure 16 and Figure 17). All patients responded with IgA to the RBD of the S GP. The antibody response of COVID-19 patients to structural proteins (e.g., spike, membrane, nucleocapsid, envelope) are more distinct in contrast to non-structural proteins for viral replication [125]. Furthermore, Covid-19 patients with moderate to more severe symptoms show a stronger and broader antibody response compared to mild cases [124, 125].
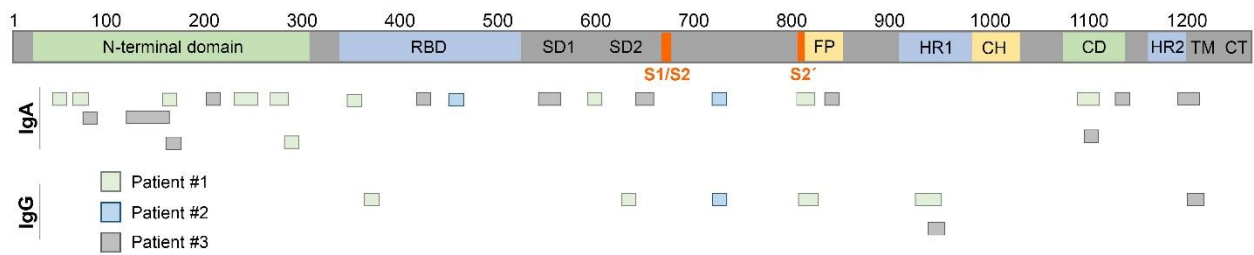
Figure 17: Map of detected linear epitopes in the S GP with IgA and IgG. The S GP domains are visualized on top (SD1/2: subdomain 1/2; S1/S2 and S2´cleavage sites, FP: fusion peptide; HR1/2: heptad repeat 1/2; CH: central helix; CD: connector domain; TM: transmembrane domain). Data originate from [123].

Moreover, glycan arrays were screened with patient serum, resulting in only a few interesting binding events. In patient #1, a higher signal for IgM against certain glycans was observed on day 22. For patient #2 the two antennae fragments mannoseα1-2mannoseα1-2mannose (GL99) and *N*-acetylneuraminic acidα-2,3galactoseβ1-4(fucoseα1-3)*N*-acetylglucosamine (GL89) were bound stronger on day 15 and 22 (see Figure 4 in the published article). For patient #3, higher signals towards some glycans (GL39, GL40, GL61, GL99) appeared on day 4 and 11 (see Figure 4 in the published article).

This study was able to detect similar epitopes of the spike protein as other studies [125-127] with PMAs covering the complete SARS-CoV-2 proteome. However, the significance of the presented data would have benefited from more patients included in the study.

Article

Longitudinal Development of Antibody Responses in COVID-19 Patients of Different Severity with ELISA, Peptide, and Glycan Arrays: An Immunological Case Series

Jasmin Heidepriem [1,†], Christine Dahlke [2,3,4,*,†], Robin Kobbe [2], René Santer [5], Till Koch [2,3,4], Anahita Fathi [2,3,4], Bruna M. S. Seco [1], My L. Ly [2,3,4], Stefan Schmiedel [2], Dorothee Schwinge [6], Sonia Serna [7], Katrin Sellrie [1], Niels-Christian Reichardt [7,8], Peter H. Seeberger [1], Marylyn M. Addo [2,3,4,*], Felix F. Loeffler [1,*] and on behalf of the ID-UKE COVID-19 Study Group [‡]

1 Department of Biomolecular Systems, Max Planck Institute of Colloids and Interfaces, Am Muehlenberg 1, 14476 Potsdam, Germany; jasmin.heidepriem@mpikg.mpg.de (J.H.); BrunaMara.SilvaSeco@mpikg.mpg.de (B.M.S.S.); Katrin.Sellrie@mpikg.mpg.de (K.S.); Peter.Seeberger@mpikg.mpg.de (P.H.S.)
2 Division of Infectious Diseases, First Department of Medicine, University Medical Center Hamburg-Eppendorf, 20251 Hamburg, Germany; r.kobbe@uke.de (R.K.); t.koch@uke.de (T.K.); a.fathi@uke.de (A.F.); m.ly@uke.de (M.L.L.); s.schmiedel@uke.de (S.S.)
3 Department of Clinical Immunology of Infectious Diseases, Bernhard Nocht Institute for Tropical Medicine, 20251 Hamburg, Germany
4 German Center for Infection Research, Partner Site Hamburg-Lübeck-Borstel-Riems, 20251 Hamburg, Germany
5 Department of Pediatrics, University Medical Center Hamburg-Eppendorf, 20251 Hamburg, Germany; r.santer@uke.de
6 I. Department of Medicine, University Medical Center Hamburg-Eppendorf, 20251 Hamburg, Germany; dschwing@uke.de
7 Glycotechnology Laboratory, Center for Cooperative Research in Biomaterials (CIC biomaGUNE), Basque Research and Technology Alliance (BRTA), Paseo de Miramon 182, 20014 Donostia San Sebastián, Spain; sserna@cicbiomagune.es (S.S.); nreichardt@cicbiomagune.es (N.-C.R.)
8 CIBER-BBN, Paseo Miramón 182, 20014 San Sebastián, Spain
* Correspondence: c.dahlke@uke.de (C.D.); m.addo@uke.de (M.M.A.); felix.loeffler@mpikg.mpg.de (F.F.L.)
† These authors contributed equally.
‡ Members of the ID-UKE COVID-19 Study Group are listed at the end of the manuscript.

Abstract: The current COVID-19 pandemic is caused by the severe acute respiratory syndrome coronavirus-2 (SARS-CoV-2). A better understanding of its immunogenicity can be important for the development of improved diagnostics, therapeutics, and vaccines. Here, we report the longitudinal analysis of three COVID-19 patients with moderate (#1) and mild disease (#2 and #3). Antibody serum responses were analyzed using spike glycoprotein enzyme linked immunosorbent assay (ELISA), full-proteome peptide, and glycan microarrays. ELISA immunoglobulin A, G, and M (IgA, IgG, and IgM) signals increased over time for individuals #1 and #2, whereas #3 only showed no clear positive IgG and IgM result. In contrast, peptide microarrays showed increasing IgA/G signal intensity and epitope spread only in the moderate patient #1 over time, whereas early but transient IgA and stable IgG responses were observed in the two mild cases #2 and #3. Glycan arrays showed an interaction of antibodies to fragments of high-mannose and core *N*-glycans, present on the viral shield. In contrast to protein ELISA, microarrays allow for a deeper understanding of IgA, IgG, and IgM antibody responses to specific epitopes of the whole proteome and glycans of SARS-CoV-2 in parallel. In the future, this may help to better understand and to monitor vaccination programs and monoclonal antibodies as therapeutics.

Keywords: SARS-CoV-2; COVID-19; full proteome; peptide microarrays; glycan microarrays

1. Introduction

The novel severe acute respiratory syndrome coronavirus 2 (SARS-CoV-2) was first described in Wuhan, China, in January 2020, as the causative agent of COVID-19 [1]. CoVs were not considered to be highly pathogenic, until the emergence of SARS-CoV [2–4] in 2002, and the Middle East respiratory syndrome (MERS)-CoV in 2012 [5]. With SARS-CoV-2, three CoVs have passed the species barriers from animal to human in the last 20 years, causing severe respiratory diseases. Based on their pathogenic and epidemic potential, the World Health Organization (WHO) has classified all three CoVs as priority pathogens to accelerate the development of vaccines and therapeutics to prevent epidemics.

The world is still confronted with the SARS-CoV-2 pandemic. This virus belongs to the *Betacoronavirus* genus of the Coronaviridae family and has genetic similarity with SARS-CoV. Within about one year, more than 114 million people have been infected globally, with more than 2.5 million reported deaths as of 2 March 2021 [6]. The infection presents with different symptoms and a wide spectrum of severity [7]. Some patients only experience very mild symptoms like a cough, while others show a very severe form of the disease that leads to bilateral pneumonia.

An efficient countermeasure to limit an outbreak includes specific and sensitive diagnostics. Polymerase chain reaction (PCR) is used to measure SARS-CoV-2 particles, whereas antibodies are measured by enzyme linked immunosorbent assay (ELISA), the gold standard for the detection of SARS-CoV-2 specific antibodies. These tests mainly rely on the binding of serum antibodies to the SARS-CoV-2 spike glycoprotein (S) [8]. The advantage of ELISAs is their simplicity and standardized protocol. A disadvantage is the limitation in sensitivity and specificity, since they lack information on specific epitopes.

Array technologies can help to fill this gap and identify epitopes that are targeted by antibodies, which in turn may be used to support the development of vaccines or monoclonal antibodies as therapeutics. High-density peptide arrays enable the rapid identification of antigen epitopes recognized by antibodies for many applications [9]. Pathogen-specific peptide arrays help to identify biomarkers for (early) detection of diseases [10]. Glycan arrays allow for the characterization and surveillance of viruses, identification of biomarkers, profiling of immune responses to vaccines, and epitope mapping [11,12].

In this study, we evaluate three distinct assays to identify the development of SARS-CoV-2 specific antibodies: (i) peptide arrays, covering the whole SARS-CoV-2 proteome as overlapping linear peptides, (ii) glycan arrays with a selected glycan library, and (iii) spike glycoprotein ELISA. We assess the ability of these assays to identify distinct epitopes, which can serve as potential biomarkers for disease progression. In combination with the clinical data of patients, we gained insights into immunoglobulin A, G, and M (IgA, IgG, and IgM) responses during COVID-19 progression.

Here, we report longitudinal antibody response data from three SARS-CoV-2-positive patients, sampled three times. While patient #1 had a moderate course of disease and was hospitalized (no ventilation), patient #2 experienced mild symptoms. Patient #3, who also had mild symptoms, was sampled only twice during disease and once 180 days before infection, which served as the negative control. Finally, for comparison, we added one sample of a single time point from another COVID-19 patient #4.

2. Materials and Methods

2.1. Patient Material

Blood samples were collected at the University Medical Center Hamburg-Eppendorf and the serum was immediately separated at 2000 g for 10 min, aliquoted, frozen, and stored at −80 °C. Table 1 lists information on patients and blood collection days.

Table 1. Patient and serum sample information; samples analyzed with peptide and glycan microarrays.

Sample	Patient ID	Gender	Age [y]	Symptoms	Hospitalized	Day of Serum Collection after Onset of Symptoms
1						d6
2	#1	Male	64	Moderate	Yes	d10
3						d22
4						d3
5	#2	Female	62	Mild	No	d15
6						d24
7						d-180
8	#3	Male	37	Mild	No	d4
9						d11
10	#4	Female	23	Mild	No	d12

2.2. Serum IgA, IgG, and IgM Elisa

Semi-quantitative SARS-CoV-2 IgA, IgG, and IgM enzyme-linked immunosorbent assay (ELISA) targeting the S1-Domain of the S-spike protein subunit were performed (Euroimmun AG, Lübeck, Germany) according to the manufacturer's instructions. Optical density was determined at a wavelength of 450 nm (OD450) and correction set to 620 nm. Ratios were calculated by Ratio = (Extinction control or sample)/(Extinction calibrator). A calibrator and positive control were provided with each ELISA kit. According to the manufacturer, a ratio of ≥ 1.1 should be regarded as positive and the manufacturer reports a specificity of 92.5 % for IgA, 99.3 % for IgG, and 98.6 % for IgM.

2.3. Peptide and Glycan Microarrays

The whole proteome of SARS-CoV-2 (GenBank ID: MN908947.3) was mapped as 4883 spots of overlapping 15-mer peptides with a lateral shift of two AA on peptide microarrays, obtained from PEPperPRINT GmbH (Heidelberg, Germany). Glycan microarrays containing a selection of 135 glycans were produced at CIC biomaGUNE (San Sebastián, Spain) [13]. Patient sera were diluted 1:200 (peptide) or 1:100 (glycan) and incubated on the arrays overnight. Afterwards, IgG, IgM, and IgA serum antibody interactions were differentially detected with fluorescently labeled secondary antibodies. For details, see Supplementary Materials.

3. Results

We collected blood of COVID-19 patients at different time points (Table 1) and used ELISA, peptide, and glycan microarrays to evaluate the kinetics of antibody development in detail.

Patient #1, a 64-year-old male, developed general weakness, myalgia and headache, intermittent episodes of very high fever, and subsequently, a productive cough. Two days after the first symptoms, he was tested positive for SARS-CoV-2 by RT-PCR. At that time point, the fever had already subsided, but a low-grade temperature recurred in the second week. An increase of C-reactive protein (53 mg/dL) required oral treatment with beta-lactamase antibiotic. The patient was hospitalized for four days and showed moderate but typical ground glass opacities on a high-resolution thorax computed tomography scan; he fully recovered without ventilation support. The patient did not require intensive care treatment or ventilation and the symptoms were moderate, due to hospitalization. Patient #2, his wife, a 62-year-old female, tested SARS-CoV-2 positive six days after her husband's first symptoms. She had high viral shedding of SARS-CoV-2 monitored by RT-PCR, although she reported only very mild clinical symptoms of COVID-19, such as sub-febrile temperatures, a mild cough, and a constant sense of well-being, as stated by Pfefferle and colleagues [14]. Patient #3 tested positive for SARS-CoV-2 with a mild course of disease, without hospitalization. Since this participant donated serum on a regular basis,

a serum sample was collected 180 days before the emergence of SARS-CoV-2, serving as a negative control. In addition, one sample served as another SARS-COV-2 positive control (#4, single time point d12, mild symptoms, see Supplementary Materials).

To evaluate the kinetics of B-cell epitopes during the mild and moderate courses of COVID-19, we first performed ELISA (EUROIMMUN, Lübeck, Germany) analysis (Figure 1, Supplementary A Table S1). This test relies on the S1 fragment of the spike glycoprotein (commercial test, likely AA1–685 of spike protein with glycosylation pattern). The IgG and IgM signals of patients #1 and #2 were below the threshold at early time points on day 6 (d6) and d3 respectively. The IgA signal of patient #1 was already highly positive on day 6 and increased until day 22. Patient #1 showed a positive signal for IgG only on day 22. The earliest positive results in patient #2 for IgG and IgM signals were measured on d15 and were also positive on d24, but only the IgG signal increased further over time. The IgA level of patient #2 showed a strong increase from the early time point d3 with an intermediate signal to the highest measured value on day 15. In patient #3, the assay failed to detect a clear positive IgG and IgM response, showing IgG signals in the intermediate level on days 4 and 32, while IgA appeared positive in all samples d-180, d4, d11 and d32 (for patient #4 see Supplementary Materials).
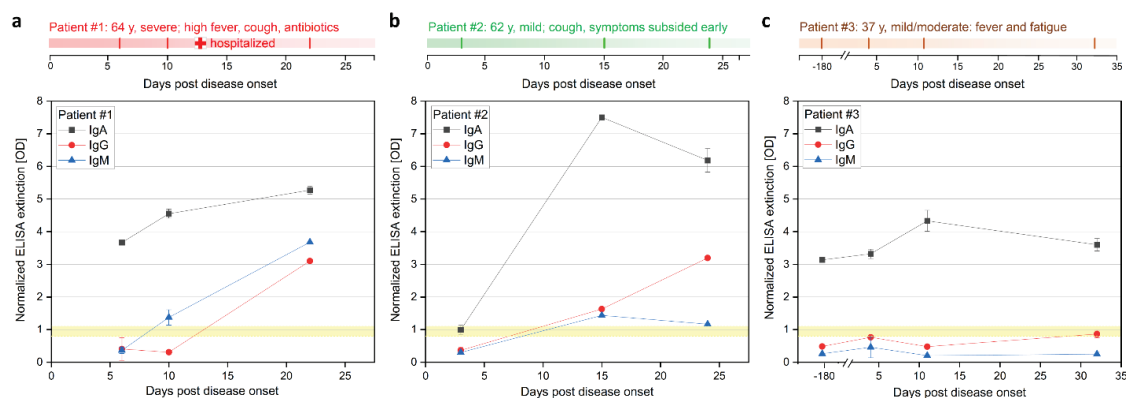
Figure 1. Longitudinal IgA, IgG, and IgM ELISA antibody response during COVID-19 disease progression in three patients. (**a**) Patients #1 (moderate), (**b**) #2 (mild), and (**c**) #3 (mild case). Patient #3 was also sampled 180 days prior infection, serving as a control. Sample from #3 collected at d32 was only analyzed with ELISA. ELISA (Euroimmune) was performed with S GP subunit 1 for detection of IgA and IgG at different days after onset of symptoms. Positive signal >1.1, negative signal <0.8, and intermediate 0.8–1.1 (highlighted yellow).

Next, we applied full-proteome peptide microarrays (see Supplementary Materials B for complete peptide microarray data). Before we evaluated the SARS-CoV-2 specific signals, an antibody threshold signal had to be established. Here, we used the serum sample from donor patient #3 (healthy negative control) 180 days before SARS-CoV-2 infection as a negative control and defined the 99.9 th percentile fluorescence intensity (i.e., 5 out of 4883 signals considered false positive) as a threshold for positive IgA- and IgG-reactive peptides (IgA: 347.8 arbitrary fluorescence units (AFU) or 6.54 transformed AFU (tAFU); IgG: 1081.4 AFU or 7.68 tAFU). Our threshold selection successfully limited the amount of presented data for intelligibility, without losing precision, as we could confirm previously published epitopes (see Discussion).

As a general trend, we observed SARS-CoV-2 protein-specific IgA and IgG responses with few defined signals, while IgM showed more signals, but without a clear trend. Thus, we focused on IgA and IgG responses. The evolution of IgA and IgG antibodies, targeting peptides of the SARS-CoV-2 proteome in patients #1 (Figure 2a,b) and #2 (Figure 2c,d) showed different dynamics: The moderate case (patient #1) showed a strong increase in IgA- and IgG-reactive peptides (above the control sample threshold) over time and eventually targeting many more epitopes (Supplementary Materials A Table S2). In comparison, the mild cases (patients #2 and #3) had a higher number of IgG- and an even higher number

of IgA-reactive SARS-CoV-2 peptides already at d3 and d4, respectively, post onset of symptoms, which decreased over time (Supplementary Materials A Table S2). At these early time points, we already detected IgA and IgG-specific epitopes in the spike protein in patients #2 and #3, while patient #1 developed a high number of antibodies targeting spike epitopes only later at d22.
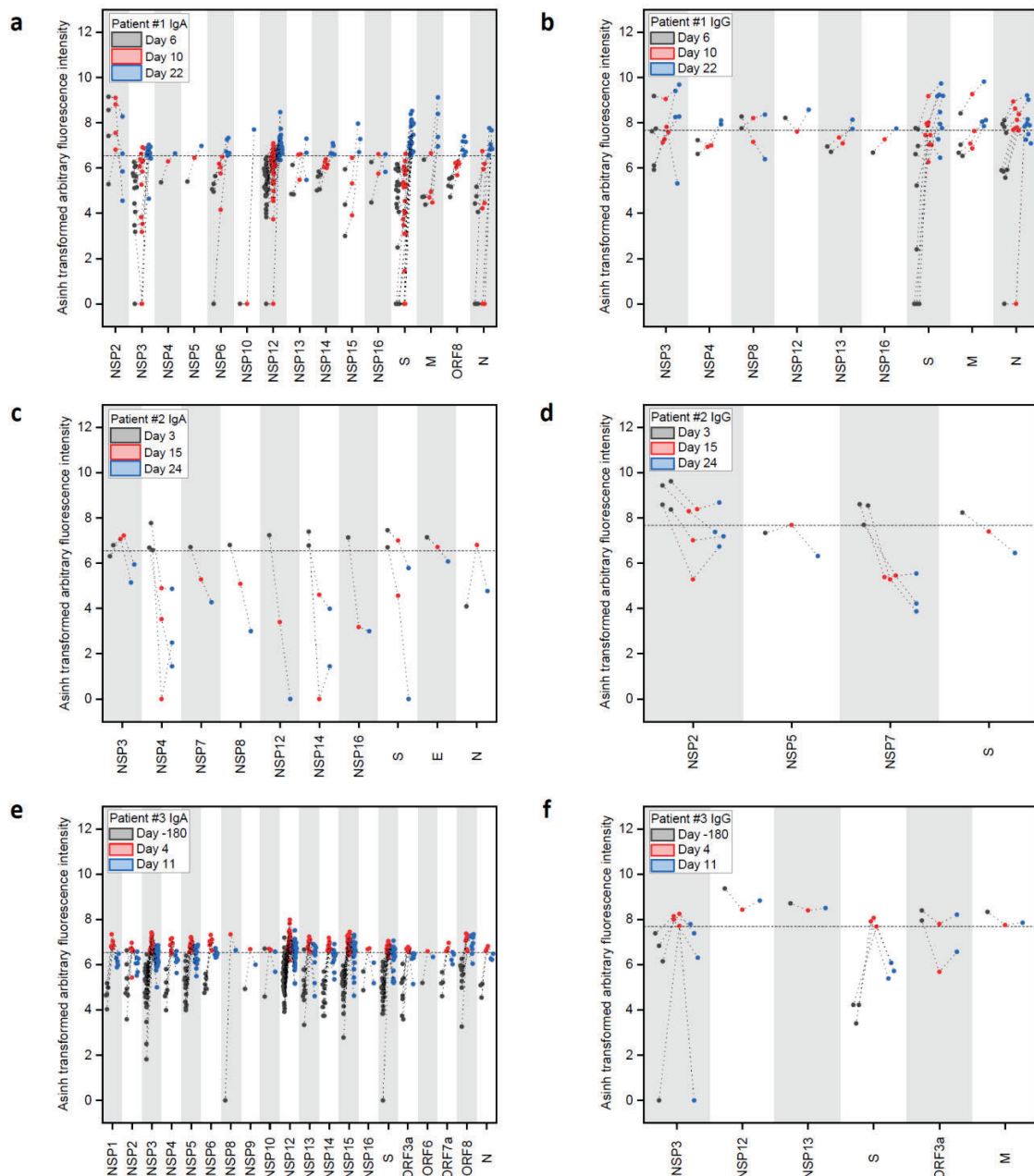

Figure 2. Longitudinal IgA and IgG antibody response against peptide epitopes above threshold from SARS-CoV-2 proteome during COVID-19 disease progression in three patients. (**a–f**) Evolution of positive IgA and IgG responses against SARS-CoV-2 peptides at different time points after onset of disease in patients #1, #2, and #3. Data were generated with peptide microarrays containing the whole SARS-CoV-2 proteome as 4883 overlapping peptides. Fluorescence intensities were transformed with the inverse hyperbolic sine (asinh function). Threshold selection shown as dashed horizontal lines: 99.9th percentile of IgA/IgG signals in healthy control sample #3 d-180, IgA: 6.54 transformed arbitrary fluorescence units, and IgG: 7.68 transformed arbitrary fluorescence units. For full array data, see Supplementary Materials B.

Patient #1 showed IgA responses at d6 (Figure 2a and Supplementary Materials A Table S2), solely targeting NSP2. The response was still limited four days later (d10), but then developed into a broad response at d22, targeting the nonstructural (NSP), the spike (S), membrane (M), ORF8, and nucleocapsid (N) proteins. The number of identified IgA-specific epitopes found in the different proteins increased over time in patient #1, with a particularly strong response to NSP3 and NSP12, while three signals for NSP2 epitopes decreased considerably. Regarding IgG responses (Figure 2b), patient #1 developed antibodies targeting the S and M protein already at d6 and the number of detected epitopes increased until d22.

In comparison, patient #2 (mild case, Figure 2c) showed a stronger and more specific IgA response already at d3 against the S, E, N, and NS proteins, while the IgG response (Figure 2d) revealed binding to NSPs and S. Patient #3 showed a strong and early response in IgA against many NSPs and the S protein (Figure 2e) comparing d-180 and d4, while the IgG (Figure 2f) only showed an increase in binding to NSP3 and S.

We visualized the identified epitopes derived from all patients (nine patient samples vs. control sample #3 d-180) on the S, M, and N proteins (Figure 3 and Supplementary Materials A Table S3). The data showed generally more IgA than IgG or IgM epitopes, with most epitopes located in the S and N protein.
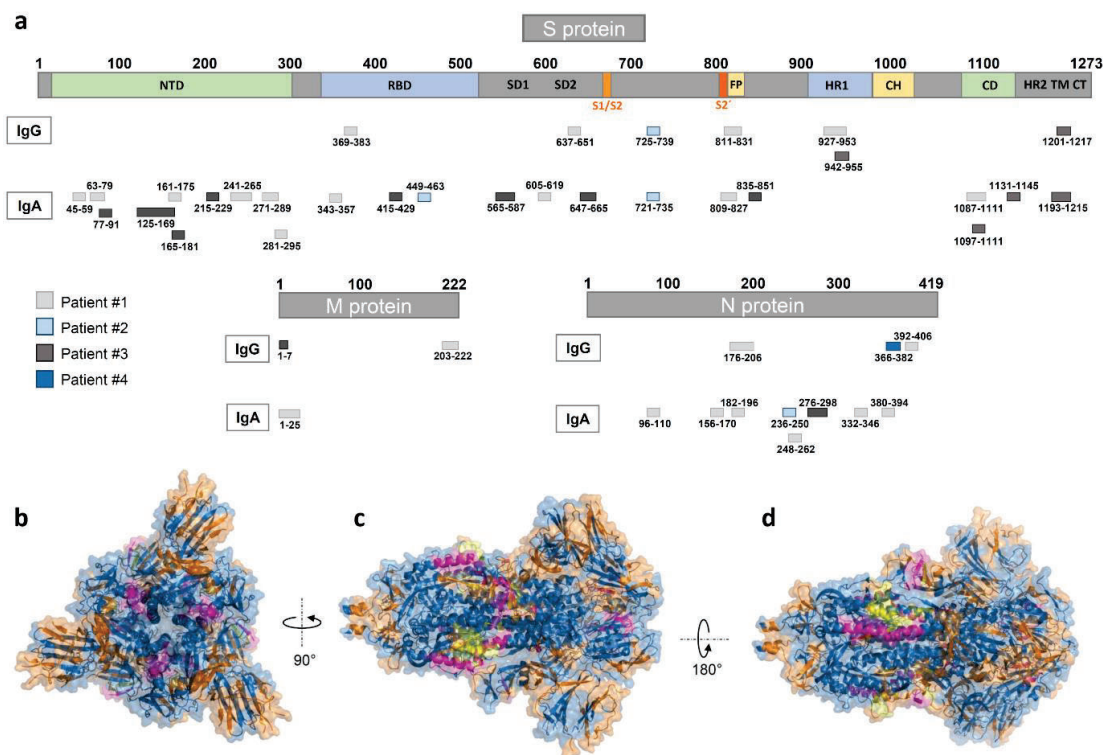
Figure 3. Mapping of peptide microarray reactive antibodies on the S, M, and N-proteins. (**a**) IgG and IgA epitopes derived from all four patients on the S (domains from [15]), M, and N proteins (see Supplementary Materials A Table S3). (**b–d**) A 3D view of the S GP structure (in blue) with the herein identified IgA (highlighted in orange), IgG (highlighted in magenta), and overlapping (highlighted in yellow) epitopes derived from all nine SARS-CoV-2 patient samples (generated with PyMOL from Protein Data Bank file 6vxx—cryo-EM structure of S GP [16]). (**b**) Top view, (**c**) side view, and (**d**) alternate side view of S GP trimer.

Finally, serum samples were analyzed with glycan microarrays, covering a diverse library of glycans (Figure 4, detailed information in Supplementary Materials C and Supplementary Materials A Figure S1). The glycans on the arrays cover several epitopes of the glycan shield of the SARS-CoV-2 surface [17]. Strong binding could be observed for the *N*-glycan core fragment ($Man_2GlcNAc_2$). Furthermore, α1-2-Man_3 showed increased

binding in convalescent time points, which hints to binding of high-mannose (M7–M9) structures, which are reported to be part of the glycan shield of SARS-CoV-2 (especially spike N234) [17]. Similar to the observed trend with the peptide microarrays, patient #1 showed a strong increase in antibody binding at d22 towards the *N*-glycan core structures (strongest increase observed in IgM), while patient #2 had generally stronger and more constant signals, except for the binding to α1-2-Man$_3$. These results confirmed the general trends observed in both peptide and glycan microarray approaches, showing a strong increase of antibody responses in patient #1 at d22.
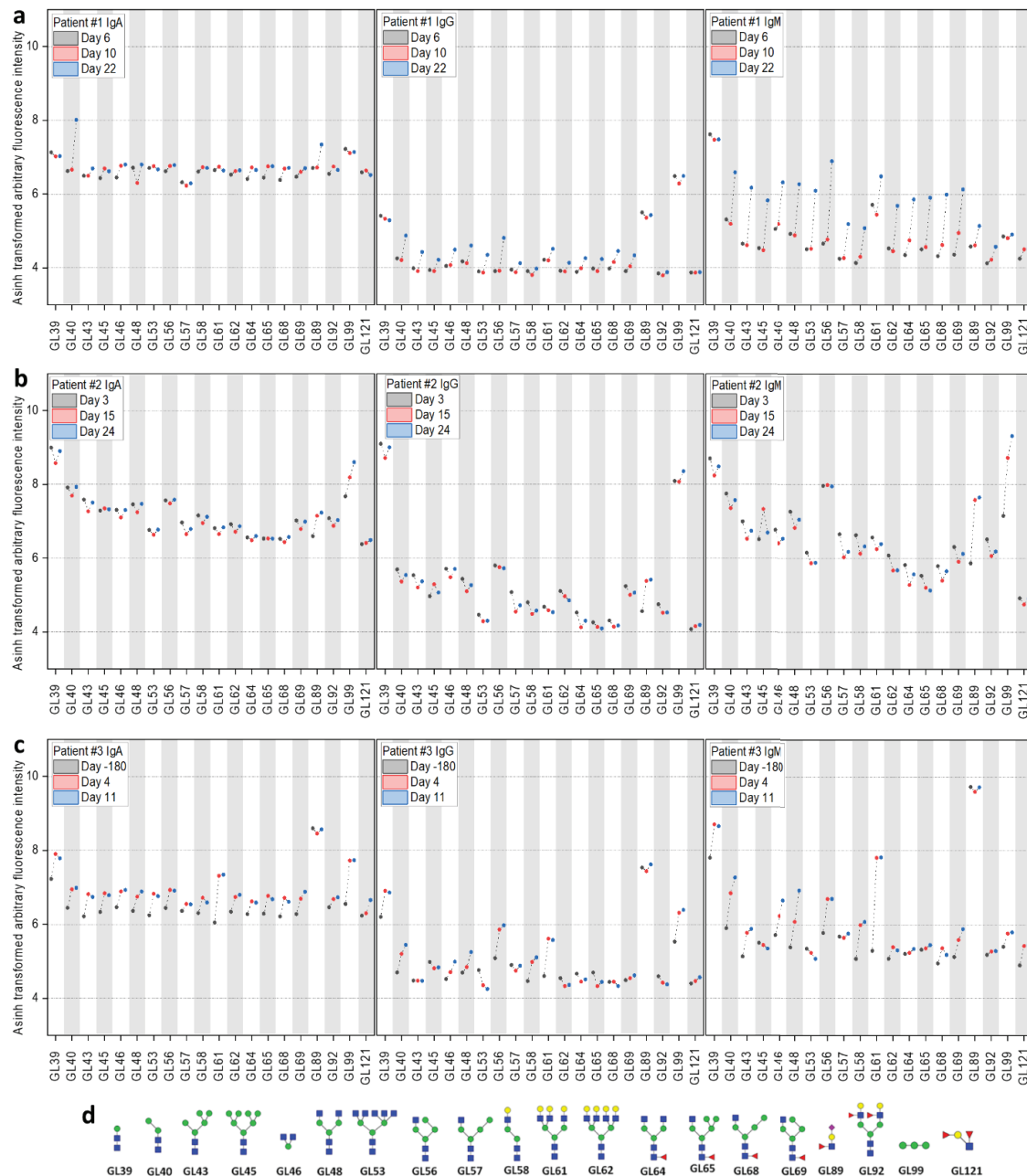
Figure 4. Longitudinal IgA, IgG, and IgM antibody response analyzed with glycan microarrays during COVID-19 disease progression in three patients. Evolution of reactive IgA, IgG, and IgM antibodies in patients #1–#3 (**a**–**c**) against a selection of glycans (**d**) on the microarrays at different time points (see Supplementary Materials C). For improved visualization, fluorescence intensities were transformed with the inverse hyperbolic sine (asinh function).

54

4. Discussion

To better understand the development of antibodies in SARS-CoV-2 infection and their consequence on the course of disease, we evaluated three assays that monitor the kinetics of B-cell epitope development in relation to clinical features. Three patients were sampled longitudinally. Two patients experienced a mild disease course (#2 and #3), another a moderate course (#1). We compared the longitudinal antibody response data using spike glycoprotein ELISA, peptide arrays of the whole SARS-CoV-2 proteome, and glycan arrays.

Serology testing for COVID-19 using ELISA is attractive because of the relatively short time to diagnosis and the ability to test for an active immune response against the virus. Comparing the three different approaches, the ELISA gives rather robust signals in the convalescent phase, while failing for early antibody detection. It is possible that the ELISA detects antibodies that either bind conformational/discontinuous epitopes or to glycopeptides. The assay gave similar positive results for both patients #1 and #2 in the convalescent phase (days 22 and 24). Comparing the data of patient #2 with mild symptoms we found that the peptide array shows a decline of binding to linear peptides over time, while the ELISA points into the opposite direction. In contrast, patient #1, with moderate symptoms, shows much stronger signals to the linear peptides on the array over time, which corresponds to the ELISA data. However, ELISA was inconclusive for patient #3, resulting in generally positive IgA and generally negative (or intermediate) IgG results for all time points, including d-180 prior infection and d32 (only analyzed by ELISA).

Recently, early antibody responses have been reported by ELISA [18], where seroconversion was found on day 7 after onset of symptoms in 50% of analyzed individuals. Another study underlined the early responses of IgA, IgM, and IgG following SARS-CoV-2 infection [19]. The authors reported a median duration of IgM and IgA antibody detection of five days and the detection of IgG 14 days after disease onset. Furthermore, Okba et al. [8] analyzed IgA and IgG responses in two mild and one moderate case using an in-house S1-ELISA. They observed an increase in the IgA response over time in a moderate case. An early or increased IgA response on arrays, as seen in our patients #2 and #3, was not observed with ELISA, possibly due to differences in the patients (sample collection dates) or assay performance. Key differences in these assays are the limitation of only using S1-proteins for the ELISA (vs. whole proteome on the microarray) and a higher sensitivity of peptide arrays towards linear epitopes. With the peptide arrays, cross-reactions to previous infections (e.g., with other coronaviruses) may become visible.

In contrast to ELISA, arrays are more time- and cost-intensive but provide more information on the development of antibodies. We identified several spike protein epitopes that are bound by IgA antibodies. We identified spike-specific IgA epitopes in the receptor binding domain, AA343-357, AA415-429, and AA449-463. The latter epitope is located in the receptor binding domain-angiotensin-converting enzyme II (RBD-ACE2)-complex and, therefore, may be the target of neutralizing antibodies [20]. In addition, we also confirm a part (AA369-383) of the SARS-CoV-2 and SARS-CoV cross-reactive IgG epitope (AA369-392) identified by Yuan et al., which is located in the receptor binding domain of spike [21]. Next, we observed IgA (AA809-827) and IgG (AA811-831) antibody binding, corresponding to the S2 cleavage site and fusion peptide. These have been described as distinctive epitopes in COVID-19 patients with neutralizing potential [20,22]. Furthermore, we could identify reactive peptides, especially in the N protein, as well as NSP3 and NSP12. Data from a partial proteome array approach was reported [23], which confirms strong binding to the N protein, although they did not cover NSP3 and NSP12. In contrast to NSP-binding antibodies, which could be cross-reactive from other viral infections, antibodies binding structural proteins like the S and N proteins, could be more distinctive for a SARS-CoV-2 infection [22]. It will be of interest to determine the longevity of these antibody responses and its impact on neutralization [24].

With the peptide arrays, we detected an early IgA response in the mild cases (patients #2 and #3). Respiratory viruses can induce efficient IgA responses in secretions as well as in sera. It was proposed that an early IgA response is predominant in COVID-19 and is

more effective in SARS-CoV-2 neutralization than IgG [25]. IgA antibodies might be valuable diagnostic markers for early SARS-CoV-2 identification especially in mild-symptom patients. Due to high sensitivity and specificity, arrays may be relevant as diagnostics for the detection of these early antibody responses. Patient #2 potentially benefited from her early IgA response, which led to a mild course of the disease.

Employing glycan arrays, we identified several glycans that correspond to small fragments of the *N*-glycan core (e.g., $Man_2GlcNAc_2$). In addition, we observed an increase in binding to α1-2-Man_3 (GL99 on the array) in patients #2 and #3. This fragment is part of the antennae of high-mannose (M7–M9) *N*-glycans, present on the spike protein (e.g., N122, N234, N343, and possibly others) [17,26]. A promising, but technically overly challenging approach, would be to screen glycopeptides with native glycan structures. Casalino et al. highlighted the modulating role of the spike protein N-glycan sites N165 and N234 for the conformation of the RBD [27]. Furthermore, a neutralizing antibody has been identified that binds a larger glycopeptide epitope of the SARS-CoV-2 spike protein [28]. Interestingly, we observe many spike-related peptide epitopes on the array, which would carry an *N*-glycosylation on the native virus (e.g., patient #1 in spike: AA63-79, AA271-289, AA343-357, AA605-619, and AA1087-1111). The glycan arrays generally show a similar trend as the peptide array results: the antibody response increases in patient #1 over time, whereas it stays constant or decreases over the course of the infection in patients #2 and #3, except for α1-2-Man_3. Since many microorganisms express α1-2-Man_3 on their surface, the SARS-CoV-2 infection might have caused a boost of a pre-existing immune response towards this epitope. Yet, data has to be evaluated in a broader context, since signals to glycans may be part of an unrelated cross-reaction or response to a larger glycopeptide epitope and multivalency can strongly influence the results.

We screened longitudinal serum samples of COVID-19 patients with different methods to get insights into their antibody responses and compared our data with findings of recent literature. A clear limitation of our study is the number of subjects, but still we were able to observe trends for the development of antibodies early after SARS-CoV-2 infection. Since all samples were collected from the same cluster of infection, which were the first detected SARS-CoV-2 infections in Hamburg, Germany, a clear chain of infection could be assured and samples could be collected repeatedly. This, and the limited access to arrays (especially glycan arrays), restricted the cohort size.

Our study emphasizes the importance of microarrays for early diagnostics and understanding of antibody development following SARS-CoV-2 infection. Arrays are able to reveal heterogeneous antibody responses in patients with different severity of symptoms. With a high assay sensitivity, antibody development in patients can be tracked during the course of disease and also early after infection. A general limitation of arrays is the use of exclusively linear peptides, which cannot identify antibodies that bind conformational or discontinuous epitopes. We exclusively considered the initially published Wuhan strain without mutations, but can quickly incorporate these mutations into the assay, since the array production method is rapid and flexible [29].

With the limitations listed above, our study contributes to the understanding of differences in the course of disease. There is still limited understanding of the immune correlates of protection. Collectively, we present an analysis of longitudinal antibody response in serum samples, comparing the degree of disease severity with three different approaches.

Author Contributions: J.H. performed all microarray related experiments and analyses. C.D. performed the immunological analyses. R.K., R.S., T.K., A.F., S.S. (Stefan Schmiedel), D.S., M.L.L. and the ID-UKE COVID-19 study group performed clinical monitoring and immunological analyses. F.F.L. supervised the microarray experiments, J.H. and F.F.L. performed the data analysis. N.-C.R., S.S. (Sonia Serna) and P.H.S. provided the glycan microarrays, B.M.S.S. and K.S. helped with their analysis. D.S. performed ELISA analyses. C.D., M.M.A. and F.F.L. supervised the project. C.D., J.H.

References

1. Zhou, P.; Yang, X.-L.; Wang, X.-G.; Hu, B.; Zhang, L.; Zhang, W.; Si, H.-R.; Zhu, Y.; Li, B.; Huang, C.-L.; et al. A pneumonia outbreak associated with a new coronavirus of probable bat origin. *Nature* **2020**, *579*, 270–273. [CrossRef]
2. Peiris, J.; Lai, S.; Poon, L.; Guan, Y.; Yam, L.; Lim, W.; Nicholls, J.; Yee, W.; Yan, W.; Cheung, M.; et al. Coronavirus as a possible cause of severe acute respiratory syndrome. *Lancet* **2003**, *361*, 1319–1325. [CrossRef]
3. Ksiazek, T.G.; Erdman, D.; Goldsmith, C.S.; Zaki, S.R.; Peret, T.; Emery, S.; Tong, S.; Urbani, C.; Comer, J.A.; Lim, W.; et al. A Novel Coronavirus Associated with Severe Acute Respiratory Syndrome. *N. Engl. J. Med.* **2003**, *348*, 1953–1966. [CrossRef]
4. Drosten, C.; Günther, S.; Preiser, W.; Van Der Werf, S.; Brodt, H.R.; Becker, S.; Rabenau, H.; Panning, M.; Kolesnikova, L.; Fouchier, R.A.M.; et al. Identification of a Novel Coronavirus in Patients with Severe Acute Respiratory Syndrome. *N. Engl. J. Med.* **2003**, *348*, 1967–1976. [CrossRef]
5. Zaki, A.; Van Boheemen, S.; Bestebroer, T.; Osterhaus, A.; Fouchier, R. Isolation of a Novel Coronavirus from a Man with Pneumonia in Saudi Arabia. *N. Engl. J. Med.* **2012**, *367*, 1814–1820. [CrossRef]
6. Dong, E.; Du, H.; Gardner, L. An interactive web-based dashboard to track COVID-19 in real time. *Lancet Infect. Dis.* **2020**, *20*, 533–534. [CrossRef]
7. Guan, W.J.; Ni, Z.Y.; Hu, Y.; Liang, W.H.; Ou, C.Q.; He, J.X.; Liu, L.; Shan, H.; Lei, C.L.; Hui, D.S.C.; et al. Clinical Characteristics of Coronavirus Disease 2019 in China. *N. Engl. J. Med.* **2020**, *382*, 1708–1720. [CrossRef]
8. Okba, N.M.; Müller, M.A.; Li, W.; Wang, C.; GeurtsvanKessel, C.H.; Corman, V.M.; Lamers, M.M.; Sikkema, R.S.; De Bruin, E.; Chandler, F.D.; et al. Severe Acute Respiratory Syndrome Coronavirus 2—Specific Antibody Responses in Coronavirus Disease Patients. *Emerg. Infect. Dis.* **2020**, *26*, 1478–1488. [CrossRef] [PubMed]
9. Szymczak, L.C.; Kuo, H.-Y.; Mrksich, M. Peptide Arrays: Development and Application. *Anal. Chem.* **2018**, *90*, 266–282. [CrossRef]
10. Jaenisch, T.; Heiss, K.; Fischer, N.; Geiger, C.; Bischoff, F.R.; Moldenhauer, G.; Rychlewski, L.; Sié, A.; Coulibaly, B.; Seeberger, P.H.; et al. High-density Peptide Arrays Help to Identify Linear Immunogenic B-cell Epitopes in Individuals Naturally Exposed to Malaria Infection. *Mol. Cell. Proteom.* **2019**, *18*, 642–656. [CrossRef] [PubMed]
11. Geissner, A.; Seeberger, P.H. Glycan Arrays: From Basic Biochemical Research to Bioanalytical and Biomedical Applications. *Annu. Rev. Anal. Chem.* **2016**, *9*, 223–247. [CrossRef]
12. Muthana, S.M.; Gildersleeve, J.C. Glycan microarrays: Powerful tools for biomarker discovery. *Cancer Biomark.* **2014**, *14*, 29–41. [CrossRef]
13. Echeverria, B.; Serna, S.; Achilli, S.; Vivès, C.; Pham, J.; Thépaut, M.; Hokke, C.H.; Fieschi, F.; Reichardt, N.-C. Chemoenzymatic Synthesis of N-glycan Positional Isomers and Evidence for Branch Selective Binding by Monoclonal Antibodies and Human C-type Lectin Receptors. *ACS Chem. Biol.* **2018**, *13*, 2269–2279. [CrossRef]
14. Pfefferle, S.; Günther, T.; Kobbe, R.; Czech-Sioli, M.; Nörz, D.; Santer, R.; Oh, J.; Kluge, S.; Oestereich, L.; Peldschus, K.; et al. Low and high infection dose transmission of SARS-CoV-2 in the first COVID-19 clusters in Northern Germany. *medRxiv* **2020**. [CrossRef]

15. Wrapp, D.; Wang, N.; Corbett, K.S.; Goldsmith, J.A.; Hsieh, C.-L.; Abiona, O.; Graham, B.S.; McLellan, J.S. Cryo-EM structure of the 2019-nCoV spike in the prefusion conformation. *Science* **2020**, *367*, 1260–1263. [CrossRef]

16. Walls, A.C.; Park, Y.J.; Tortorici, M.A.; Wall, A.; McGuire, A.T.; Veesler, D. Structure, function, and antigenicity of the SARS-CoV-2 spike glycoprotein. *Cell* **2020**, *181*, 281–292. [CrossRef] [PubMed]

17. Watanabe, Y.; Allen, J.D.; Wrapp, D.; McLellan, J.S.; Crispin, M. Site-specific glycan analysis of the SARS-CoV-2 spike. *Science* **2020**, *369*, 330–333. [CrossRef]

18. Wölfel, R.; Corman, V.M.; Guggemos, W.; Seilmaier, M.; Zange, S.; Müller, M.A.; Niemeyer, D.; Jones, T.C.; Vollmar, P.; Rothe, C.; et al. Virological assessment of hospitalized patients with COVID-2019. *Nat. Cell Biol.* **2020**, *581*, 465–469. [CrossRef]

19. Guo, L.; Ren, L.; Yang, S.; Xiao, M.; Chang, D.; Yang, F.; Cruz, C.S.D.; Wang, Y.; Wu, C.; Xiao, Y.; et al. Profiling Early Humoral Response to Diagnose Novel Coronavirus Disease (COVID-19). *Clin. Infect. Dis.* **2020**, *71*, 778–785. [CrossRef]

20. Wang, H.; Wu, X.; Zhang, X.; Hou, X.; Liang, T.; Wang, D.; Teng, F.; Dai, J.; Duan, H.; Guo, S.; et al. SARS-CoV-2 Proteome Microarray for Mapping COVID-19 Antibody Interactions at Amino Acid Resolution. *ACS Cent. Sci.* **2020**, *6*, 2238–2249. [CrossRef]

21. Yuan, M.; Wu, N.C.; Zhu, X.; Lee, C.C.D.; So, R.T.Y.; Lv, H.; Mok, C.K.P.; Wilson, I.A. A highly conserved cryptic epitope in the receptor binding domains of SARS-CoV-2 and SARS-CoV. *Science* **2020**, *368*, 630–633. [CrossRef] [PubMed]

22. Shrock, E.; Fujimura, E.; Kula, T.; Timms, R.T.; Lee, I.-H.; Leng, Y.; Robinson, M.L.; Sie, B.M.; Li, M.Z.; Chen, Y.; et al. Viral epitope profiling of COVID-19 patients reveals cross-reactivity and correlates of severity. *Science* **2020**, *370*, eabd4250. [CrossRef]

23. Jiang, H.W.; Li, Y.; Zhang, H.; Wang, W.; Yang, X.; Qi, H.; Li, H.; Men, D.; Zhou, J.; Tao, S.C. SARS-CoV-2 proteome microarray for global profiling of COVID-19 specific IgG and IgM responses. *Nat. Commun.* **2020**, *11*, 3581. [CrossRef]

24. Seow, J.; Graham, C.; Merrick, B.; Acors, S.; Steel, K.J.A.; Hemmings, O.; O'Bryne, A.; Kouphou, N.; Pickering, S.; Galao, R.P.; et al. Longitudinal evaluation and decline of antibody responses in SARS-CoV-2 infection. *medRxiv* **2020**. [CrossRef]

25. Sterlin, D.; Mathian, A.; Miyara, M.; Mohr, A.; Anna, F.; Claër, L.; Quentric, P.; Fadlallah, J.; Devilliers, H.; Ghillani, P.; et al. IgA dominates the early neutralizing antibody response to SARS-CoV-2. *Sci. Transl. Med.* **2021**, *13*, eabd2223. [CrossRef]

26. Shajahan, A.; Supekar, N.T.; Gleinich, A.S.; Azadi, P. Deducing the N-and O-glycosylation profile of the spike protein of novel coronavirus SARS-CoV-2. *Glycobiology* **2020**, *30*, 981–988. [CrossRef]

27. Casalino, L.; Gaieb, Z.; Goldsmith, J.A.; Hjorth, C.K.; Dommer, A.C.; Harbison, A.M.; Fogarty, C.A.; Barros, E.P.; Taylor, B.C.; McLellan, J.S.; et al. Beyond Shielding: The Roles of Glycans in the SARS-CoV-2 Spike Protein. *ACS Cent. Sci.* **2020**, *6*, 1722–1734. [CrossRef]

28. Pinto, D.; Park, Y.J.; Beltramello, M.; Walls, A.C.; Tortorici, M.A.; Bianchi, S.; Jaconi, S.; Culap, K.; Zatta, F.; de Marco, A.; et al. Cross-neutralization of SARS-CoV-2 by a human monoclonal SARS-CoV antibody. *Nature* **2020**, *583*, 290–295. [CrossRef]

29. Stadler, V.; Felgenhauer, T.; Beyer, M.; Fernandez, S.; Leibe, K.; Güttler, S.; Gröning, M.; König, K.; Torralba, G.; Hausmann, M.; et al. Combinatorial Synthesis of Peptide Arrays with a Laser Printer. *Angew. Chem. Int. Ed.* **2008**, *47*, 7132–7135. [CrossRef] [PubMed]

Supporting Information

Longitudinal development of antibody responses in COVID-19 patients of different severity with ELISA, peptide, and glycan arrays: an immunological case series

Christine Dahlke, Jasmin Heidepriem, Robin Kobbe, René Santer, Till Koch, Anahita Fathi, Bruna M. S. Seco, My L. Ly, Stefan Schmiedel, Dorothee Schwinge, Sonia Serna, Katrin Sellrie, Niels-Christian Reichardt, ID-UKE COVID-19 study group, Peter H. Seeberger, Marylyn M. Addo, Felix F. Loeffler

Enzyme linked immunosorbent assay – ELISA

ELISA of the S1 subunit of spike glycoprotein (EUROIMMUN Medizinische Labordiagnostika AG, https://www.euroimmun.com) was used to analyze antibody titers of IgA, IgG, and IgM in patients. The assay was performed according to the manufacturer's protocol. Optical density (OD) was detected at 450 nm and we calculated a ratio of the reading of each sample to the reading of the included calibrator for each sample (normalized OD). A positive signal is assumed for an OD above 1.1 and a negative signal below 0.8, whereas a signal between 0.8 – 1.1 is considered as intermediate.

Table S1. Normalized extinction [OD] of ELISA. Classification: negative < 0.8, intermediate 0.8 – 1.1, and positive > 1.1.

Sample	IgA	IgG	IgM
Positive control	3.7	2.4	3.0
Negative control	0.5	0.5	0.2
Patient #1 d6	3.7	0.4	0.4
Patient #1 d10	4.6	0.3	1.4
Patient #1 d22	5.3	3.1	3.7
Patient #2 d3	1.0	0.4	0.3
Patient #2 d15	7.5	1.6	1.4
Patient #2 d24	6.2	3.2	1.2
Patient #3 d-180	3.1	0.5	0.3
Patient #3 d4	3.3	0.8	0.5
Patient #3 d11	4.3	0.5	0.2
Patient #3 d32	3.6	0.9	0.2
Patient #4 d12	3.2	0.8	0.7

Peptide microarrays

The whole proteome of SARS-CoV-2 (GenBank ID: MN908947.3) was mapped as overlapping sequences on peptide microarrays. The sequences of ORF1ab polyprotein, spike glycoprotein (S), ORF3a protein, envelope protein (E), membrane glycoprotein (M), ORF6 protein, ORF7a protein, ORF8 protein, nucleocapsid phosphoprotein (N), and ORF10 protein were elongated and linked by neutral GSGSGSG linkers to avoid truncated peptides. The elongated protein sequences were translated into 4 883 different 15 amino acid peptides printed in duplicate (9 766 peptide spots) with a peptide-peptide overlap of 13 amino acids for high resolution epitope data. Peptide microarrays were obtained from PEPperPRINT GmbH (Heidelberg, Germany). Regarding the reproducibility of the peptide microarray assay, according to the vendor PEPperPRINT GmbH, the coefficient of determination between the batch control array of our microarray batch (all our arrays were from the same batch) and the general standard control microarray was $R^2 = 0.888$. Since all our peptide arrays were from the same batch, the intra-batch R^2 is expected to be > 0.9. To estimate the limit of detection (LoD), blank arrays were incubated with all secondary antibodies, anti-human IgG Dylight680 (Bethyl, A80-304D6) 0.5 mg/mL 1:1000, anti-human IgA Dylight800 (Rockland, 609-145-006) 1.0 mg/mL 1:1600, anti-human IgM Dylight 549 (Rockland, 609-142-007) 1.0 mg/mL 1:2000, control anti-HA (BioXcell, RT0168) 1.0 mg/ml labeled 680 1:2000. The secondary antibodies show negligible (unspecific) binding to the slide surface (< 50 AFU). The LoD was calculated according to Armbruster & Pry, 2008.[1] Using the blank control (= staining only with secondary antibodies), in the traditional approach, the LoD is calculated as the mean of blank control +2x standard deviation. This results in estimations for LoD IgG (700nm) = 134 AFU + 2x 36 AFU = 206 AFU, LoD IgA (800nm) = 118 AFU + 2x 48 AFU = 214 AFU, LoD IgM (532nm) = 177 AFU + 2x 59 AFU = 295 AFU. However, the LoD of the assay is impacted by its semi-quantitative nature of screening many interactions in parallel, which include false positive hits, as well as cross-reactive epitopes. Therefore, we chose to use the negative control serum as the background, to reduce the impact of false positive and cross-reactive epitopes.

Glycan microarrays

Glycan microarrays were prepared as previously described.[2] Briefly, solutions of aminopentyl functionalized carbohydrates (50 µM, 1.25 nL, 5 drops, drop volume: 250 pL) in printing buffer (300 mM sodium phosphate + 0.005 % Tween® 20) were arrayed on N-hydroxysuccinimide (NHS) activated glass slides (Nexterion® slide H, Schott AG) employing a piezoelectric non-contact printer (SciFLEXARRAYER S11, Scienion). Each carbohydrate was printed in 4 replicates, generating 7 identical subarrays per slide. After printing, slides were incubated at

humidity over 75 % overnight at RT. After immobilization, the remaining NHS groups were quenched (50 mM ethanolamine in sodium borate buffer 50 mM pH = 9) at RT for one hour. To estimate the limit of detection of the glycan arrays, we incubated the arrays only with the secondary antibodies, to have a blank control value for the detection without sample: Anti-human IgG Alexa Fluor 647 (SouthernBiotech, 2048-31) 0.5 mg/ml 1:400, anti-human IgA Rhodamine (Rockland, 609-1006) 2.0 mg/ml 1:400, anti-human IgM Alexa Fluor 594 (Invitrogen, A21216) 2.0 mg/ml 1:400. Again, LoD was calculated according to Armbruster & Pry, 2008.[2] Using the blank control, the LoD is calculated as the mean of blank control +2x standard deviation of the blank control (= staining only with secondary antibodies). This results in LoD IgG (635 nm) = 30 AFU + 2x 51 AFU = 132 AFU, LoD IgA (532 nm) = 258 AFU + 2x 85 AFU = 428 AFU, LoD IgM (594 nm) = 53 AFU + 2x 64 AFU = 181 AFU. Due to the higher autofluorescence (glass, coating, etc.) in this wavelength, the IgA signal has a higher LoD signal.

Processing and analysis of peptide microarrays

Before incubation of the serum samples, the arrays were pre-swollen for 15 min with 1.6 mL PBST (0.05 % (v/v) Tween 20 in PBS) at room temperature and orbital shaking at 100 rpm. To avoid nonspecific binding of the serum proteins, the arrays were incubated with blocking buffer (MB-070, Rockland Immunochemicals Inc., Limerick, USA) for 30 min at 100 rpm and room temperature. After short washing with PBST, 1.6 mL of sera, diluted 1:200 in staining buffer (10 % (v/v) blocking buffer in PBST), were incubated overnight at 100 rpm and 4 °C. To remove unbound serum components, the arrays were washed quickly three times with PBST. The human serum antibody classes IgG, IgM and IgA were detected with fluorescently labeled secondary antibodies: 0.5 mg/ml anti-human IgG-Fc fragment cross-adsorbed DyLight 680 conjugated (A80-304D6, Bethyl Laboratories, Montgomery, USA), 1.0 mg/ml anti-human IgM (mu chain) DyLight 549 conjugated (609-142-007, Rockland Immunochemicals Inc., Limerick, USA), 1.0 mg/ml anti-human IgA (alpha chain) antibody DyLight 800 conjugated (609-145-006, Rockland Immunochemicals Inc., Limerick, USA). The HA control peptides on the array were detected with 1.0 mg/ml anti-HA-peptide antibody (RT028, Bio X Cell, New Hampshire, USA) labeled with Lightning-Link Rapid Dylight 680 (327-0010, Innova Biosciences Ltd., Cambridge, United Kingdom). The secondary antibodies were diluted in staining buffer (anti-human IgG 1:1 000, anti-human IgA 1:1 600, anti-human IgM 1:2 000 and anti-HA-peptide 1:2 000) and applied to the microarrays for 30 min at 100 rpm at room temperature in the dark. To remove unbound secondary antibodies, the arrays were washed quickly three times with PBST. Finally, the arrays were dipped in 1 mM Tris HCl pH 7.4 and dried in a jet of air. The arrays were scanned and

fluorescence signals were detected at 700 nm and 800 nm using an Odyssey Scanner (LI-COR Biotechnology Inc., Lincoln, Nebraska, USA) and at 532 nm with a Genepix 4000B (Molecular Devices, San José, USA). Analysis of the scans was performed using PepSlide Analyzer software (SICASYS Software GmbH, Heidelberg, Germany). For quantification, the fixed-spot detection method was used, the intensity values were derived as aggregate foreground median values (the intensity median of two spot duplicates was calculated), while the local spot background was subtracted.

Processing and analysis of glycan microarrays

To avoid nonspecific binding of the serum proteins, the arrays were incubated with 1 % (w/v) BSA in PBS for 60 min at 120 rpm and room temperature. After three times washing with PBS, 200 µL of sera, diluted 1:100 in 1 % (w/v) BSA in PBS, were incubated overnight at 120 rpm and 4 °C. To remove unbound serum components, the arrays were washed quickly three times with PBS. The human serum antibody classes IgG, IgM and IgA were detected with fluorescently labeled secondary antibodies: 0.5 mg/ml anti-human IgG Fc Alexa Fluor 647 (2048-31, SouthernBiotech, Birmingham, USA), 2.0 mg/ml anti-human IgA (alpha chain) Rhodamine (609-1006, Rockland Immunochemicals Inc., Limerick, USA), 2.0 mg/ml anti-human IgM (Heavy chain) Alexa Fluor 594 (A21216, Invitrogen, Carlsbad, USA). The secondary antibodies were diluted 1:400 in 1 % (w/v) BSA in PBS and applied to the microarrays for 60 min at 120 rpm at room temperature in the dark. To remove unbound secondary antibodies, the arrays were washed quickly three times with PBST. Finally, the arrays were dipped in water and dried in a jet of air. The arrays were scanned and fluorescence signals were detected at 532 nm, 594 nm, and 635 nm using a GenePix 4300A (Molecular Devices, San José, USA). Analysis of the scans was performed using PepSlide Analyzer software (SICASYS Software GmbH, Heidelberg, Germany).

Table S2. Number of reactive SARS-CoV-2 peptides at different time points targeted by IgA, IgG, and IgM antibodies above the threshold for fluorescence intensity (99.9th percentile IgA: 347.8 A.F.U.; 99.9th percentile IgG: 1081.4 A.F.U.; 99.5th percentile IgM: 4239.1 A.F.U.) of patients #1 – #4. Data derived from peptide microarray data, showing hits for ORF1ab polyprotein, spike glycoprotein, and all proteins.

IgA		# of peptides above threshold (99.9th percentile of healthy control sample*)									
	Patient ID		#1			#2			#3		#4
	Days after onset of symptoms	d6	d10	d22	d3	d15	d24	d-180	d4	d11	d12
Protein	NSP1	0	0	0	0	0	0	0	5	0	1
	NSP2	3	4	2	0	0	0	1	6	1	3
	NSP3	0	3	12	1	2	0	0	32	12	10
	NSP4	0	0	1	3	0	0	0	5	1	1
	NSP5	0	0	1	0	0	0	0	16	7	0
	NSP6	0	0	5	0	0	0	0	6	2	0
	NSP7	0	0	0	1	0	0	0	0	0	0
	NSP8	0	0	0	1	0	0	0	1	1	1
	NSP9	0	0	0	0	0	0	0	1	0	0
	NSP10	0	0	1	0	0	0	1	2	1	0
	NSP11	0	0	0	0	0	0	0	0	0	0
	NSP12	0	10	34	1	0	0	2	48	31	0
	NSP13	0	2	2	0	0	0	1	11	6	1
	NSP14	0	0	5	2	0	0	0	11	2	1
	NSP15	0	0	3	0	0	0	0	21	15	0
	NSP16	0	1	1	1	0	0	0	2	0	0
	Surface glycoprotein	0	1	24	2	1	0	0	21	9	0
	ORF3a protein	0	0	0	0	0	0	0	8	0	4
	Envelope protein	0	0	0	1	1	0	0	0	0	1
	Membrane glycoprotein	0	1	4	0	0	0	0	0	0	1
	ORF6 protein	0	0	0	0	0	0	1	0	0	1
	ORF7a protein	0	0	0	0	0	0	0	4	1	0
	ORF8 protein	0	0	6	0	0	0	0	10	8	0
	Nucleocapsid phosphoprotein	0	1	7	0	1	0	0	3	0	0
	ORF10 protein	0	0	0	0	0	0	0	0	0	0
	Total	**3**	**23**	**108**	**13**	**5**	**0**	**5**	**214**	**97**	**25**

IgG		# of peptides above threshold (99.9th percentile of healthy control sample*)									
	Patient ID		#1			#2			#3		#4
	Days after onset of symptoms	d6	d10	d22	d3	d15	d24	d-180	d4	d11	d12
Protein	NSP1	0	0	0	0	0	0	0	0	0	0
	NSP2	0	0	0	4	2	1	0	0	0	0
	NSP3	2	2	4	0	0	0	0	4	1	0
	NSP4	0	0	2	0	0	0	0	0	0	0
	NSP5	0	0	0	0	1	0	0	0	0	0
	NSP6	0	0	0	0	0	0	0	0	0	0
	NSP7	0	0	0	3	0	0	0	0	0	0
	NSP8	2	1	1	0	0	0	0	0	0	0
	NSP9	0	0	0	0	0	0	0	0	0	0
	NSP10	0	0	0	0	0	0	0	0	0	0
	NSP11	0	0	0	0	0	0	0	0	0	0
	NSP12	1	0	1	0	0	0	1	1	1	0
	NSP13	0	0	2	0	0	0	1	1	1	0
	NSP14	0	0	0	0	0	0	0	0	0	0
	NSP15	0	0	0	0	0	0	0	0	0	0
	NSP16	0	0	1	0	0	0	0	0	0	1
	Surface glycoprotein	2	4	7	1	0	0	0	3	0	0
	ORF3a protein	0	0	0	0	0	0	2	1	1	1
	Envelope protein	0	0	0	0	0	0	0	0	0	0
	Membrane glycoprotein	1	1	4	0	0	0	1	1	1	0
	ORF6 protein	0	0	0	0	0	0	0	0	0	0
	ORF7a protein	0	0	0	0	0	0	0	0	0	0
	ORF8 protein	0	0	0	0	0	0	0	0	0	0
	Nucleocapsid phosphoprotein	3	7	6	0	0	0	0	0	0	2
	ORF10 protein	0	0	0	0	0	0	0	0	0	0
	Total	**11**	**15**	**28**	**8**	**3**	**1**	**5**	**11**	**5**	**4**

IgM		# of peptides above threshold (99.5th percentile of healthy control sample*)									
	Patient ID		#1			#2			#3		#4
	Days after onset of symptoms	d6	d10	d22	d3	d15	d24	d-180	d4	d11	d12
Protein	NSP1	0	0	0	0	0	0	0	0	0	0
	NSP2	0	0	0	2	0	0	3	4	3	2
	NSP3	0	0	1	14	0	1	9	11	10	18
	NSP4	0	0	0	0	0	0	0	0	0	0
	NSP5	0	0	0	0	0	0	0	0	0	0
	NSP6	0	0	0	0	0	0	0	0	0	0
	NSP7	0	0	0	0	0	0	0	0	0	0
	NSP8	0	0	0	0	0	0	0	0	0	0
	NSP9	0	0	0	0	0	0	0	0	0	0
	NSP10	0	0	0	0	0	0	1	1	1	0
	NSP11	0	0	0	0	0	0	0	0	0	0
	NSP12	1	1	1	4	0	0	3	2	1	0
	NSP13	0	0	0	1	0	0	3	1	2	0
	NSP14	0	0	0	0	0	0	2	0	0	0
	NSP15	0	0	0	0	1	0	0	0	1	0
	NSP16	1	1	1	0	0	0	2	0	0	0
	Surface glycoprotein	0	0	8	0	0	0	1	0	1	0
	ORF3a protein	0	0	0	0	0	0	1	1	0	1
	Envelope protein	1	1	1	1	0	0	0	0	0	0
	Membrane glycoprotein	0	0	0	0	0	0	0	0	0	0
	ORF6 protein	0	0	0	1	0	0	0	0	0	0
	ORF7a protein	0	0	0	0	0	0	0	0	0	0
	ORF8 protein	0	0	0	0	0	0	0	0	0	0
	Nucleocapsid phosphoprotein	0	0	1	0	0	0	0	0	0	0
	ORF10 protein	0	0	0	0	0	0	0	0	0	0
	Total	3	3	13	23	1	1	25	20	19	21

Table S3. Positive SARS-CoV-2 peptides in IgG, IgA, and IgM response for the spike glycoprotein, membrane glycoprotein, and nucleocapsid phosphoprotein.

Spike glycoprotein (S)					
IgG		**IgA**		**IgM**	
Position	Peptide	Position	Peptide	Position	Peptide
		45-59	SSVLHSTQDLFLPFF	45-59	SSVLHSTQDLFLPFF
		63-91	TWFHAIHVSGTNGTKRFDNPVLPFNDGVY		
		125-181	NVVIKVCEFQFCNDPFLGVYYHKNNKSWMESEFRVYSSANNCTFEYVSQPFLMDLEG		
		215-229	DLPQGFSALEPLVDL		
		241-265	LLALHRSYLTPGDSSSGWTAGAAAY	241-265	LLALHRSYLTPGDSSSGWTAGAAAY
		271-295	QPRTFLLKYNENGTITDAVDCALDP		
369-383	YNSASFSTFKCYGVS	343-357	NATRFASVYAWNRKR		
		415-429	TGKIADYNYKLPDDF		
		449-463	YNYLYRLFRKSNLKP		
		565-587	FGRDIADTTDAVRDPQTLEILDI		
		605-619	SNQVAVLYQDVNCTE		
637-651	STGSNVFQTRAGCLI	647-665	AGCLIGAEHVNNSYECDIP		
725-739	EILPVSMTKTSVDCT	721-735	SVTTEILPVSMTKTS		
811-831	KPSKRSFIEDLLFNKVTLADA	809-827	PSKPSKRSFIEDLLFNKVT		
927-955	FNSAIGKIQDSLSSTASALGKLQDVVNQN	835-851	KQYGDCLGDIAARDLIC		
		1087-1111	AHFPREGVFVSNGTHWFVTQRNFYE		
		1131-1145	GIVNNTVYDPLQPEL	1127-1141	DVVIGIVNNTVYDPL
1201-1217	QELGKYEQYIKWPWYIW	1193-1215	LNESLIDLQELGKYEQYIKWPWY	1143-1157	PELDSFKEELDKYFK

Membrane glycoprotein (M)			
IgG		**IgA**	
Position	Peptide	Position	Peptide
1-7	MADSNGT	1-25	MADSNGTITVEELKKLLEQWNLVIG
203-222	NYKLNTDHSSSSDNIALLVQ		

Nucleocapsid phosphoprotein (N)					
IgG		**IgA**		**IgM**	
Position	Peptide	Position	Peptide	Position	Peptide
		96-110	GGDGKMKDLSPRWYF		
		156-170	AIVLQLPQGTTLPKG		
176-206	SRGGSQASSRSSSRSRNSSRNSTPGSSRGTS	182-196	ASSRSSSRSRNSSRN	182-196	ASSRSSSRSRNSSRN
		236-262	GKGQQQQGQTVTKKSAAEASKKPRQKR		
		276-298	RRGPEQTQGNFGDQELIRQGTDY		
366-382	TEPKKDKKKKADETQAL	332-346	TYTGAIKLDDKDPNF		
392-406	VTLLPAADLDDFSKQ	380-394	QALPQRQKKQQTVTL		
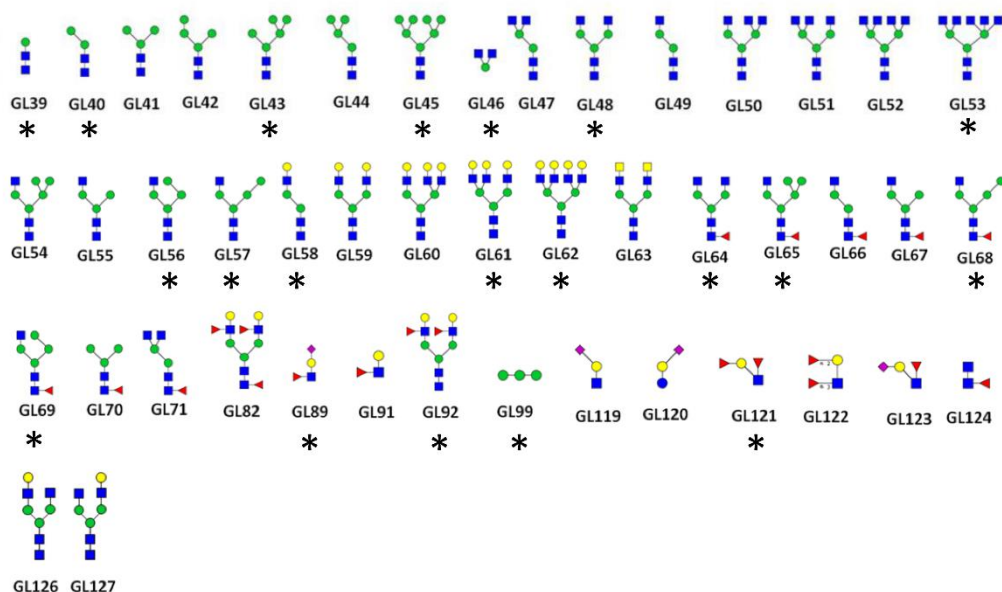
Figure S1. Glycans on the glycan microarrays (only human relevant structures of the in total 135 glycan structures are shown, see Supporting Information C for all glycans and data). Glycans with statistically significant signals are labeled with an asterisk (GL39, GL40, GL43, GL45, GL46, GL48, GL53, GL56–58, GL61, GL62, GL64, GL65, GL68, GL69, GL89, GL92, GL99, GL121).

References

1.   Armbruster, D.A., and Pry, T. Limit of Blank, Limit of Detection and Limit of Quantitation. Clinical Biochemist Reviews, 2008. 29(Suppl 1): p. 49–52.

2.   Echeverria, B., et al., Chemoenzymatic Synthesis of N-glycan Positional Isomers and Evidence for Branch Selective Binding by Monoclonal Antibodies and Human C-type Lectin Receptors. ACS Chemical Biology, 2018. 13(8): p. 2269-2279.

3.3 Automated Laser-Transfer Synthesis of High-Density Microarrays for Infectious Disease Screening

G. Paris, J. Heidepriem, A. Tsouka, Y. Liu, D. S. Mattes, S. Pinzón Martín, P. Dallabernardina, M. Mende, C. Lindner, R. Wawrzinek, C. Rademacher, P. H. Seeberger, F. Breitling, F. R. Bischoff, T. Wolf, F. F. Loeffler

Author contributions

Rationale and summary of this publication

Automated chemical synthesis reduces error-prone manual work and is especially useful for repetitive operations. Particularly, microarray synthesis relies on high precision instruments to ensure a well-defined miniaturized surface patterning. Different technologies have been developed and some have been even commercialized. At first, the SPOT synthesis [74] and the photolithographic synthesis [81] have been proposed for PMA synthesis. The SPOT synthesis is reliable but generates large spots on a cellulose membrane. Moreover, the synthesized peptides need to be cleaved from the membrane and printed onto a glass surface to produce microarrays. The photolabile synthesis allows for high spot densities but requires laborious repetitive steps for building block deposition. The particle-based printing enables an easy automated deposition of

different AAs in form of polymer particles [93]. This facilitates simultaneous coupling and deprotection of the complete surface layer, which significantly increases the process speed. However, the spot pitch of the in situ produced PMAs is relatively big (500 – 1200 peptides per cm^2). Finally, the laser-based transfer (cLIFT) combines a fast transfer of building blocks in small polymer spots as well as simultaneous coupling and deprotection of the complete surface layer [106]. Initially, the approach was lacking precise automation of slide positioning to speed up the process and reduce manual steps. It was not able to facilitate the synthesis with all AAs. Furthermore, the process was not technically mature enough at that time for robust peptide synthesis. The proof of concept study only resulted in 64 9-mer peptides with only two different AAs residues per position [106]. The major aim of in situ PMA production is to synthesize thousands of different peptides.

Because of the potential to fabricate high density PMAs with the cLIFT method, this project aimed for the development of a synthesis procedure to allow for full combinatorial PMA production. This demanded extensive investigation and optimizations of all process parameters. Furthermore, we aspired to synthesize also other molecules than peptides in the MA format.

We strived to produce PMAs with different spot pitches (spot density) to achieve the maximum feasible peptide density in the most efficient process. On the one hand, a precise and reproducible spot transfer is indispensable for in situ fabrication of MAs. Therefore, we engineered an automated synthesizer for slide transport in combination with individual spot pattern generation by laser transfer. On the other hand, we needed to establish the synthesis procedure for peptides with at least 15 residues using all AAs and different spot pitches. Therefore, we implemented an optimization pipeline for the in situ synthesis of peptides. It included various parameters, such as lasing power and duration, coupling cycles, donor slide stability, and reusability (see Figure 20). We determined suitable staining strategies to visualize the surface bound AAs and measure the spot width and the fluorescence intensity. We assumed that the fluorescence intensity correlates positively with the coupling yield [78].
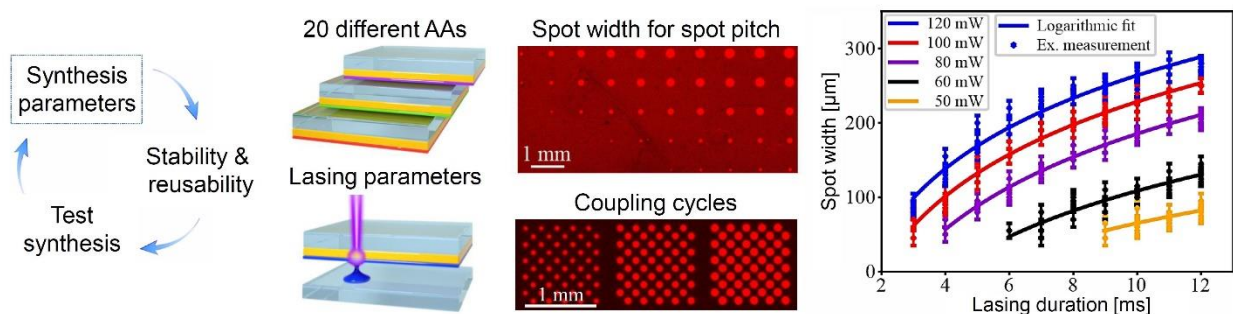
Figure 18: Optimization of in situ peptide synthesis by laser transfer. Synthesis parameters (e.g., AA concentration, lasing parameters for spot width, and coupling cycles) have to be determined for every AA and the targeted spot pitch. The stability and reusability of donor slides is analyzed and a test synthesis is performed.

Additionally, automated spot detection assisted the quantification of spot width and fluorescence intensity of the coupled AA. First, we determined a suitable material film composition for the donor slide preparation, which include a compatible polymer and the concentration of AAs. The AAs used for the donor slide preparation were Fmoc-protected and activated with OPfp. Second, we analyzed the correlation of lasing parameters (laser power and duration) to the spot width, which is limited by the targeted spot pitch. The deposited amount of material is dependent on the lasing parameters, the material composition of the donor slide film, and the properties of the acceptor slide surface. Since every donor slide showed a different transfer behavior, we identified individual lasing parameters for each AA and spot pitch (100, 150, 250 µm). Next, the stability and the reusability of the donor slide film were investigated. The solid polymer film was able to protect the AAs for several days. After an initial material transfer, most donor slides could be reused for further material depositions. This facilitates the synthesis process by reducing the necessary number of donor slides.

Then, we performed a first test synthesis of the HA and Flag epitopes with a 150 µm spot pitch (4444 peptides per cm^2) using three coupling cycles for each AA residue layer. We assumed that the cycles of material transfer and AA coupling have to be repeated several times to produce a complete spot pattern and reach a high coupling yield. We synthesized the 8-mer Flag peptides and the 9-mer HA peptides with an additional first C-terminal AA (one of all 20 AAs) to see the influence of each AA on the synthesis yield. To validate the peptide synthesis, the peptides were stained with antibodies, because the loading of typically 1-2 nmol per cm^2 does not allow for chemical analysis methods. We observed that the fluorescence intensity of individual peptides is influenced by the first C-terminal AA. We concluded that the coupling yield is dependent on the AA. Afterwards, we determined necessary coupling cycles for each AA and spot pitch. In addition, we increased the AA concentration for some donor slides to increase the coupling yield. Moreover, we observed varying spot sizes of the individual peptides. Therefore, we introduced a pre-patterning step to produce low variance spot widths. In detail, before synthesizing the peptides we transferred and coupled a pattern of either aspartic acid or glutamic acid to the modified surface of the acceptor slide. Then, we capped the surrounding surface functional groups and attached β-alanine from solution as starting point for the first AA residue coupling.

To evaluate the influence of the pre-patterning on the peptide yield and spot width, we performed another test synthesis. We synthesized the 8-mer Flag peptides with an additional first C-terminal AA (X) and with (D/E) or without pre-patterning. Specifically, aspartic acid (D) pre-patterning was resulting in homogenous spot widths for peptides starting with different AAs (see Figure 19).
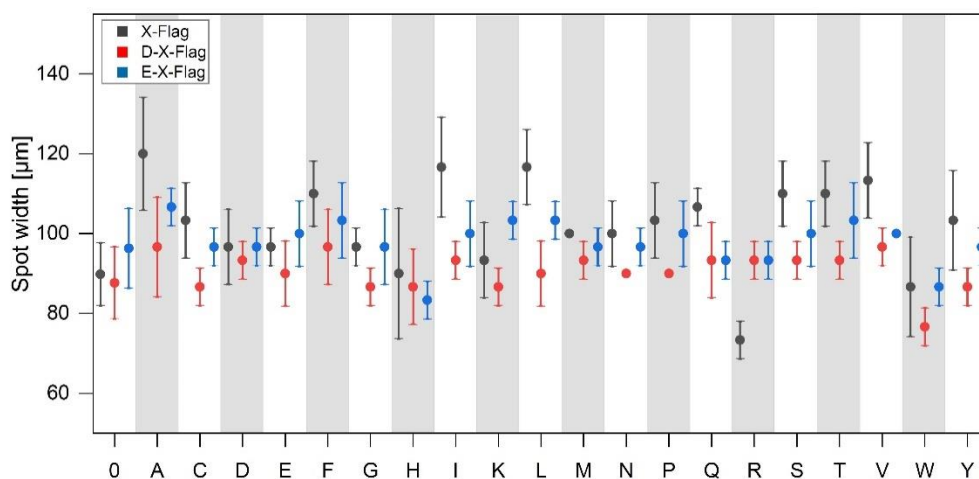
Figure 19: Analysis of Flag peptide spot widths with and without pre-patterning (DYKDDDDK-X-D in red, DYKDDDDK-X-E in blue, DYKDDDDK-X in grey) and one of all 20 AAs (X), as well as the wild-type Flag peptide DYKDDDDK (0). Peptides were stained with anti-Flag Cyanine3. Mean and standard deviation of spot width (µm) are shown. Data originate from [128].

For most C-terminal AAs, the fluorescence intensity of the corresponding peptides at 250 µm spot pitch was increased with the pre-patterning (see Figure 4 in the published article). However, the same peptides showed lower intensities with pre-pattering using a 100 µm spot pitch (see Figure S37 in supporting information).

After introducing the optimized parameters, we analyzed the synthesis of longer peptides. We chose the Flag peptide, because we determined the minimal epitope (DYKDD) of the monoclonal anti-Flag antibody to be in the N-terminus (see Figures S35 and S36 in the supporting information). Thereby, we could introduce other AAs in the C-terminus without affecting the antibody binding and only observe the influence of the coupling yield on the synthesis quality. We synthesized the Flag epitopes with or without pre-patterning and a growing C-terminal glycine-serine spacer to synthesize up to 20-mer peptides. An important goal of this synthesis was to prove the ability of the method to produce 15-mer peptides. For the synthesis, we used the 250 and 100 µm spot pitch (1600 and 10 000 peptides per cm^2) and the adjusted coupling cycles. We correlated the fluorescence intensity of antibody binding with the synthesis yield of peptides with growing length. Using a 250 µm spot pitch, the intensity of the 20-mer peptide decreased to 59% without and to 32% with pre-patterning in comparison to the wild-type 8-mer Flag peptide (see Figure 22). This leads to an average yield of 95.7% and 90.2% for the AA coupling steps. For the synthesis with a 100 µm spot pitch, the yield dropped significantly in comparison to the wild-type peptide with a 250 µm spot pitch (see Figure 22). The overall normalized fluorescence intensity of the peptides with a 100 µm spot pitch was about 1/4 of the 250 µm spot pitch (see Figure 22). Nevertheless, sufficient antibody binding was measured for the PMA with a 100 µm spot pitch. This test synthesis proved

the ability of the cLIFT method to produce peptides with at least 15 AA residues without loss of sufficient binding by the corresponding antibody.
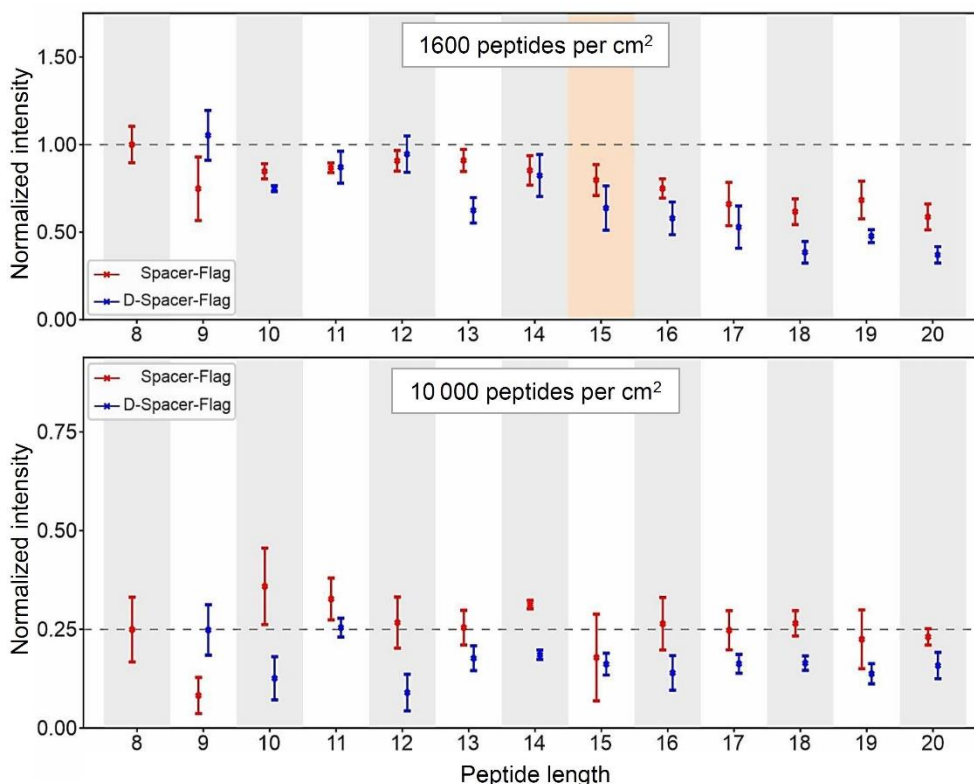
Figure 20: Analysis of the influence of the peptide length (8-20 residues) on the synthesis yield. Peptides were synthesized with and without pre-patterning (DYKDDDDK-$(SG)_{0.5}$-D in blue, DYKDDDDK-$(SG)_{0.5}$ in red). On top, the normalized fluorescence intensity of peptides synthesized with a 250 μm spot pitch is presented. Below, the normalized intensity of peptides synthesized with a 100 μm spot pitch is presented. Mean and standard deviation of the normalized fluorescence intensity (intensity/intensity$_{\text{wild-type Flag}}$) are shown. The intensity of the wild-type 8-mer Flag peptide with a 250 μm spot pitch was used for normalization. Peptides were stained with anti-Flag Cyanine3. Data originate from [128].

Next, we investigated a possible reduction of the coupling time, to speed up the synthesis. We determined similar or higher fluorescence intensities on average for AAs coupled for 10 min instead of 60 min (see Figure S33 in the supporting information). For glycine and proline, the intensity was increasing drastically with a shorter coupling period. Since we correlated the fluorescence intensity with the coupling yield, we assumed that the coupling yield of some AAs benefits from shorter coupling times.

The final parameters were applied for the synthesis of full combinatorial PMAs with three different spot pitches. To validate our optimized laser-based synthesis, we synthesized overlapping 15-mer peptides of the EBOV GP with an offset of one AA and compared antibody binding with a commercial PMA, produced by particle-based synthesis, carrying the same peptides. We incubated the PMAs with serum of an EVD survivor to detect IgG epitopes. Furthermore, we synthesized the whole proteome of the EBOV as overlapping peptides with a spot pitch of 100 μm and 150 μm and

investigated the IgG response of the EVD survivor on these PMAs. We observed a much higher fluorescence intensity for IgG bound peptides on the synthesized PMAs with a spot pitch of 250 µm (1600 peptides per cm^2) and 150 µm (4444 peptides per cm^2) than for the commercial PMA (maximum 1200 peptides per cm^2) (see Figure 23). Only the 100 µm spot pitch (10 000 peptides per cm^2) PMA showed a lower intensity similar to the intensity measured with the commercial PMA (see Figure 23). With our PMAs, we were able to detect the same epitopes as with the commercial PMA and also four additional epitopes (see Figure 23). These four epitopes were only detected on the cLIFT-fabricated PMAs, because they exceeded the fluorescence intensity threshold.
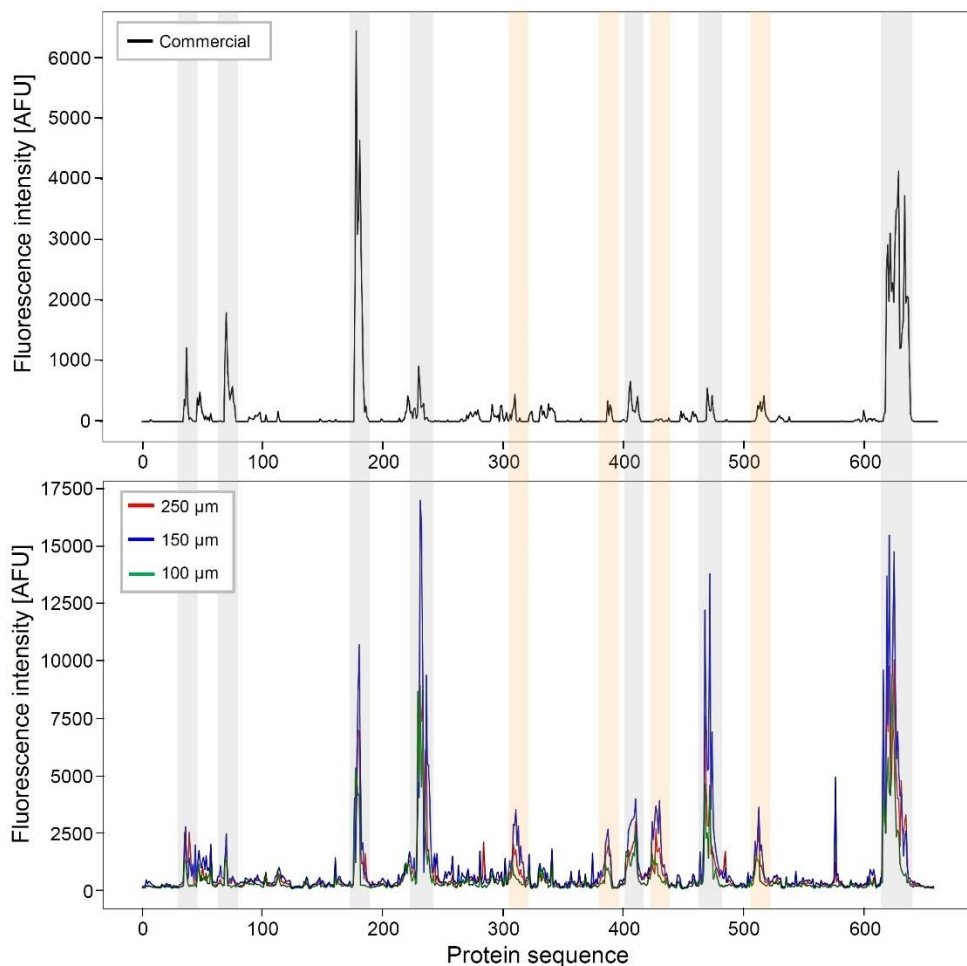
Figure 21: Fluorescence intensity profile of EBOV GP PMAs stained with EVD survivor IgG. On top, profile of the commercial PMA with maximum 1200 peptides per cm^2 is presented. Below, profiles of cLIFT fabricated PMAs with 1600 (red), 4444 (blue), and 10 000 (green) peptides per cm^2 are presented. Common epitopes are highlighted in grey and additional epitopes detected by the cLIFT fabricated PMAs in orange. IgG of the EVD survivor was detected with anti-human IgG Fc DyLight 650. Data originate from [128].

All synthesized PMAs showed high reproducibility for epitope detection. The best rate of high fluorescence intensity, high peptide density, as well as production speed was achieved for the PMA synthesis with the 150 µm spot pitch. The synthesis of overlapping peptides of the other EBOV proteins showed stronger fluorescence intensities for the PMAs with 150 µm spot pitch than for the

100 µm (see Figures S41, S42, S43, S44, S45, S46, S47 in the supporting information). This indicated that the synthesis of PMAs with a density of 10 000 peptides per cm^2 resulted in a lower synthesis yield and therefore weaker antibody binding.

To prove the versatility of our cLIFT method for MA fabrication, we additionally synthesized a fluorophore in a two-step reaction on the surface (see Figure 6 in the published article). With the optimization pipeline and the automated synthesizer, the cLIFT method can be applied for various MA syntheses and applications.

Automated Laser-Transfer Synthesis of High-Density Microarrays for Infectious Disease Screening

Grigori Paris, Jasmin Heidepriem, Alexandra Tsouka, Yuxin Liu, Daniela S. Mattes, Sandra Pinzón Martín, Pietro Dallabernardina, Marco Mende, Celina Lindner, Robert Wawrzinek, Christoph Rademacher, Peter H. Seeberger, Frank Breitling, Frank Ralf Bischoff, Timo Wolf, and Felix F. Loeffler*

Laser-induced forward transfer (LIFT) is a rapid laser-patterning technique for high-throughput combinatorial synthesis directly on glass slides. A lack of automation and precision limits LIFT applications to simple proof-of-concept syntheses of fewer than 100 compounds. Here, an automated synthesis instrument is reported that combines laser transfer and robotics for parallel synthesis in a microarray format with up to 10 000 individual reactions cm⁻². An optimized pipeline for amide bond formation is the basis for preparing complex peptide microarrays with thousands of different sequences in high yield with high reproducibility. The resulting peptide arrays are of higher quality than commercial peptide arrays. More than 4800 15-residue peptides resembling the entire Ebola virus proteome on a microarray are synthesized to study the antibody response of an Ebola virus infection survivor. Known and unknown epitopes that serve now as a basis for Ebola diagnostic development are identified. The versatility and precision of the synthesizer is demonstrated by in situ synthesis of fluorescent molecules via Schiff base reaction and multi-step patterning of precisely definable amounts of fluorophores. This automated laser transfer synthesis approach opens new avenues for high-throughput chemical synthesis and biological screening.

1. Introduction

Automated chemical synthesis reduced repetitive manual operations and revolutionized the discovery of functional compounds. Most sophisticated automated synthesis instruments are optimized to perform successive iterations of robust reactions for a single compound class: The well-defined and iterative character of peptide and oligonucleotide syntheses led to the development of automated solid-phase synthesis strategies that provide quick access to oligomers.[1,2] Inspired by these approaches, the automated synthesis of oligosaccharides[3] has significantly progressed and recently, the concept was adapted to the synthesis of small molecules.[4] The latter automated synthesis approaches focus on the generation of a single target molecule at a time. Proteome-wide epitope screening that requires the synthesis of thousands of peptides, cannot

G. Paris, J. Heidepriem, A. Tsouka, Y. Liu, S. Pinzón Martín,
P. Dallabernardina, M. Mende, C. Lindner, R. Wawrzinek,
P. H. Seeberger, F. F. Loeffler
Department of Biomolecular Systems
Max Planck Institute of Colloids and Interfaces
Am Muehlenberg 1, 14476 Potsdam, Germany
E-mail: Felix.Loeffler@mpikg.mpg.de

G. Paris
Department of System Dynamics and Friction Physics
Institute of Mechanics
Technical University of Berlin
Str. des 17. Juni 135, 10623 Berlin, Germany

J. Heidepriem, A. Tsouka, Y. Liu, S. Pinzón Martín, P. H. Seeberger
Institute of Chemistry and Biochemistry
Freie Universität Berlin
Arnimallee 22, 14195 Berlin, Germany

D. S. Mattes, F. Breitling
Institute of Microstructure Technology
Karlsruhe Institute of Technology
Hermann-von-Helmholtz-Platz 1, 76344 Eggenstein-Leopoldshafe,
Germany

C. Rademacher
Department of Pharmaceutical Sciences
University of Vienna
Althanstr. 14, Vienna 1090, Austria

C. Rademacher
Department of Microbiology and Immunobiology
Max F. Perutz Laboratories GmbH
Dr.-Bohr-Gasse 9, Vienna 1030, Austria

F. R. Bischoff
Department of Functional Genome Analysis
German Cancer Research Center
Im Neuenheimer Feld 580, 69120 Heidelberg, Germany

T. Wolf
Infectious Diseases Unit
Department of Medicine
Goethe University Hospital
Theodor-Stern-Kai 7, 60590 Frankfurt am Main, Germany

**ADVANCED
SCIENCE NEWS**

www.advancedsciencenews.com

**ADVANCED
MATERIALS**

www.advmat.de

Table 1. Commercially established technologies for the synthesis of high-density peptide microarrays.

	SPOT	Photolithographic	Particle-based	Laser-based (this work)
Synthesis approach	membrane, Fmoc-protection	glass, photo-labile protecting groups	glass, Fmoc-protection	glass, Fmoc-protection
Deposition procedure	syringe delivery	microfluidic delivery	xerography	laser transfer
Spot density [cm^{-2}]	up to 25[18]	up to 22 000[19]	up to 1250[20]	up to 10 000
Peptide length	up to 25 residues	up to 12 residues	up to 20 residues	up to 20 residues
Spot morphology	stable, coffee-ring	stable, ghost spots	stable, blurred	stable
Coupling yield	≈95%, purification after cleavage possible	≈75%[17]	≈90%[10]	≈95%

be addressed with this approach. Parallel peptide production in an array format increases synthesis throughput and decreases the cost of goods. This high-throughput synthesis concept was introduced in the 1980s[5] and since continues to evolve.[6–16]

The SPOT,[6] photolithographic,[7] and particle-based[10] syntheses are now commercialized[18–20] and commonly used to prepare peptides for binding studies.[21–23] However, each approach has at least one major drawback in regards to the peptide spot density, the possible peptide length, or the resulting peptide spot morphology (**Table 1**). To overcome these limitations, laser-induced forward transfer can be used for the in situ generation of high-density peptide microarrays: Different types of pre-activated polymer embedded amino acids are precisely

transferred by laser irradiation from easily exchangeable donor slides to a functionalized acceptor slide in a polymer spot pattern (**Figure 1**). Then, the resulting nanometer thin polymer spots, serving as "solid" solvent, allow for an on-demand heat-induced coupling reaction in parallel. Heated above the glass transition temperature of the polymer, in each spot, the specific pre-activated amino acid (AA) type reacts with the amino-functionalized acceptor slide. Consecutively, the acceptor slide can be washed (removal of excess AA and polymer), capped (acetylation of non-reacted amino groups on the surface), and deprotected, which enables coupling of subsequent AAs. By repeating the procedure, the in situ built-up of the desired peptide sequences in the array format is performed.
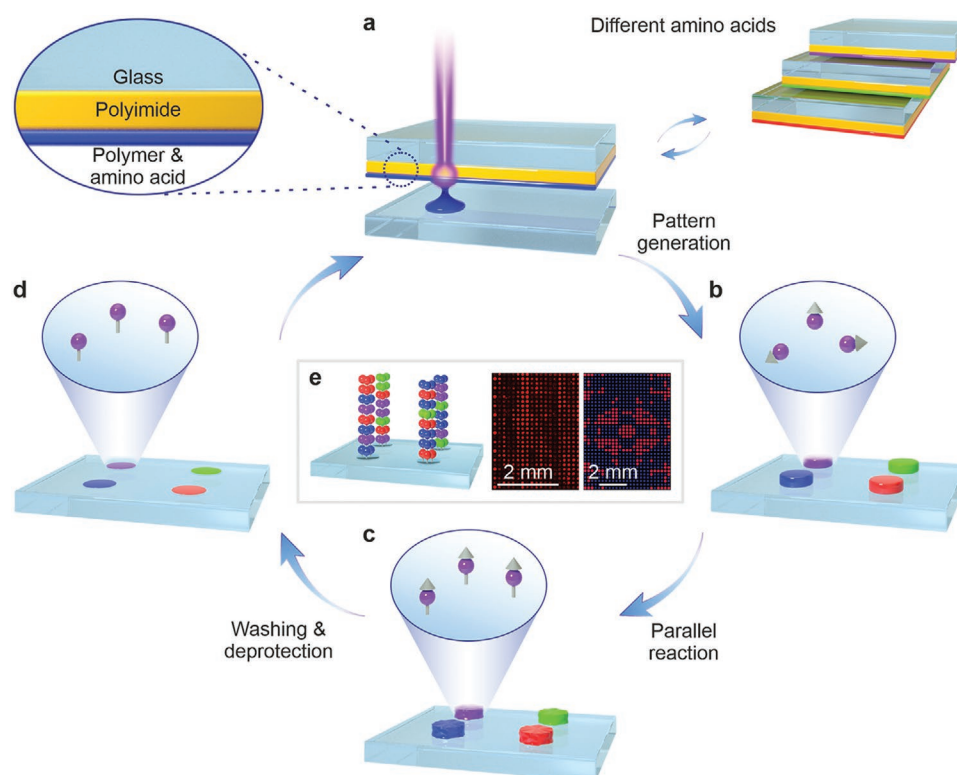
Figure 1. Principle of the laser-based peptide microarray synthesis. a) Material is transferred from different types of amino acid donor slides to a functionalized acceptor slide in a b) polymer reactor spot pattern. c) The polymer pattern is heated above the glass transition temperature allowing the pre-activated amino acids to couple to the amino-functionalized surface. d) Subsequently, the acceptor slide is washed, capped, and deprotected. e) Repeating the procedure enables the in situ synthesis of peptides in a microarray format.

2200359 (2 of 12)

Compared to liquid solvent-based in situ microarray synthesis approaches[16,24] that require hydrophobic functionalization of the synthesis surface, the laser-based polymer transfer does not require this pre-treatment. Moreover, such technology is especially useful for rapidly generating individually customized arrays, which can aid diagnosis and monitoring of infectious[25] or autoimmune diseases[26] as rationally designed antigen variants can be quickly screened.

We described the principle previously,[14] but until today the process was limited to simple array syntheses of up to 64 short (9-residue) peptides,[14,27] due to insufficient robustness and reproducibility of the process. Recent progress in the theoretical and experimental understanding of the laser transfer mechanism helped to overcome these obstacles. Precise and reproducible patterning is now possible,[28] while the laser process temperature can be adjusted for more demanding AAs.[29]

Here, we report an automated laser-based synthesizer that produces arrays with a spot density of up to 10 000 spots cm^{-2}. Combined with an optimization pipeline that can be adapted for various other in situ printing techniques, we are now able to synthesize complex microarrays containing thousands of different molecules in high yield and high reproducibility. The synthesis quality of this new methodology is superior as illustrated by comparing our peptide microarrays with a commercially available reference. The complete Ebola virus proteome was synthesized on a microarray with >4800 15-residue peptides to study the recognition of B cell epitopes in an Ebola virus disease survivor. Finally, we show the versatility and precision of the synthesizer by in situ synthesis of fluorescent molecules via Schiff base reaction and multi-step patterning of precisely definable amounts of fluorophores. This offers a new way for high-throughput chemical reaction screening in polymer reactors.

2. Results and Discussion

2.1. Automated Laser-Based High-Precision Synthesizer

The key characteristics of in situ generated peptide microarrays are the resulting spot density, spot morphology, and synthesis yield. These three features heavily rely on a precise and reproducible AA transfer. Therefore, we developed a microarray synthesizer (**Figure 2**; Figures S1–S3, Supporting Information) that utilizes our laser-based transfer approach with a reproducible and high transfer precision, automated by a robotic arm. A graphical user interface enables non-specialists to initiate the automated procedure. The synthesizer contains four expandable modules (Movie S1, Supporting Information): 1) Up to four acceptor and 23 different donor slides can be manually loaded into the slide holder. 2,3) A robot transports these slides between the slide holder and the positioning table, 4) while the laser system automatically transfers the AAs. An acceptor slide is reproducibly aligned on the positioning table by three positioning bolts. Then, different donor slides are placed successively on top of the acceptor slide and the laser transfer is performed. To prohibit local overheating of the donor slide material during the laser transfer process, we implemented
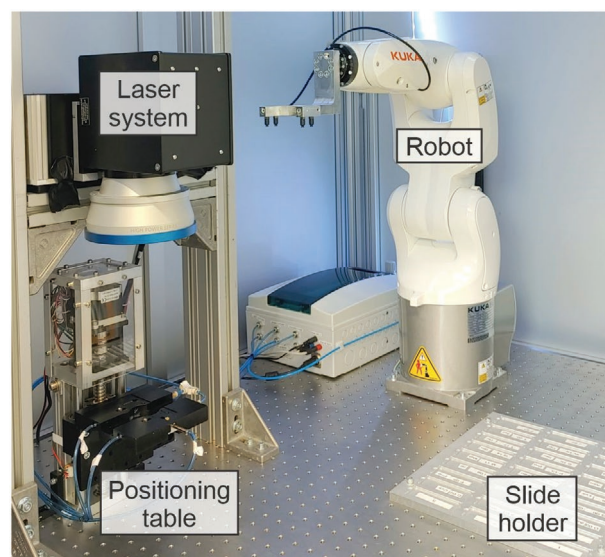
Figure 2. Automated laser-based microarray synthesizer. The system comprises: a slide holder for acceptor and donor slides; a robot with gripper tool for transportation of acceptor and donor slides; a positioning table with automated alignment of acceptor slides; a laser system with a 405 nm diode laser and laser scanning system.

a random spot transfer algorithm (Figure S4, Supporting Information).

2.2. Optimization of the Laser-Based In Situ Peptide Microarray Synthesis

Upon increasing the spot density, all in situ synthesis technologies eventually suffer from yield and spot morphology problems. Therefore, we developed an optimization pipeline for our laser-based in situ solid-phase peptide synthesis approach to optimize the transfer and coupling of the 20 AAs, which requires hundreds of experiments (**Figure 3**). While optimized for our process, the pipeline can quickly be adapted to any in situ synthesis approach, based on other printing technologies.

Initially, we needed a robust quantification procedure of the resulting AA spots (spot morphology and yield). A commonly used approach for the detection of AAs on functionalized surfaces is by fluorescence labeling and imaging. we investigated three different labeling procedures, such as direct dye labeling with or without side chain deprotection or indirect biotin-streptavidin labeling (Figure 3a; Figure S5, Supporting Information). we obtained reliable and comparable results by side chain deprotection of the AAs and direct DyLight 633 N-hydroxy-succinimide ester labeling. Furthermore, we assumed a positive correlation between fluorescence intensity and AA coupling efficiency: higher AA coupling results in higher fluorescence intensity (Figure S6, Supporting Information). This correlation was also previously observed by others.[16] Moreover, to enable a fast analysis of thousands of fluorescent spots from various experiments (e.g., transfer parameters of 20 AAs), we developed an automated image detection software based on the open-source framework OpenCV.[30]
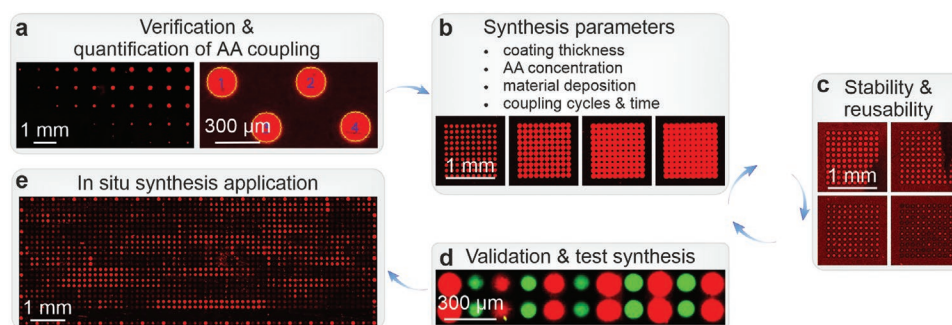
Figure 3. Optimization pipeline for the laser-based in situ peptide microarray synthesis. a) Verification and quantification of AA coupling is achieved by fluorescence labeling of amino groups and automated spot detection. b) To obtain an optimal spot size and synthesis yield, parameters such as styrene-acrylic copolymer coating thickness, AA concentration, and AA dependent material deposition, as well as AA coupling cycles and time are investigated. c) Afterward, the stability and reusability of all AAs is assessed and d) a validation synthesis is performed to determine the synthesis quality and yield of the found parameter sets. After several iterations, optimal parameters are obtained for all AAs, e) which can be used for various applications (e.g., combinatorial peptide synthesis).

Next, we needed to precisely control the deposited material of each transferred AA, which defines the final spot size and shape. Thus, we optimized the polymer coating thickness and AA concentration of an example AA donor slide (Figure 3b; Figures S7,S8, Supporting Information). Styrene-acrylic copolymer (SLEC; Figure S9, Supporting Information) was chosen, because in contrast to other polymers (Figure S10, Supporting Information), it offers the most robust spot sizes resulting in the highest synthesis resolution of 10 000 spots cm^{-2}. Alanine was selected as the representative AA, because solubility issues should first arise for small and unpolar AAs. we varied the amount of SLEC and AA for the preparation of donor slides between 18–31.5 mg SLEC with 6.7–11.7% w/w AA. Even higher amounts of SLEC and AA resulted in highly variable spot sizes, while being less material saving. For 27 mg of SLEC and 3 mg of AA, we observed the most robust transfer (<100 μm width). However, since different AAs lead to different glass transition temperatures of the SLEC composite,[10] the same laser parameters lead to different spot widths for each AA. Therefore, by varying lasing power and duration in a range (50–120 mW and 3–12 ms) for each AA, we extracted the optimal experimental parameters (Figures S11–S15, Supporting Information). Finally, as repeating coupling cycles of the same AA is typically performed in solid-phase peptide synthesis to increase the synthesis yield, we initially assumed three repeating coupling cycles per AA necessary, with a standard coupling time of 60 min each.

Employing these synthesis parameters, we investigated the potential to store the donor slides over a duration of seven days and reuse identical donor slide positions up to six times (Figure 3c; Figure S16, Supporting Information). This significantly reduces material consumption and preparation time. As we compared the fluorescence intensity and spot size to a fresh transfer (i.e., single transfer after one day of storage), we observed the trend of decreasing intensity and spot size over storage time and number of reuses. Particularly, the number of reuses strongly depends on the amount of previously transferred material and the deformation of the donor slide that is influenced by the lasing parameters (i.e., strong lasing parameters result in strong deformation) and is not a result of AA denaturation (Figure S17–S30, Supporting Information).

As a criterion before discarding a donor slide, we introduced empirical thresholds that took the use of multiple (repeated) coupling cycles into account: For spot densities of 1600 spots cm^{-2} and 10 000 spots cm^{-2}, we required a minimum of 60% and 50% of the average fluorescence intensity and spot area. These values guaranteed saturated fluorescence intensity (and assumed coupling) over the entire spot.

To validate our first optimization iteration, we synthesized HA and Flag epitope variants (4444 spots cm^{-2}), containing one additional C-terminal AA (YPYDVPDYAX and DYKDDDDKX, X = one of 20 AA; Figure 3d; Figure S31, Supporting Information), and measured specific antibody binding. For the Flag epitope, we observed a quantifiable trend, because the antibody binding appeared independent of the C-terminal AA, while the HA epitope binding was strongly influenced by the C-terminal AA. Yet, Flag peptides with a C-terminal histidine, proline, arginine, and tryptophan showed a (potentially) poor coupling efficiency. To overcome these assumed shortcomings, we performed an additional optimization iteration: For the poorly coupling AA, we increased the AA concentration to 20% w/w and repeated the analysis of optimal process parameters. Then, we investigated the optimal number of coupling cycles for each of the 20 AA (Figure S32, Supporting Information), where we defined the optimal number as maximum fluorescence intensity and non-overlapping spots. Interestingly, while the spot area increased over repeating coupling cycles, we observed a decrease in fluorescence intensity for some AAs after reaching maximum within the previous cycle. Hence, we used this observation as stop criterion. Consecutively, we investigated different coupling durations. A reduction from 60 min to 10 min is possible without a loss in coupling efficiency (Figure S33, Supporting Information). Finally, as we observed varying spot sizes for different AAs that will result in varying peptide spot widths, we introduced a pre-patterning of the acceptor slide with aspartic acid (Figure S34, Supporting Information). This restricted the growing peptide to the size of the initial aspartic acid spot pattern. we chose aspartic acid, because its negative charge at neutral pH is known to prevent unspecific interaction between most antibodies and the surface[31] and the transfer resulted in small and stable spots after coupling.
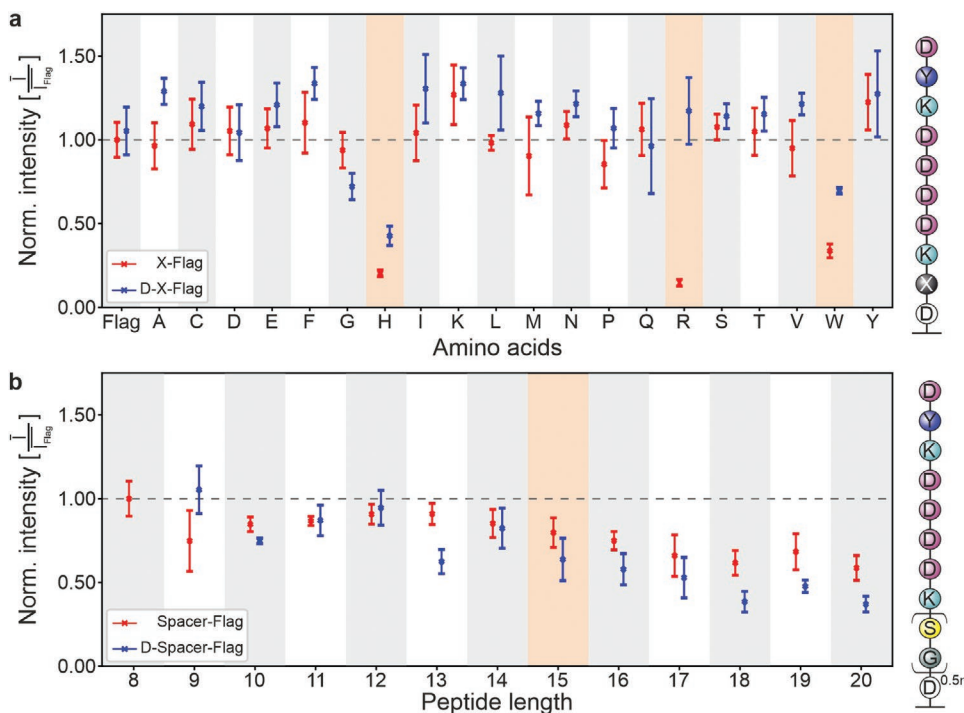
**ADVANCED
SCIENCE NEWS**

www.advancedsciencenews.com

**ADVANCED
MATERIALS**

www.advmat.de

Figure 4. Validation of synthesis yield via antibody binding fluorescence analysis of a peptide microarray (1600 spots cm^{-2}). Peptides were synthesized without and with aspartic acid pre-patterning. a) Intensities of the synthesized Flag peptides with an additional C-terminal AA of the 20 AAs. Histidine, arginine, and tryptophan show low binding, which is improved by aspartic acid pre-patterning. b) Flag peptides synthesized with a C-terminally growing glycine-serine spacer, resulting in up to 20-residue peptides. Fluorescence intensities are normalized against the wild-type Flag epitope (I_{Flag}) and presented as mean ± SD, $n = 3$.

2.3. Validation of Optimized Parameters

Using the optimized parameters, we synthesized a microarray with 1600 spots cm^{-2} containing Flag epitopes variants with an additional C-terminal AA, a 1–12 AA long glycine-serine spacer,[32] and an aspartic acid pre-patterning. The variants with the 20 different AAs at the C-terminus still showed a decreased antibody binding for histidine, arginine, or tryptophan (**Figure 4**a). However, antibody binding increased after including the pre-patterning. This indicates that the coupling of these AAs can be strongly affected by the preceding AA, which has previously been reported.[33] In comparison, variants with an increasing glycine-serine spacer without (Figure 4b) and with (Tables S1 and S2, Supporting Information) a C-terminal AA inclusion showed an expected behavior: The elongated Flag epitope (max. 20 residues) had an almost stable antibody binding up to a length of 15 residues. Then, a linear decrease to ≈59% and ≈32% without and with the pre-patterning was observed (compared to the reference peptide). This corresponds to an average yield of ≈95.7% and ≈90.2% respectively. Furthermore, we could verify that the minimal Flag epitope, which is responsible for the antibody recognition, is located at the N-terminus (Figure S35, Supporting Information). This is further supported by the performed Flag epitope substitution analysis (Figure S36, Supporting Information). Thus, due to this N-terminal epitope region, we could validate our 20-residue peptide microarray synthesis. In addition, we synthesized microarrays containing the same Flag variants with a spot density of 10 000 spots cm^{-2} and repeated our evaluation (Figure S37,

Tables S3 and S4, Supporting Information). A lower antibody binding was evident compared to the 1600 spots cm^{-2} microarray synthesis. Nevertheless, sufficient antibody binding could be measured for most synthesized peptides. To support our assumption that the antibody binding correlates with the AA coupling efficiency, we analyzed the synthesis yield of representative AAs by measuring the N-(9H-Fluoren-9-ylmethyl)-piperidine absorbance after transferring one large AA spot pattern. While the measurement correlates with the antibody binding trend (e.g., low yield histidine, high yield glycine), it appeared less reliable (Figure S38, Supporting Information). Fluctuating synthesis yields between different acceptor slides were observed, which are strongly dependent on the coupled area (i.e., spot size upon labeling). Depending on this, the results varied up to ≈60%.

2.4. Validation and Application of the Laser-Assisted Peptide Synthesis

To validate our optimized parameter sets (Tables S5–S7, Supporting Information) for an application, we performed a fully combinatorial peptide microarray synthesis with 1600, 4444, and 10 000 spots cm^{-2}. The Ebola virus surface glycoprotein was mapped as 662 individual 15-residue peptide spots with a lateral shift of one AA, which we used to screen the serum IgG antibody response of an Ebola virus disease survivor (**Figure** 5b and c). The IgG response of the three microarrays with different spot densities displayed a strong monotonic

**ADVANCED
SCIENCE NEWS**

www.advancedsciencenews.com
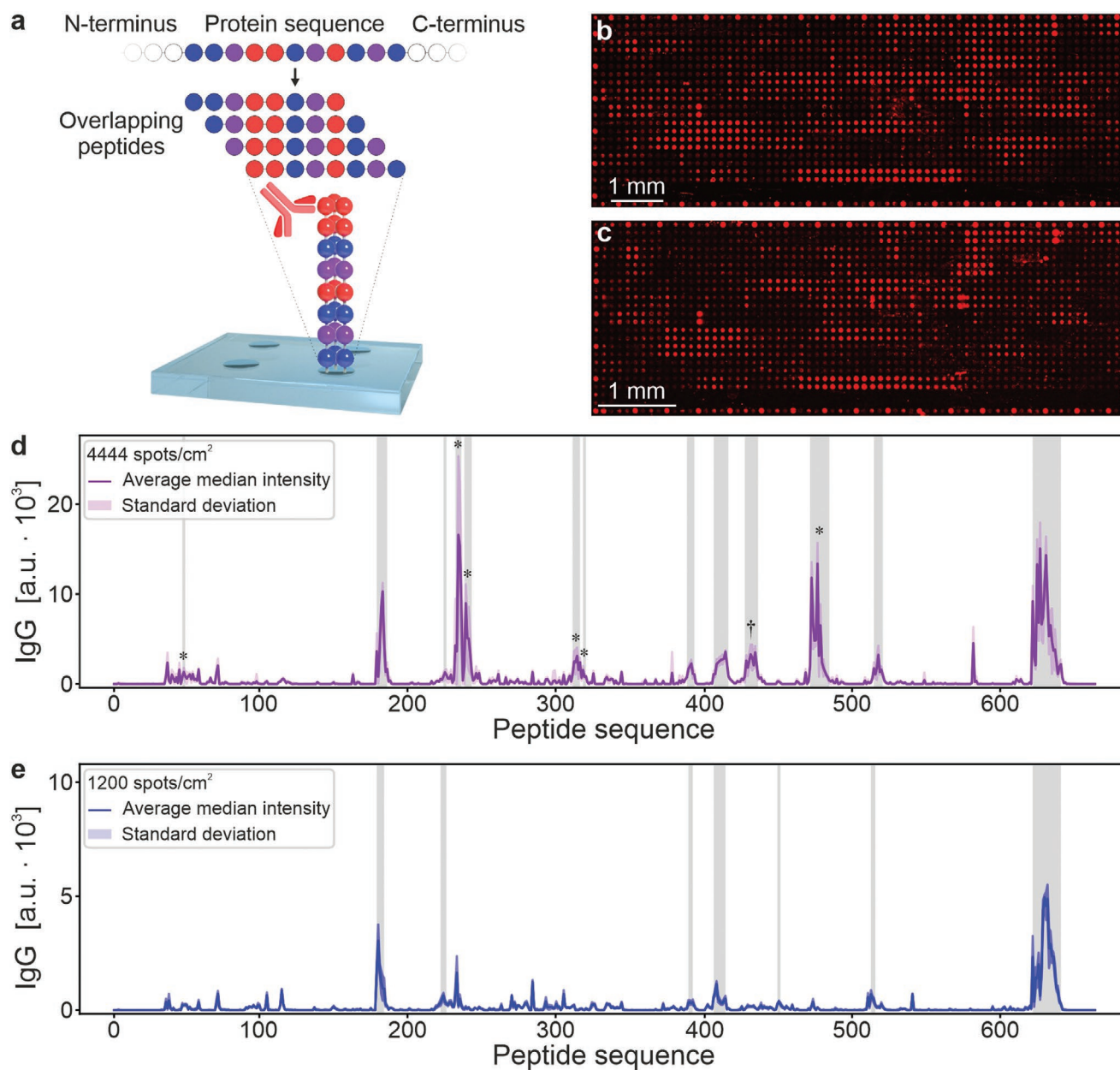
**ADVANCED
MATERIALS**

www.advmat.de

Figure 5. Synthesized Ebola virus surface glycoprotein peptide microarrays for IgG antibody screening of a disease survivor. a) The Ebola virus surface glycoprotein sequence was mapped as 662 overlapping 15-residue peptides with a lateral shift of one AA (as spot duplicates). After serum incubation, antibody binding to arrays with b) 4444 and c) 10 000 spots cm^{-2} was analyzed with fluorescence imaging and data presented as mean (of median IgG value) $\pm$ SD. d) The resulting signals of the 4444 spots cm^{-2} ($n = 10$, background subtraction of 400 a.u.) and e) commercial reference microarrays ($n = 8$, background subtraction of 162 a.u.) are shown. Our synthesized microarray was able to detect more epitopes than the commercial array. Epitopes are highlighted in grey (*: known from literature; †: newly identified).

correlation (Figure S39, Supporting Information), which shows that our process is sufficiently robust to detect IgG epitopes independent of the spot density.

Next, to validate if we not only produced consistent microarrays but also detected significant epitopes, we screened the IgG response of an Ebola virus disease survivor on a commercial reference peptide microarray (produced with particle-based synthesis) containing the same peptides of the Ebola virus surface glycoprotein. This comparison showed that we could identify the same IgG epitopes as the commercial reference

(Table S8, Supporting Information), except for one minor signal (Figure 5d,e). Additionally, we found four previously reported epitopes,[34,35] as well as one to our knowledge unreported epitope (AA 430–448), which highlights that we can produce fully combinatorial high quality peptide microarrays. Subsequently, we synthesized microarrays of the complete Ebola virus proteome in single AA resolution (4805 individual peptides) on separate 8.18 × 13.36 mm^2 and 4.54 × 10.70 mm^2 areas to perform a comprehensive epitope study of the Ebola virus disease survivor (Figures S40–S47 and Tables S8–S15, Supporting

**ADVANCED
SCIENCE NEWS**

www.advancedsciencenews.com

**ADVANCED
MATERIALS**

www.advmat.de

Information). This was only possible with our increased microarray spot density, since a larger array surface area requires a higher than usually available amount of such a valuable serum sample. While the analysis of the complete Ebola proteome with peptide arrays has not been reported yet, our data coincide well with Becquart et al.,[35] who have analyzed VP35, VP40, nucleoprotein, and glycoprotein with a peptide ELISA assay.

2.5. Laser-Based Synthesis of Fluorophore Microarrays

To show the chemical flexibility of our process and its capability to precisely tune the transferred material, we produced fluorophore microarrays (**Figure 6**). Besides the amide bond formation, we performed the Schiff base condensation reaction (imine formation) to synthesize a fluorophore array (Figure 6a). The Schiff base reaction can be used to synthesize various molecules[36] or materials,[37] such as fluorescent dyes for sensing applications.[38,39] This makes them a highly attractive class of small molecules, which may be explored in microarray screenings. To synthesize the 2-((3-(carboxymethoxy)benzylidene) amino)benzoic acid on the microarray (Figure 6b), we carried out two steps: 1) Laser transfer and amide bond coupling of pentafluorophenyl activated 2-(3-formylphenoxy)acetic acid to the functionalized substrate 2) and consecutive laser transfer and Schiff base reaction of 2-aminobenzoic acid with 2-(3-formylphenoxy)acetic acid.
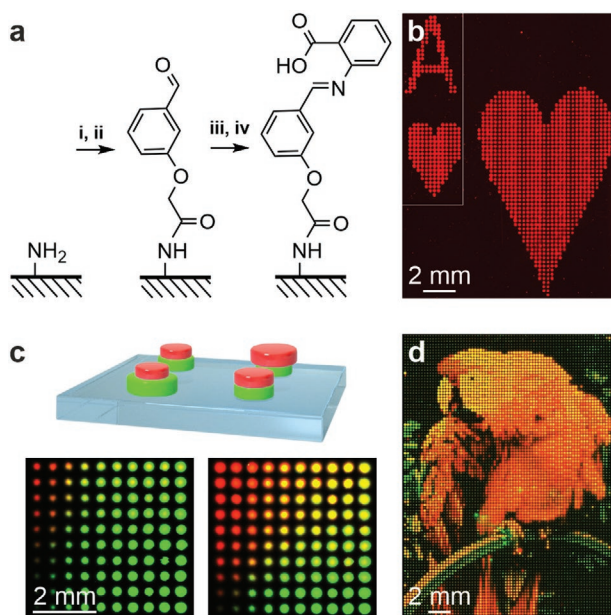
Figure 6. Laser-based synthesis of fluorophore microarrays. a-i,ii) Pentafluorophenyl activated 2-(3-formylphenoxy)acetic acid was transferred and coupled for 10 min at 95 °C to the surface via amide bond formation. iii,iv) 2-aminobenzoic acid was transferred and reacted for 90 min at 90 °C, forming the Schiff base 2-((3-(carboxymethoxy)benzylidene) amino)benzoic acid. b) Fluorescence image of the synthesized Schiff base microarray. c) Experimental screening of laser transfer parameters for two fluorescent dyes in SLEC (green: Rhodamine 6G, red: Nile blue A) to obtain a precise red-green color mixing (resulting in yellow). d) Optimal parameters enable the production of a 75 × 100 pixel (i.e., spot) image with thousands of different color ratios.

Moreover, we exploited the high precision of our system to precisely transfer defined amounts of SLEC containing red and green fluorophores onto a standard glass slide (Figure 6c,d). Recently, Whitesides et al. used inkjet printing to create fluorescent patterns for long-term data storage.[40] While the authors required seven different dyes to store 8-bit information in one pixel, in our approach, we can create >256 distinguishable ratios in one spot by using only two fluorophores. To achieve this, we screened many nested lasing parameter gradients (Figure S48, Supporting Information) to obtain optimum parameters for a precise red-green color mixing. Beyond data storage, this approach can enable the transfer of different chemicals in the microarray format for high-throughput reaction screening.

3. Conclusion

We developed a modular and robust automated high-throughput and high-precision laser-based microarray synthesizer that can generate up to 20-residue peptides with a spot density of 10 000 spots cm⁻² in high yield. we established an analysis pipeline (material transfer, visualization, and quantification) to optimize our laser-based process in regards to transfer precision and reproducibility, as well as the resulting spot morphology and coupling efficiency. Through this optimization, we were able to advance our technology to synthesize thousands of different high quality peptides containing all 20 AAs and up to 20 residues. we synthesized 1600, 4444, and 10 000 spots cm⁻² peptide microarrays containing the Ebola virus surface glycoprotein and analyzed the IgG response of an Ebola virus disease survivor. The results showed a high reproducibility with robust epitope detection, independent of the spot density. Compared to a commercial reference Ebola virus surface glycoprotein microarray, we not only identified the same epitopes with improved signal to noise ratio, but also detected additional epitopes that are known from literature using ELISA peptide screening platforms. These results imply that we achieve high quality syntheses. High-density peptide microarrays (4444 and 10 000 spots cm⁻²) containing the complete Ebola virus proteome for the first time in single amino acid resolution (4805 individual peptides) provide an excellent tool to study the IgG response of an Ebola virus infection survivor. we illustrate the chemical flexibility of our process and its capability to precisely tune the amounts of transferred material by synthesizing a Schiff base fluorophore microarray. we refined the transfer for a highly precise mixing of two compounds, enabling high-throughput reaction screening in the microarray format. In the future, we will combine the automated system that drastically reduces manual labor,[25,41] with our recently developed high-resolution donor slide,[42] for automated microarray syntheses with densities of >100 000 spots cm⁻².

4. Experimental Section

Laser-Based Synthesizer: The lasing system consisted of a 405 nm wavelength diode laser with a Gaussian beam profile and a maximum of 300 mW power (iBeam smart 405-S, TOPTICA Photonics AG), which is lead through a laser scanning system (intelliSCAN III 10, SCANLAB),

**ADVANCED
SCIENCE NEWS**

www.advancedsciencenews.com

**ADVANCED
MATERIALS**

www.advmat.de

linked to an f-theta-lens (JENar 170-355-140, JENOPTIK Optical Systems GmbH). The measured maximum power in the actual lasing area was 210 mW.

The transport of acceptor and donor slides was automated between the slide holder and the lasing area with a KUKA AGILUS six KR 3 R540 robot (KUKA AG), which has a precision of 20 μm and maximum axis velocities of A1:530, A2:529, A3:538, A4:600, A5:600, and A6:800 per s. To guarantee a stable process, each axis was reduced to 20% of its maximum possible velocity. As robot tool, a gripper (with four 2 mm diameter rubber suction cups) was used, which was connected to a pneumatics system that initiated and released vacuum for transportation.

Within the lasing area, a simple pressure based mechanical alignment, was introduced controlled by the pneumatics system, which ensured the same (<10 μm precision[43]) acceptor slide position for every laser transfer. In specific, after the robot placed the acceptor slide into the lasing area, a soft vacuum suction (−30 kPa) was applied to keep the acceptor slide level. Then, pneumatic springs with curved bolts placed the acceptor slide into the desired location. A strong vacuum (−80 kPa) suction was applied to keep the acceptor slide in place during the process.

Finally, the entire setup (laser scanning system, transportation robot, pneumatics system, time management, etc.) was controlled through a self-designed control system.[44] A python-based application that uses the RoboDK python API (version 3.4.7, RoboDK) was built to control the transportation robot and remote control laserDESK application (version 1.4.3.1, SCANLAB GmbH) to control the laser scanning system. The pneumatics systems and safety control was read out through a serial connection and in addition to the automation procedure, a graphical user interface was developed for non-expert use.

Evaluation of Amino Acid and Peptide Spots: The measured average fluorescence intensity of an AA spot was calculated through the averaged vertical and horizontal line intensity (obtained through ImageJ[45]) and automatically evaluated threshold values that detect the spot edge. This approach guaranteed a measurement error below ±2 pixel = ±10 μm. Furthermore, the average AA spot area was approximated through the vertical and horizontal width to obtain the lowest spot area in case of deformation (i.e., worst-case approximation).

Automatically detected peptide spots of the produced microarrays were evaluated with a developed spot detection program,[46] which resulted in a maximum error of ±4 pixel = ±20 μm.

Measured peptide spots of the produced microarrays with a fixed spot size were evaluated with the GenePix Pro software (version 7 Analysis Only, Molecular Devices, LLC.). If not stated otherwise, a fixed feature (spot width) of 55, 90, and 110 μm was used for the evaluation of microarrays with a spot density of 1600, 4444, and 10 000 spots cm^{-2}.

Commercial microarrays were evaluated with the PepSlide Analyzer software (version 1.5.8, SICASYS Software GmbH) using the fixed-spot detection method with a spot width of 250 μm and spot height of 400 μm. The printed region was 190 μm × 338 μm.

Donor Slide Preparation: For the preparation of a blank donor slide, a microscope glass slide was covered with self-adhesive polyimide foil (Kapton HN, DuPont, 25 μm polyimide layer with a 45 μm siloxane-based adhesive layer; CMC Klebetechnik), which acted as a support. Then, different mixtures of styrene acrylic copolymer (SLEC; SLEC LT 7552, Sekisui Chemical CO., LTD), pre-dissolved in 450 μL dichloromethane (DCM), and a chemical compound, pre-dissolved in 50 μL N,N-dimethylformamide (DMF), which resulted in 500 μL of spin coating solution, were prepared. These solutions were spin-coated (80 rps) on top of a blank donor slide resulting in a variety of donor slide compositions (Table S16, Supporting Information). Materials, spin coating parameters, and resulting theoretical coating thicknesses (Tables S17 and S18, Supporting Information) were derived from Danglad-Flores et al.[47,48]

Acceptor Slide Preparation and Amino Acid Coupling: For the peptide microarray synthesis, PEGMA-*co*-MMA (PEPperPRINT GmbH) slides with a terminal N-[(9H-Fluoren-9-ylmethoxy)carbonyl]-protected (Fmoc-protected) β-alanine were used as solid support (acceptor slides). All

solvent incubation steps were carried out at room temperature (rt). Furthermore, for every solvent incubation step, the acceptor slide was placed in a petri dish, fully covered with solvent, and vibrated on an orbital shaker.

Pre-swelling of the PEGMA-*co*-MMA coating was achieved by immersing the acceptor slide in DMF for 20 min. For Fmoc-deprotection the acceptor slide was immersed in 20% v/v piperidine in DMF for 20 min. After washing the acceptor slide 3× for 3 min in DMF, 1× for 2 min in methanol (MeOH), and 1× for 1 min in DCM (in the following called wash), it was dried in a jet of air.

Following laser-assisted material transfer, the coupling reaction was performed: By heating the acceptor slide to 95 °C for 60 min under inert gas atmosphere, the pentafluorophenyl ester-activated (OPfp-activated) AA reacted with the functional groups of the acceptor slide. If not stated otherwise, AAs were Fmoc-protected and OPfp-activated (Novabiochem, Merck KGaA). Due to the OPfp activation of the AAs, a low rate of racemization was expected,[49] which have been shown for cysteine (Figures S48 and S49, Supporting Information) and tyrosine (Figures S50 and S51, Supporting Information).

Direct Labeling of Amino Groups with a Fluorescent Dye: The acceptor slide preparation protocol, as described in *acceptor slide preparation and amino acid coupling*, was followed. After the AA was transferred and coupled, the remaining amino groups of the acceptor slide were capped twice by immersing the slide in a solution of 10% acetic anhydride, 20% N,N-diisopropylethylamine (DIPEA), and 70% DMF v/v/v. The first capping cycle included 2 min in an ultrasonic bath, followed by 30 min on a shaker. The second cycle was carried out with a fresh capping solution for 30 min. Then, the slide was washed and dried. Afterwards, the Fmoc-protected amino groups of the AAs were deprotected (*acceptor slide preparation and amino acid coupling*) and the slides were washed and dried. For AAs with protected side chains, the acid labile protecting groups were deprotected by immersing the acceptor slide 3× for 30 min in a solution of 51% trifluoroacetic acid (TFA), 44% DCM, 3% triisobutylsilane, and 2% water v/v/v/v. Next, the acceptor slide was washed for 5 min in DCM and then, immersed in 5% v/v DIPEA in DMF for 20 min. Following side chain deprotection and neutralization, the acceptor slide was washed and dried. Next, to visualize the resulting AA spots, the amino groups were stained with DyLight 633 N-hydroxysuccinimide ester (NHS; Thermo Fisher Scientific Inc.). The acceptor slide was immersed in 0.05% v/v Tween 20 (Sigma-Aldrich) in phosphate-buffered saline (PBST) containing 0.1 μg mL^{-1} DyLight 633 NHS ester for 60 min. Finally, the slide was rinsed with water, washed 2× for 10 min in PBST, rinsed multiple times with water, washed 2× for 10 min in DMF, washed 1× for 1 min with DCM, and dried.

Indirect labeling of amino groups with biotin and streptavidin: The acceptor slide preparation protocol and AA coupling (acceptor slide preparation and amino acid coupling), capping, and deprotection were carried out (direct labeling of amino groups with a fluorescent dye). Subsequently, 250 μL of a solution containing 20 μmol mL^{-1} biotin (Fluka BioChemika), 60 μmol mL^{-1} N,N′-diisopropylcarbodiimide (DIC; Acros Organics B.V.B.A), and 20 μmol mL^{-1} pentafluorophenol (PfpOH; Acros Organics B.V.B.A) in DMF were carefully spread on one acceptor slide. A second acceptor slide was placed on top of the first to functionalize both simultaneously overnight. Afterward the slides were washed and dried. To avoid unspecific binding, the acceptor slide was blocked with blocking buffer (MB-070, Rockland Immunochemicals Inc.) for 30 min on a shaker. Next, the slide was incubated with 0.4 μg mL^{-1} CF633 streptavidin (29 037, Biotium, Inc.) in staining buffer (10% v/v blocking buffer in PBST) for 60 min on a shaker. Finally, the acceptor slide was shortly washed 3× with PBST, dipped in 1 mmol L^{-1} tris(hydroxymethyl) aminomethane (Tris) buffer (Carl Roth GmbH + Co. KG) with pH 7.4, and dried in a jet of air.

Reversed-Phase High Performance Liquid Chromatography Coupled to Mass Spectrometry of Single AA: To analyze the potential of AA denaturation during laser-assisted transfer, reversed-phase high performance liquid chromatography (RP-HPLC) coupled to mass spectrometry (MS) measurements of valine, phenylalanine, and tyrosine (reuse values of 2, 4, and 6 respectively) were performed. The

AA were transferred over an area of 20×60 mm^2 onto microscope glass slides and then, heated for 10 min. New and reused donor slides were used separately for the transfer onto the microscope glass slides. Following laser-assisted transfer and heating, the material was washed from the glass slides with acetone and dried in a Buchi Rotavapor R-210. Additionally, measurements of phenylalanine after five cycles of transferring and heating were performed to investigate the influence of above optimal coupling cycles. References of each AA were also analyzed, as well as transferred SLEC, which is present in all transferred samples. Following laser-assisted transfer and heating, the material was washed from the glass slides with acetone and dried in a Buchi Rotavapor R-210. Samples containing AA and SLEC were dissolved in 100 µL of dioxane. AA references were diluted to 0.5 mg mL^{-1} in dioxane. RP-HPLC-MS was performed with an Agilent Technologies 1260 Infinity II coupled to InfinityLab LC/MSD single quadrupole mass spectrometer. For separation of the AA SLEC mixture, the following methods were used—method A: Agilent InfinityLab Proshell 120 EC-C18, 3.0×150 mm, 2.7 µm, flow rate 0.7 mL min^{-1} with 5 min 50% B in A, 50% to 100% B in A in 35 min, 5 min 100% B, (A = 0.1% formic acid in water, B = acetonitrile).

Peptide Array Synthesis—Acceptor Slide Modification: First, a PEGMA-*co*-MMA Fmoc-β-alanine acceptor slide was pre-swollen, deprotected, washed, and dried (*acceptor slide preparation and amino acid coupling*). For the Ha and Flag epitope syntheses, 250 µL of a solution containing 20 µmol mL^{-1} OPfp-activated Fmoc-protected aspartic acid in DMF were carefully spread on top of one acceptor slide and a second acceptor slide was placed on top to functionalize both slides simultaneously overnight. In contrast, for the produced Ebola virus surface glycoprotein/proteome peptide microarrays, the aforementioned step was replaced by laser-assisted material transfer and coupling of the OPfp-activated Fmoc-protected aspartic acid (i.e., pre-patterning). Subsequently, the slides were washed, dried, capped twice (*direct labeling of amino groups with a fluorescent dye*), washed, dried, Fmoc-deprotected (*acceptor slide preparation and amino acid coupling*). Then, washed and dried again. Likewise, a second functionalization step with a solution containing 20 µmol mL^{-1} Fmoc-protected β-alanine, 60 µmol mL^{-1} DIC, and 20 µmol mL^{-1} hydroxybenzotriazole (HOBt; Sigma-Aldrich) was performed and again, the slides were washed, dried, capped twice, washed, and dried.

Peptide Array Synthesis—Coupling Reaction: A PEGMA-*co*-MMA β-alanine aspartic acid Fmoc-β-alanine functionalized slide was used (*peptide array synthesis—acceptor slide modification*). The slide was pre-swollen, Fmoc-deprotected, washed, dried, and the AAs transferred and coupled (*acceptor slide preparation and amino acid coupling*). The laser-assisted transfer of AA patterns from different donor slides to the acceptor was performed, followed by coupling at 95 °C for 60 min (or 10 min for the Ebola virus surface glycoprotein/proteome microarrays) under inert gas atmosphere. Before the laser-assisted transfer of all AAs was repeated with identical patterns, the acceptor slide was washed $2\times$ in acetone for 2 min and dried. After completion of all coupling cycles (coupling of one AA layer), two capping cycles (for the first AA layer three times) were carried out (*direct labeling of amino groups with a fluorescent dye*). From the third AA layer on, the capping duration was reduced to 15 min per capping cycle. Next, the acceptor slide was Fmoc-deprotected (*acceptor slide preparation and amino acid coupling*), washed, and dried. The aforementioned steps (laser-assisted transfer, coupling, capping, and Fmoc-deprotection) were repeated to synthesize the desired peptides in the array format. Then, the *N*-terminus of the peptide was acetylated (*direct labeling of amino groups with a fluorescent dye*) and the slides were washed and dried. Concluding the peptide synthesis, the side chains of the AAs were deprotected (*direct labeling of amino groups with a fluorescent dye*), neutralized, washed, and dried.

HA and Flag Epitope Array Staining: The synthesized HA and Flag epitope arrays were detected with ReadyTag anti-HA (RT028, Bio X Cell, Inc.; 1.0 mg mL^{-1}) labeled with Lightning-Link Rapid Cy5 Labeling Kit (342-0005, Expedeon Ltd.) and Anti-Flag M2-Cy3 (A9594, Sigma-Aldrich; 1.0 mg mL^{-1}). To avoid unspecific binding of the serum antibodies, the arrays were blocked with blocking buffer for 30 min with orbital shaking.

Subsequently, the arrays were incubated with 1:1000 diluted anti-HA and/or anti-Flag antibodies in staining buffer for 30 min on a shaker. To remove unbound antibodies, the arrays were shortly washed $3\times$ with PBST. Finally, the arrays were dipped in 1 mmol L^{-1} Tris HCl buffer pH 7.4 and dried in a jet of air.

For the validation of synthesis yield via antibody binding fluorescence analysis by peptide microarray (Figure 4), the negative controls (i.e., copies of all synthesized peptides with an additional C-terminal SLEC spot without any AA) were $\approx$10% of the wild type Flag epitope.

Coupling Analysis of Amino Acids via N-(9H-Fluoren-9-ylmethyl)-piperidine Absorbance: The following procedure was adapted from Loeffler et al.:[14] For pre-swelling, 1 mL of DMF was pipetted onto an acceptor slide and incubated for 20 min. To avoid evaporation, a tissue, moisturized with DMF, was placed inside the petri dish. Then, Fmoc-deprotection was performed by replacing the DMF with 1 mL of 20% v/v piperidine in DMF and incubation for 20 min. The deprotection solution was collected and the acceptor slide rinsed with additional 200 µL 20% v/v piperidine in DMF, which were collected as well. The absorbance of N-(9H-Fluoren-9-ylmethyl)-piperidine at 301 nm within the deprotection solution was measured to determine the loading of the acceptor slide with β-alanine. After the acceptor slide was washed and dried in a jet of air, a large AA pattern was transferred onto this acceptor slide and coupled for 10 min at 95 °C under inert gas atmosphere. The slide was capped $2\times$ for 20 min and $1\times$ for 30 min with a fresh solution of 10% acetic anhydride, 20% DIPEA, and 70% DMF v/v/v, as well as washed and dried in a jet of air. Consecutively, the Fmoc-deprotection and absorbance measurement (at 301 nm) were repeated. Finally, to calculate the loading after AA transfer, the coupled area was detected by labeling with DyLight 633 NHS ester (*direct labeling of amino groups with a fluorescent dye*). Loading formula:

$$\text{loading}\left[\frac{\text{nmol}}{\text{cm}^2}\right] = \frac{E \, V \, 10^6}{d \, \varepsilon \, A}$$

(*E*: measured extinction; *V*: volume [mL], 1.2 mL; *d*: distance [cm], 1 cm; ε: molar absorption coefficient [L mol^{-1} cm^{-1}], 5129 L mol^{-1} cm^{-1}; *A* = area [cm^2], 19.76 cm^2 or measured).

Ebola Virus Proteome Array Generation and Patient Sample Analysis: For the generation of the Ebola virus proteome arrays, the NCBI reference sequence NC_002549.1 was used and cut into overlapping 15-residue peptides, which were synthesized on the arrays. Prior to the incubation with serum (Ebola virus disease survivor, voluntary donor with informed consent,[50] as agreed with the ethics committee of the Goethe University Hospital, Frankfurt), the arrays were incubated with the subsequently explained steps, including the secondary antibodies without the use of a serum sample. This was carried out to monitor unspecific binding of the secondary antibodies to the peptide arrays (false positive signals).

Before incubation, the arrays were pre-swollen for 15 min with PBST at rt and orbital shaking. To avoid unspecific binding of the serum antibodies, the arrays were blocked with blocking buffer for 30 min with orbital shaking. Following a short washing step with PBST, 1:200 diluted serum in staining buffer was incubated overnight with shaking at 4 °C. To remove unbound serum components, the arrays were shortly washed $3\times$ with PBST. Next, the human serum antibodies were detected with 1:1000 diluted Anti-Human IgG Fc cross-adsorbed DyLight 650 (A80-304D5, Bethyl Laboratories, Inc., USA; 0.5 mg mL^{-1}), 1:2000 diluted Anti-Human IgM (mμ chain) DyLight 549 (609-142-007, Rockland Immunochemicals, Inc.; 1.0 mg mL^{-1}) in staining buffer. In parallel, control peptides were detected with 1:2000 diluted anti-HA and anti-Flag in staining buffer. Thus, the diluted secondary antibodies were applied simultaneously to the microarrays for 30 min at rt and orbital shaking. Finally, to remove unbound secondary antibodies, the arrays were shortly washed $3\times$ with PBST, dipped in 1 mmol L^{-1} Tris HCl buffer pH 7.4, and dried in a jet of air.

Vertical Scanning Interferometry: Vertical scanning interferometry was performed with a smartWLI compact (Gesellschaft für Bild- und Signalverarbeitung (GBS) GmbH, Ilmenau, Germany) attached to a 5× magnification lens. Resulting measurements were evaluated with the developed spot software.[46]

Size Exclusion Chromatography: Size exclusion chromatography was conducted in tetrahydrofuran (VWR, ACS grade, predistilled) with

**ADVANCED
SCIENCE NEWS**

www.advancedsciencenews.com

**ADVANCED
MATERIALS**

www.advmat.de

toluene as internal standard at 25 °C using a column system by PSS SDV 100/1000/100 000 column (8 × 300 mm, 5 μm particle size) with a PSS SDV precolumn (8 × 50 mm), a SECcurity RI detector, SECcurity UV/VIS detector, and a calibration with PS standards or PEO standards from PSS.

Reversed-Phase High Performance Liquid Chromatography Coupled to Mass Spectrometry of Peptide Epimers: To analyze potential racemization of AAs during peptide synthesis, RP-HPLC-MS measurements of short 4-residue peptides (CFDD and YFDD) were performed. Either Fmoc-Cys(Trt)-OPfp or Fmoc-Tyr(tBu)-OPfp in DMF (0.1 mmol/mL) were coupled at 95 °C for 15 min (ensuring at least 10 min at 95 °C) to Rink amide resin (855001, Novabiochem Merck), carrying 3-residue peptide (FDD), in a 1.5 mL reaction tube using an Eppendorf ThermoMixer C. The prepared peptides were Fmoc-deprotected and cleaved from the solid support with simultaneous deprotection of side chain groups by using 90% TFA, 5% triisopropylsilane, 5% water v/v/v for 2 h. Cold diethyl ether was added to the crude peptide containing solution and cleaved product solution and after 30 min on ice, the supernatant was decanted after centrifugation. This process was repeated and the crystallized product was dried. Finally, the product was dissolved in water and lyophilized with Christ Alpha 2–4 LD plus freeze dryer.

For the analysis, the peptides were dissolved in water. The references containing a 1:1 mixture of L-CFDD and D-CFDD or L-YFDD and D-YFDD were diluted to 0.5 mg mL^{-1} in water. RP-HPLC-MS was performed with an Agilent Technologies 1260 Infinity II coupled to InfinityLab LC/MSD single quadrupole mass spectrometer. For separation of the L/D-peptide epimers, method B: Agilent InfinityLab Proshell 120 EC C18, 3.0 × 150 mm, 2.7 μm, flow rate 0.7 mL min^{-1} with 5 min 100% A, 0% to 60% B in A in 35 min, 5 min 60% B (A = 0.1% formic acid in water, B = acetonitrile), was used.

NMR Spectroscopy: The NMR spectra were measured at rt and recorded on a Varian 400-MR (400 MHz; Varian Medical Systems) or Bruker Ascend 400 (400 MHz; Bruker Corporation) spectrometer. Chemical shifts δ were reported in ppm and adjusted to internal standards of the residual proton signal of the deuterated solvent (CDCl$_3$: 7.26 ppm for ^{1}H and 77.0 ppm for ^{13}C; D$_2$O: 4.80 ppm for ^{1}H; DMSO-d$_6$: 2.50 ppm for ^{1}H and 39.52 ppm for ^{13}C). The center of the signal was given for symmetrical signals and the area for multiplets. Thereby, the following common abbreviations were used for multiplicities: s = singlet, d = doublet, t = triplet, q = quartet, m = multiplet, or for combinations dd = doublet of doublet, dt = doublet of triplet, etc. Coupling constants (J) were given in Hz.

Mass Spectrometry: High-resolution mass spectrometry (HRMS) was performed on a 6210 ESI-TOF mass spectrometer (Agilent Technologies). The abbreviation [M+Na]$^+$ referred to the product–sodium adduct. The abbreviation [M-H]$^-$ refers to the product without a proton adduct.

Synthesis of Fluorophore 2-((3-(Carboxymethoxy)benzylidene)amino) benzoic Acid 3: 2-aminobenzoic acid 1 (137 mg, 1.00 mmol, 1.00 equiv.) and 2-(3-formylphenoxy)acetic acid 2 (216 mg, 1.20 mmol, 1.20 equiv.) were respectively dissolved in ethanol (5 mL) at rt. Afterward, the two prepared solutions were mixed under vigorous stirring (800 rpm). The mixture was heated to 60 °C for 180 min and then, cooled down to room temperature. Subsequently, the precipitations were respectively filtered and washed three times with ethanol and diethyl ether. The crude product was purified by flash chromatography using pure methanol as eluent. Finally, the product was obtained as a yellowish solid in 79% yield (237 mg, 790 μmol). For details, also see Figures S52 and S53 in the Supporting Information.

^{1}H-NMR (400 MHz, DMSO-d$_6$): δ = 4.89 (s, 2H, −CH$_2$COO), 7.06–7.21 (m, 3H, Ar), 7.41–7.60 (m, 3H, Ar), 7.72 (s, 1H, H-1), 7.84 (d, J = 7.6 Hz, 1H, Ha-2), 8.06 (d, J = 7.6 Hz, 1H, Hb-2), 8.96 (s, 1H, −CH=N−) ppm.

^{13}C-NMR (101 MHz, DMSO-d$_6$): δ = 65.19, 113.36, 121.10, 124.09, 125.63, 126.68, 127.10, 129.68, 131.95, 133.37, 136.25, 152.25, 156.85, 158.11, 167.08, 170.04 ppm.

HRMS (ESI, m/z): calcd. for C$_{16}$H$_{14}$NO$_5$ [M-H]$^-$: 300.0794; found: 300.0853.

Fluorescence Analysis of 2-((3-(Carboxymethoxy)benzylidene)amino) benzoic Acid: The 2D fluorescence spectrum of 2-((3-(carboxymethoxy) benzylidene)amino)benzoic acid (Figure S54, Supporting Information) was measured through the spectrofluorometer FP-8300 (JASCO Deutschland GmbH). The testing solution was prepared by dissolving 2-((3-(carboxymethoxy)benzylidene)amino)benzoic acid in methanol (analytical grade) with a final concentration of 75 μg mL^{-1}. The normal fluorescence spectra of 2-(3-formylphenoxy)acetic and 2-aminobenzoic acid were tested with the same procedure at a fixed excitation wavelength of 532 nm (Figure S55, Supporting Information).

Computational Simulation of 2-((3-(Carboxymethoxy)benzylidene)amino) benzoic Acid: The simulation was performed with GaussView 5.0 and Gaussian 09. Molecular orbital amplitude plots of 2-((3-(carboxymethoxy) benzylidene)amino)benzoic acid for the highest occupied (HOMO) and lowest unoccupied molecular orbital (LUMO) were calculated through density functional theory with the B3LYP hybrid functional and a basis set level of 6-31G* (Figure S56, Supporting Information).

Fluorophore Microarray Synthesis Using the Schiff Base Reaction: Blank donor slides and spin-coating parameters were used as described in *donor slide preparation*. For the 2-(3-formylphenoxy)acetic acid donor slide, 27 mg SLEC was pre-dissolved in 450 μL DCM and then, mixed with 50 μL DMF containing DIC (2.78 mg, 22.0 μmol, 1.00 equiv.), PfpOH (7.00 mg, 38.0 μmol, 1.73 equiv.), and 2-(3-formylphenoxy) acetic acid 2 (4.00 mg, 22.0 μmol, 1.00 equiv.; 152153, Sigma-Aldrich). The 2-aminobenzoic acid donor slide was prepared by simultaneously dissolving 27 mg SLEC and 10 mg 2-aminobenzoic acid 1 (A89855, Sigma-Aldrich) in 500 μL acetone.

Next, the acceptor slide preparation protocol, as described in *acceptor slide preparation and amino acid coupling*, was followed. Consecutively, laser-assisted material (Table S19) transfer and the coupling reaction was performed: By heating the acceptor slide to 95 °C for 10 min under inert gas atmosphere, the OPfp-activated 2-(3-formylphenoxy)acetic acid 2 reacted with the functional groups of the acceptor slide. The material transfer and coupling procedure was performed three times. After each coupling, the acceptor slide was washed 3× for 5 min in MeOH and then dried in a jet of air. For 2-aminobenzoic acid 1, the material transfer was performed once and a coupling duration of 90 min was used. Finally, before fluorescence imaging (Figure 6b), the acceptor slide was washed 3× for 5 min in MeOH, 1× for 1 min in DCM, and dried in a jet of air.

Fluorescence Imaging: Fluorescence image acquisition for all experiments was performed with the fluorescence scanner Genepix 4000B (Molecular Devices) with a resolution of 5 μm and a laser power of 33%. The different parameters for the wavelength detection and photo multiplier gain (PMT) are listed in Table S20, Supporting Information.

Statistical Analysis: Data was acquired from unprocessed fluorescence image data. If applicable, applied transformations (e.g., normalization and background subtraction) are stated within the caption of each figure/table. Except for data points that were strongly affected by process irregularities (e.g., dirt), outliers were considered. Quantitative data was presented as measurement value ± measurement error, mean ± standard deviation (SD), or mean with min/max value boundaries. For all single AA experiments, the sample size was increased until a trend was observable. At least three data points per experiment were acquired, except for the evaluation of the proteome data that contained two data points. Statistical significance of the spearman rank correlation was assessed using python scipy.stats.spearmanr; a *p*-value of at least $p < 10^{-10}$ was measured for all experiments. All statistical analyses were carried out with python and the developed analysis tools (*Evaluation of amino acid and peptide spots*). IgG epitopes within the Ebola virus proteome were detected by surpassing a threshold value that is based on the limit of blank, which were acquired from the fluorescence intensity of secondary antibodies. For the synthesized microarrays, the threshold value was at least ten times above the limit of blank.

Supporting Information

Supporting Information is available from the Wiley Online Library or from the author.

**ADVANCED
SCIENCE NEWS**

www.advancedsciencenews.com

**ADVANCED
MATERIALS**

www.advmat.de

Conflict of Interest

F.B. and F.F.L. are named on a patent application related to laser-based microarray synthesis. All other authors declare that they have no competing interests.

Author Contributions

G.P. and J.H. contributed equally to this work. Conceptualization: G.P., J.H., F.F.L.; Data curation: G.P., J.H.; Formal analysis: G.P., J.H.; Funding acquisition: F.F.L.; Investigation: G.P., J.H., A.T., Y.L., D.M., C.L., F.R.B.; Methodology: G.P., J.H., S.P.M., M.M.; Project administration: G.P., J.H.; Resources: R.W., C.R., P.H.S., F.B., T.W., F.F.L.; Software: G.P.; Supervision: F.B., F.F.L.; Validation: G.P., J.H., A.T., Y.L., D.M., S.P.M., P.D., M.M., F.F.L.; Visualization: G.P., J.H., A.T., Y.L.; Writing—original draft: G.P., J.H., F.F.L.; Writing—review and editing: G.P., J.H., D.M., M.M., C.R., P.H.S., F.F.L.

Data Availability Statement

The data that support the findings of this study are available in the supplementary material of this article.

[1] R. B. Merrifield, *Science* **1965**, *150*, 178.

[2] M. H. Caruthers, *Science* **1985**, *230*, 281.

[3] O. J. Plante, E. R. Palmacci, P. H. Seeberger, *Science* **2001**, *291*, 1523.

[4] J. Li, S. G. Ballmer, E. P. Gillis, S. Fujii, M. J. Schmidt, A. M. E. Pallazzolo, J. W. Lehmann, G. F. Morehouse, M. D. Burke, *Science* **2015**, *347*, 1221.

[5] H. M. Geysen, R. H. Meloen, S. J. Barteling, *Proc. Natl. Acad. Sci. U. S. A.* **1984**, *81*, 3998.

[6] R. Frank, *Tetrahedron* **1992**, *48*, 9217.

[7] S. P. Fodor, J. L. Read, M. C. Pirrung, L. Stryer, A. T. Lu, D. Solas, *Science* **1991**, *251*, 767.

[8] J. P. Pellois, X. Zhou, O. Srivannavit, T. Zhou, E. Gulari, X. Gao, *Nat. Biotechnol.* **2002**, *20*, 922.

[9] M. Beyer, A. Nesterov, I. Block, K. König, T. Felgenhauer, S. Fernandez, K. Leibe, G. Torralba, M. Hausmann, U. Trunk, F. R. Bischoff, V. Stadler, F. Breitling, *Science* **2007**, *318*, 1888.

[10] V. Stadler, T. Felgenhauer, M. Beyer, S. Fernandez, K. Leibe, S. Güttler, M. Gröning, K. König, G. Torralba, M. Hausmann, V. Lindenstruth, A. Nesterov, I. Block, R. Pipkorn, A. Poustka, F. R. Bischoff, F. Breitling, *Angew. Chem., Int. Ed.* **2008**, *47*, 7132.

[11] J. V. Price, S. Tangsombatvisit, G. Xu, J. Yu, D. Levy, E. C. Baechler, O. Gozani, M. Varma, P. J. Utz, C. Liu, *Nat. Med.* **2012**, *18*, 1434.

[12] S. Buus, J. Rockberg, B. Forsström, P. Nilsson, M. Uhlen, C. Schafer-Nielsen, *Mol. Cell. Proteomics* **2012**, *11*, 1790.

[13] J. B. Legutki, Z. Zhao, G. Greving, N. Woodbury, S. A. Johnston, P. Stafford, *Nat. Commun.* **2014**, *5*, 4785.

[14] F. F. Loeffler, T. C. Foertsch, R. Popov, D. S. Mattes, M. Schlageter, M. Sedlmayr, B. Ridder, F. X. Dang, C. v. Bojničić-Kninski, L. K. Weber, A. Fischer, J. Greifenstein, V. Bykovskaya, I. Buliev, F. R. Bischoff, L. Hahn, M. A. R. Meier, S. Bräse, A. K. Powell, T. S. Balaban, F. Breitling, A. Nesterov-Mueller, *Nat. Commun.* **2016**, *7*, 11844.

[15] C. Moreno-Yruela, M. Bæk, A. Vrsanova, C. Schulte, H. M. Maric, C. A. Olsen, *Nat. Commun.* **2021**, *12*, 62.

[16] W. Lin, S. Gandhi, A. R. Oviedo Lara, A. K. Thomas, R. Helbig, Y. Zhang, *Adv. Mater.* **2021**, *33*, 2102349.

[17] D. Shin, K. Lee, B. Yoo, J. Kim, M. Kim, Y. Kim, Y. Lee, *J. Comb. Chem.* **2010**, *12*, 463.

[18] JPT Peptide Technology GmbH, https://www.jpt.com (accessed: August 2021).

[19] LC Sciences, https://www.lcsciences.com (accessed: August 2021).

[20] PEPperPRINT GmbH, https://www.pepperprint.com (accessed: August 2021).

[21] A. Chandra, N. Latov, G. P. Wormser, A. R. Marques, A. Alaedini, *Clin. Immunol.* **2011**, *141*, 103.

[22] B. A. R. Williams, C. W. Diehnelt, P. Belcher, M. Greving, N. W. Woodbury, S. A. Johnston, J. C. Chaput, *J. Am. Chem. Soc.* **2009**, *131*, 17233.

[23] J. Tan, B. K. Sack, D. Oyen, I. Zenklusen, L. Piccoli, S. Barbieri, M. Foglierini, C. SilacciFregni, J. Marcandalli, S. Jongo, S. Abdulla, L. Perez, G. Corradin, L. Varani, F. Sallusto, B. K. L. Sim, S. L. Hoffman, C. Daubenberger, I. A. Wilson, A. Lanzavecchia, *Nat. Med.* **2018**, *24*, 401.

[24] M. Benz, A. Asperger, M. Hamester, A. Welle, S. Heissler, P. A. Levkin, *Nat. Commun.* **2020**, *11*, 5391.

[25] K. Heiss, J. Heidepriem, N. Fischer, L. K. Weber, C. Dahlke, T. Jaenisch, F. F. Loeffler, *J. Proteome Res.* **2020**, *19*, 4339.

[26] M. Koenig, C. Bentow, M. Satoh, M. J. Fritzler, J. Senécal, M. Mahler, *Rheumatology* **2019**, *58*, 1784.

[27] S. Eickelmann, A. Tsouka, J. Heidepriem, G. Paris, J. Zhang, V. Molinari, M. Mende, F. F. Loeffler, *Adv. Mater. Technol.* **2019**, *4*, 1900503.

[28] G. Paris, A. Klinkusch, J. Heidepriem, A. Tsouka, J. Zhang, M. Mende, D. S. Mattes, D. Mager, H. Riegler, S. Eickelmann, F. F. Loeffler, *Appl. Surf. Sci.* **2020**, *508*, 144973.

[29] S. Eickelmann, S. Ronneberger, J. Zhang, G. Paris, F. F. Loeffler, *Adv. Mater. Interfaces* **2021**, *8*, 2001626.

[30] OpenCV, Open Source Computer Vision Library **2015**, https://opencv.org/ (accessed: April 2022).

[31] A. Fukunaga, S. Maeta, B. Reema, M. Nakakido, K. Tsumoto, *Biochem. Biophys. Rep.* **2018**, *15*, 81.

[32] M. v. Rosmalen, M. Krom, M. Merkx, *Biochemistry* **2017**, *56*, 6565.

[33] N. Hartrampf, A. Saebi, M. Poskus, Z. P. Gates, A. J. Callahan, A. E. Cowfer, S. Hanna, S. Antilla, C. K. Schissel, A. J. Quartararo, X. Ye, A. J. Mijalis, M. D. Simon, A. Loas, S. Liu, C. Jessen, T. E. Nielsen, B. L. Pentelute, *Science* **2020**, *368*, 980.

[34] J. Heidepriem, V. Krähling, C. Dahlke, T. Wolf, F. Klein, M. M. Addo, S. Becker, F. F. Loeffler, *Biotechnol. J.* **2020**, *15*, 2000069.

[35] P. Becquart, T. Mahlakõiv, D. Nkoghe, E. M. Leroy, *PLoS One* **2014**, *9*, e96360.

[36] L. Fabbrizi, *J. Org. Chem.* **2020**, *85*, 12212.

[37] Y. Jia, J. Li, *Chem. Rev.* **2015**, *115*, 1597.

[38] A. L. Berhanu, Gaurav, I. M. , A. K. Malik, J. S. Aulakh, V. Kumar, K. Kim, *Trends Anal. Chem.* **2019**, *116*, 74.

[39] V. S. Padalkar, S. Seki, *Chem. Soc. Rev.* **2016**, *45*, 169.

[40] A. A. Nagarkar, S. E. Root, M. J. Fink, A. S. Ten, B. J. Cafferty, D. S. Richardson, M. Mrksich, G. M. Whitesides, *ACS Cent. Sci.* **2021**, *7*, 1728.

[41] M. Mende, A. Tsouka, J. Heidepriem, G. Paris, D. S. Mattes, S. Eickelmann, V. Bordoni, R. Wawrzinek, F. F. Fuchsberger, P. H. Seeberger, C. Rademacher, M. Delbianco, A. Mallagaray, F. F. Loeffler, *Chem. - Eur. J.* **2020**, *26*, 9655.

[42] J. Zhang, Y. Liu, S. Ronneberger, N. V. Tarakina, N. Merbouh, F. F. Loeffler, *Adv. Mater.* **2022**, *34*, 2108493.

[43] G. Paris, J. Heidepriem, A. Tsouka, M. Mende, S. Eickelmann, F. F. Loeffler, in *SPIE BiOS 2019*, SPIE, San Francisco **2019**.

[44] G. Paris Python scripts, available on github: App.py, laserClient.py, robot.py, and SAT in Spots we Trust.py, https://github.com/Grigori-Paris/Grigori-Paris-PhD-code (accessed: April 2021).

[45] C. A. Schneider, W. S. Rasband, K. W. Eliceiri, *Nat. Methods* **2012**, *9*, 671.

[46] G. Paris Python scripts, available on github: HoughCircleSynthesis.py and HoughCircleSynthesisApp.py, https://github.com/Grigori-Paris/Grigori-Paris-PhD-code (accessed: March 2021).

[47] J. Danglad-Flores, S. Eickelmann, H. Riegler, *Chem. Eng. Sci.* **2018**, *179*, 257.

[48] J. Danglad-Flores, S. Eickelmann, H. Riegler, *Eng. Rep.* **2021**, *3*, e12390.

[49] C. P. Gordon, *Org. Biomol. Chem.* **2018**, *16*, 180.

[50] T. Wolf, G. Kann, S. Becker, C. Stephan, H. R. Brodt, P. de Leuw, T. Grunewald, T. Vogl, V. A. Kempf, O. T. Keppler, K. Zacharowski, *Lancet* **2015**, *385*, 1428.

ADVANCED MATERIALS

Supporting Information

Automated Laser-Transfer Synthesis of High-Density Microarrays for Infectious Disease Screening

Grigori Paris, Jasmin Heidepriem, Alexandra Tsouka, Yuxin Liu, Daniela S. Mattes, Sandra Pinzón Martín, Pietro Dallabernardina, Marco Mende, Celina Lindner, Robert Wawrzinek, Christoph Rademacher, Peter H. Seeberger, Frank Breitling, Frank Ralf Bischoff, Timo Wolf, and Felix F. Loeffler*

Supporting Information

Automated laser-transfer synthesis of high-density microarrays for infectious disease screening

Grigori Paris†, Jasmin Heidepriem†, Alexandra Tsouka, Yuxin Liu, Daniela S. Mattes, Sandra Pinzón Martín, Pietro Dallabernardina, Marco Mende, Celina Lindner, Robert Wawrzinek, Christoph Rademacher, Peter H. Seeberger, Frank Breitling, F. Ralf Bischoff, Timo Wolf, Felix F. Loeffler*
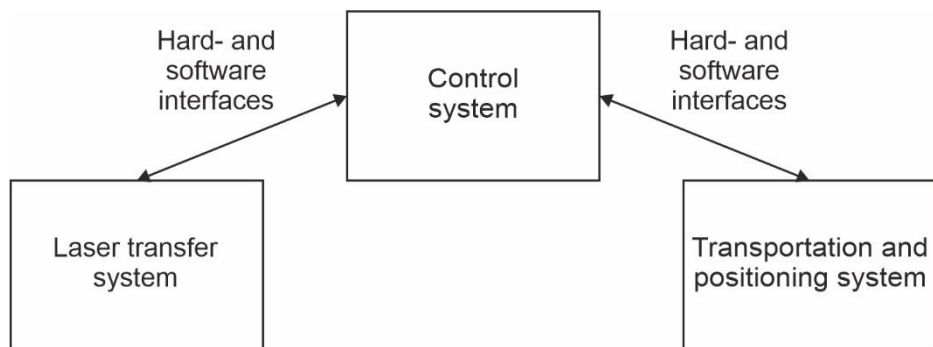
Figure S1. Simplified synthesizer concept. The concept of the synthesizer is separated into a (1) laser transfer system, which utilizes the LIFT material deposition principle, (2) a transportation and positioning system to automatically handle acceptor and donor slides, as well as increase versatility within iterative processes, and (3) a control system for the user interaction, process scheduling, and communication with the laser transfer, transportation, and positioning system.
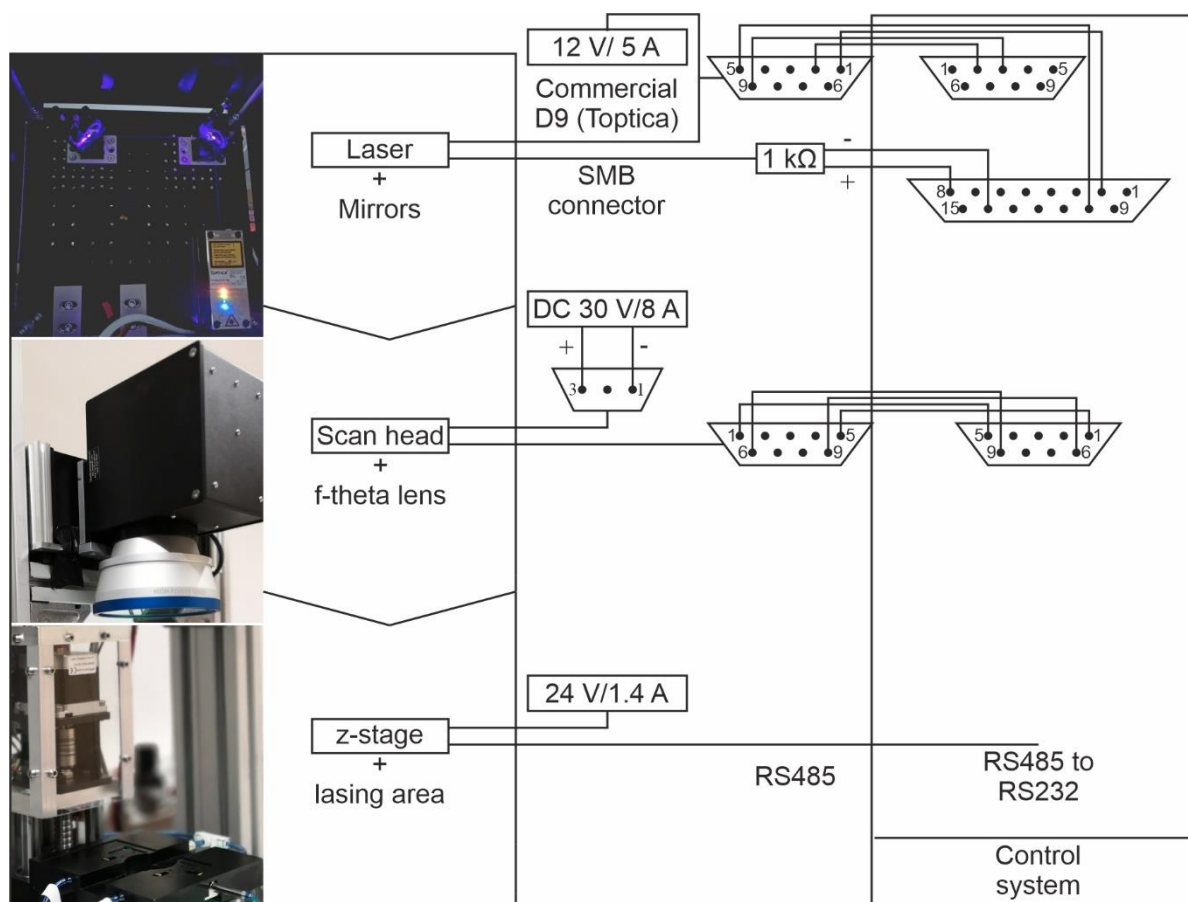
Figure S2. Details of the laser transfer system. The laser transfer system consists of a 405 nm wavelength 300 mW diode laser, which is led through a laser scanning system equipped with a telecentric f-theta-lens. The setup generates a precise focal plane in the lasing area. In addition, a z-stage is connected to the positioning table to simplify the calibration of the lasing area. All necessary hardware connections, regarding the control system and power supplies of the laser transfer system are shown. A 1 kΩ resistance was implemented to prevent overcurrent from damaging the diode laser.
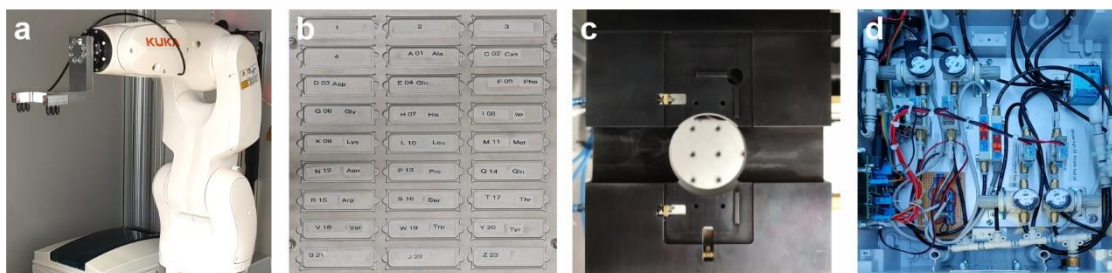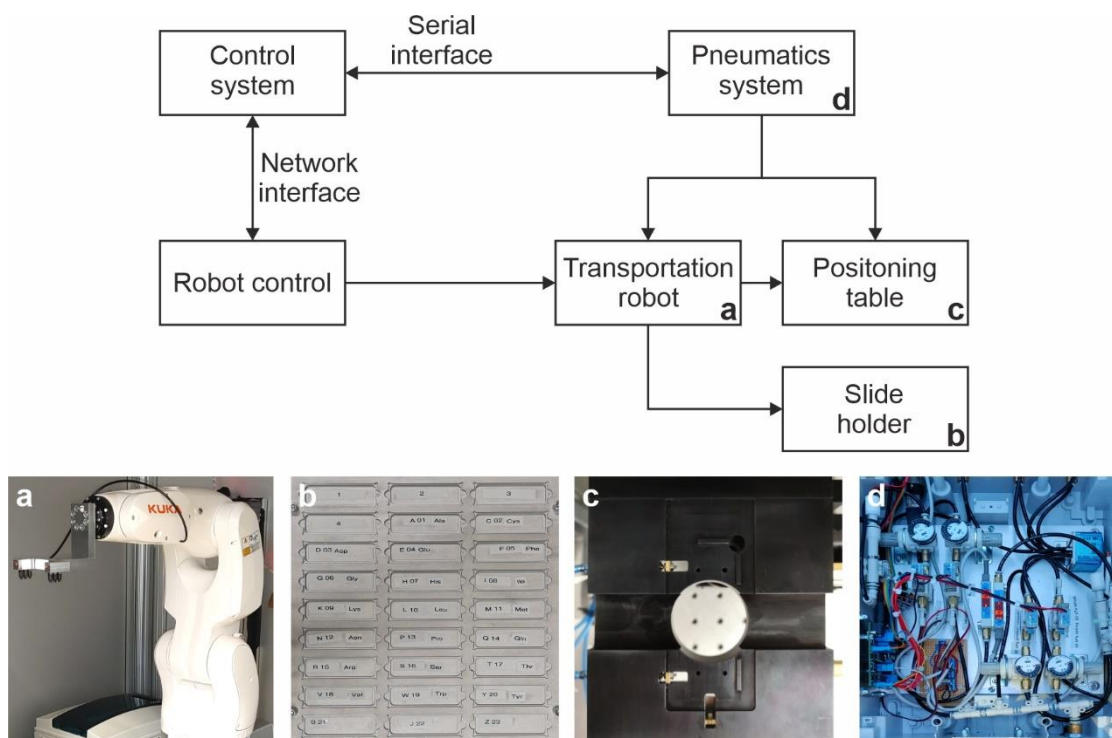
Figure S3. Details of the transportation and positioning system. A fast and high-precision robot (**a**), equipped with a vacuum gripper, moves acceptor and donor slides back and forth between the slide holder (**b**) and the positioning table (**c**). Specifically, an acceptor slide is first placed into the positioning table and an alignment procedure is carried out. Afterwards, the transportation robot places a donor on top of the acceptor slide, material is deposited via laser irradiation, and the donor is placed back to its original position. This procedure is repeated until the desired combinatorial pattern is deposited. The pressure control for the transportation robot and the positioning table is scheduled by a pneumatics system (**d**) with seven ports. These ports separately control the robot gripper, positioning table suction, and positioning table bolts. For completeness, the control system interacts with the pneumatics system and robot control via serial and network interface respectively.
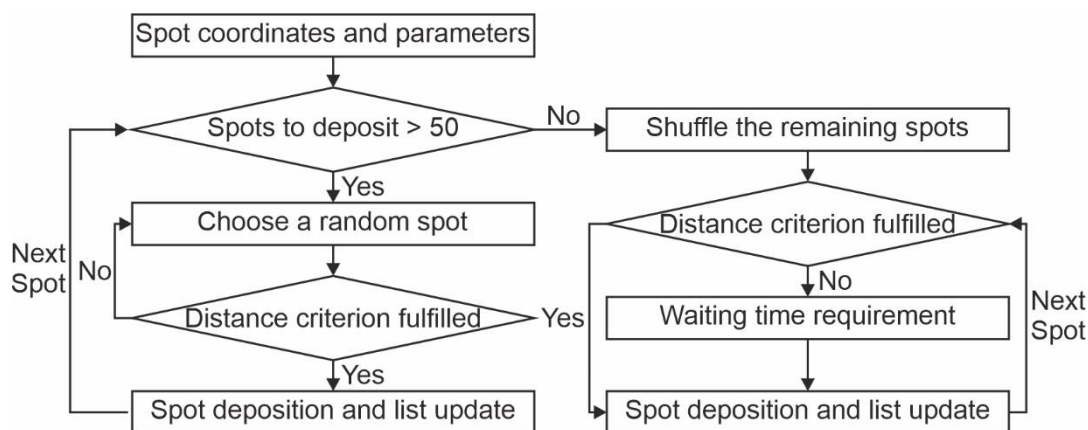
Figure S4. Spot transfer algorithm. To avoid neighbor effects of spot transfers (e.g., increased temperature), a transfer algorithm was designed. First, the spot locations of all spots and transfer parameters are accessed. Afterwards, a locations list of the last three transferred spots is initialized with three random spots. Subsequently, it is evaluated whether the number of spots to transfer exceeds 50. If there are more than 50 spots to transfer, a random spot is chosen and the distances to the three previously transferred spots are calculated. If all distances are above the distance criterion of 4x the distance between spot centers (depending on the spot density), the spot is transferred and the next random spot is chosen and evaluated. If the threshold is not met, another random spot is chosen and evaluated. This procedure is repeated until there are 50 spots left to transfer. Then, the remaining spots are shuffled and evaluated in order. Now, the distance condition is applied, but only for the (single) previous spot. If the condition is true, the spot is transferred, otherwise, a waiting period of 3x the current lasing duration is introduced and then, the spot is transferred. This procedure is repeated until all spots are transferred.
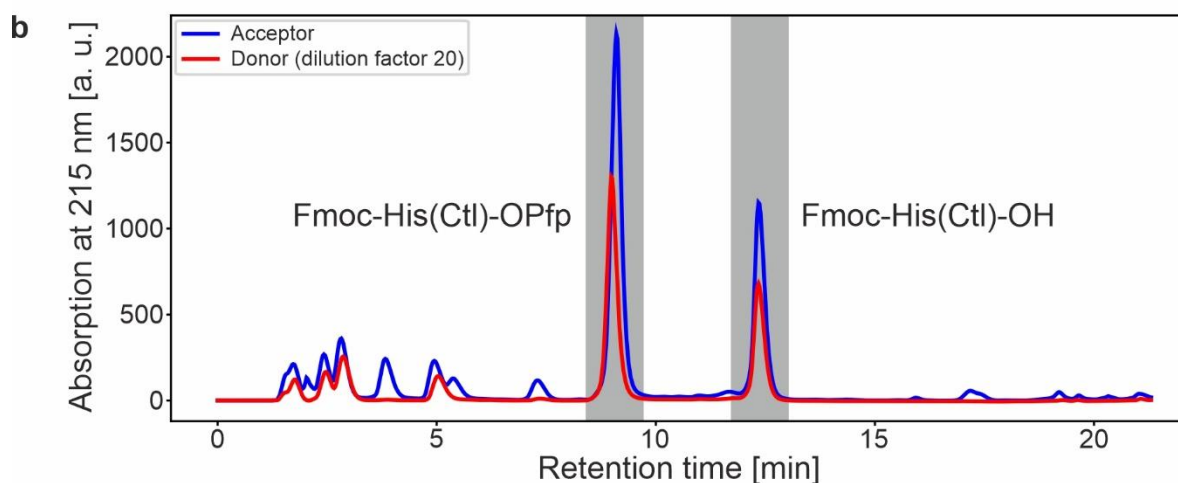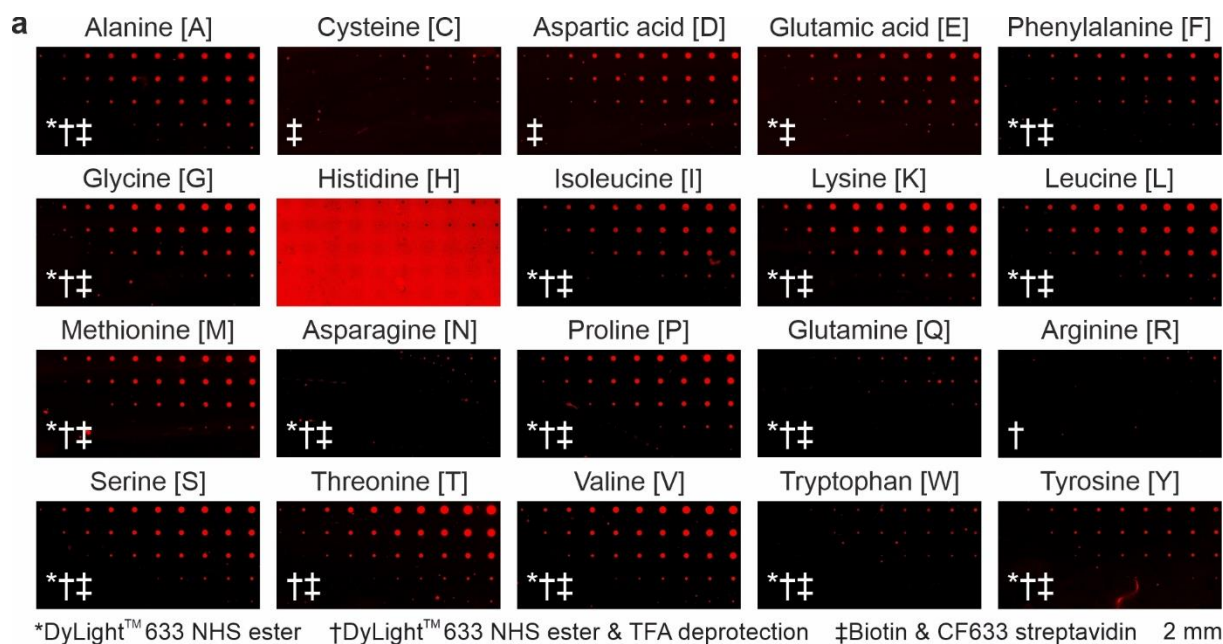
Figure S5. AA labeling procedures. Parameter variations in lasing power and duration (50 mW, 60 mW, 80 mW, 100 mW, 120 mW, and 3 – 12 ms) of the transferred AAs are shown (**a**), which verify AA couplings after material deposition. If multiple labeling procedures are applicable for an AA, the corresponding shown parameter variation is chosen in the following order: (1) direct labeling without side chain deprotection – DyLight™ 633 NHS ester, (2) direct labeling with side chain deprotection – DyLight™ 633 NHS ester & TFA deprotection, (3) indirect labeling – Biotin & CF633 streptavidin

HPLC measurement of Fmoc-His(Ctl)-OPfp and Fmoc-His(Ctl)-OH within a donor slide and after laser-assisted material transfer was performed for the verification of histidine (**b**). For the measurement, an ÄKTA Purifier 10 (Amersham Pharmacia Biotech, Inc.) with CC 8/3 Nucleosil 100-3 C18 and CC 125/3 Nucleosil 100-3 C18 HD (Macherey-Nagel GmbH & Co. KG) were used (buffer A: 0.05 mol/L triethyl ammonium phosphate pH 2.25 and buffer B: 10 % buffer A in 90 % acetonitrile). The sample material after laser-assisted material transfer was suspended in 500 µL

acetone, dried, and resuspended in 10 µL dioxane. For the donor slide, 10 µL of sample material were measured, which were previously suspended in 200 µL dioxane (dilution factor = 20). As reference 5 µg of Fmoc-His(Ctl)-OPfp were used.
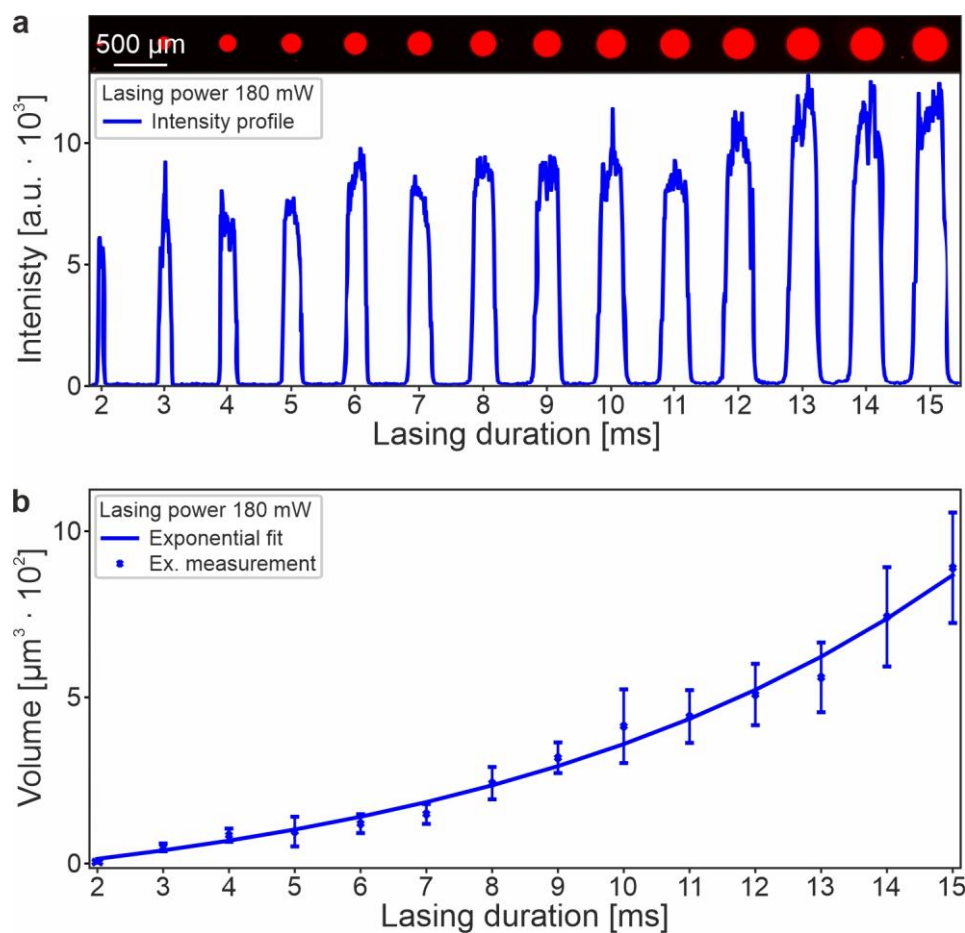
Figure S6. Correlation between fluorescence intensity and spot volume. Fluorescence intensities (**a**) and volume (**b**) of transferred (2 – 15 ms lasing duration and constant lasing power of 180 mW) alanine spots from a donor prepared by a spin-coating solution containing 27.0 mg SLEC dissolved in 450 µL DCM and 3.0 mg alanine dissolved in 50 µL DMF. With increasing lasing duration, a rise of total fluorescence intensity is observed, which correlates to an increased spot volume (i.e., increased alanine amount). Data presented as mean ± SD, n = 3.
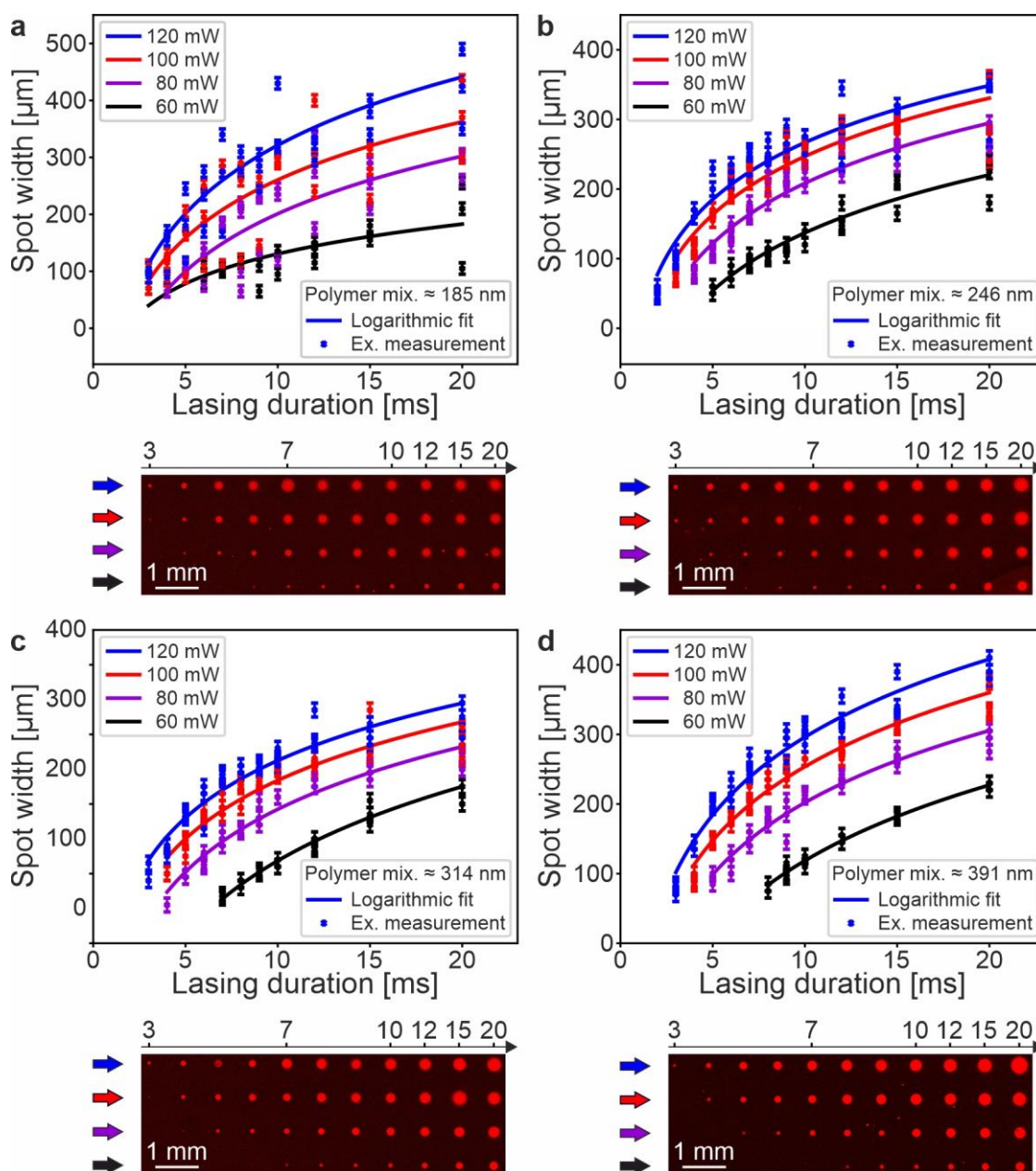
Figure S7. Polymer coating thickness influence. Transfer parameter variations in lasing power and duration for varying polymer coating thicknesses (185 nm (**a**), 246 nm (**b**), 314 nm (**c**), and 391 nm (**d**)). The different coating thicknesses were produced through polymer mixtures that contained 2.0 mg. 2.5 mg, 3.0 mg, and 3.5 mg of alanine dissolved in 50 µL DMF and mixed with 18.0 mg. 22.5 mg, 27.0 mg, and 31.5 mg polymer dissolved in 450 µL DCM. For all experiments, an increase of the deposited spot width with larger lasing powers and durations is evident and the smallest spot widths are found for a polymer coating thickness of 314 nm. For the respective lasing parameters, the data points are presented as measurement value ± measurement error.
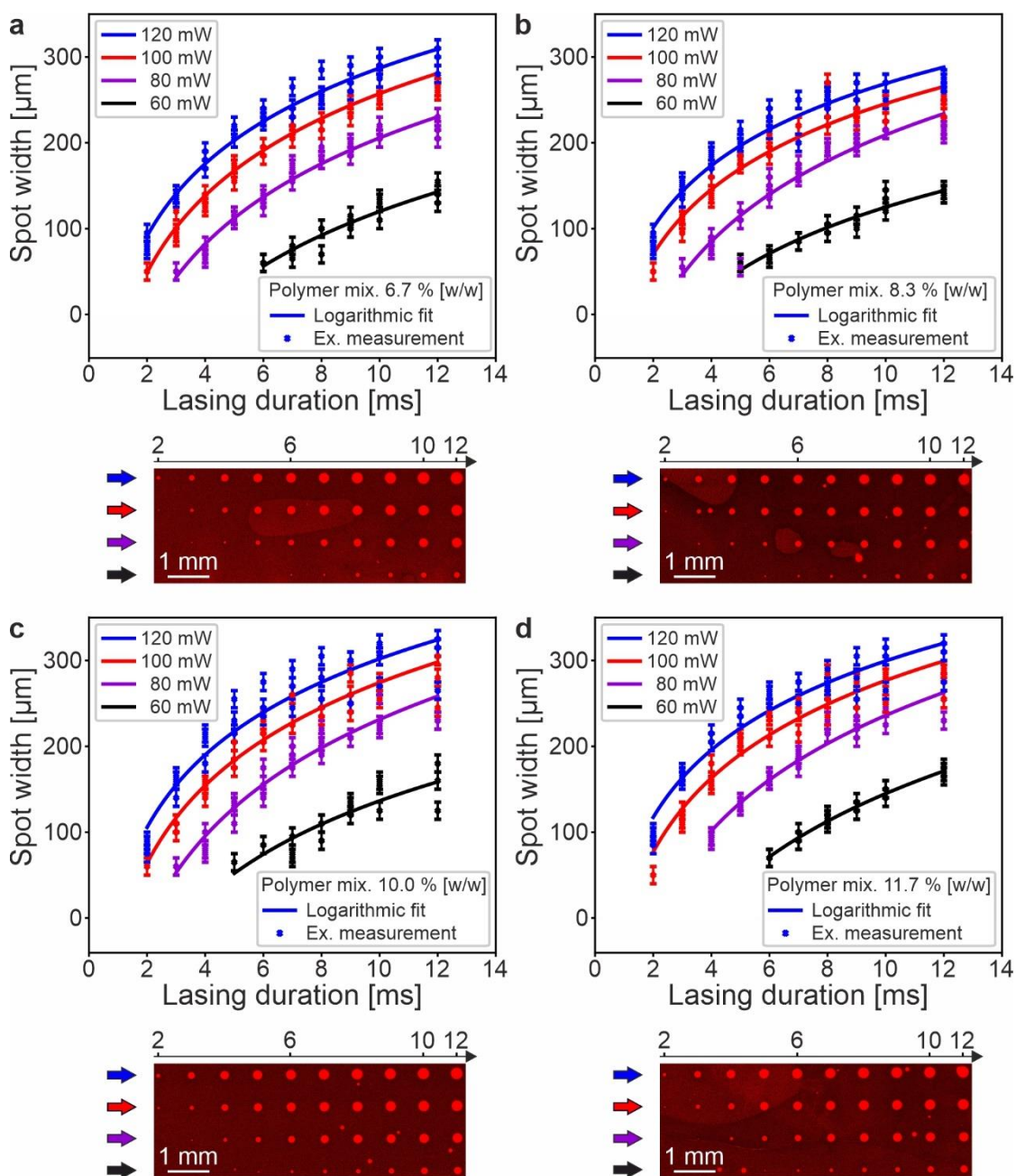
Figure S8. Amino acid concentration influence. Transfer parameter variations in lasing power and duration for a fixed polymer coating thickness of 314 nm and varying alanine concentrations (6.7 % [w/w] (**a**), 8.3 % [w/w] (**b**), 10.0 % [w/w] (**c**), and 11.7 % [w/w] (**d**)). Only marginal differences are noticeable for the spot widths between all transferred ratios. Nevertheless, the highest ratio, which still small robust spots (spot width < 100 µm) is 10 % [w/w] of alanine in polymer. For the respective lasing parameters, the data points are presented as measurement value ± measurement error.
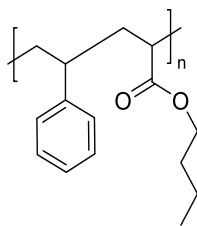
**Figure S9.** Styrene-acrylic copolymer (SLEC). Molecular weight: Mw = 33916 g mol^{-1}; molecular weight: Mn = 15985 g mol^{-1}; *polydispersity* D = 2.1217; glass transition temperature[1] Tg = 336.65 K.
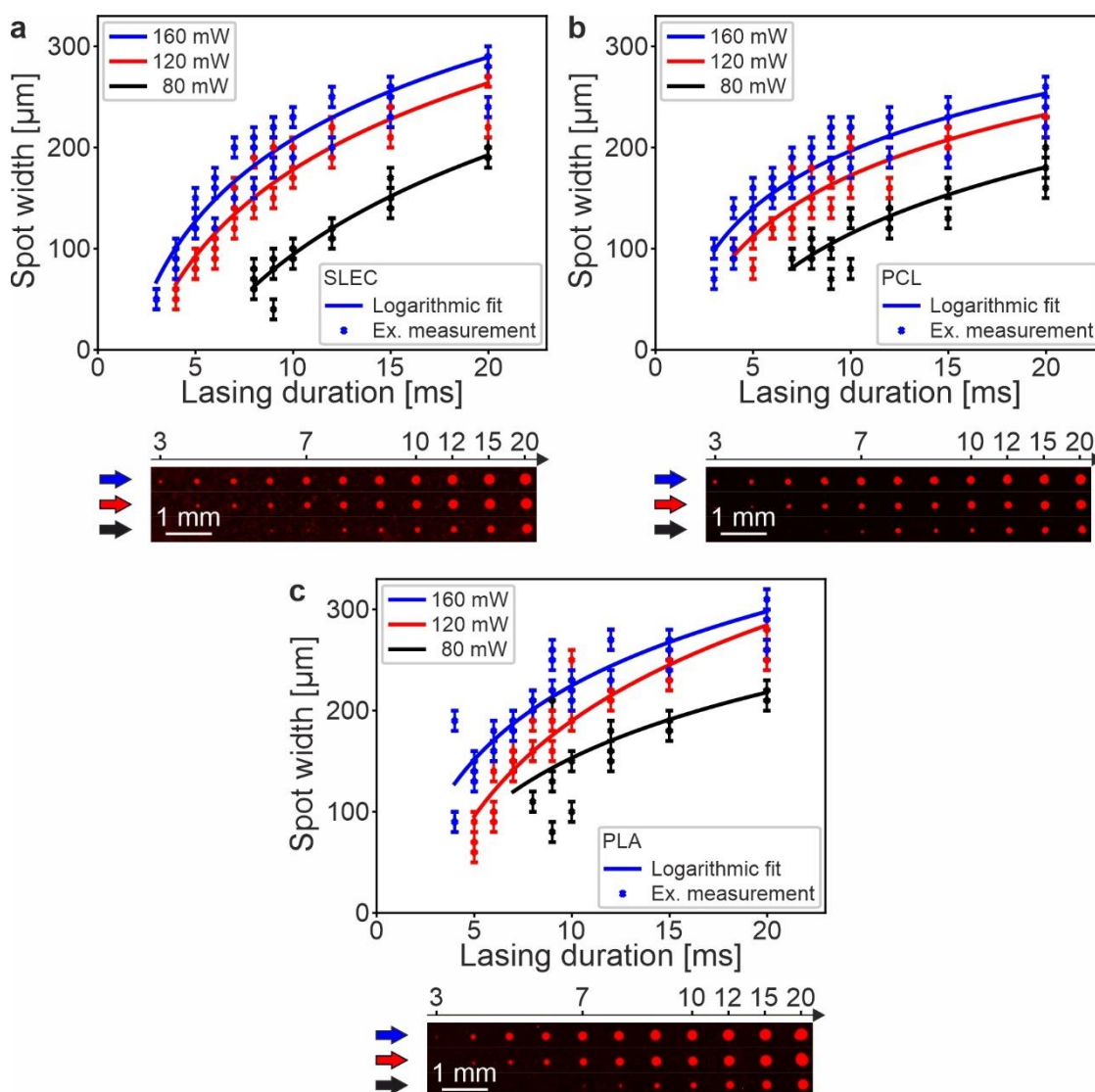
Figure S10. Spot width comparison between styrene-acrylic copolymer (SLEC, SLEC LT 7552, Sekisui Chemical CO., LTD), polycaprolactone (PCL, 440752, Sigma-Aldrich), and polylactic acid (PLA, CDX-P0013, Chemodex AG). Spot widths of transferred (3 – 20 ms lasing duration; lasing power of 80 – 160 mW) SLEC (**a**), PCL (**b**), and PLA (**c**) spots from a donor slide prepared with a spin-coating solution containing 18.0 mg SLEC/PCL/PLA dissolved in 450 µL DCM and 2.0 mg alanine dissolved in 50 µL DMF. For all experiments, an increase of the deposited spot width with larger lasing powers and durations is evident. Most robust transfers for small spot widths (i.e., spot width < 100 µm) are identified for SLEC. For the respective lasing parameters, the data points are presented as measurement value ± measurement error.
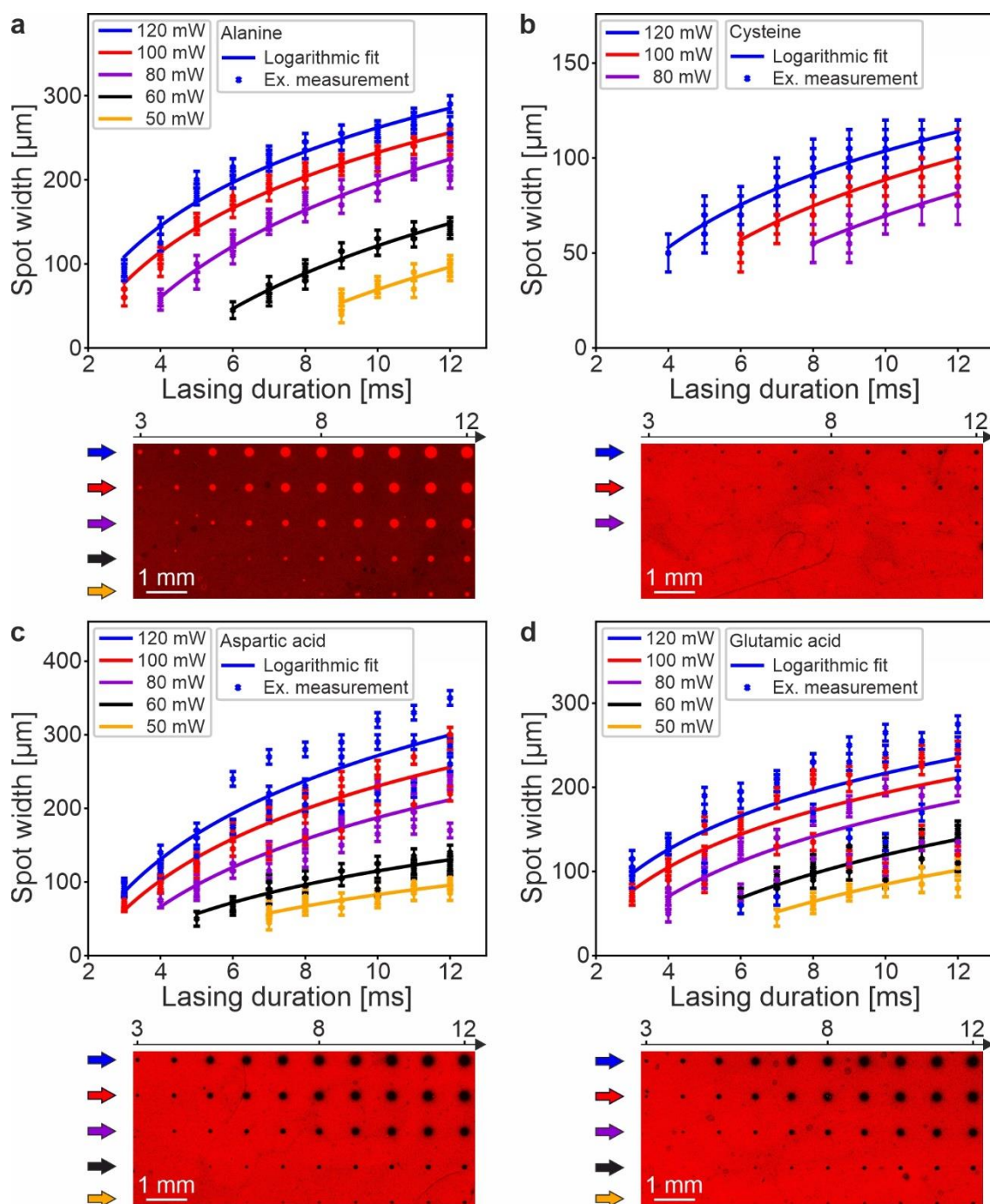
**Figure S11.** Parameter variation mapping of alanine (**a**), cysteine (**b**), aspartic acid (**c**), and glutamic acid (**d**) from 50 – 120 mW lasing intensity and 3 – 12 ms lasing duration. The spot widths follow a logarithmic growth with increasing lasing power and duration. Cysteine generally shows smaller spots with low spot width deviations and aspartic, as well as glutamic acid show stronger deviations for lasing powers above 80 mW. For the respective lasing parameters, the data points are presented as measurement value ± measurement error.
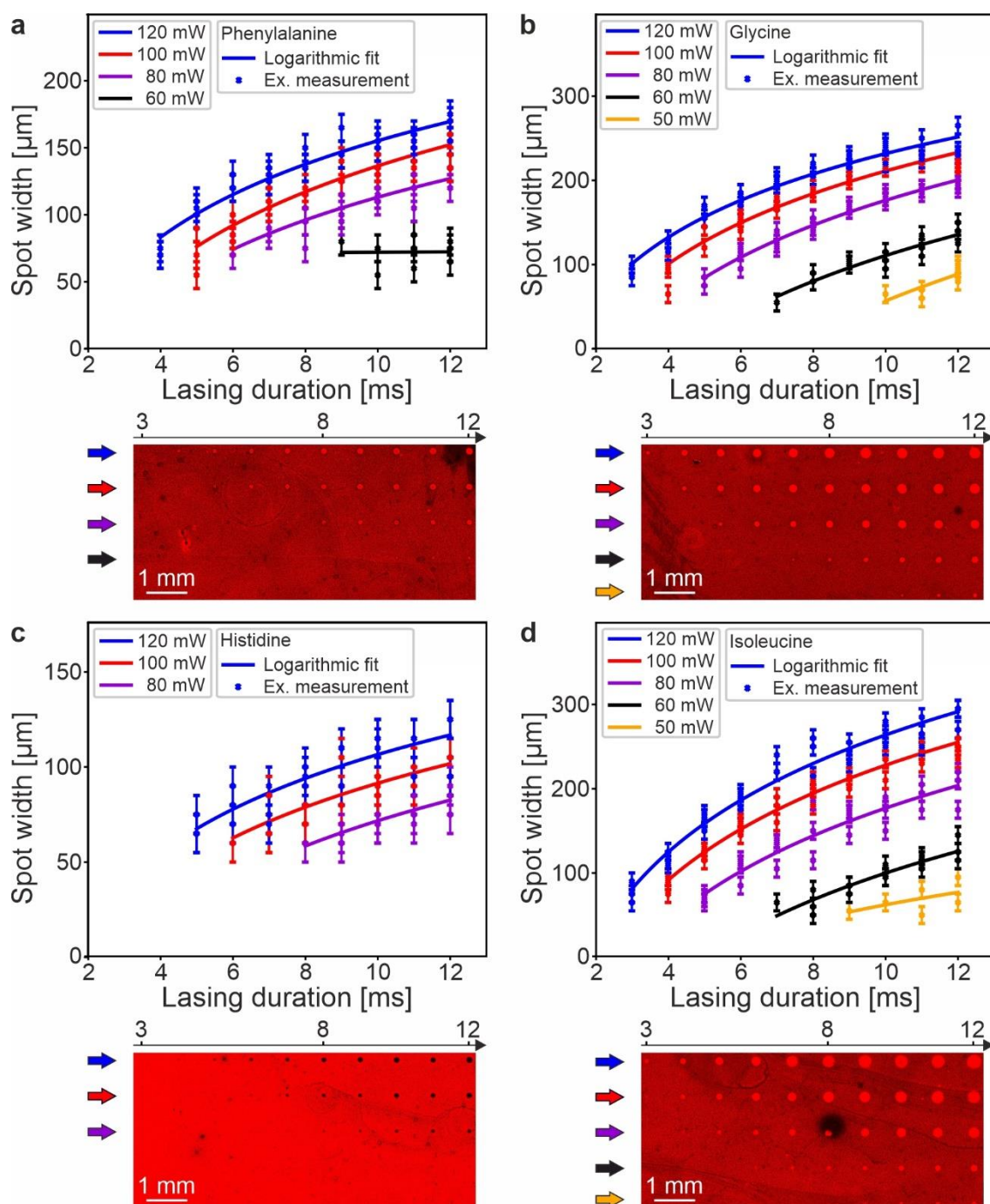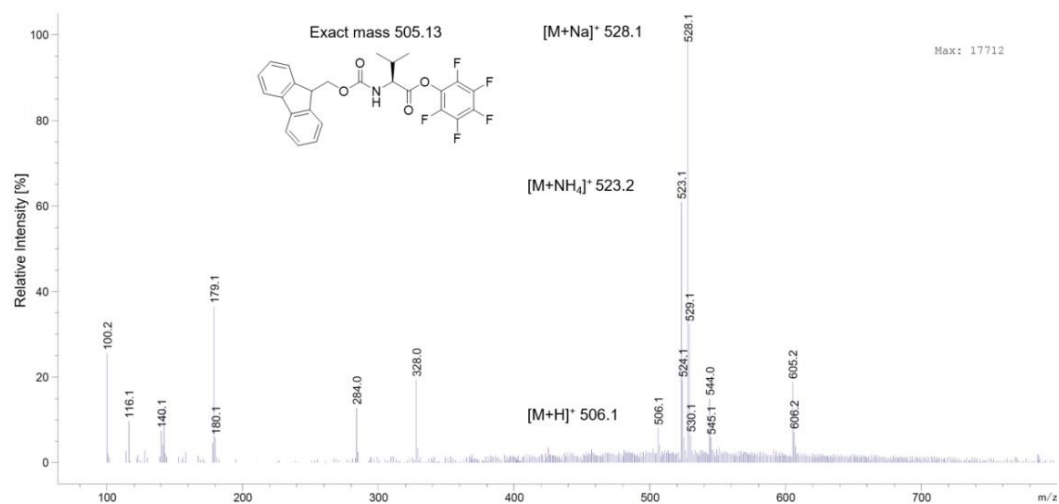
Figure S12. Parameter variation mapping of phenylalanine (**a**), glycine (**b**), histidine (**c**), and isoleucine (**d**) from 50 – 120 mW lasing power and 3 – 12 ms lasing duration. The spot widths follow a logarithmic growth with increasing lasing intensity and duration. Phenylalanine shows a constant spot width for 60 mW lasing power and histidine generally smaller spots. The deviation of spot width is low. For the respective lasing parameters, the data points are presented as measurement value ± measurement error.
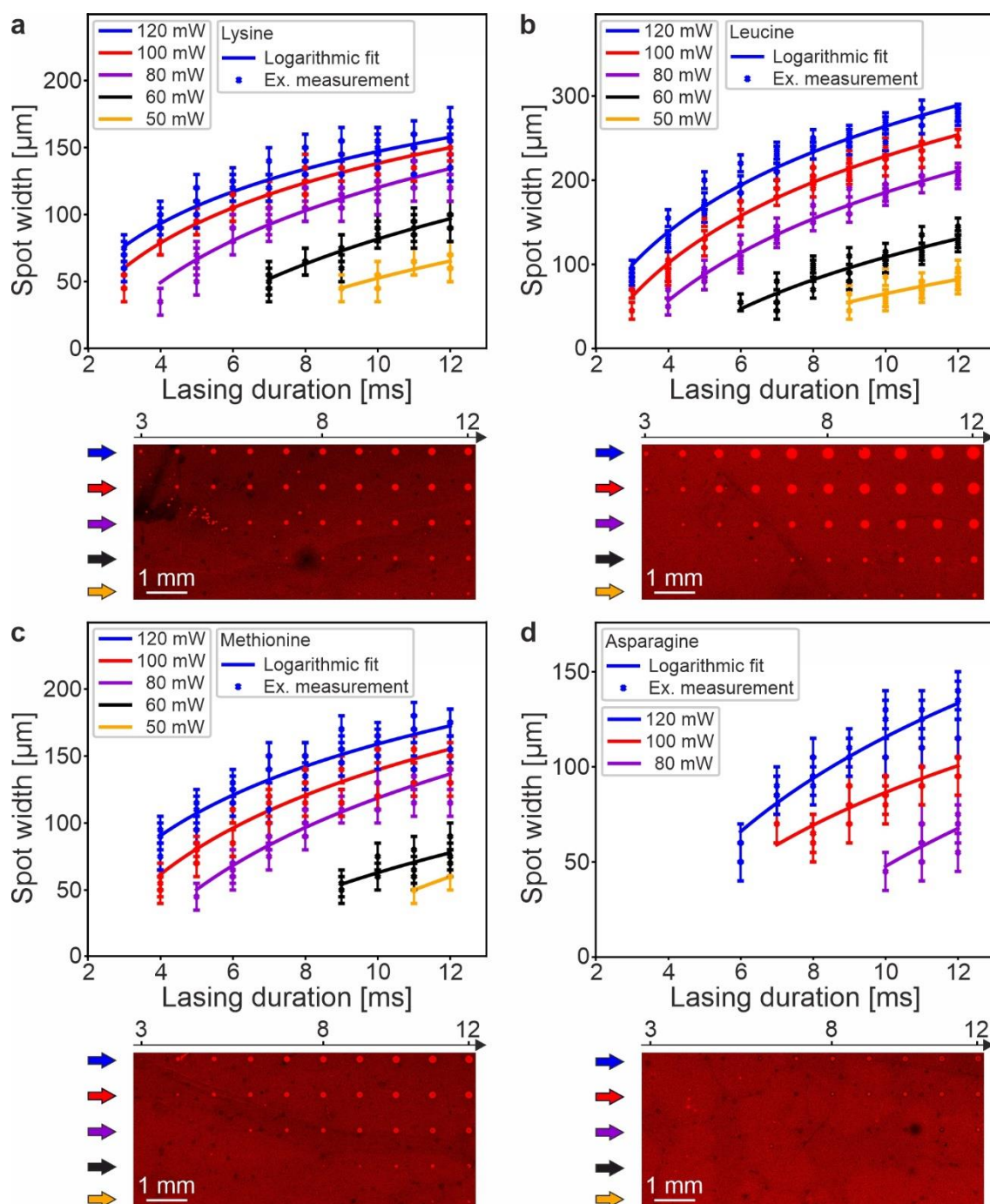
Figure S13. Parameter variation mapping of lysine (**a**), leucine (**b**), methionine (**c**), and asparagine (**d**) from 50 – 120 mW lasing power and 3 – 12 ms lasing duration. The spot widths follow a logarithmic growth with increasing lasing power and duration. All transfers, except for asparagine, which shows an almost linear growth, follow a logarithmic growth with increasing lasing intensity and duration. Methionine shows an increase in spot width deviation above 100 mW lasing power and 9 ms lasing duration. Asparagine shows generally smaller spots. For the respective lasing parameters, the data points are presented as measurement value ± measurement error.
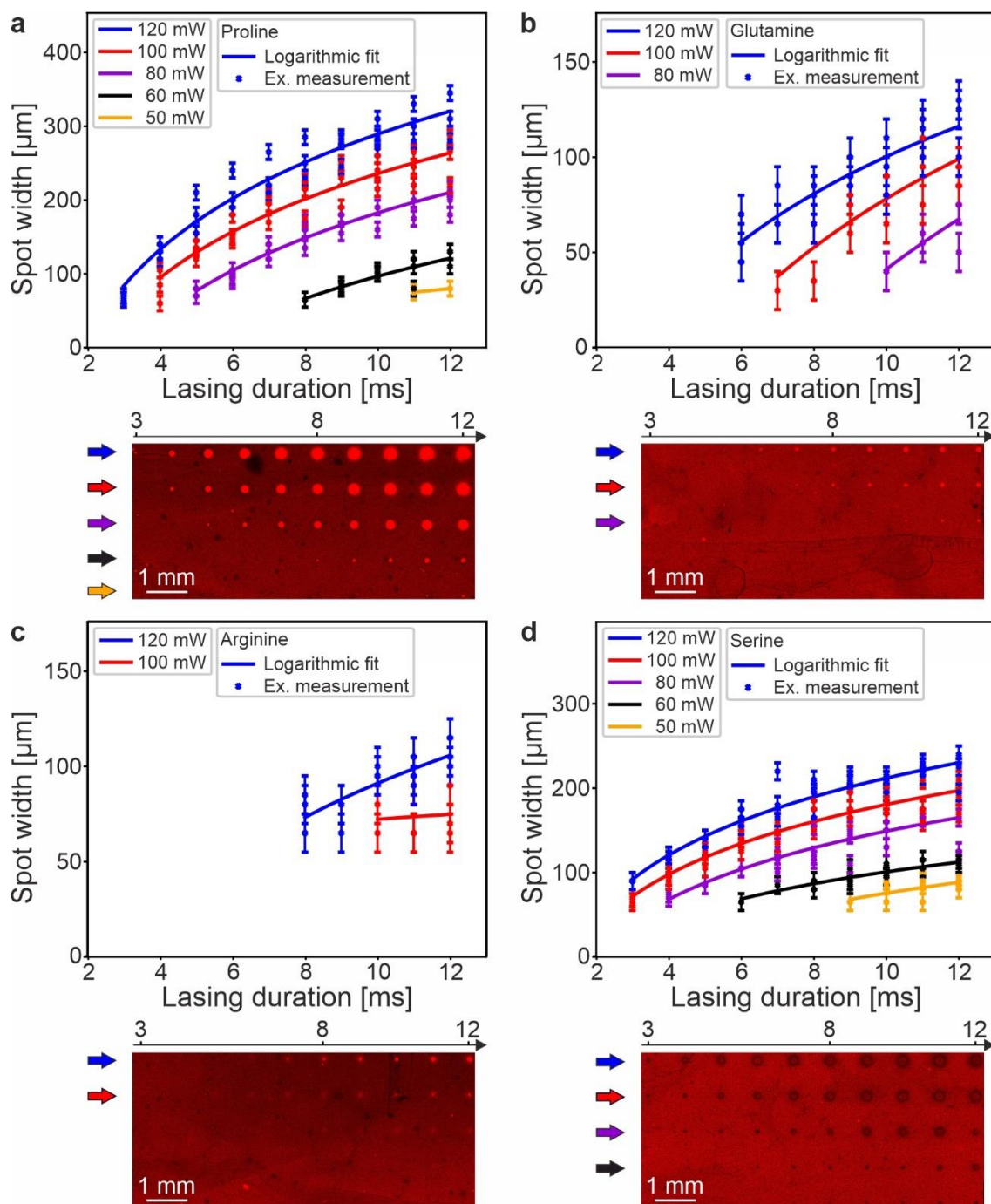
Figure S14. Parameter mapping of proline (**a**), glutamine (**b**), arginine (**c**), and serine (**d**) from 50 – 120 mW lasing power and 3 – 12 ms lasing duration. The spot widths follow a logarithmic growth with increasing lasing power and duration. Arginine shows a constant spot width for 100 mW lasing power. The spot width deviation is low. For the respective lasing parameters, the data points are presented as measurement value ± measurement error.
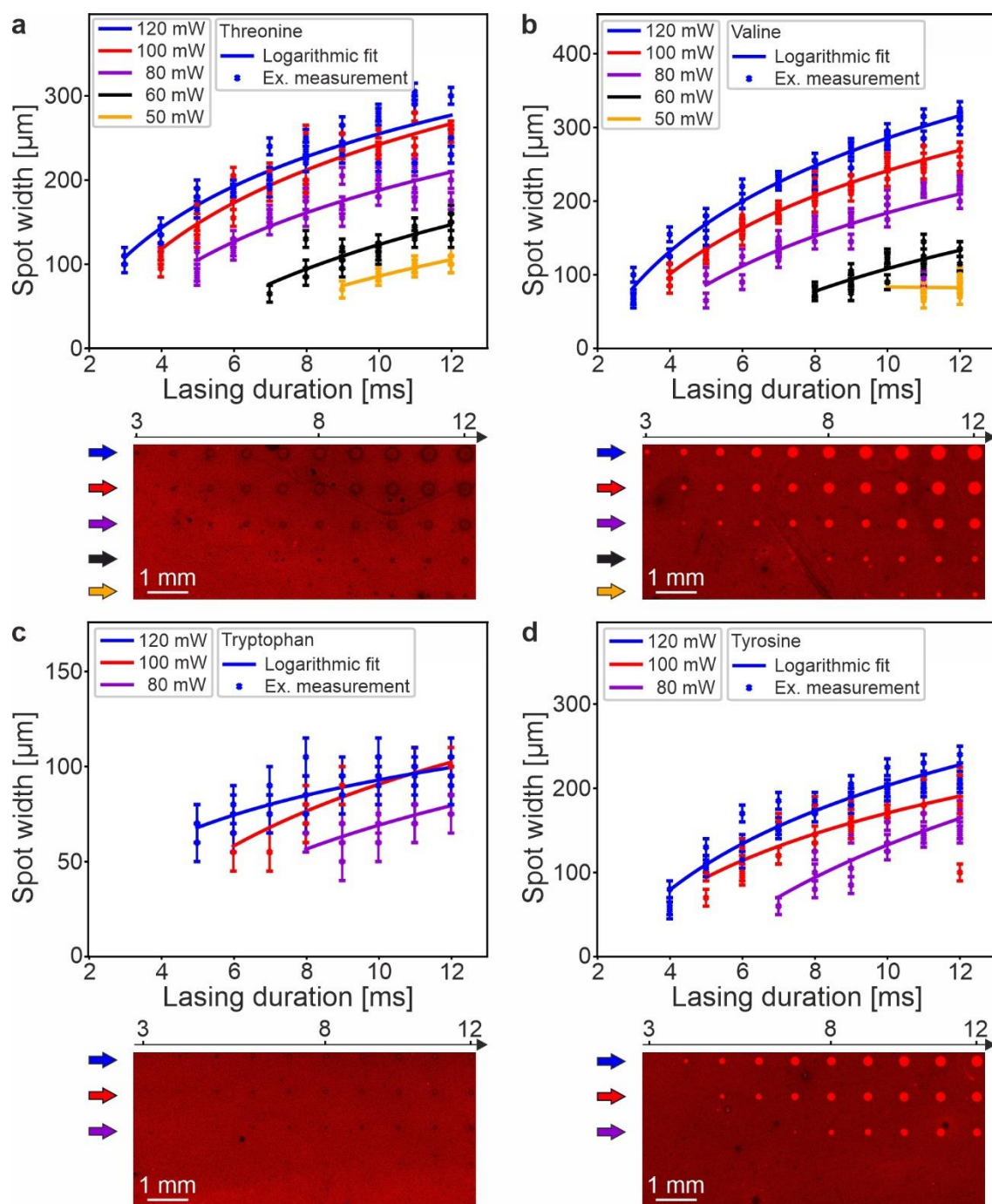
Figure S15. Parameter variation mapping of threonine (**a**), valine (**b**), tryptophan (**c**), and tyrosine (**d**) from 50 – 120 mW lasing power and 3 – 12 ms lasing duration. The spot widths follow a logarithmic growth with increasing lasing power and duration. Threonine shows logarithmic growth in lasing power and lasing duration with low deviation of spot width, except for the parameter sets above 120 mW lasing power and 10 ms lasing duration. For the respective lasing parameters, the data points are presented as measurement value ± measurement error.
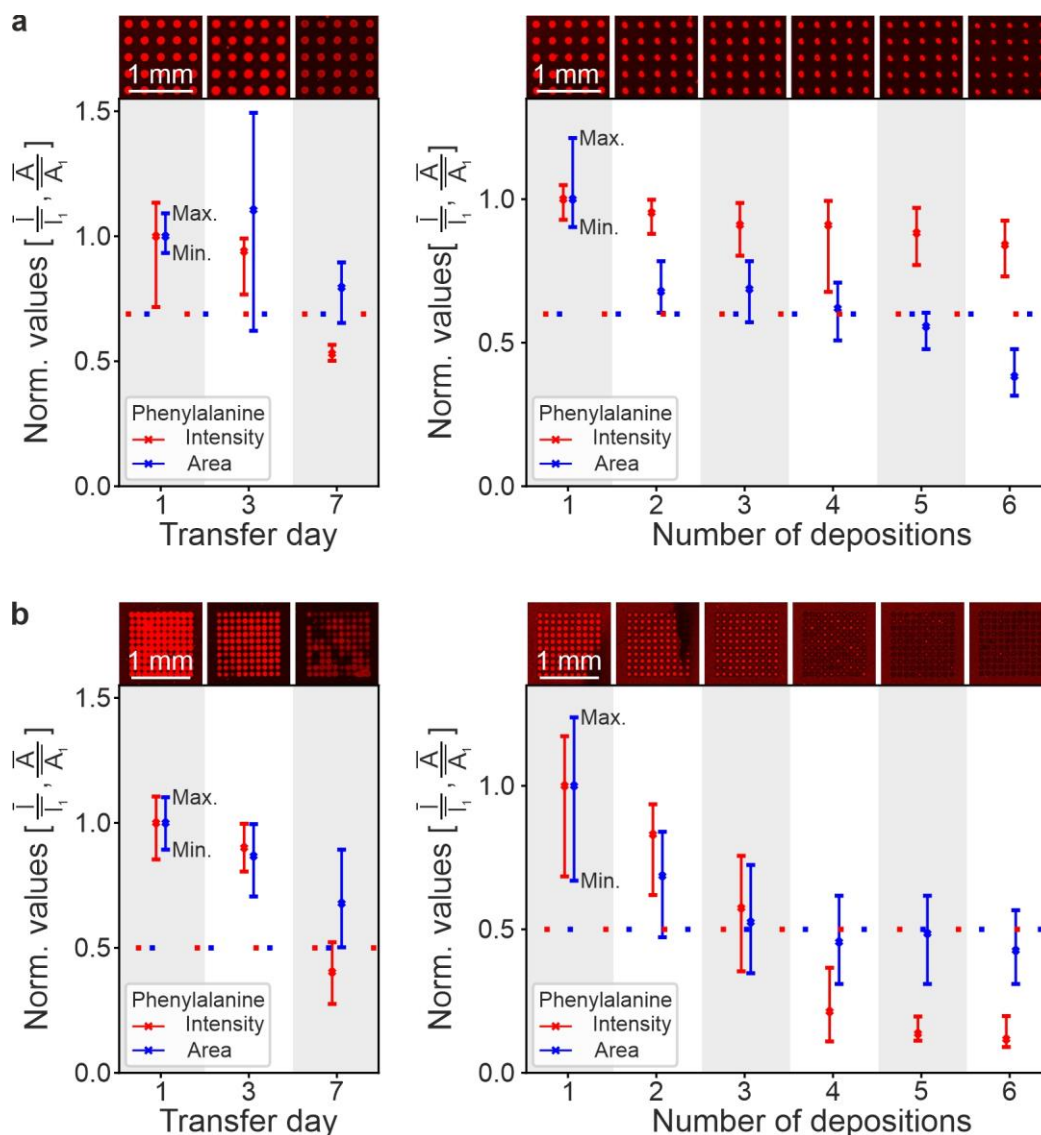
Figure S16. Investigation of stored and repeatedly used donor slides. Representatively, the fluorescence intensity decrease of phenylalanine over seven days and six depositions for a spot density of 1600 spots/cm^2 (**a**) and 10000 spots/cm^2 (**b**) is shown. Empirical thresholds (60 % and 50 % of the average measurement) were set for the fluorescence intensity and spot area. Intensity (I) and area (A) measurements are normalized against the transfer of day one or the initial material deposition and presented as mean with min/max value boundaries, n = (16, **a** left), (25, **a** right), (20, **b** left), and (16, **b** right).

Figure S17. RP-HPLC-MS of 5 µg Fmoc-Val-OPfp (reference).

New Donor Fmoc-Val-OPfp: RP-HPLC of Fmoc-Val-OPfp t_R 15.1 min, 280 nm, Method A
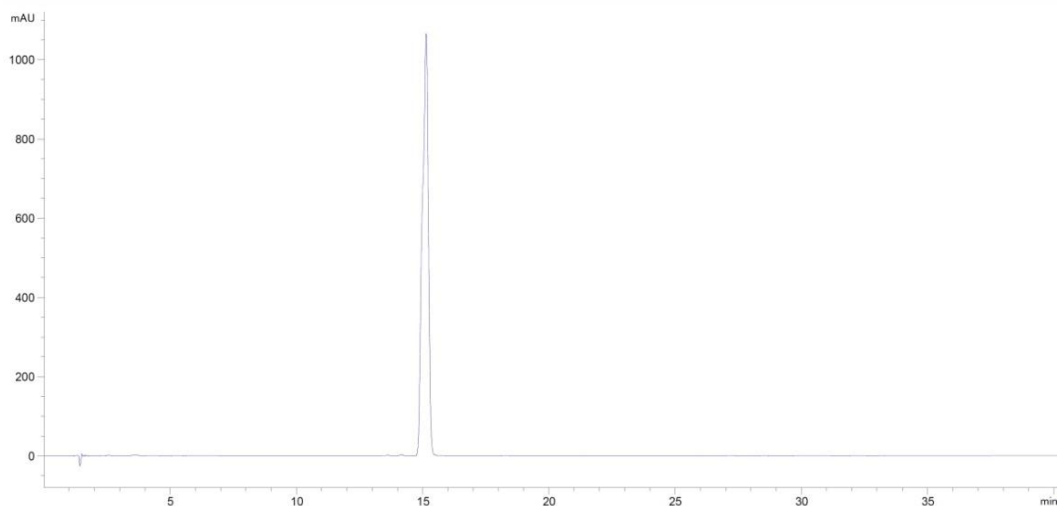
New Donor Fmoc-Val-OPfp: Positive mode ion mass spectrometry of Fmoc-Val-OPfp t_R 15.1 min
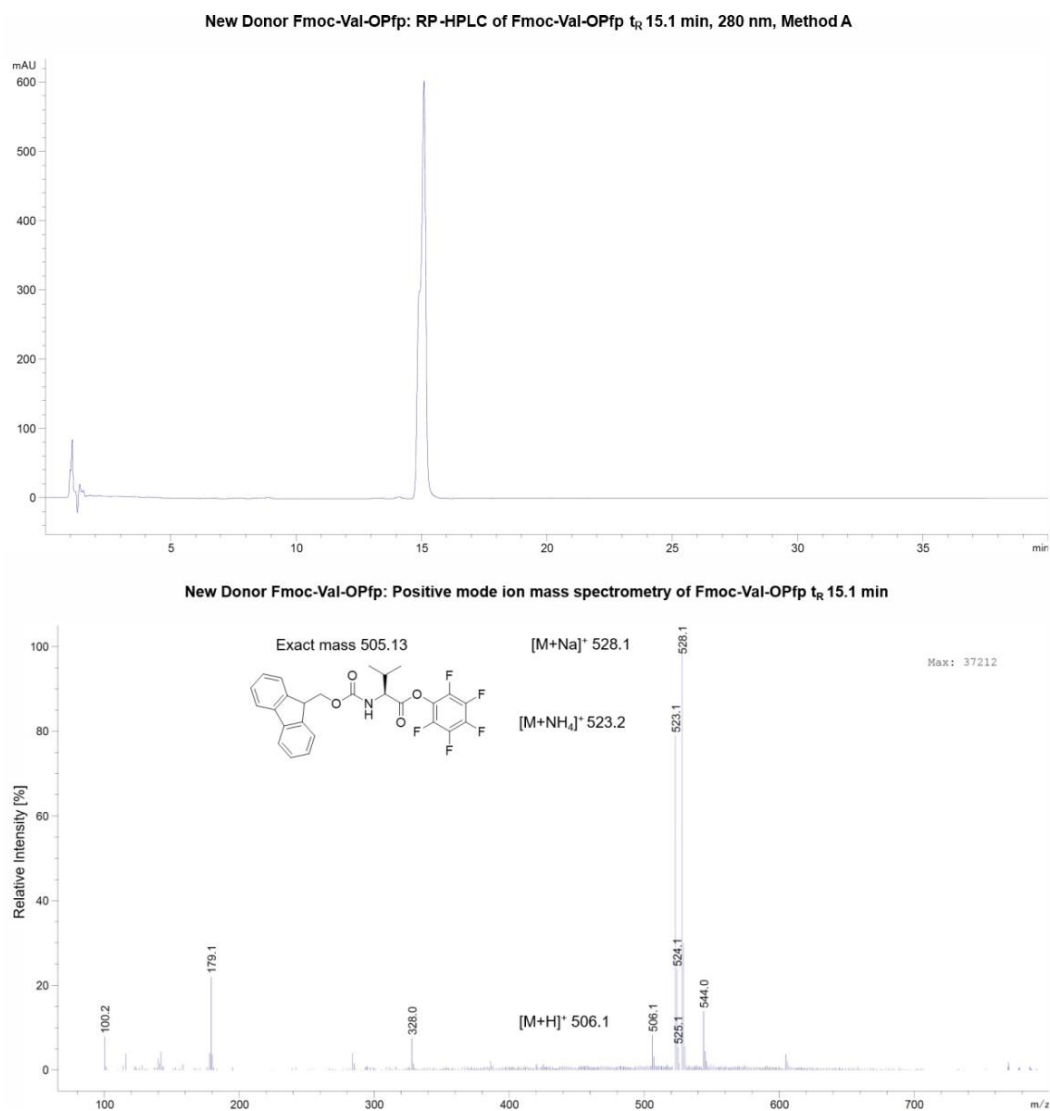
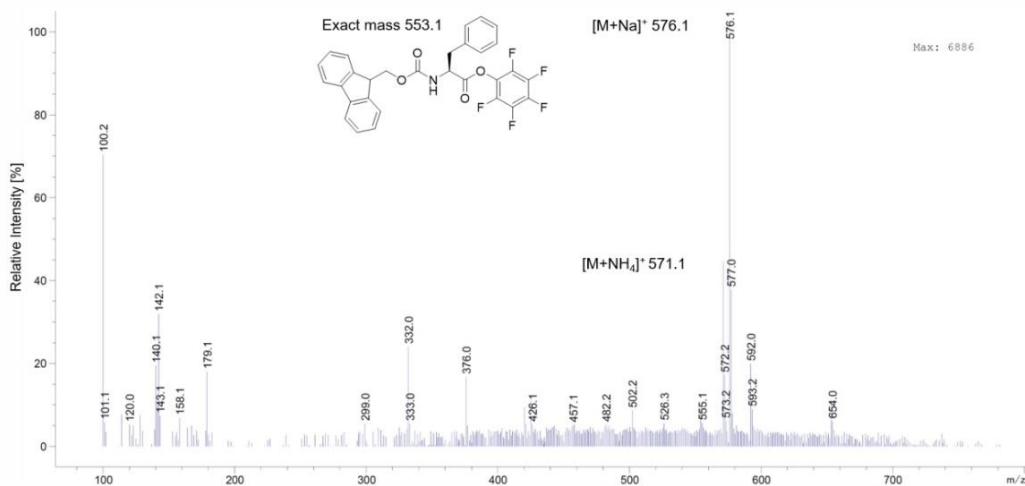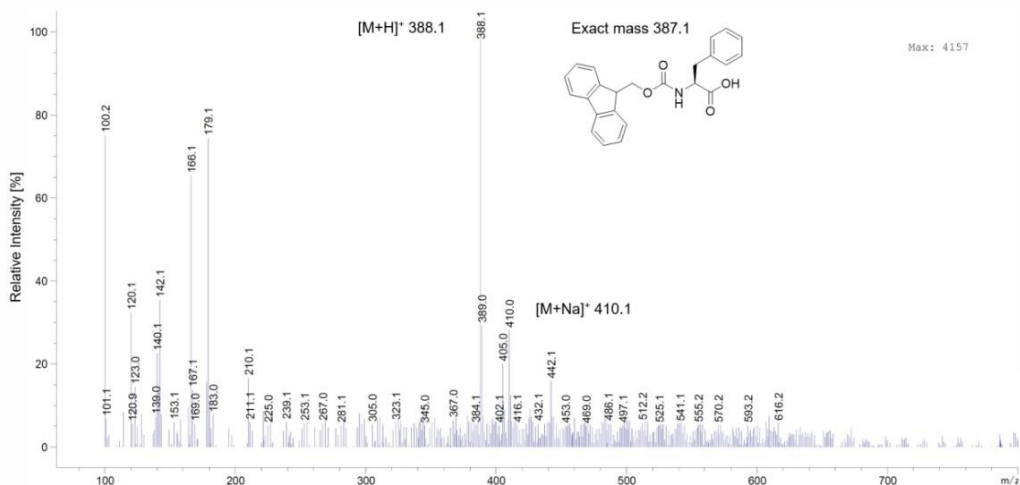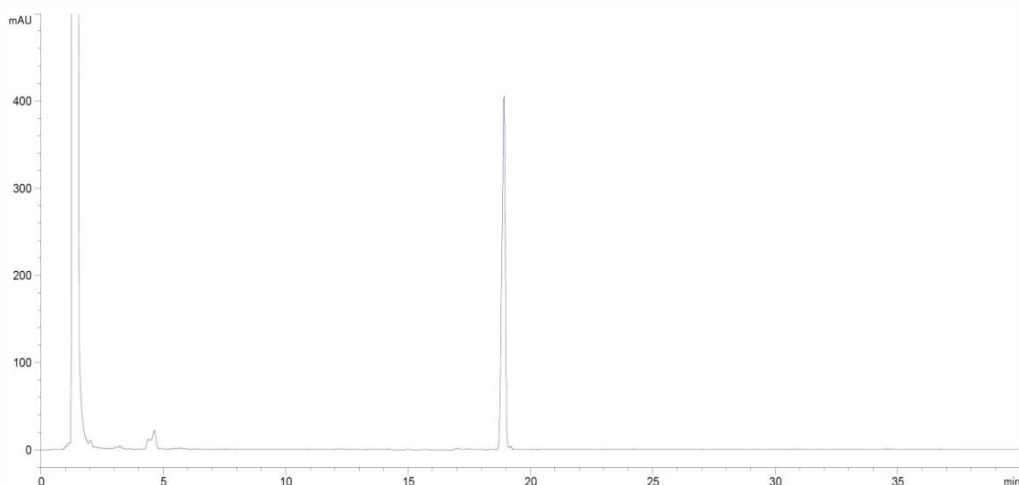**Figure S18.** RP-HPLC-MS of Fmoc-Val-OPfp after laser-assisted transfer from new donor slides.

Reused Donor Fmoc-Val-OPfp: RP-HPLC of Fmoc-Val-OPfp t_R 15.7 min and Fmoc-Val-OH t_R 3.1 min, 280 nm, Method A
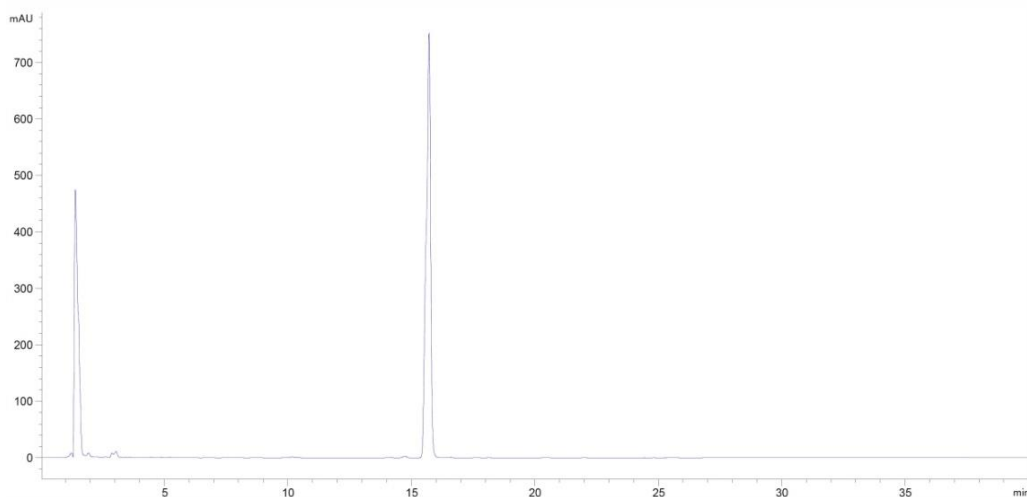
Reused Donor Fmoc-Val-OPfp: Positive mode ion mass spectrometry of Fmoc-Val-OPfp t_R 15.7 min
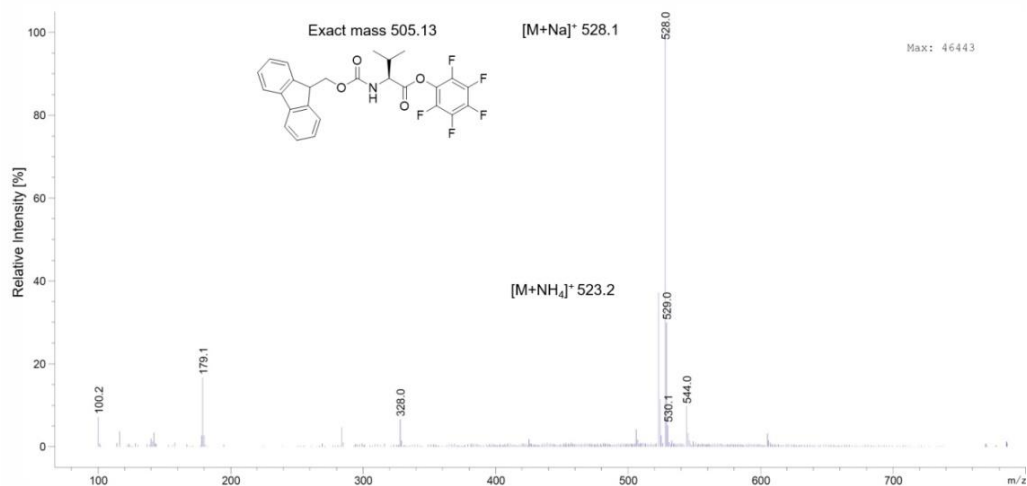
Reused Donor Fmoc-Val-OPfp: Positive mode ion mass spectrometry of Fmoc-Val-OH t_R 3.1 min
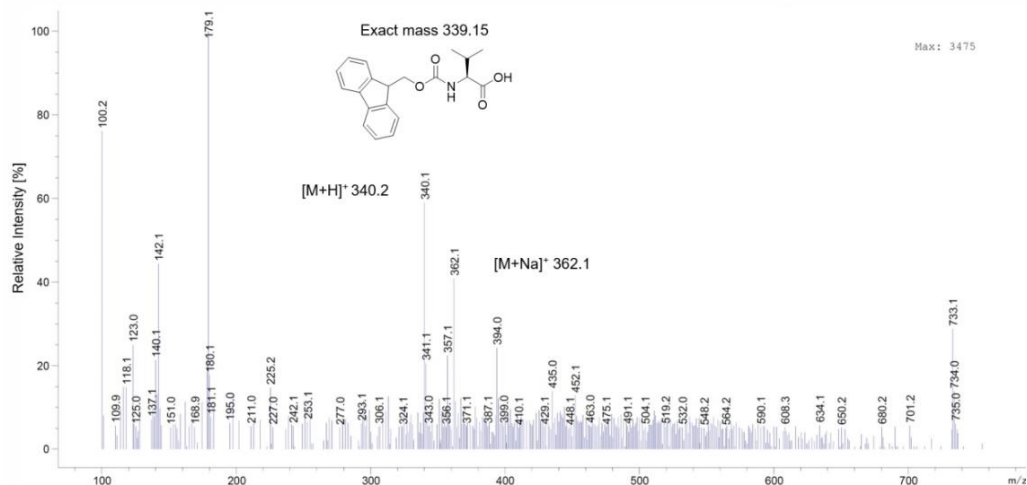
Figure S19. RP-HPLC-MS of Fmoc-Val-OPfp after laser-assisted transfer from reused donor slides.

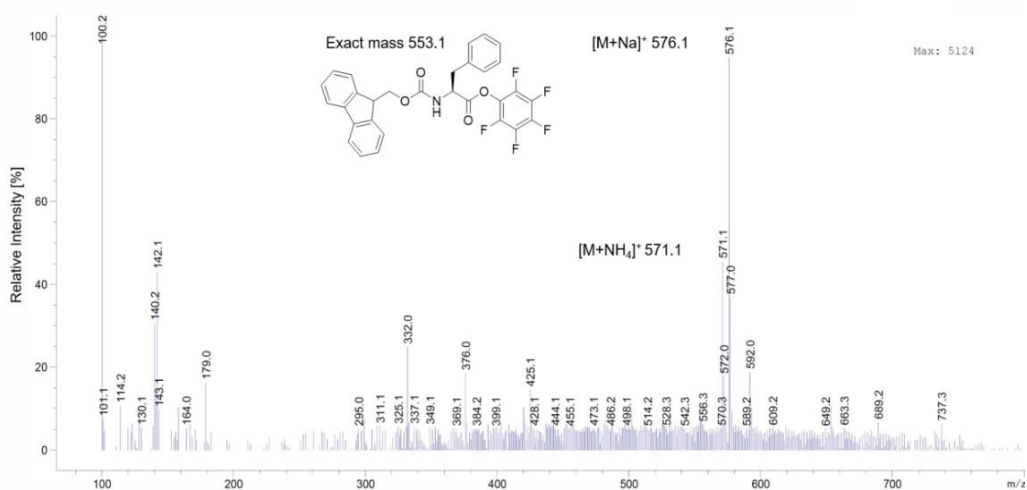**Figure S20.** RP-HPLC-MS of 5 µg Fmoc-Phe-OPfp (reference).

Figure S21. RP-HPLC-MS of Fmoc-Phe-OPfp after laser-assisted transfer from new donor slides.

Reused Donor Fmoc-Phe-OPfp: RP-HPLC of Fmoc-Phe-OPfp t_R 18.9 min and Fmoc-Phe-OH t_R 4.6 min, 280 nm, Method A
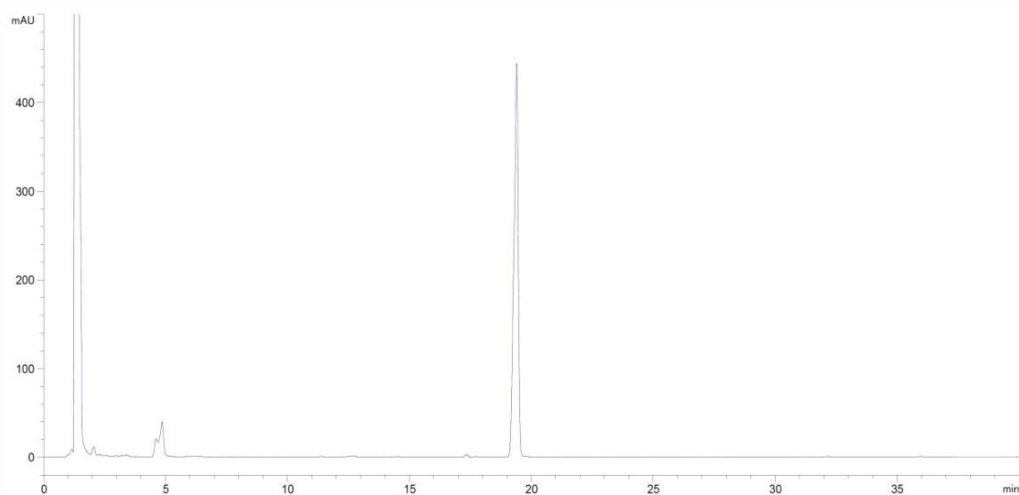
Reused Donor Fmoc-Phe-OPfp: Positive mode ion mass spectrometry of Fmoc-Phe-OPfp t_R 18.9 min

Reused Donor Fmoc-Phe-OPfp: Positive mode ion mass spectrometry of Fmoc-Phe-OH t_R 4.6 min
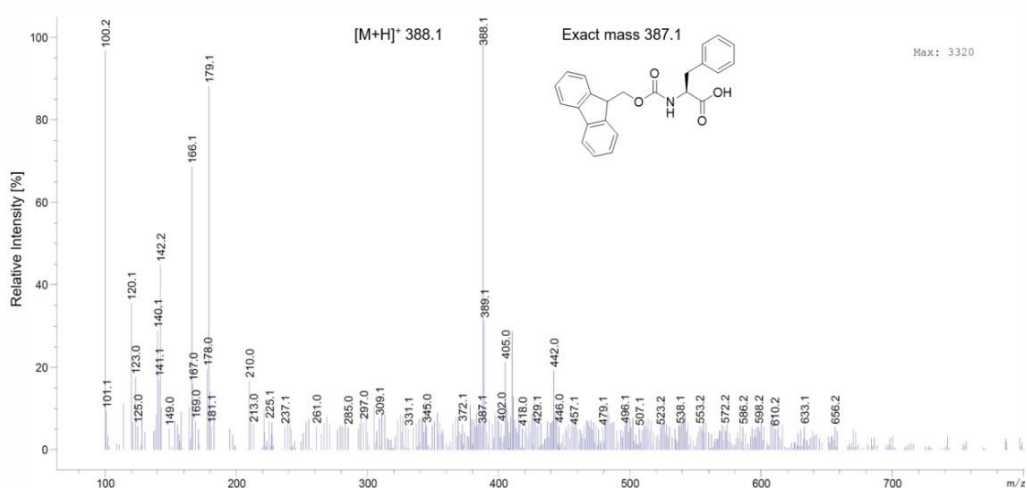

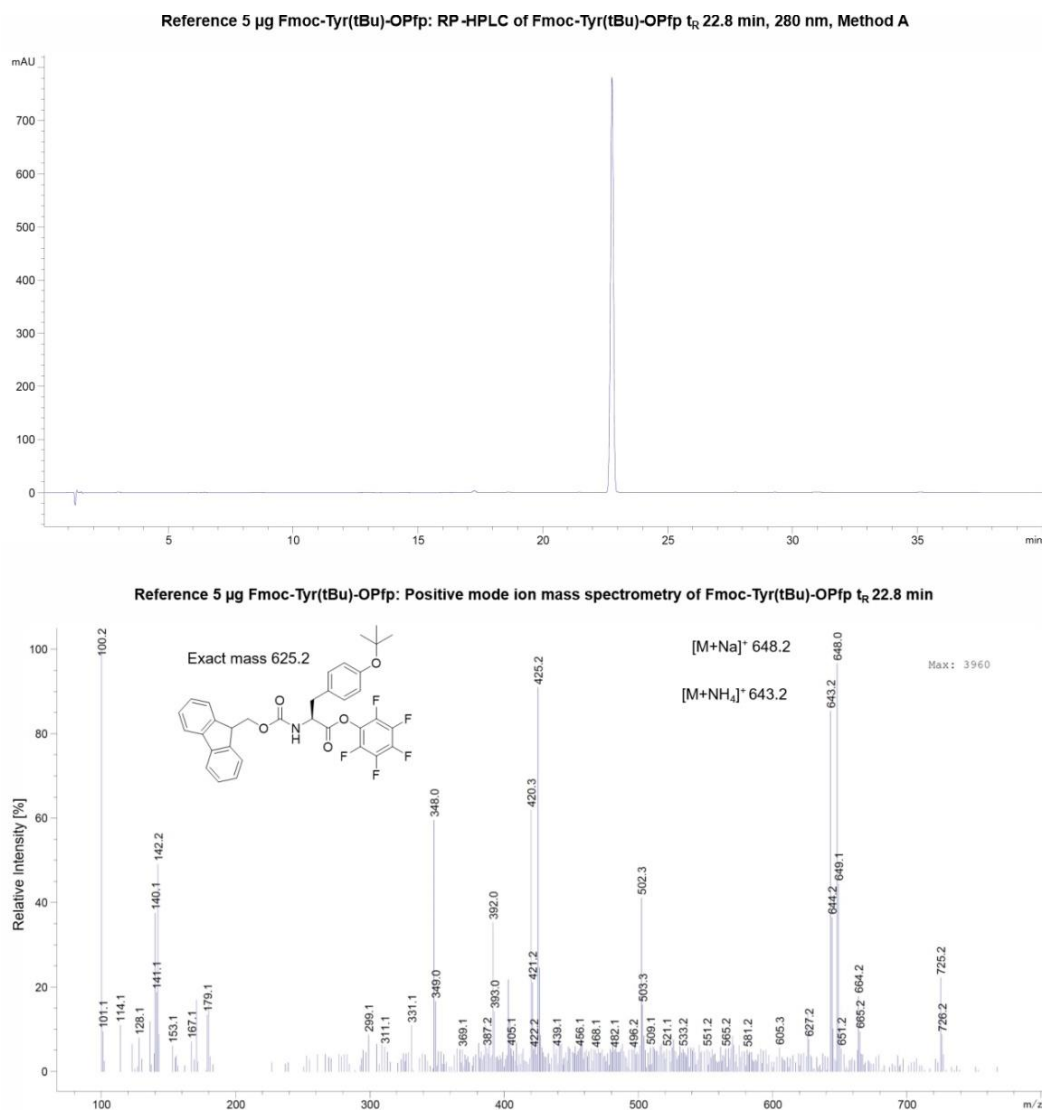**Figure S22.** RP-HPLC-MS of Fmoc-Phe-OPfp after laser-assisted transfer from reused donor slides.

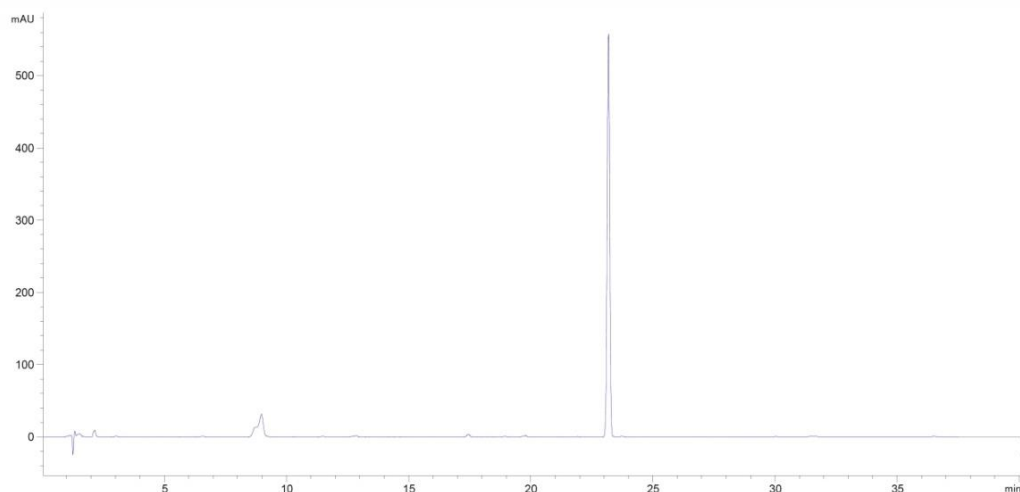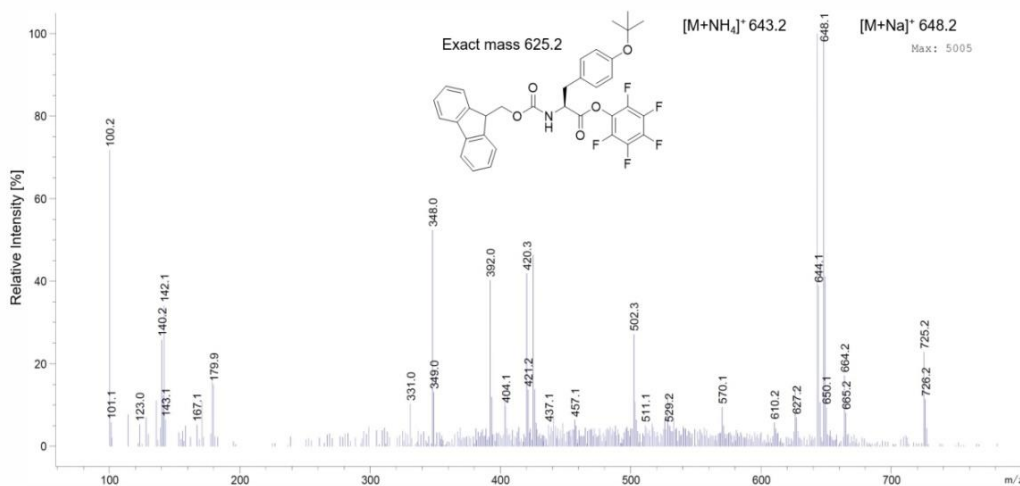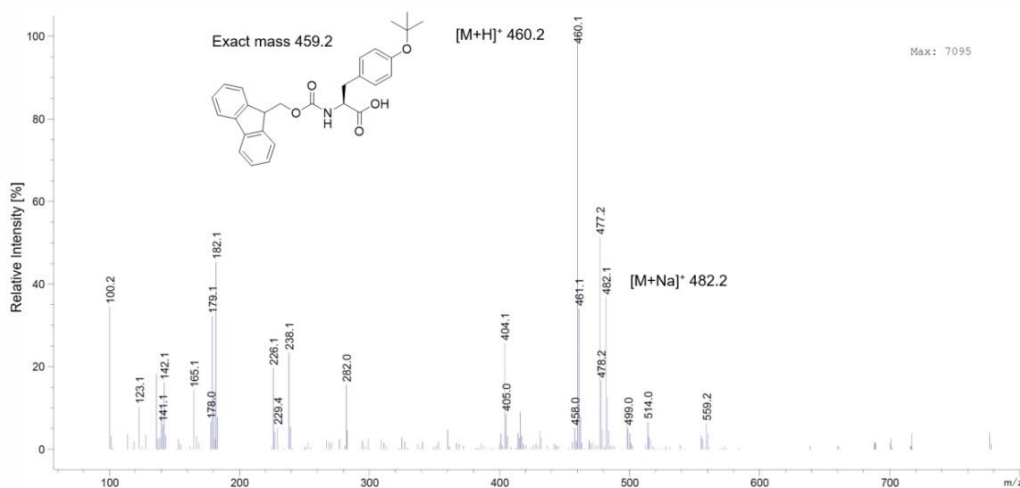**Figure S23.** RP-HPLC-MS of 5 µg Fmoc-Try(tBu)-OPfp (reference).

Figure S24. RP-HPLC-MS of Fmoc-Try(tBu)-OPfp after laser-assisted transfer from new donor slides.
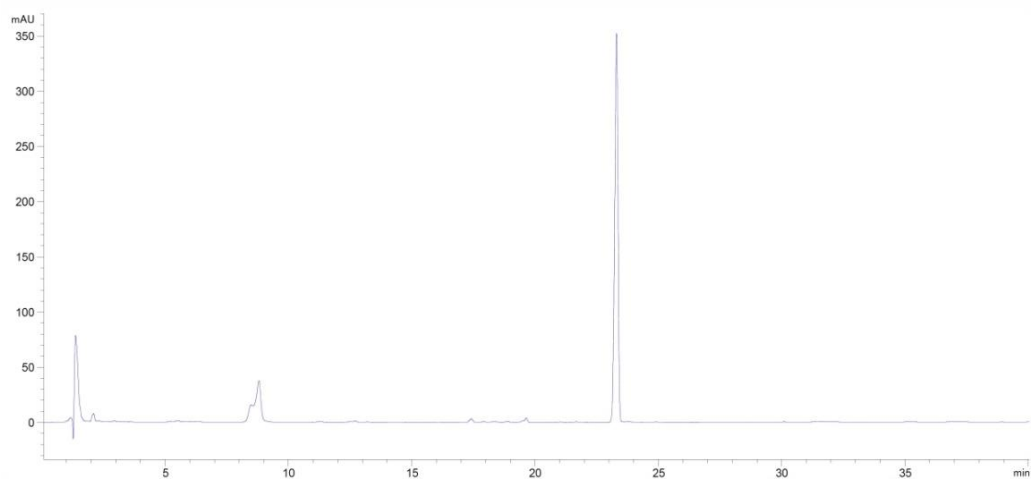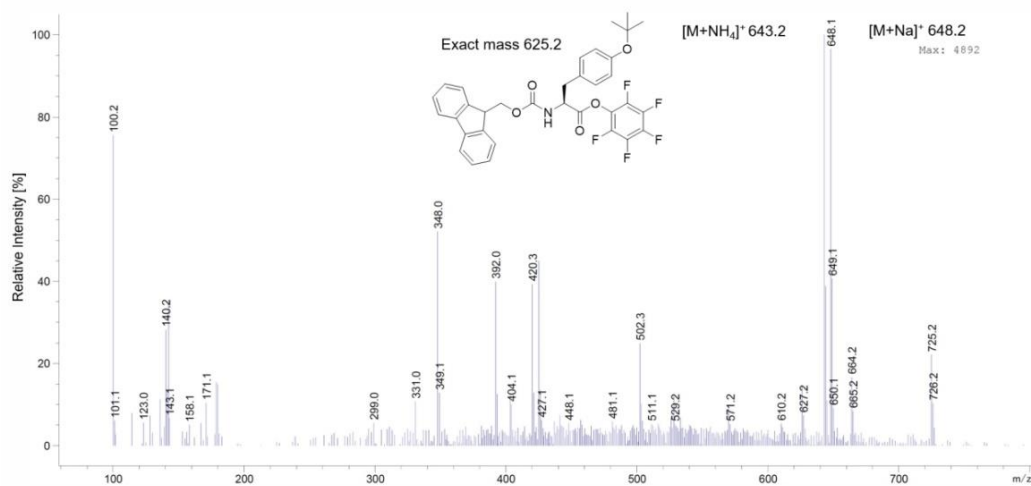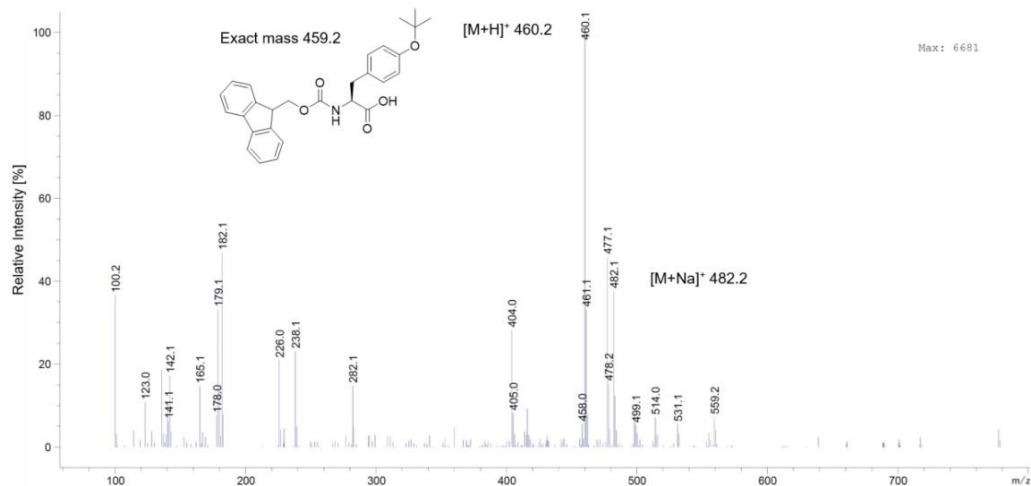
Figure S25. RP-HPLC-MS of Fmoc-Try(tBu)-OPfp after laser-assisted transfer from reused donor slides.

RP-HPLC of SLEC: t_{R1} 1.4 min, t_{R2} 1.9 min, t_{R3} 14.8 min, 280 nm, Method A

RP-HPLC of SLEC: t_{R1} 1.4 min, t_{R2} 1.9 min t_{R3} 10.0 min, t_{R4} 14.8 min, t_{R5} 16.6 min, t_{R6} 18.2 min, t_{R7} 20.6 min, 210 nm, Method A
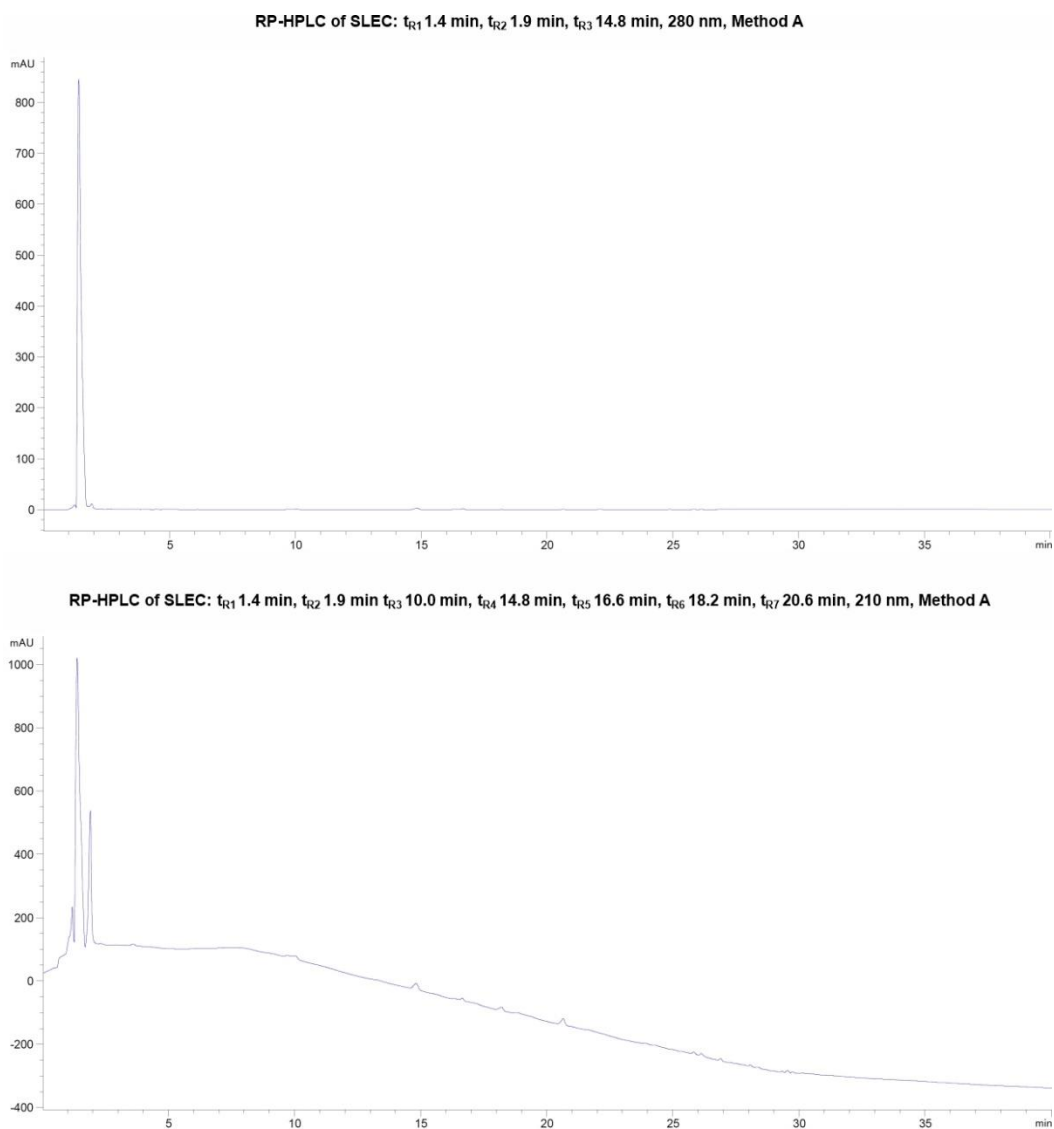
Figure S26. RP-HPLC of SLEC after laser-assisted transfer with detection at 280 nm and 210 nm.
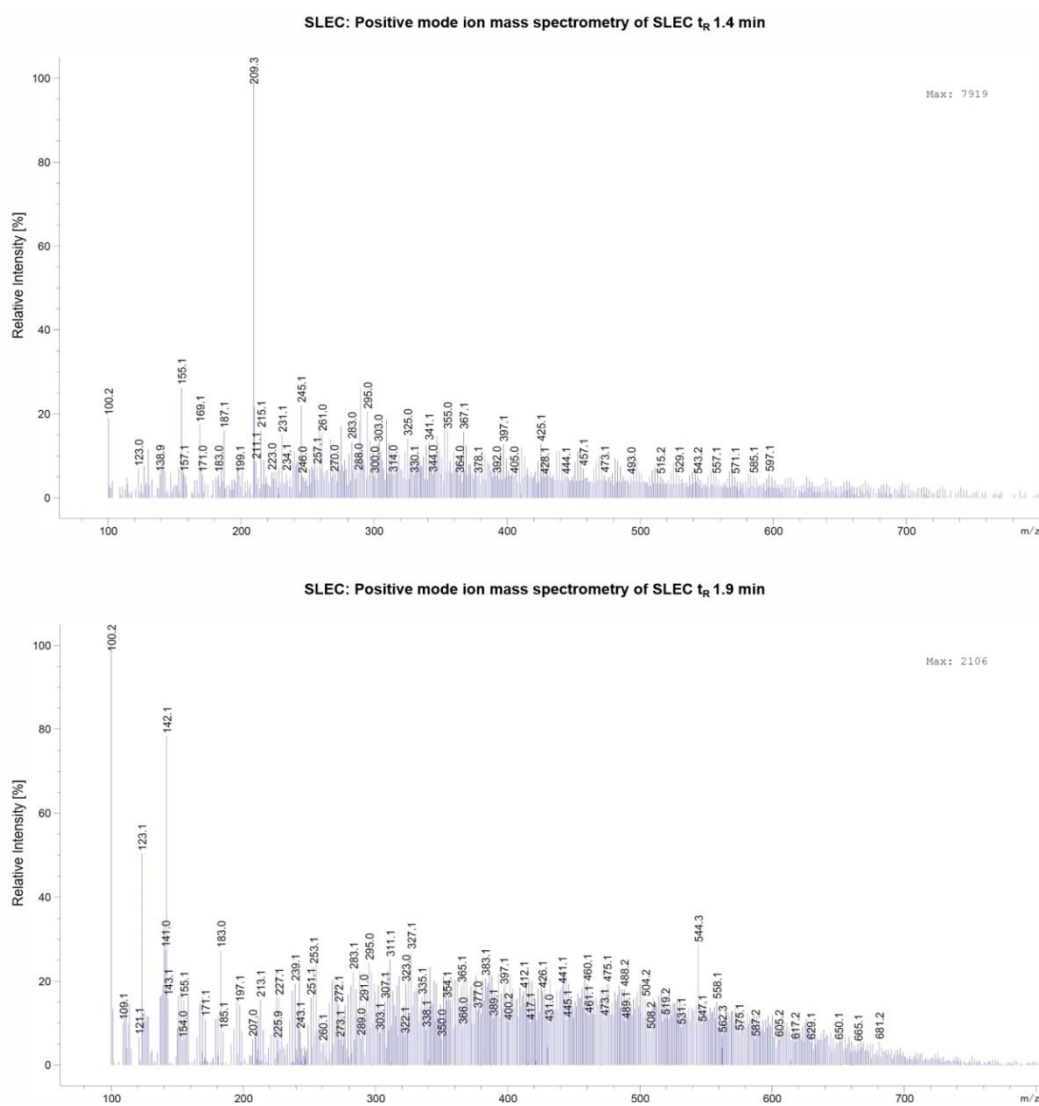
Figure S27. ESI-MS of SLEC after laser-assisted transfer with retention times $t_{R1} = 1.4$ min and $t_{R2} = 1.9$ min.

SLEC: Positive mode ion mass spectrometry of SLEC t_R 10.0 min

SLEC: Positive mode ion mass spectrometry of SLEC t_R 14.8 min
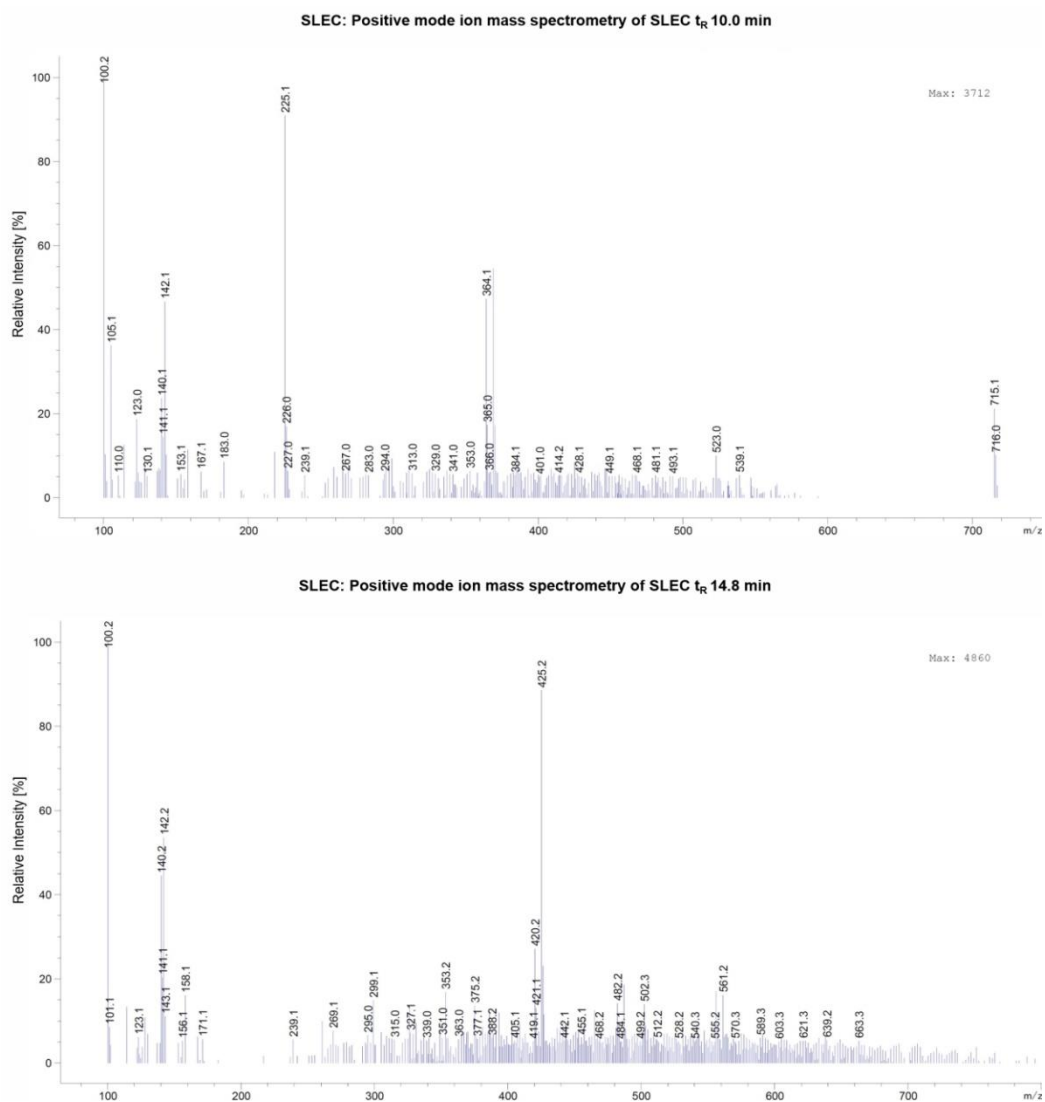
Figure S28. ESI-MS of SLEC after laser-assisted transfer with retention times t_{R1} = 10.0 min and t_{R2} = 14.8 min.
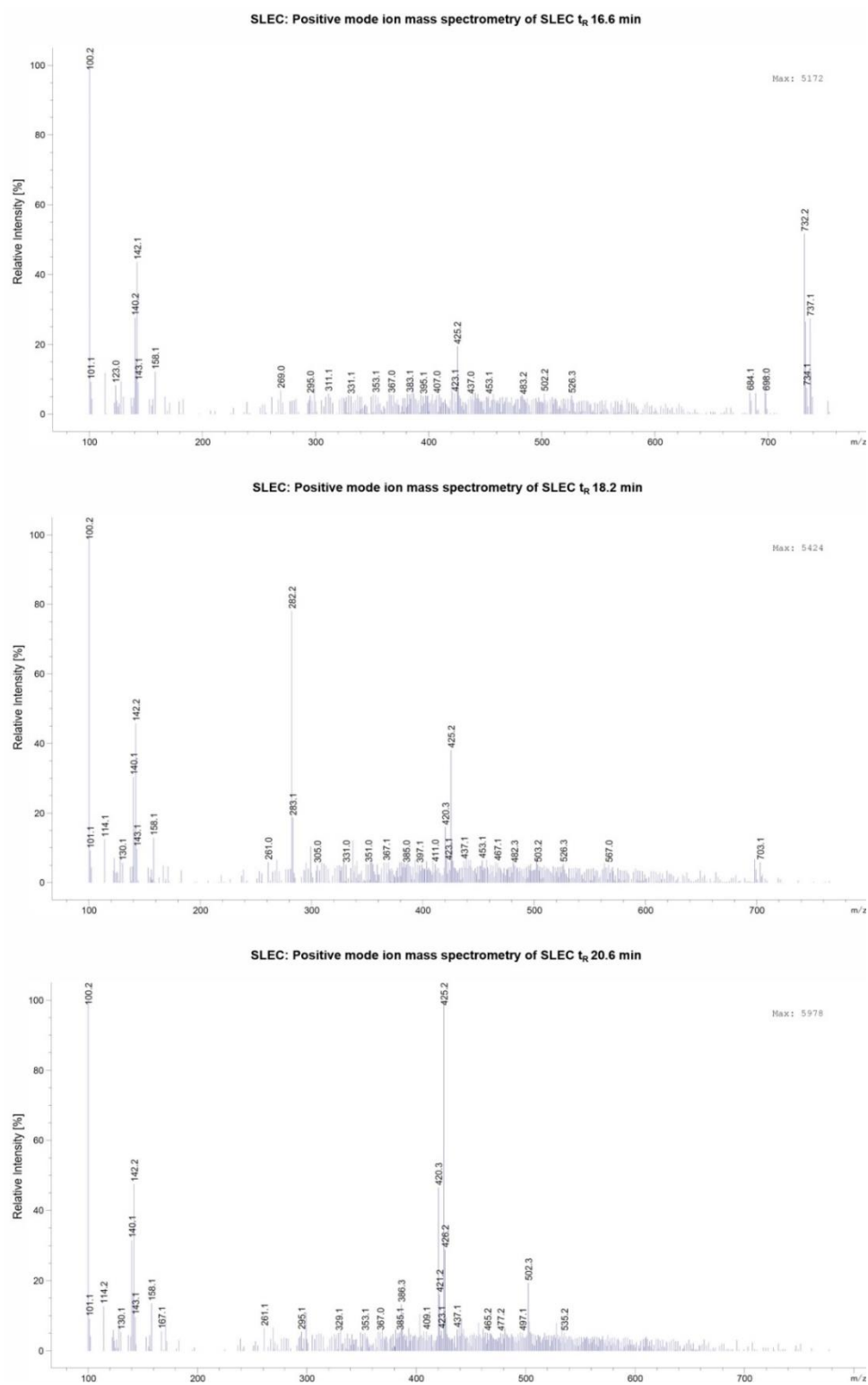
Figure S29. ESI-MS of SLEC after laser-assisted transfer with retention times t_{R1} = 16.6 min, t_{R1} = 18.2 min, and t_{R2} = 20.6 min.

Figure S30. RP-HPLC-MS of Fmoc-Phe-OPfp after five cycles.
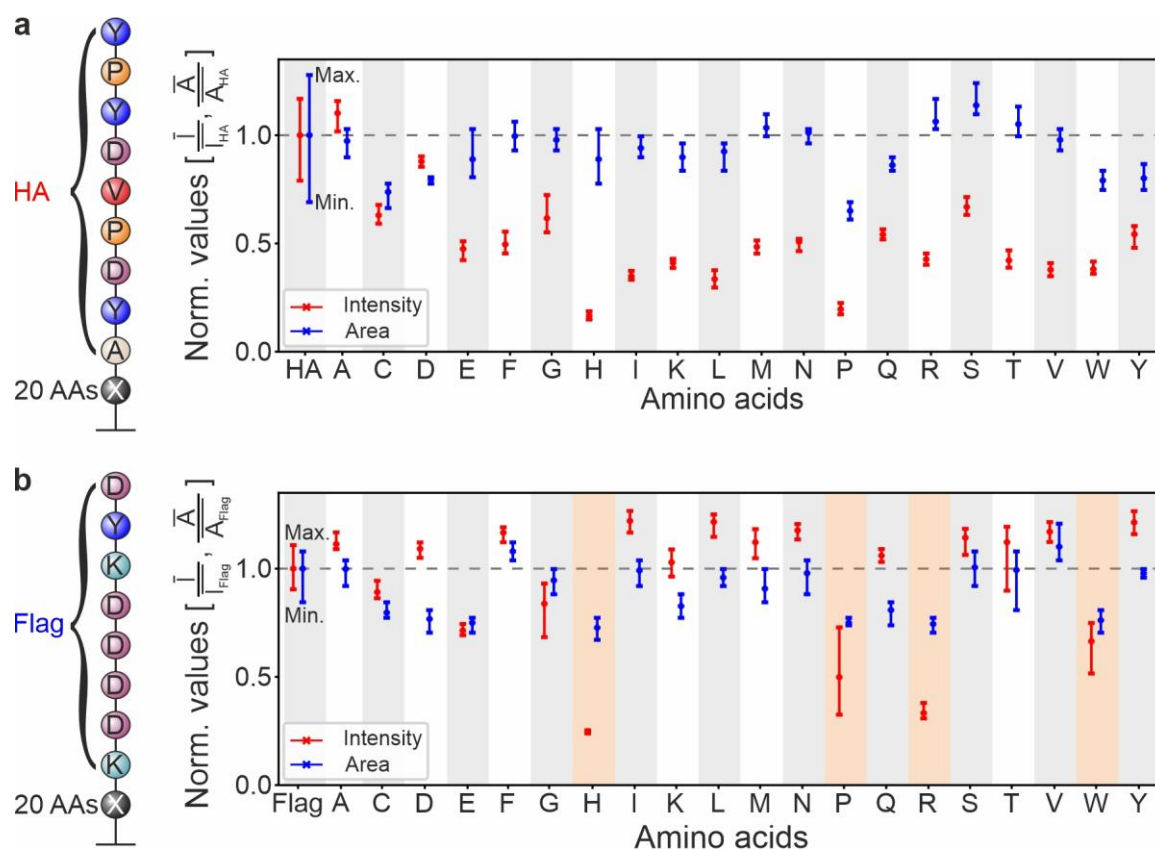
Figure S31. Synthesis of peptides (density of 4444 spots/cm^2) containing the HA and Flag epitope. The synthesis of the HA (**a**) and Flag epitope (**b**) is shown with (X = one of 20 AAs) and without (HA and Flag wild-type) an additional C-terminal layer. The synthesized peptides containing the HA epitope show strongly varying fluorescence intensities and spot sizes. In contrast, peptides containing the Flag epitope only show varying spot sizes, but have stable fluorescence intensities of around 100 % of the wild-type Flag epitope. Due to this property, four potentially low coupling AAs (histidine, proline, arginine, and tryptophan) with a fluorescence intensity below 70 % are identified. Intensity (I) and area (A) measurements are normalized against the values of the wild-type HA or Flag epitope and presented as mean with min/max value boundaries, n = 80 for the wild-type epitopes and n = 6 for all other data.
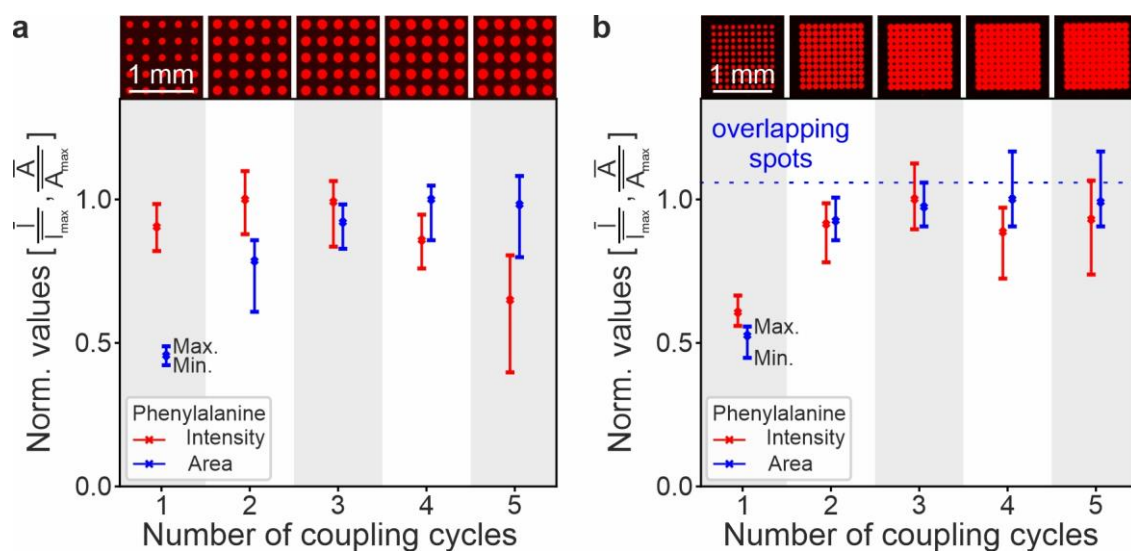
Figure S32. Coupling cycle investigation. The fluorescence intensity increase of phenylalanine with up to five cycles for a spot density of 1600 spots/cm^2 (**a**) and 10000 spots/cm^2 (**b**) is shown. This example highlights the two stop criterions – a converged fluorescence intensity and overlapping spots (spot width above the distance between spot centers). Intensity (I) and area (A) measurements are normalized against the maximum mean value of the experiment. Data presented as mean with min/max value boundaries, n = 25.
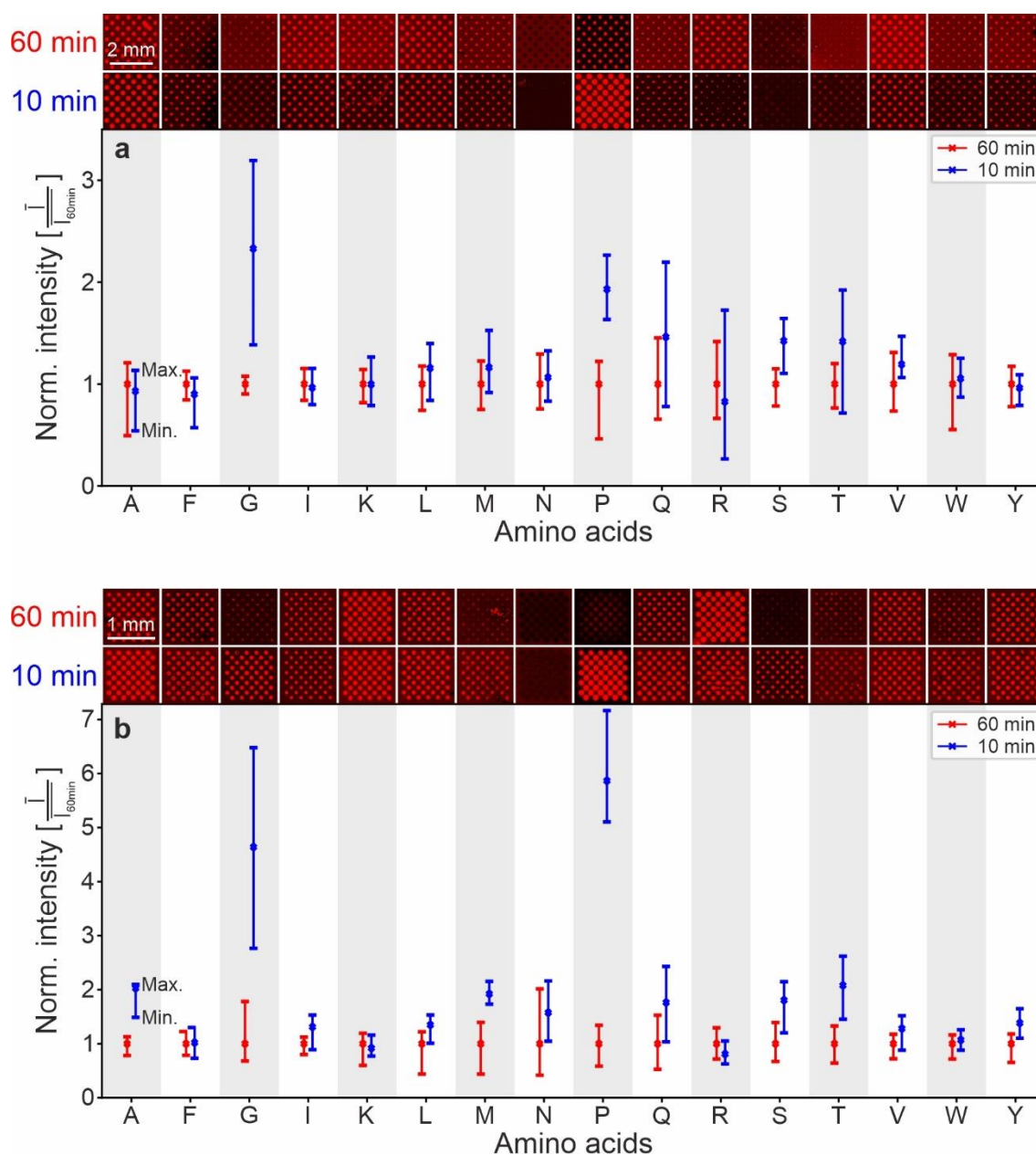
Figure S33. Coupling time investigation. The fluorescence intensity of 16 AAs (possible to label with the standard procedure) with a coupling time of 60 min and 10 min for a spot density of 1600 spots/cm^2 (**a**) and 10000 spots/cm^2 (**b**) is shown. Intensity (I) measurements are normalized against the mean 60 min coupling duration. Data presented as mean with min/max value boundaries, n = 50.
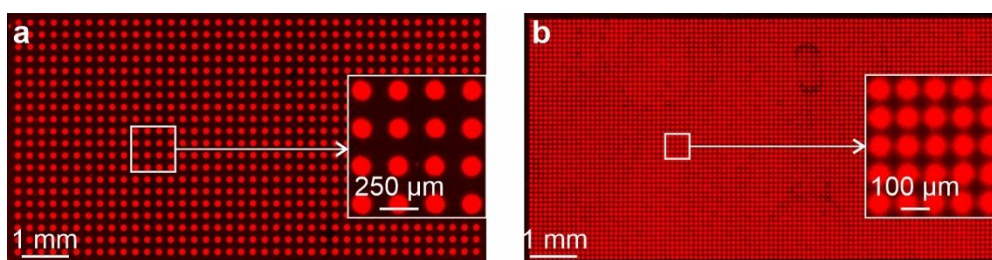
Figure S34. Aspartic acid acceptor slide pre-patterning. The acceptor slide pre-patterning for a spot density of 1600 spots/cm^2 (**a**) and 10000 spots/cm^2 (**b**) is shown (labeled with Biotin and CF633 streptavidin).
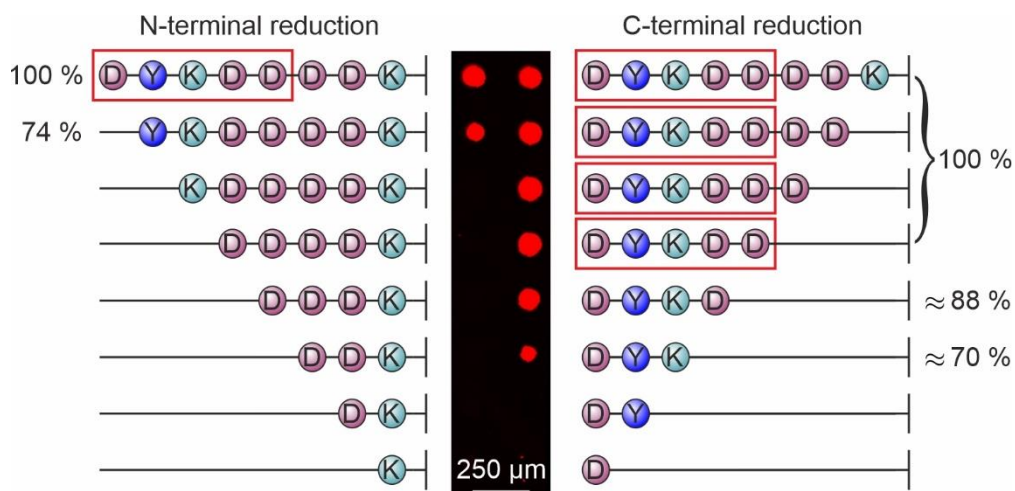
Figure S35. Reduced Flag epitope from N-terminus and C-terminus. The synthesized Flag epitope and its reduction from the N-terminus and C-terminus is shown. Through these peptides the minimal Flag epitope DYKDD was identified, since the reduced sequences YKDD, DYKD, and DYK show a decrease in fluorescence intensity by ≈ 74 %, ≈ 70 %, and ≈ 88 % respectively.
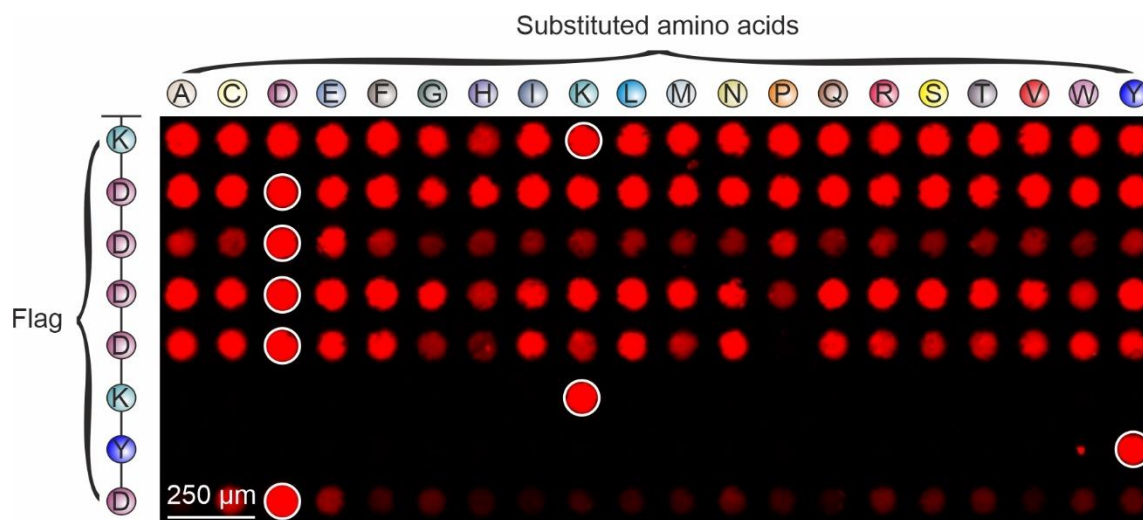
Figure S36. Flag epitope substitution analysis. The encircled spots correspond to the wild-type Flag epitope, which always show a strong fluorescence intensity. All other spot contain exactly one substituted amino acid. Specifically, to investigate the epitope-specific antibody binding, each position within the wild-type Flag epitope was substituted by 20 different amino acids. As previously reported,[2] the tyrosine and lysine in position two and three are required for the binding of Flag antibodies and the aspartic acid in position one and six are highly influential on the binding of Flag antibodies.
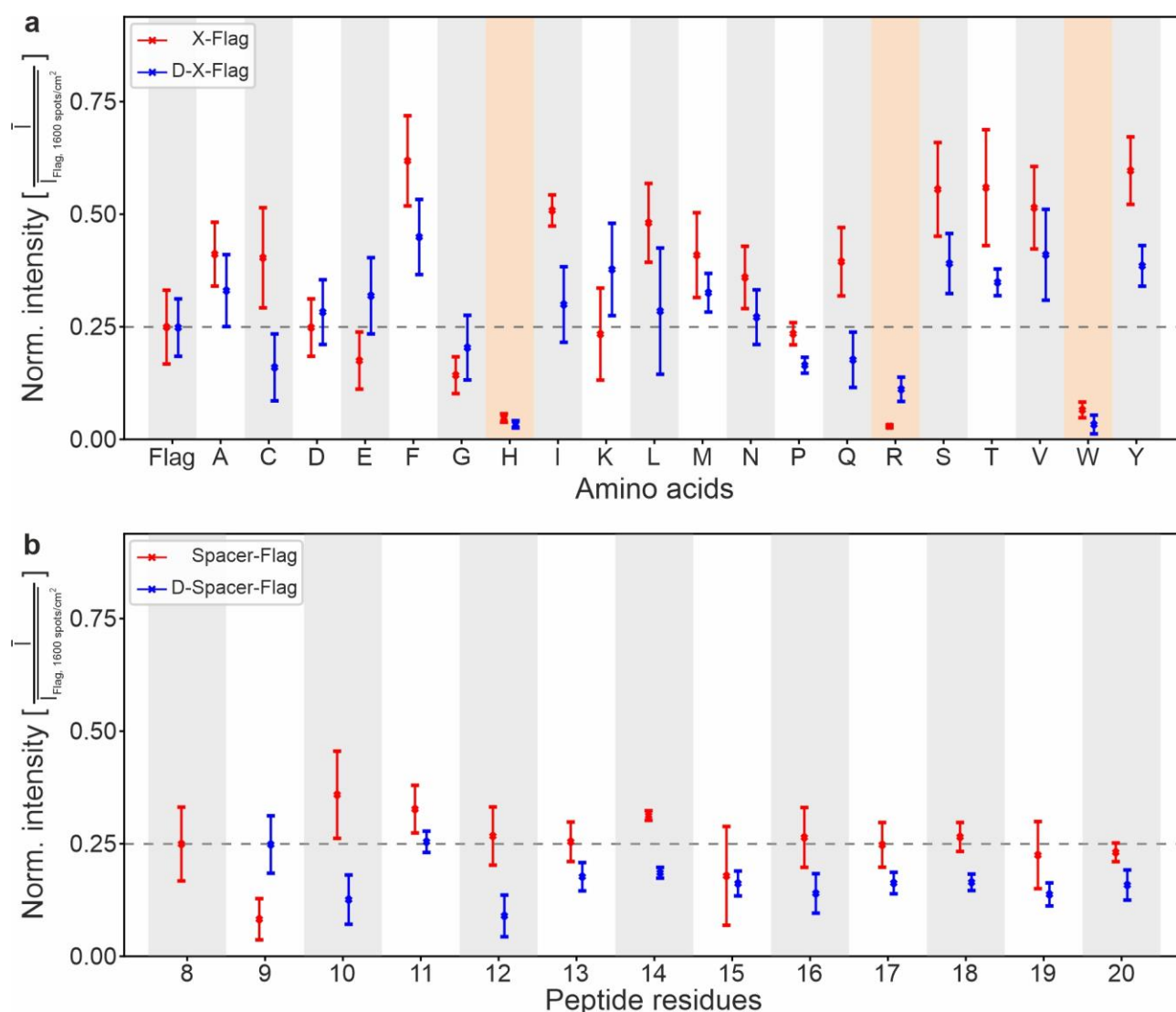
Figure S37. Validation of synthesis yield via antibody binding fluorescence analysis of a peptide microarray (1600 spots/cm²). Peptides were synthesized without and with aspartic acid pre-patterning. (**a**) Intensities of the synthesized Flag peptides with an additional C-terminal AA of the 20 AAs. Histidine, arginine, and tryptophan show low binding, which is improved by aspartic acid pre-patterning. (**b**) Flag peptides synthesized with a C-terminally growing glycine-serine spacer, resulting in up to 20-residue peptides. The negative controls (i.e., copies of all synthesized peptides with an additional C-terminal polymer spot without any AA) are $\approx 2\%$ of the wild-type Flag epitope (1600 spots/cm² microarrays synthesis). Fluorescence intensities are normalized against the wild-type Flag epitope ($I_{Flag, 1600\ spost/cm²}$) of the 1600 spots/cm² microarray synthesis (main manuscript **Figure 4**) and presented as mean $\pm$ SD, n = 3.
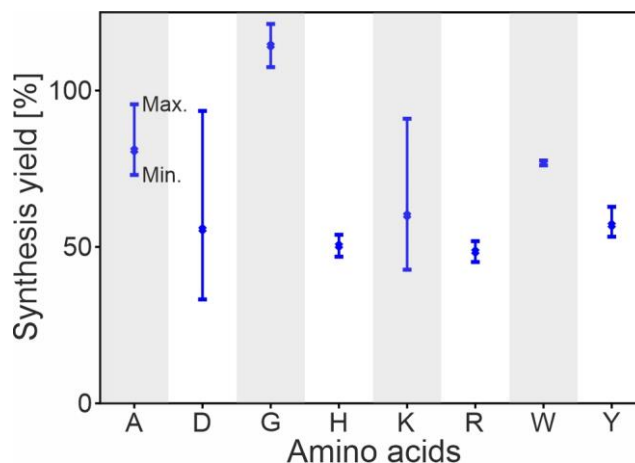
Figure S38. *N*-(9*H*-Fluoren-9-ylmethyl)-piperidine absorbance based synthesis yield measurement for three repetitive coupling reactions. The synthesis yield of eight representative AAs resembles the observed antibody binding measurement trend: High synthesis yields for alanine and glycine, as well as low synthesis yields for histidine and arginine are obtained. However, large fluctuations of up to ≈ 60 % for measurements from different acceptor slides are observed. These are mainly the result of the varying coupling area detection (i.e., spot size upon labeling), which strongly influence the synthesis yield calculation. Data presented as mean with min/max value boundaries, n = (A, 3), (D, 3), (G, 2), (H, 2), (K, 5), (R, 2), (W, 2), and (Y, 3).
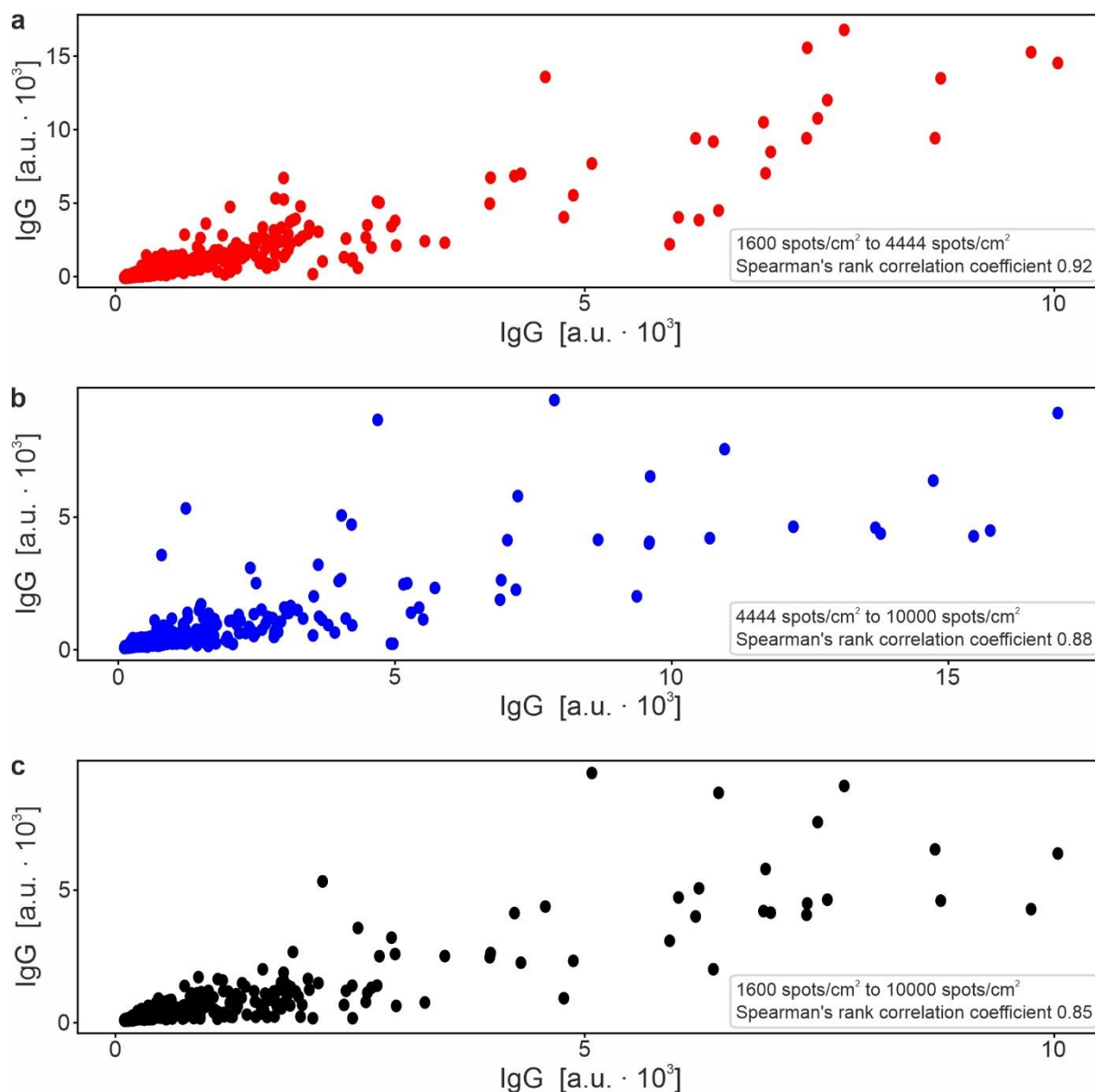
Figure S39. Correlation between synthesized microarrays. A strong correlation between all synthesized microarrays is verified by Spearman's rank correlation. Specifically, a correlation of 0.92, 0.88, and 0.85 is measured between the 1600 spots/cm^2 to 4444 spots/cm^2 (**a**), 4444 spots/cm^2 to 10000 spots/cm^2 (**b**), and 1600 spots/cm^2 to 10000 spots/cm^2 (**c**) microarrays. Spearman's rank correlation is used for the correlation of the synthesized microarrays, since only a correlating monotony can be assumed. Mean IgG values is used for the calculation, n = 662. *P*-values are calculated using python scipy.stats.spearmanr, $P < 10^{-10}$ for all correlations.

Figure S40. IgG antibody profile against the Ebola virus surface glycoprotein. Shown are the measured fluorescence intensities of the Ebola virus surface glycoprotein microarray, in which the protein is mapped as individual 662 15-residue peptide spots with a lateral shift of one AA. The mean (of median IgG value) ± SD of the synthesized 1600 spots/cm^2 (**a**), 4444 spots/cm^2 (**b**), and 10000 spots/cm^2 (**c**) microarrays, as well as the commercial reference microarray (PEPperPRINT GmbH) with 1200 spots/cm^2 (**d**) are calculated through 14, 10, 30, and 8 data points. The fluorescence intensities are based on Ebola virus disease survivor IgG binding to the peptide spots. Additionally,

a background subtraction of 400 a. u. (162 a. u. for the commercial reference) was performed and the detected epitopes are highlighted in grey (Table S8).

Figure S41. IgG antibody profile against the Ebola virus nucleoprotein. Shown are the measured fluorescence intensities of the Ebola virus nucleoprotein microarray, in which the protein is mapped as individual 725 15- residue peptide spots with a lateral shift of one AA. The mean (of median IgG value) ± SD of the synthesized 4444 spots/cm² (**a**) and 10000 spots/cm² (**b**) microarrays are calculated through two points. The fluorescence intensities are based on Ebola virus disease survivor IgG binding to the peptide spots. Additionally, a background subtraction of 400 a. u. was performed and the detected epitopes are highlighted in grey (Table S9).
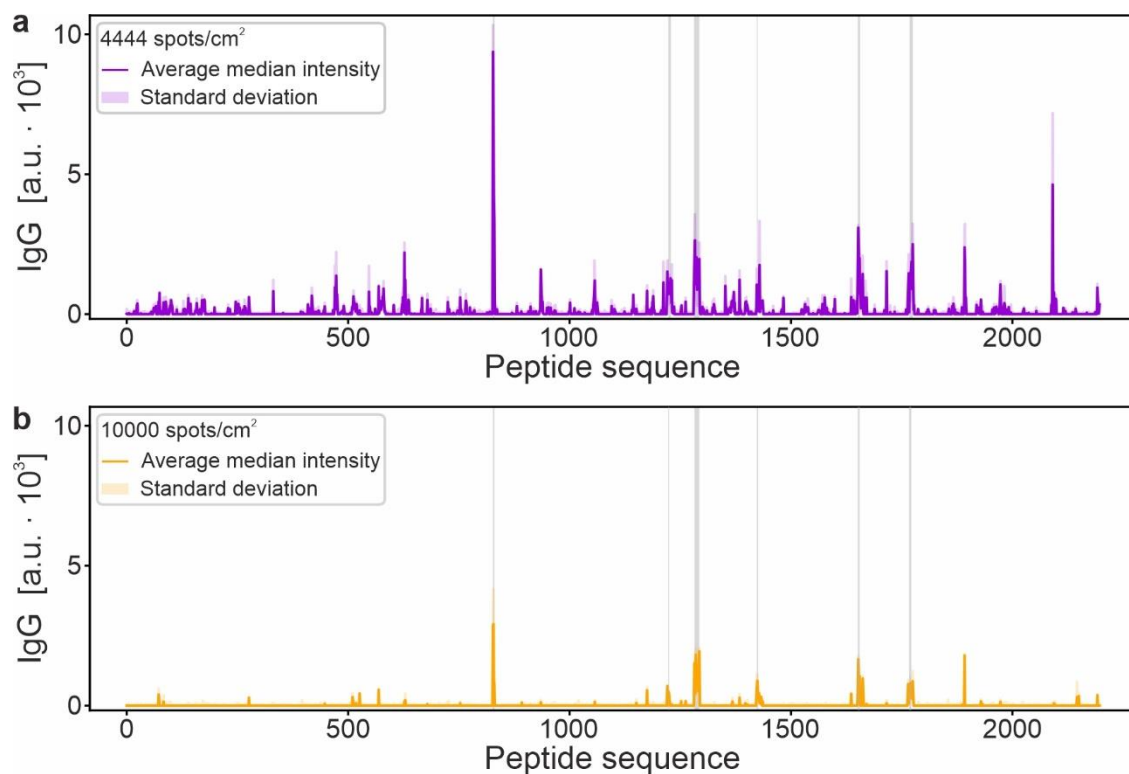
Figure S42. IgG antibody profile against the Ebola virus RNA-directed RNA polymerase L. Shown are the measured fluorescence intensities of the Ebola virus RNA-directed RNA polymerase L microarray, in which the protein is mapped as individual 2198 15- residue peptide spots with a lateral shift of one AA. The mean (of median IgG value) ± SD of the synthesized 4444 spots/cm^2 (**a**) and 10000 spots/cm^2 (**b**) microarrays are calculated through two points. The fluorescence intensities are based on Ebola virus disease survivor IgG binding to the peptide spots. Additionally, a background subtraction of 400 a. u. was performed and the detected epitopes are highlighted in grey (Table S10).
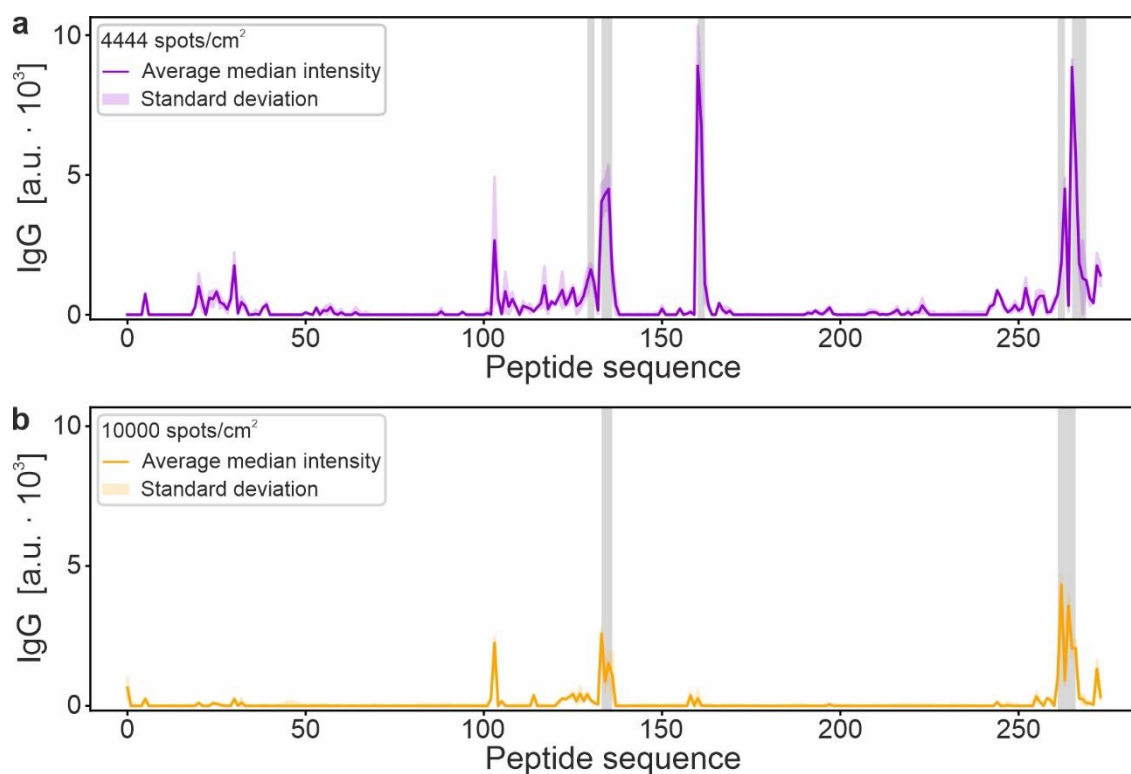
Figure S43. IgG antibody profile against the Ebola virus transcriptional activator VP30. Shown are the measured fluorescence intensities of the Ebola virus transcriptional activator VP30 microarray, in which the protein is mapped as individual 274 15- residue peptide spots with a lateral shift of one AA. The mean (of median IgG value) ± SD of the synthesized 4444 spots/cm² (**a**) and 10000 spots/cm² (**b**) microarrays are calculated through two points. The fluorescence intensities are based on Ebola virus disease survivor IgG binding to the peptide spots. Additionally, a background subtraction of 400 a. u. was performed and the detected epitopes are highlighted in grey (Table S11).
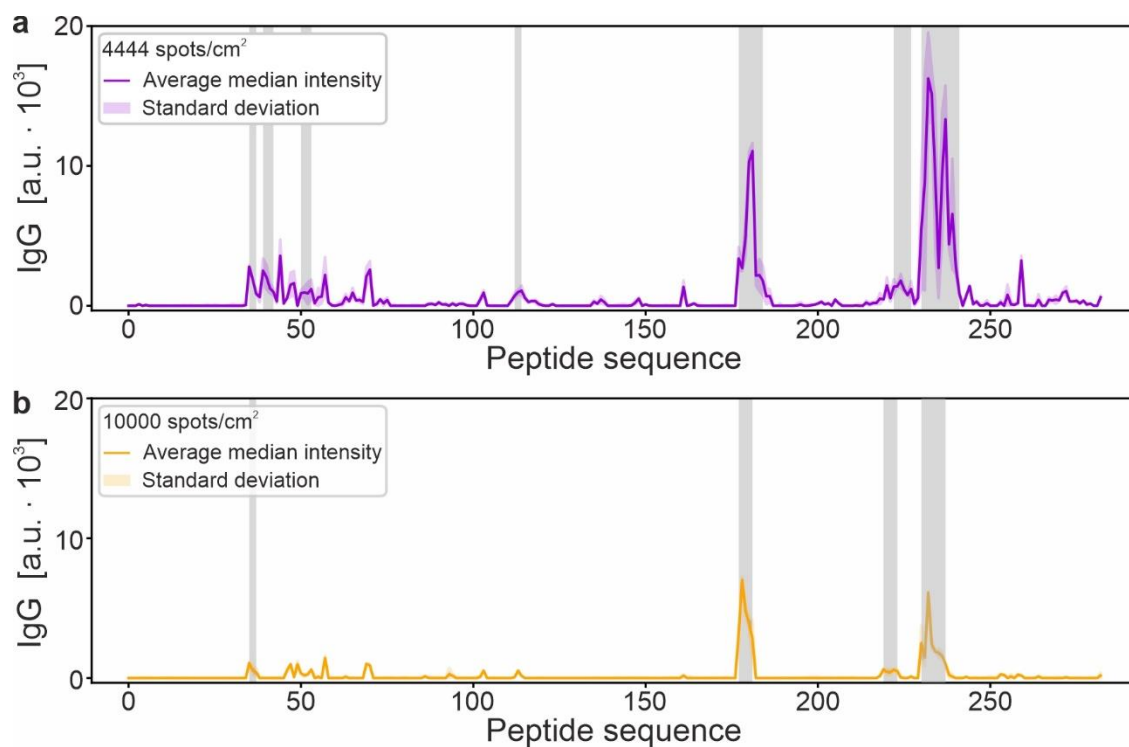
Figure S44. IgG antibody profile against the Ebola virus small secreted glycoprotein. Shown are the measured fluorescence intensities of the Ebola virus small secreted glycoprotein microarray, in which the protein is mapped as individual 283 15- residue peptide spots with a lateral shift of one AA. The mean (of median IgG value) ± SD of the synthesized 4444 spots/cm^2 (**a**) and 10000 spots/cm^2 (**b**) microarrays are calculated through two points. The fluorescence intensities are based on Ebola virus disease survivor IgG binding to the peptide spots. Additionally, a background subtraction of 400 a. u. was performed and the detected epitopes are highlighted in grey (Table S12).
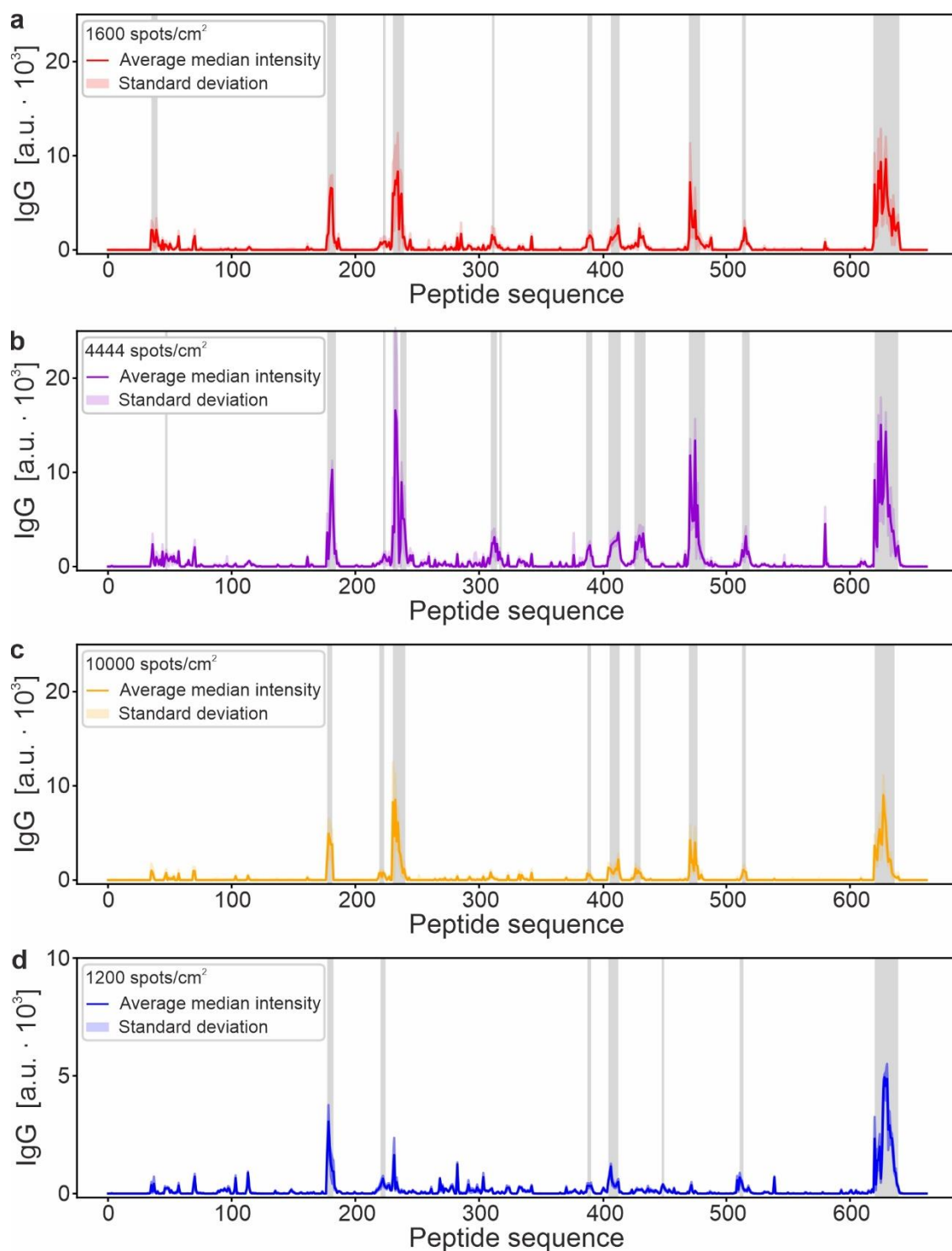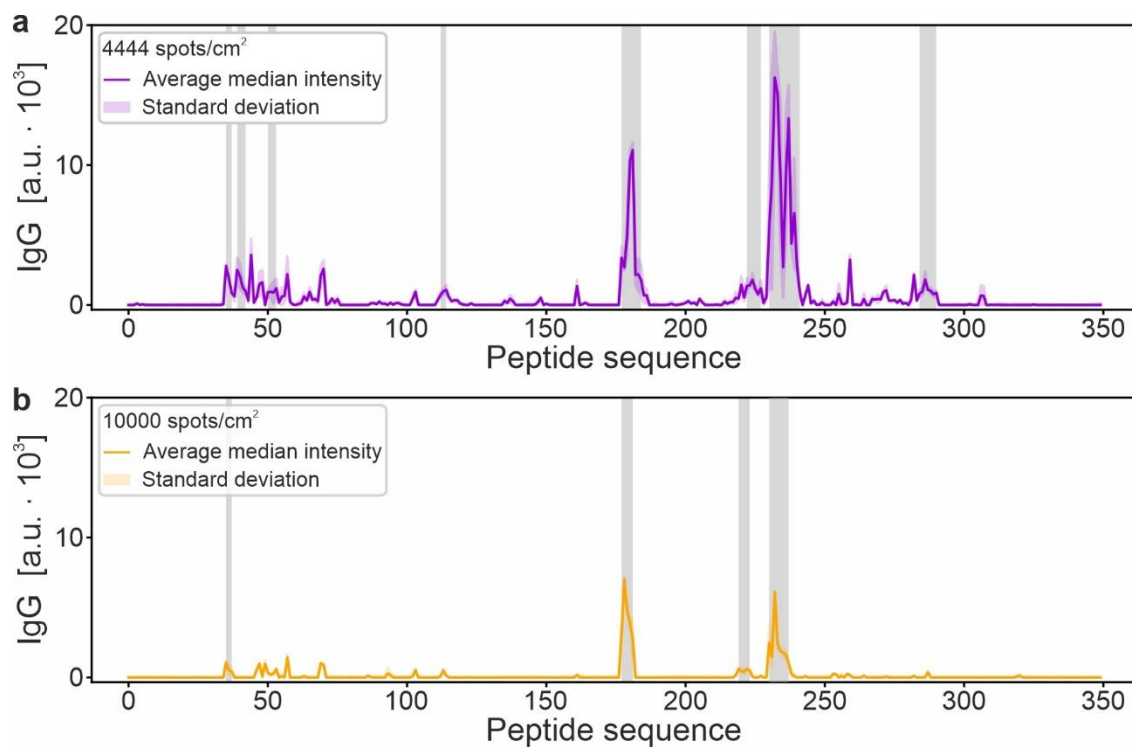
Figure S45. IgG antibody profile against the Ebola virus secreted glycoprotein. Shown are the measured fluorescence intensities of the Ebola virus secreted glycoprotein microarray, in which the protein is mapped as individual 350 15- residue peptide spots with a lateral shift of one AA. The mean (of median IgG value) ± SD of the synthesized 4444 spots/cm^2 (**a**) and 10000 spots/cm^2 (**b**) microarrays are calculated through two points. The fluorescence intensities are based on Ebola virus disease survivor IgG binding to the peptide spots. Additionally, a background subtraction of 400 a. u. was performed and the detected epitopes are highlighted in grey (Table S13).
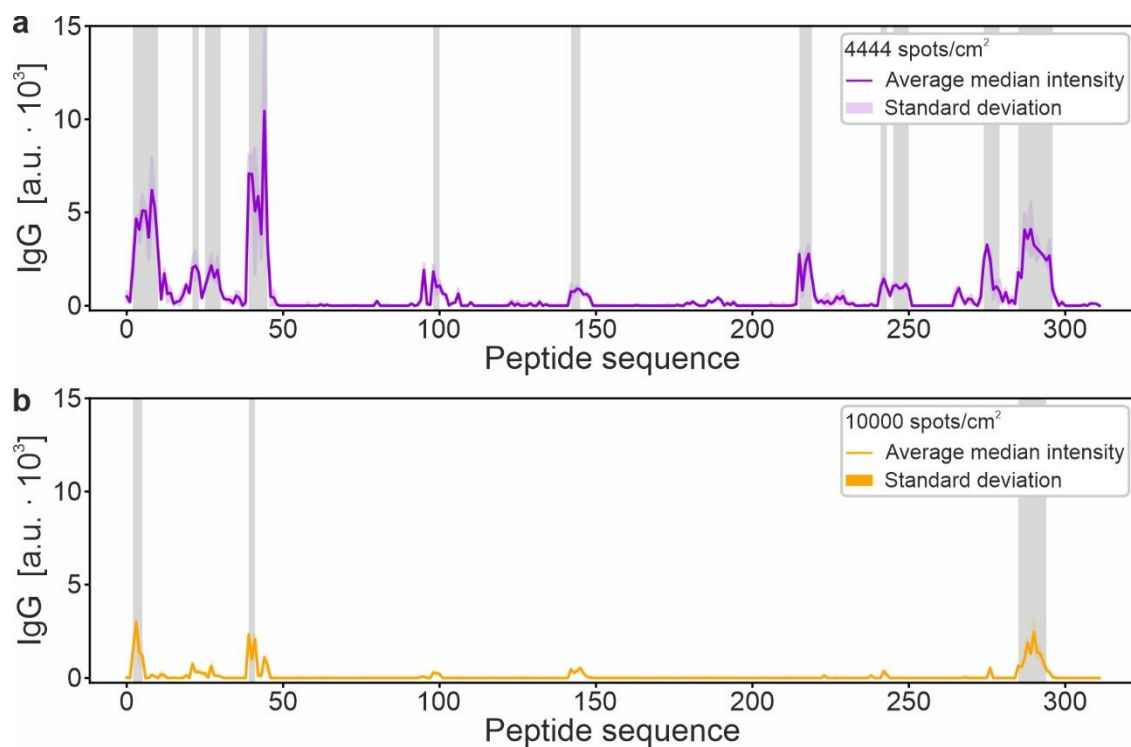
Figure S46. IgG antibody profile against the Ebola virus matrix protein VP40. Shown are the measured fluorescence intensities of the Ebola virus matrix protein VP40 microarray, in which the protein is mapped as individual 312 15- residue peptide spots with a lateral shift of one AA. The mean (of median IgG value) ± SD of the synthesized 4444 spots/cm^2 (**a**) and 10000 spots/cm^2 (**b**) microarrays are calculated through two points. The fluorescence intensities are based on Ebola virus disease survivor IgG binding to the peptide spots. Additionally, a background subtraction of 400 a. u. was performed and the detected epitopes are highlighted in grey (Table S14).
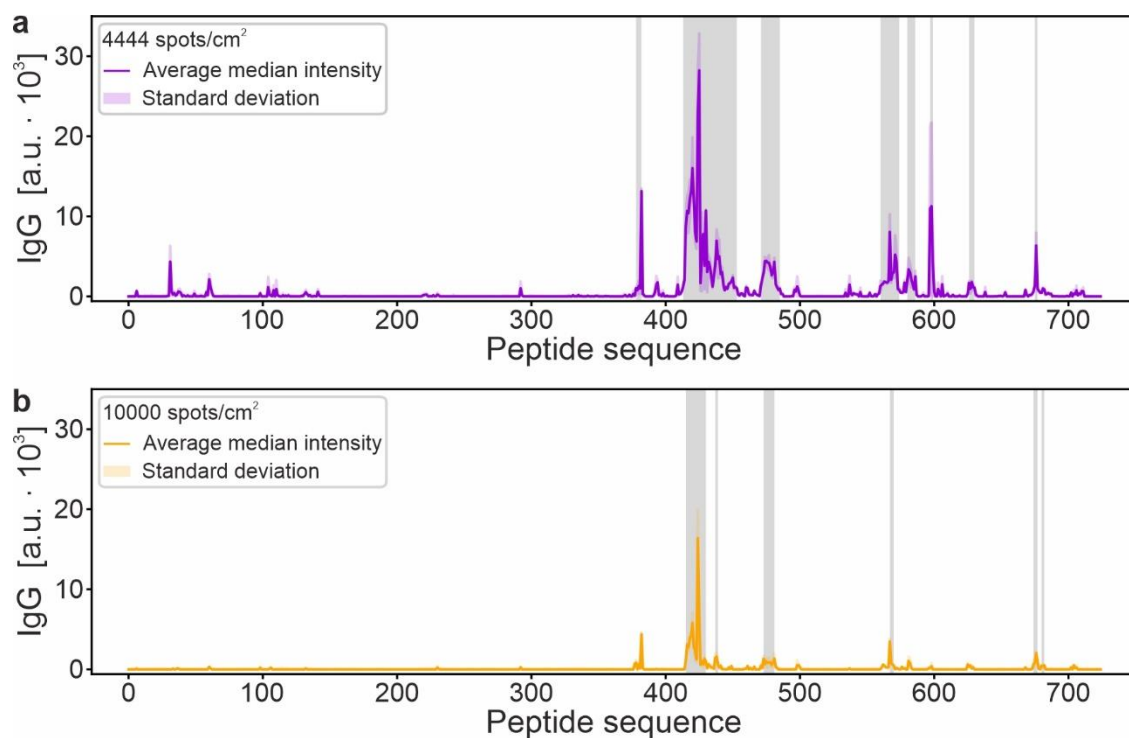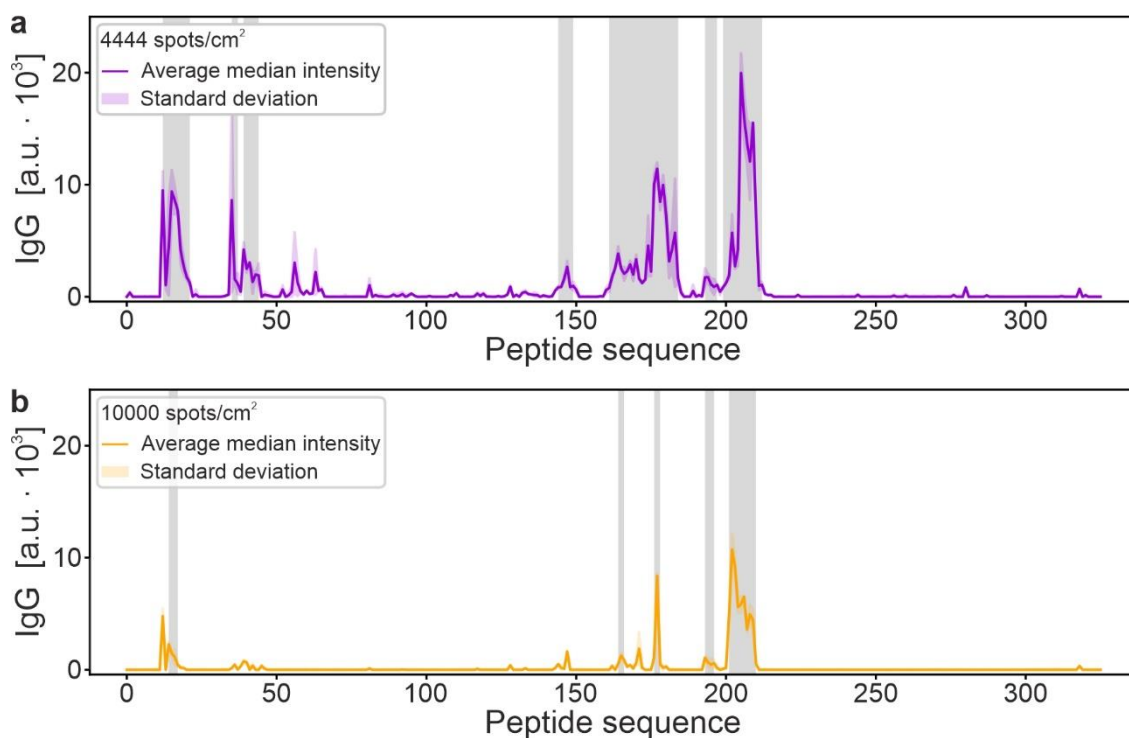
Figure S47. IgG antibody profile against the Ebola virus polymerase cofactor VP35. Shown are the measured fluorescence intensities of the Ebola virus polymerase cofactor VP35 microarray, in which the protein is mapped as individual 326 15- residue peptide spots with a lateral shift of one AA. The mean (of median IgG value) ± SD of the synthesized 4444 spots/cm^2 (**a**) and 10000 spots/cm^2 (**b**) microarrays are calculated through two points. The fluorescence intensities are based on Ebola virus disease survivor IgG binding to the peptide spots. Additionally, a background subtraction of 400 a. u. was performed and the detected epitopes are highlighted in grey (Table S15).
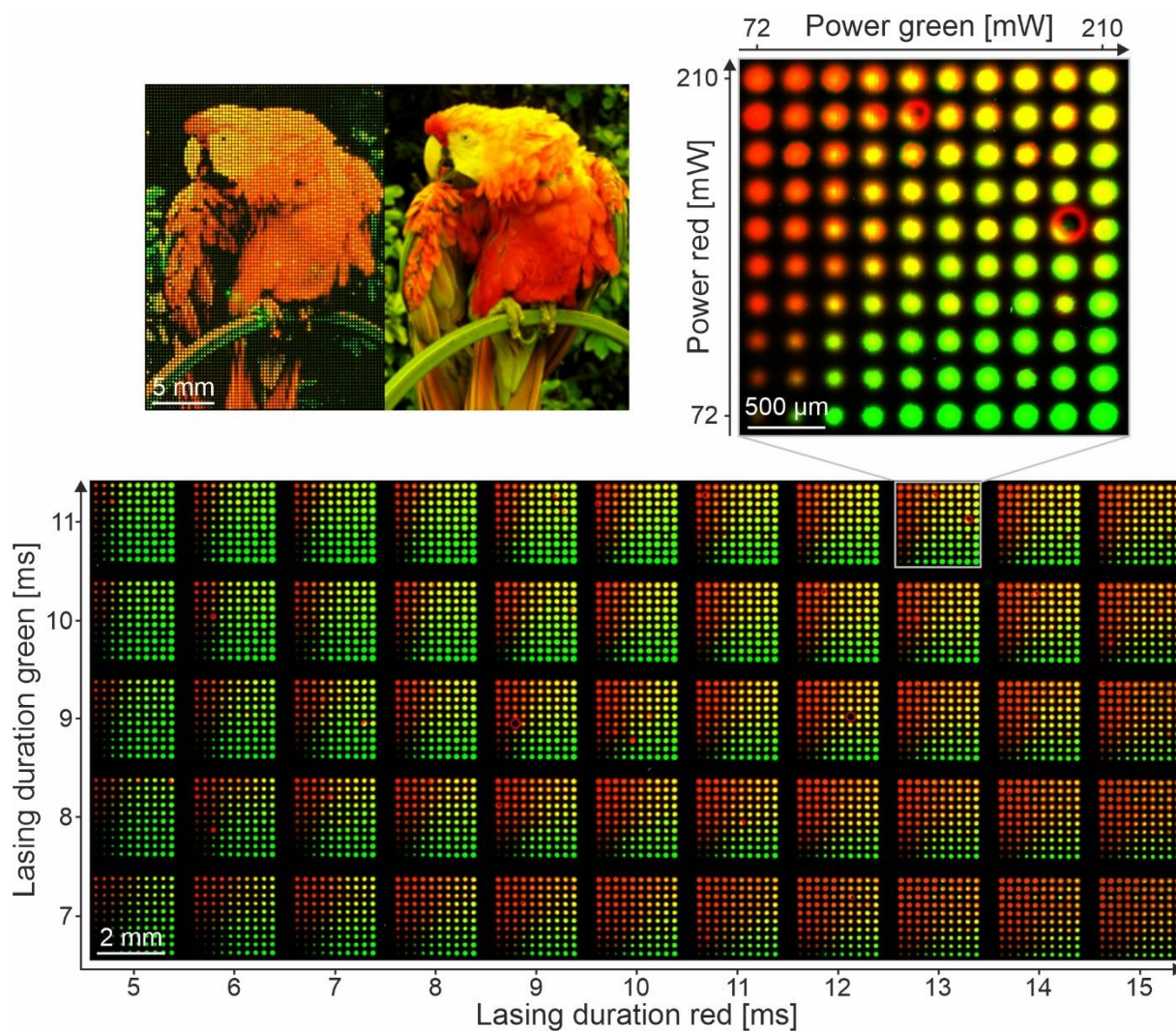
Figure S48. Optimized red-green fluorescent dye ratios. Nested lasing parameter gradients of the transferred donor slides containing Rhodamine 6G and Nile Blue A (Table S16) with a lasing power range of 72 – 210 mW and lasing duration range of 7 – 11 ms (Rhodamine 6G) and 5 – 15 ms (Nile Blue A). For the generation of red-green images, an optimized lasing duration of 11 ms and 13 ms for Rhodamine 6G and Nile Blue A was observed, which was used to generate a red-green image of a parrot.[5] The laser processing files were generated through the developed graphical user interface.[6]

Reference mixture L-CFDD and D-CFDD: RP-HPLC of L-CFDD t_R 13.4 min, D-CFDD t_R 15.5 min, 254 nm, Method B
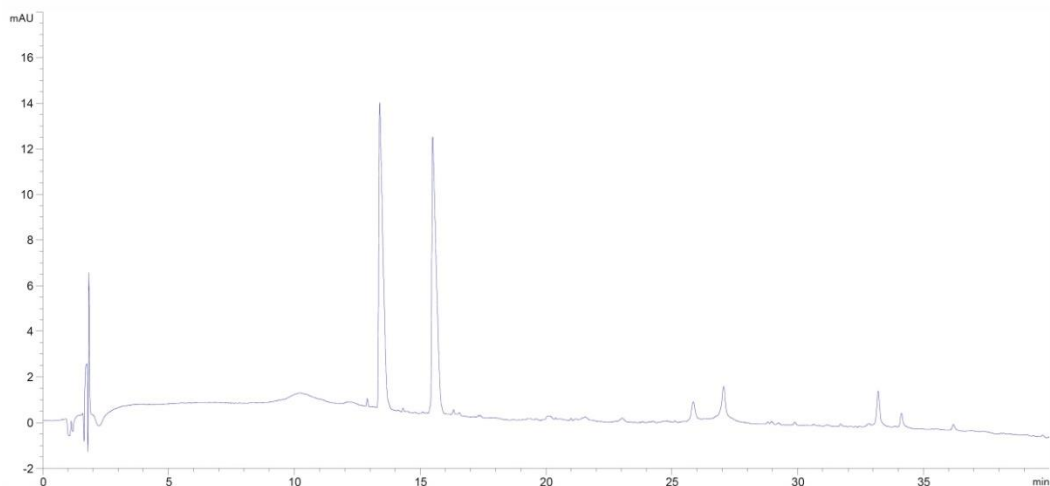
Reference mixture L-CFDD and D-CFDD: Positive mode ion mass spectrometry of L-CFDD t_R 13.4 min
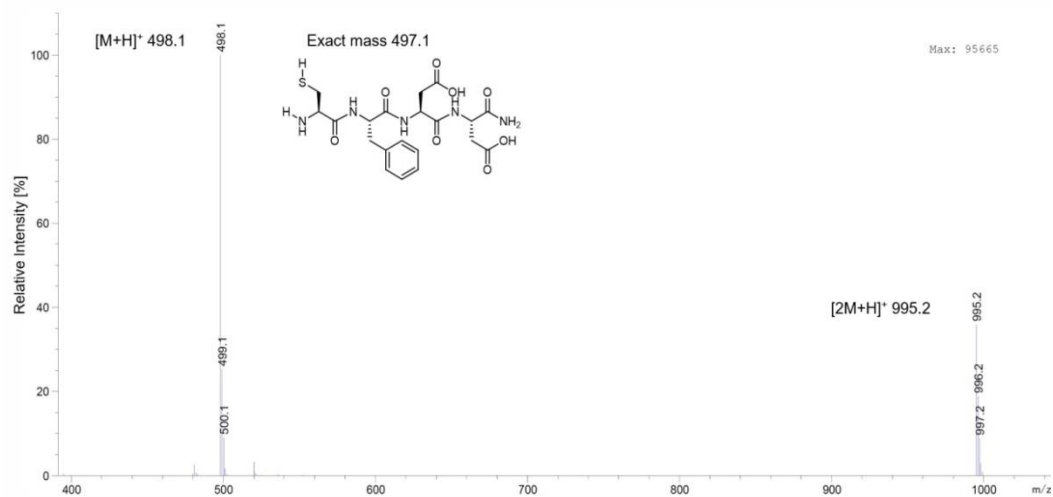
Reference mixture L-CFDD and D-CFDD: Positive mode ion mass spectrometry of D-CFDD t_R 15.5 min
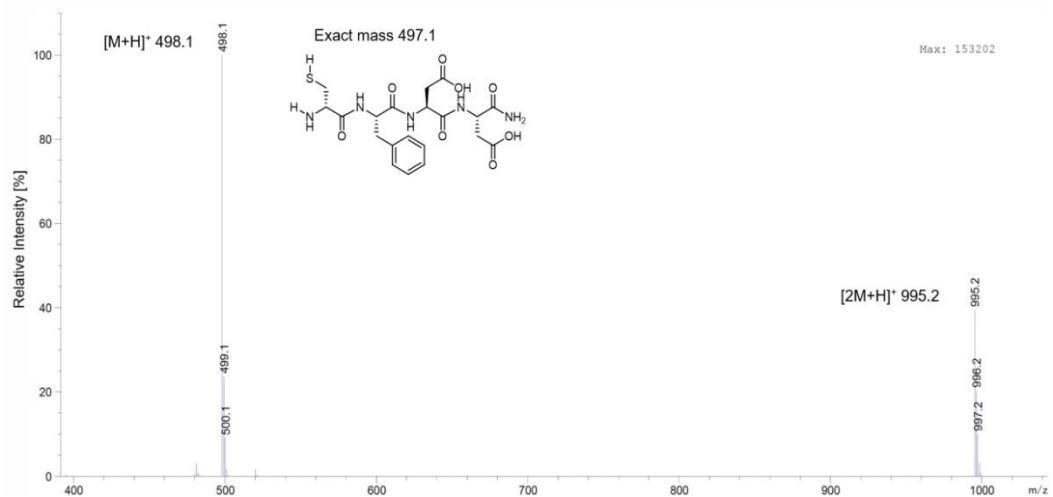
Figure S48: RP-HPLC-MS of L-YFDD and D-YFDD mixture (reference).

Coupling 95 C Beads YFDD: RP-HPLC of L-YFDD tR 14.9 min, 280 nm, Method B

Coupling 95 °C Beads YFDD: Positive mode ion mass spectrometry of L-YFDD tR 14.9 min
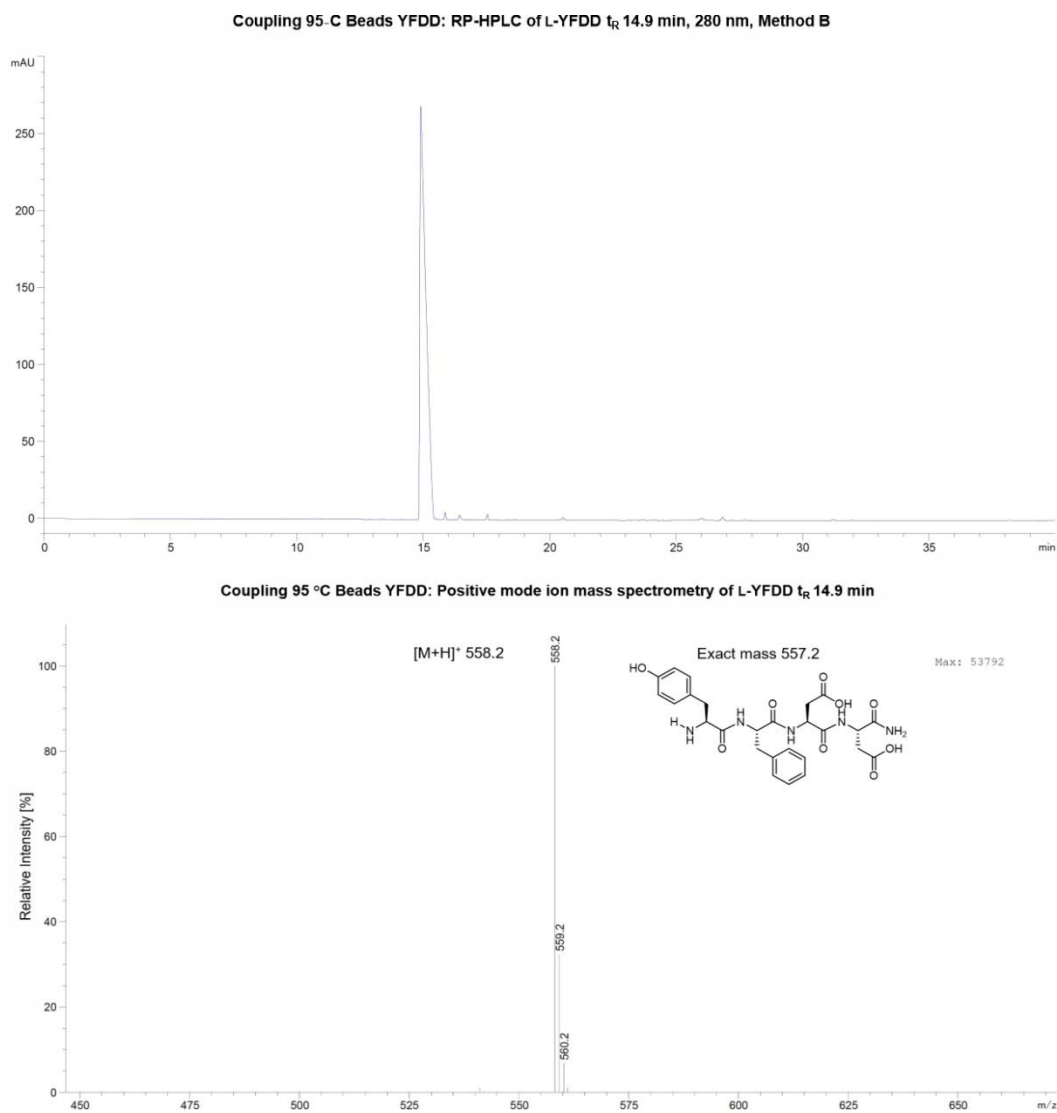
Figure S49: RP-HPLC-MS of L-YFDD after on resin coupling at 95°C for 15 min.
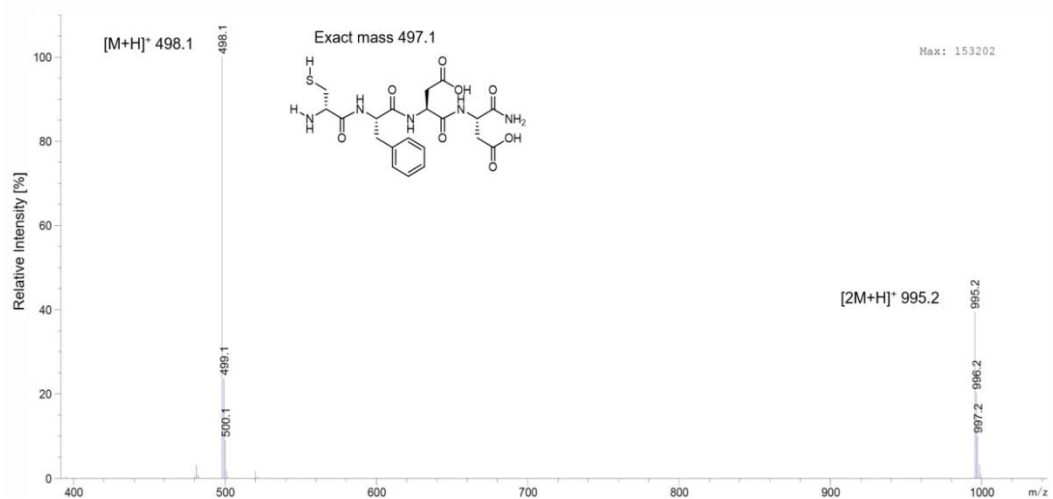
Figure S50: RP-HPLC-MS of ʟ-CFDD and ᴅ-CFDD mixture (reference).

Coupling 95 -C Beads CFDD: RP-HPLC of L-YFDD t$_R$ 13.3 min and D-YFDD t$_R$ 15.2 min 254 nm, Method B
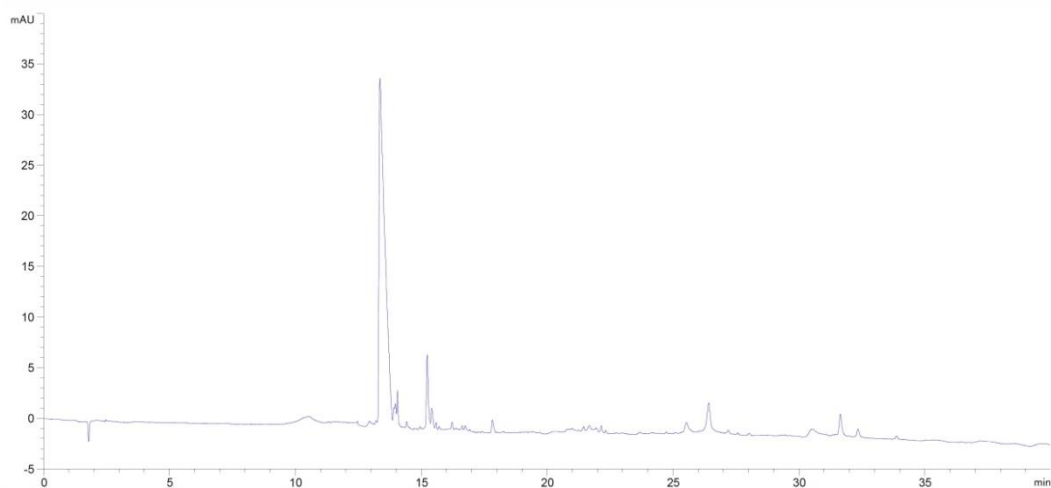
Coupling 95 °C Beads CFDD: Positive mode ion mass spectrometry of L-CFDD t$_R$ 13.3 min
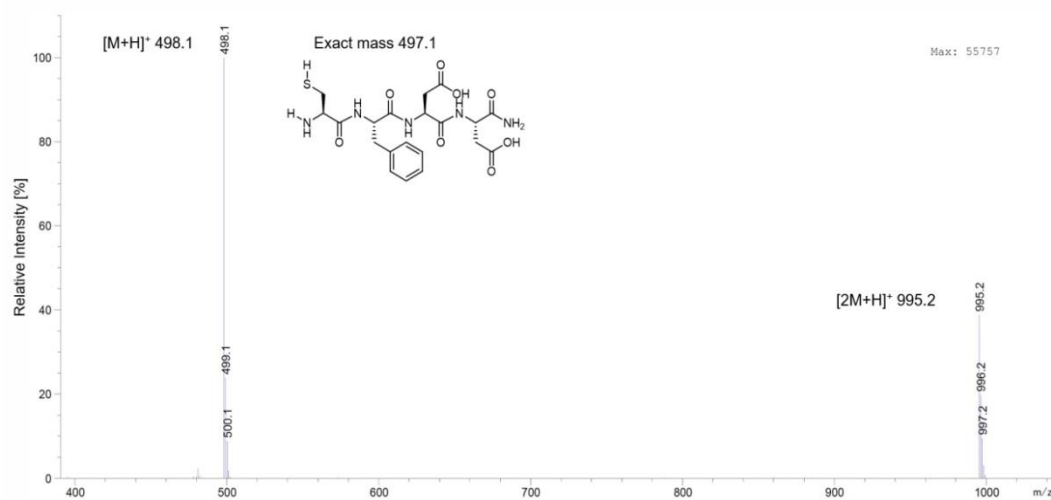
Coupling 95 °C Beads CFDD: Positive mode ion mass spectrometry of D-CFDD t$_R$ 15.2 min
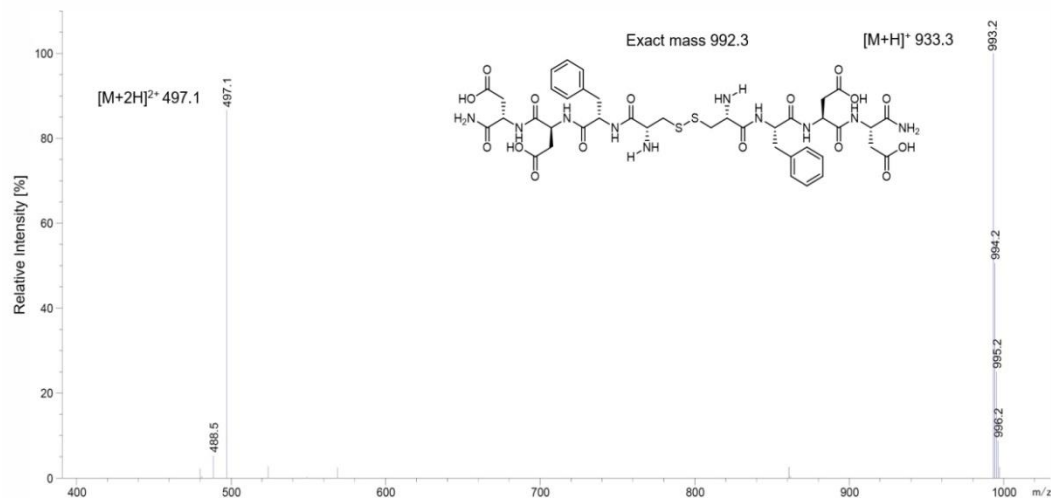
Figure S51: RP-HPLC-MS of L-CFDD and D-CFDD after on resin coupling at 95°C for 15 min.
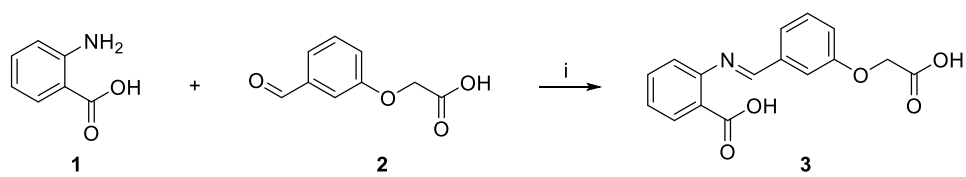
Figure S52. Synthesis of 2-((3-(carboxymethoxy)benzylidene)amino)benzoic acid in solution. i) Ethanol, 60 ºC, 180 min.
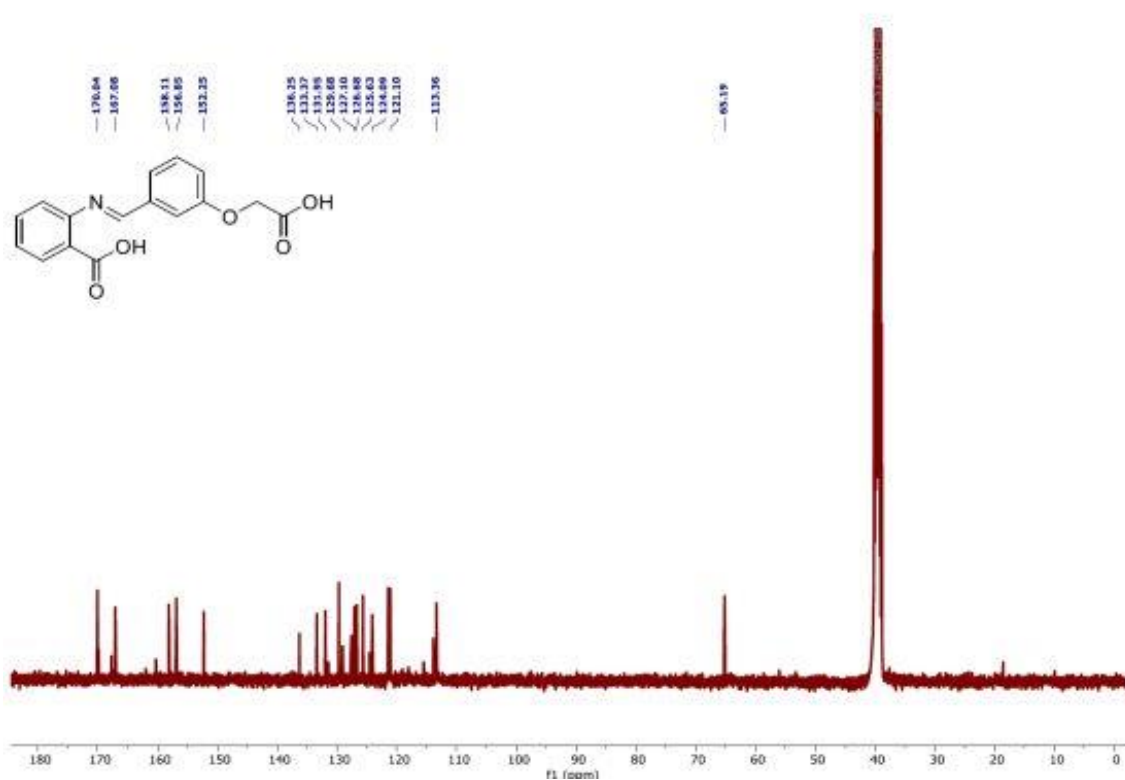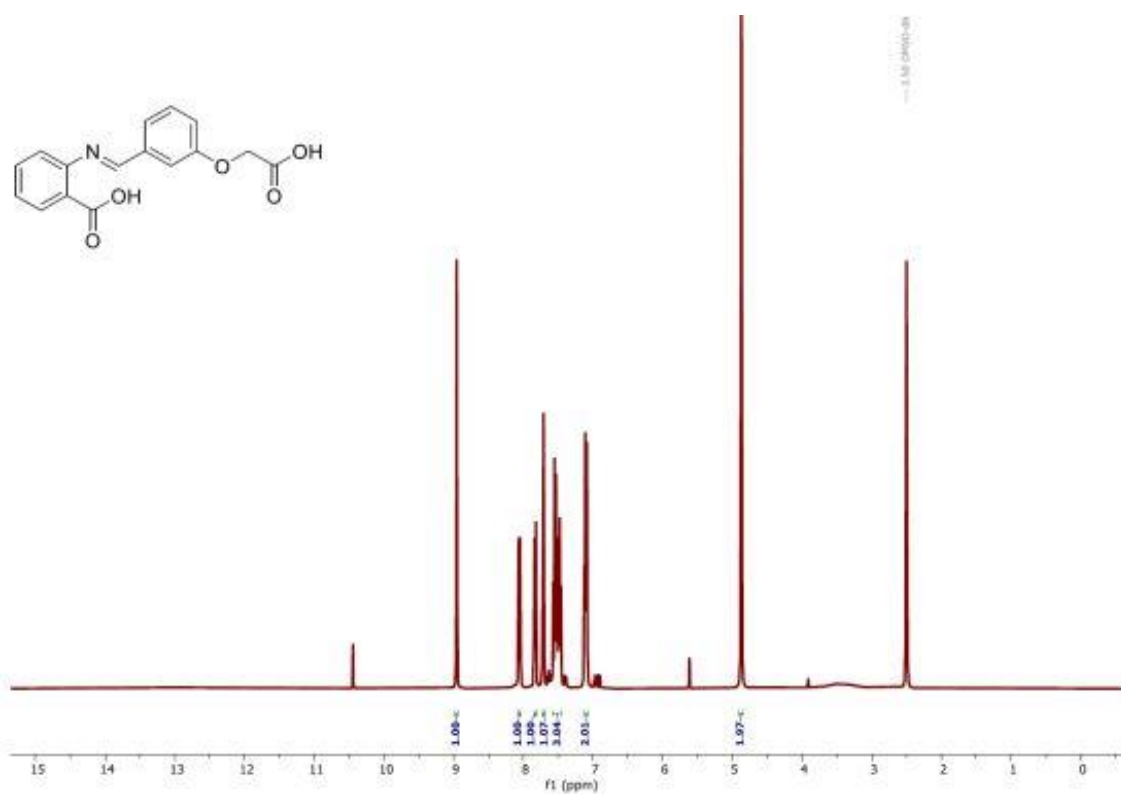
Figure S53. ^{1}H NMR and ^{13}C NMR of 2-((3-(carboxymethoxy)benzylidene)amino)benzoic acid **3** in CDCl$_3$.
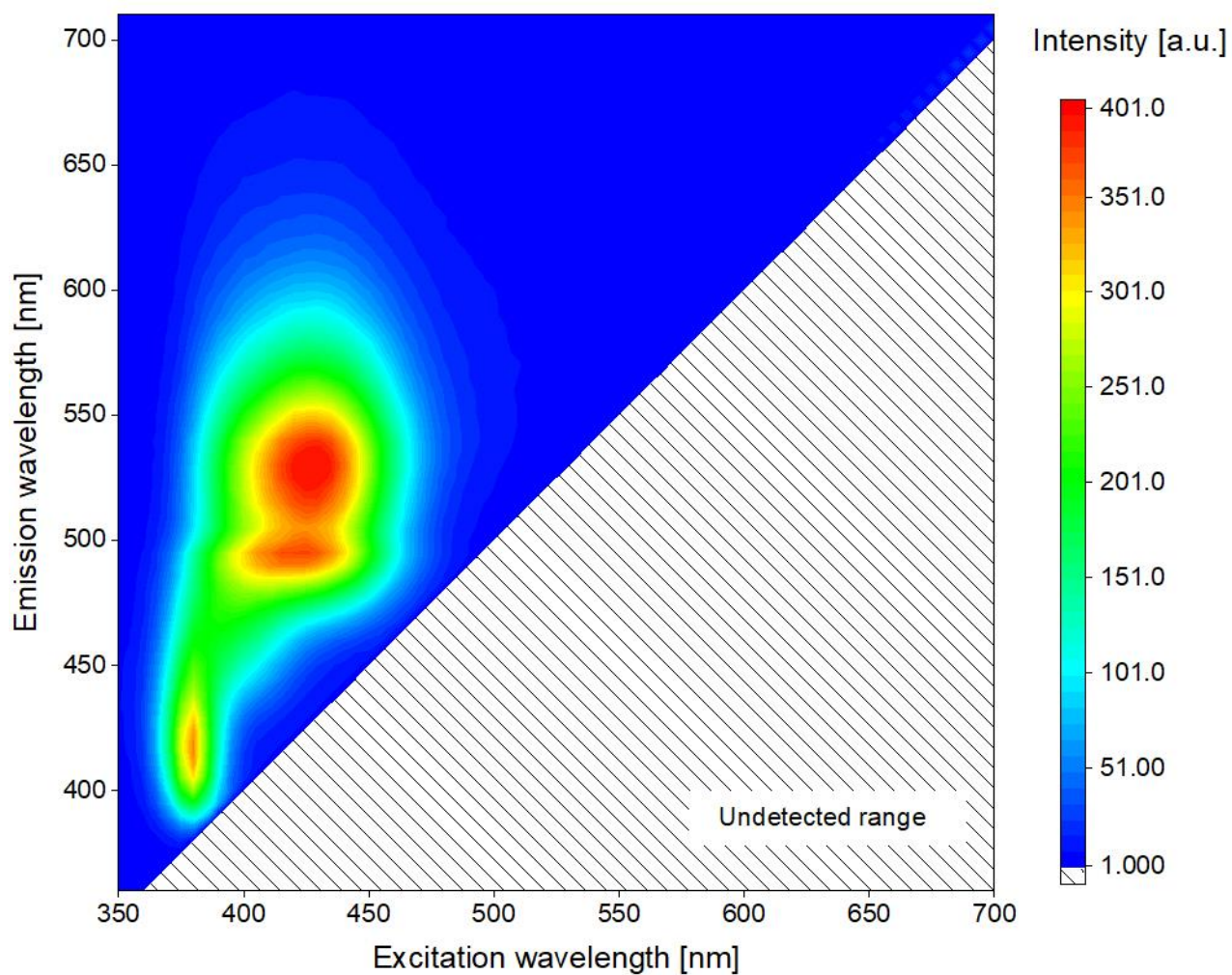
Figure S54. 2D fluorescence spectrum of 2-((3-(carboxymethoxy)benzylidene)amino)benzoic acid. The emission range was chosen according to the corresponding excitation wavelength under the condition emission wavelength ≥ excitation wavelength + 10 nm.
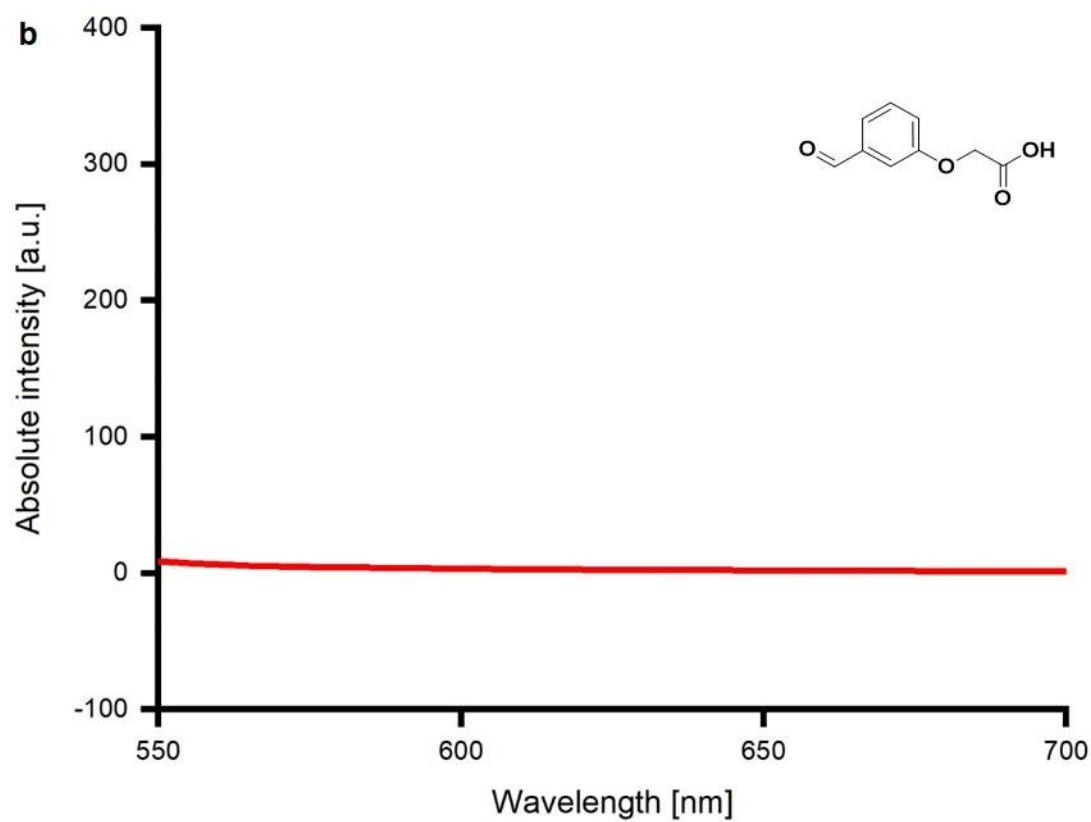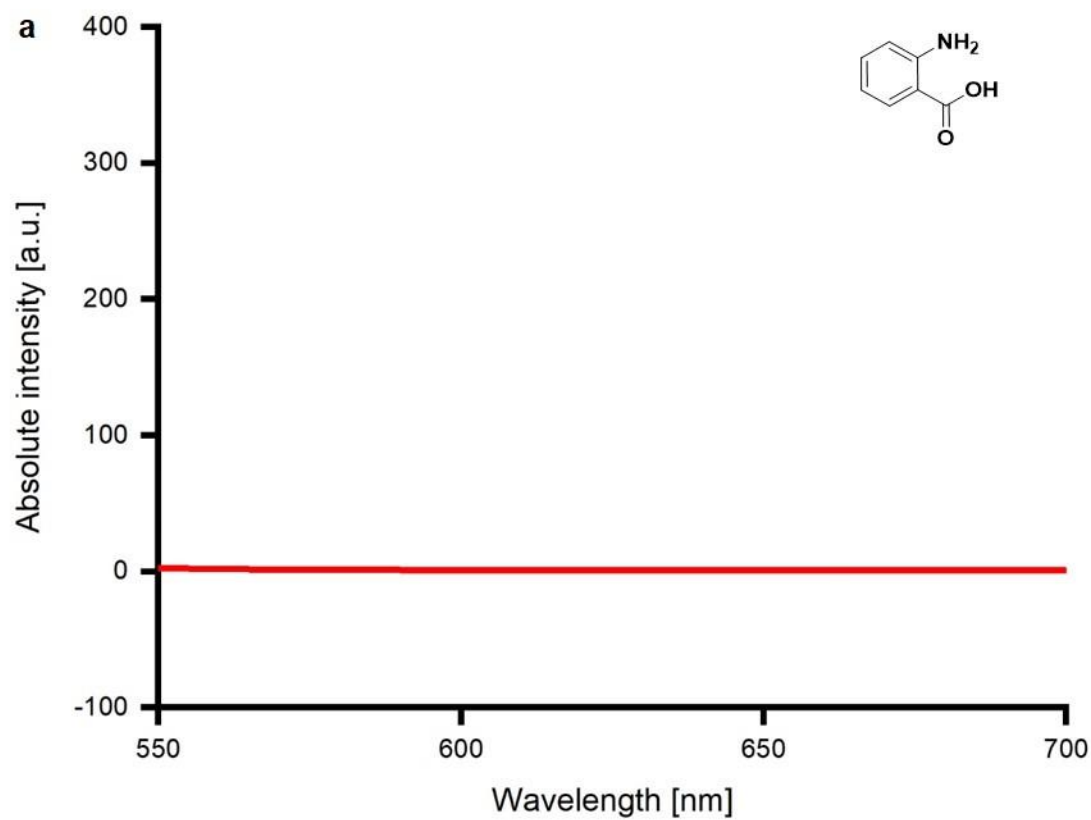
Figure S55. Normal fluorescence spectra of 2-aminobenzoic acid (**a**) and 2-(3-formylphenoxy)acetic acid (**b**).

HOMO   LUMO
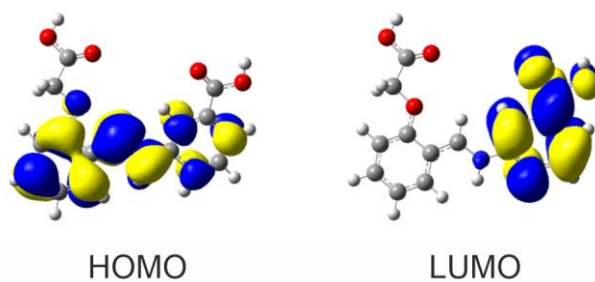
Figure S56. 2-((3-(carboxymethoxy)benzylidene)amino)benzoic acid molecular orbital amplitude plots. Electron distribution for the HOMO and LUMO energy levels of 2-((3-(carboxymethoxy)benzylidene)amino)benzoic acid. Molecular models are optimized before simulation.

Table S1. Fixed spot size coupling efficiency investigation – 1600 spots/cm^2 synthesis. Measured normalized (100 % = 8-residue wild-type Flag epitope of the 1600 spots/cm^2 synthesis) average median fluorescence intensities after antibody staining of the synthesized 9-residue, 10-residue, 15-residue, and 20-residue for a spot density of 1600 spots/cm^2 with a fixed spot diameter of 130 µm. Data presented as mean $\pm$ SD, normalized against the 8-residue wild-type Flag epitope of the 1600 spots/cm² synthesis, n = 3.

Amino acid	X-Spacer-Flag			D-X-Spacer-Flag		
	9-residue [%]	15-residue [%]	20-residue [%]	10-residue [%]	15-residue [%]	20-residue [%]
A	121 ± 10	114 ± 10	82 ± 8	124 ± 9	85 ± 4	63 ± 3
C	113 ± 10	92 ± 4	84 ± 6	112 ± 4	89 ± 4	73 ± 10
D	111 ± 7	96 ± 5	78 ± 5	96 ± 13	82 ± 1	64 ± 3
E	110 ± 8	102 ± 7	75 ± 3	112 ± 4	82 ± 6	62 ± 4
F	120 ± 12	124 ± 3	100 ± 2	128 ± 10	102 ± 4	82 ± 6
G	89 ± 10	97 ± 1	91 ± 3	61 ± 4	74 ± 3	73 ± 10
H	21 ± 4	24 ± 8	23 ± 2	45 ± 1	28 ± 2	30 ± 3
I	119 ± 13	121 ± 5	90 ± 6	121 ± 10	98 ± 7	75 ± 7
K	113 ± 8	119 ± 7	106 ± 4	117 ± 9	99 ± 4	83 ± 4
L	116 ± 11	105 ± 5	90 ± 1	119 ± 6	87 ± 7	63 ± 6
M	95 ± 11	106 ± 1	87 ± 2	113 ± 7	82 ± 8	71 ± 6
N	100 ± 5	119 ± 4	107 ± 3	116 ± 5	96 ± 2	90 ± 12
P	113 ± 3	85 ± 2	66 ± 3	109 ± 11	97 ± 6	61 ± 7
Q	103 ± 6	112 ± 2	101 ± 3	114 ± 3	95 ± 10	81 ± 5
R	12 ± 1.5	45 ± 1	56 ± 2	122 ± 3	90 ± 15	68 ± 6
S	110 ± 4	106 ± 3	93 ± 3	109 ± 8	98 ± 6	81 ± 3
T	107 ± 10	116 ± 7	97 ± 4	111 ± 4	103 ± 3	97 ± 3
V	107 ± 5	113 ± 5	86 ± 6	117 ± 1	99 ± 6	71 ± 6
W	32 ± 7	35 ± 1	37 ± 1	61 ± 3	36 ± 2	38 ± 4
Y	129 ± 7	117 ± 5	98 ± 4	113 ± 26	104 ± 3	82 ± 7

Table S2. Adjusted spot size coupling efficiency investigation – 1600 spots/cm^2 synthesis. Measured normalized (100 % = 8-residue wild-type Flag epitope of the 1600 spots/cm^2 synthesis) average median fluorescence intensities after antibody staining of the synthesized 9-residue, 10-residue, 15-residue, and 20-residue for a spot density of 1600 spots/cm^2 with an adjusted spot size. Data presented as mean ± SD, normalized against the 8-residue wild-type Flag epitope of the 1600 spots/cm² synthesis, n = 3.

Amino acid	X-Spacer-Flag			D-X-Spacer-Flag		
	9-residue [%]	15-residue [%]	20-residue [%]	10-residue [%]	15-residue [%]	20-residue [%]
A	96 ± 14	108 ± 9	66 ± 6	129 ± 8	49 ± 3	31 ± 2
C	109 ±15	71 ± 5	64 ± 5	120 ± 14	65 ± 2	40 ± 3
D	105 ± 14	65 ± 3	41 ± 6	104 ± 17	53 ± 8	29 ± 4
E	107 ± 12	81 ± 15	39 ± 12	121 ± 13	54 ± 2	32 ± 4
F	110 ± 18	110 ± 5	79 ± 5	134 ± 10	62 ± 6	35 ± 3
G	94 ± 11	80 ± 10	71 ± 10	72 ± 8	47 ± 6	35 ± 2
H	20 ± 2	21 ± 7	18 ± 3	43 ± 6	21 ± 2	22 ± 1
I	104 ± 17	111 ± 16	70 ± 5	131 ± 20	60 ± 10	32 ± 4
K	127 ± 18	110 ± 7	55 ± 9	134 ± 10	57 ± 11	31 ± 2
L	98 ± 4	87 ± 7	70 ± 7	128 ± 22	56 ± 11	32 ± 3
M	90 ± 23	92 ± 5	72 ± 5	116 ± 7	60 ± 14	35 ± 3
N	109 ± 8	93 ± 11	74 ± 3	122 ± 8	67 ± 5	42 ± 8
P	85 ± 14	74 ± 10	46 ± 3	107 ± 12	77 ± 4	34 ± 5
Q	106 ± 16	108 ± 5	83 ± 5	96 ± 28	69 ± 10	34 ± 2
R	15 ± 2	35 ± 4	39 ± 1	117 ± 20	65 ± 7	34 ± 3
S	108 ± 8	104 ± 2	74 ± 3	114 ± 7	66 ± 13	36 ± 3
T	105 ± 14	99 ± 6	80 ± 6	115 ± 10	78 ± 18	40 ± 2
V	95 ± 17	107 ± 2	69 ± 7	121 ± 6	60 ± 17	32 ± 1
W	34 ± 4	33 ± 4	31 ± 3	70 ± 2	29 ± 2	25 ± 4
Y	123 ± 17	100 ± 18	70 ± 10	127 ± 26	59 ± 3	37 ± 5

Table S3. Fixed spot size coupling efficiency investigation – 10000 spots/cm^2 synthesis. Measured normalized (100 % = 8-residue wild-type Flag epitope of the 1600 spots/cm^2 synthesis) average median fluorescence intensities after antibody staining of the synthesized 9-residue, 10-residue, 15-residue, and 20-residue for a spot density of 10000 spots/cm^2 with a fixed spot diameter of 70 µm. Data presented as mean ± SD, normalized against the 8-residue wild-type Flag epitope of the 1600 spots/cm² synthesis, n = 3.

Amino acid	X-Spacer-Flag			D-X-Spacer-Flag		
	9-residue [%]	15-residue [%]	20-residue [%]	10-residue [%]	15-residue [%]	20-residue [%]
A	45 ± 1	17 ± 1	19 ± 4	29 ± 9	10 ± 2	14 ± 1
C	31 ± 7	23 ± 6	18 ± 2	11 ± 5	7 ± 1	15 ± 1
D	23 ± 4	11 ± 1	16 ± 2	20 ± 5	11 ± 2	14 ± 1
E	22 ± 2	6 ± 1	12 ± 1	24 ± 7	10 ± 0 (0.4)	12 ± 2
F	77 ± 5	48 ± 6	34 ± 2	36 ± 6	13 ± 0 (0.4)	16 ± 3
G	12 ± 4	12 ± 4	28 ± 4	15 ± 4	8 ± 1	13 ± 1
H	3 ± 1	1 ± 0 (0.2)	3 ± 1	2 ± 0 (0.5)	2 ± 0 (0.4)	7 ± 0 (0.4)
I	71 ± 5	22 ± 1	21 ± 1	26 ± 6	9 ± 2	13 ± 1
K	17 ± 5	9 ± 2	18 ± 2	30 ± 11	11 ± 0 (0.4)	15 ± 1
L	67 ± 4	19 ± 2	20 ± 1	26 ± 4	10 ± 2	14 ± 1
M	40 ± 7	26 ± 3	24 ± 5	24 ± 2	9 ± 2	14 ± 0 (0.1)
N	51 ± 9	39 ± 2	32 ± 4	17 ± 3	10 ± 2	21 ± 4
P	29 ± 1	14 ± 1	16 ± 3	12 ± 1	6 ± 1	15 ± 1
Q	59 ± 3	41 ± 5	34 ± 3	14 ± 3	7 ± 1	16 ± 1
R	2 ± 0 (0.4)	3 ± 1	14 ± 2	8 ± 2	7 ± 2	15 ± 1
S	75 ± 4	34 ± 0 (0.3)	25 ± 0 (0.1)	31 ± 5	11 ± 1	16 ± 1
T	75 ± 2	32 ± 6	34 ± 0 (0.4)	30 ± 2	14 ± 1	16 ± 1
V	73 ± 5	23 ± 1	22 ± 2	34 ± 9	10 ± 2	13 ± 1
W	6 ± 1	4 ± 0 (0.2)	5 ± 1	2 ± 1	2 ± 0 (0.4)	9 ± 1
Y	71 ± 0 (0.4)	40 ± 1	34 ± 2	32 ± 0 (0.2)	13 ± 1	18 ± 1

Table S4. Adjusted spot size coupling efficiency investigation – 10000 spots/cm^2 synthesis. Measured normalized (100 % = 8-residue wild-type Flag epitope of the 1600 spots/cm^2 synthesis) average median fluorescence intensities after antibody staining of the synthesized 9-residue, 10-residue, 15-residue, and 20-residue for a spot density of 10000 spots/cm^2 with an adjusted spot size. Data presented as mean ± SD, normalized against the 8-residue wild-type Flag epitope of the 1600 spots/cm² synthesis, n = 3.

Amino acid	X-Spacer-Flag			D-X-Spacer-Flag		
	9-residue [%]	15-residue [%]	20-residue [%]	10-residue [%]	15-residue [%]	20-residue [%]
A	41 ± 7	15 ± 1	17 ± 3	33 ± 8	12 ± 3	14 ± 1
C	40 ± 11	27 ± 6	14 ± 4	16 ± 7	9 ± 5	15 ± 3
D	25 ± 6	13 ± 5	14 ± 2	28 ± 7	14 ± 6	13 ± 2
E	17 ± 6	8 ± 1	12 ± 1	32 ± 8	13 ± 2	11 ± 3
F	62 ± 10	36 ± 4	29 ± 1	45 ± 8	16 ± 2	14 ± 3
G	14 ± 4	19 ± 12	22 ± 4	20 ± 7	11 ± 5	13 ± 2
H	5 ± 1	2 ± 0 (0.4)	4 ± 2	3 ± 1	3 ± 1	9 ± 1
I	51 ± 3	23 ± 2	18 ± 2	30 ± 8	11 ± 3	13 ± 2
K	23 ± 10	15 ± 3	18 ± 3	38 ± 10	13 ± 5	15 ± 2
L	48 ± 9	17 ± 2	18 ± 1	28 ± 14	13 ± 5	13 ± 1
M	41 ± 9	26 ± 6	17 ± 2	33 ± 4	13 ± 5	15 ± 1
N	36 ± 7	30 ± 6	24 ± 4	27 ± 6	14 ± 7	18 ± 5
P	23 ± 2	24 ± 1	19 ± 5	16 ± 2	7 ± 2	15 ± 2
Q	39 ± 8	32 ± 2	30 ± 4	18 ± 6	11 ±1	15 ± 2
R	3 ± 0 (0.3)	5 ± 2	12 ± 2	11 ± 3	11 ± 2	13 ± 1
S	56 ± 10	27 ± 1	22 ± 1	39 ± 7	16 ± 1	15 ± 1
T	56 ± 13	28 ± 8	29 ± 1	35 ± 3	20 ± 3	17 ± 1
V	51 ± 9	22 ± 2	19 ± 3	41 ± 10	14 ± 4	13 ± 2
W	7 ± 2	5 ± 1	7 ± 2	3 ± 2	3 ± 1	10 ± 1
Y	60 ± 7	35 ± 3	29 ± 3	60 ± 7	15 ± 5	17 ± 1

Table S5. Peptide synthesis parameters – 1600 spots/cm^2 synthesis. Transfer parameters for AA donor slides with a 10 % AA concentration. Donor slides containing a 20 % AA concentration are highlighted in red.

Amino acid	Lasing duration [ms]	Lasing power [mW]	Donor slide reuses	Storable days	Coupling cycles
A	9	80	6	7	2
C	11	120	5	7	3
D	6	80	6	7	3
E	12	60	6	7	3
F	12	80	4	3	3
G	7	80	6	3	3
H	15	140	1	7	3
I	12	60	4	3	3
K	10	80	6	3	2
L	12	60	4	3	3
M	11	80	4	7	3
N	12	120	2	3	3
P	12	80	2	7	3
Q	11	140	2	3	3
R	15	160	2	3	3
S	10	80	4	7	3
T	12	60	4	3	3
V	7	80	2	3	3
W	12	100	4	7	3
Y	10	80	6	7	3

Table S6. Peptide synthesis parameters – 4444 spots/cm^2 synthesis. Transfer parameters for AA donor slides with a 10 % AA concentration. Donor slides containing a 20 % AA concentration are highlighted in red.

Amino acid	Lasing duration [ms]	Lasing power [mW]	Donor slide reuses	Storable days	Coupling cycles
A	9	60	3	3	3
C	10	100	5	7	3
D	10	60	6	7	3
E	12	50	6	7	3
F	11	80	4	3	3
G	10	60	5	3	3
H	13.5	100	2	7	4
I	11	60	4	3	3
K	12	60	6	3	3
L	9	60	4	3	3
M	9	80	4	7	3
N	11	120	2	3	3
P	13	60	2	7	4
Q	12	100	2	7	3
R	11.5	120	1	3	4
S	9	80	4	7	3
T	11	60	4	3	3
V	10.5	60	2	3	3
W	12.5	80	4	7	3
Y	9	80	6	7	3

Table S7. Peptide synthesis parameters – 10000 spots/cm^2 synthesis. Transfer parameters for AA donor slides with a 10 % AA concentration. Donor slides containing a 20 % AA concentration are highlighted in red.

Amino acid	Lasing duration [ms]	Lasing power [mW]	Donor slide reuses	Storable days	Coupling cycles
A	9	50	2	3	5
C	11	80	6	7	3
D	10	50	6	7	4
E	10	50	6	7	4
F	7.5	80	3	3	2
G	11	50	4	3	4
H	15	80	2	7	5
I	10.5	50	5	3	3
K	9	60	6	3	4
L	10	50	4	3	4
M	10	60	4	7	4
N	8	100	2	3	4
P	9.5	60	4	7	5
Q	10	100	2	7	4
R	14	100	1	3	5
S	12	50	6	3	4
T	11.5	50	6	3	4
V	10	50	4	3	4
W	9	80	5	7	4
Y	7.25	80	5	7	3

Table S8. Ebola virus surface glycoprotein epitopes. The identified IgG bound epitopes of the Ebola virus surface glycoprotein for the synthesized 1600 spots/cm^2, 4444 spots/cm^2, 10000 spots/cm^2 microarrays, as well as the commercial reference (CR) microarray with 1200 spots/cm^2 of the Ebola virus disease survivor are shown (Figure S40). Here, an epitope is defined by at least three consecutive peptides with fluorescence intensities above the limit of detection (1110 a. u., 1110 a. u., and 740 a. u. for the 1600 spots/cm^2, 4444 spots/cm^2, 10000 spots/cm^2 microarray). This equals 15, 15, and 10 times the limit of blank (74 a. u. = mean + 3.2 standard deviation; measured from the fluorescence intensity of the secondary antibodies). The limit of detection for the commercial reference microarray is 427 a. u., which equals seven times the limit of blank of 61 a. u.

Position	Sequence	1600	4444	10000	CR
36-55[3, 4]	GVIHNSTLQVSDVDKLVCRD	+	-	-	-
47-63[4]	DVDKLVCRDKLSSTNQL	-	+	-	-
70-92[3]	LEGNGVATDVPSATKRWGFRSGV	-	-	-	-
178-199[3]	EGVVAFLILPQAKKDFFSSHPL	+	+	178-196	178-197
223-239[4]	TGFGTNETEYLFEVDNL	+	+	220-238	221-239
231-254[3, 4]	EYLFEVDNLTYVQLESRFTPQFLL	+	231-249	231-255	-
237-256	DNLTYVQLESRFTPQFLLQL	-	+	-	-
311-327[4]	VSNGAKNISGQSPARTS	+	310-329	-	-
317-333[4]	NISGQSPARTSSDPGTN	-	+	-	-
388-406[4]	THNTPVYKLDISEATQVEQ	+	387-406	388-405	388-405
407-428[3]	HHRRTDNDSTASDTPSATTAAG	+	405-429	405-428	405-427
430-448	PKAENTNTSKSTDFLDPAT	+	426-449	426-445	-
448-464	TTTSPQNHSETAGNNNT	-	-	-	+
470-493[3, 4]	GEESASSGKLGLITNTIAGVAGLI	+	470-496	470-491	-
513-530	PNLHYWTTQDEGAAIGLA	+	513-533	+	511-527
619-654[3]	ITDKIDQIIHDFVDKTLPDQGDNDN WWTGWRQWIPA	+	620-653	620-650	620-653

Table S9. Ebola virus nucleoprotein epitopes. The identified IgG bound epitopes of the Ebola virus nucleoprotein for the synthesized 4444 spots/cm^2 and 10000 spots/cm^2 microarrays of the Ebola virus disease survivor are shown (Figure S41). Here, an epitope is defined by at least three consecutive peptides with fluorescence intensities above the limit of detection (1110 a. u. and 740 a. u. for the 4444 spots/cm^2 and 10000 spots/cm^2 microarrays). This equals 15 and 10 times the limit of blank (74 a. u. = mean + 3.2 standard deviation; measured from the fluorescence intensity of the secondary antibodies).

Position	Sequence	4444	10000
379-397[4]	FHQKKNEISFQQTNAMVTL	+	-
414-468[4]	LPKTSGHYDDDDDIPFPGPINDDDNPG HQDDDPTDSQDTTIPDVVVDPDDGSYGE	+	416-445
438-454	NPGHQDDDPTDSQDTTI	-	+
472-500[4]	YSENGMNAPDDLVLFDLDEDDEDTKPVPN	+	474-496
561-589	MLTPINEEADPLDDADDETSSLPPLESDD	+	568-585
581-601	SLPPLESDDEEQDRDGTSNRT	+	-
598-614	SNRTPTVAPPAPVYRDH	+	-
627-645	DQDHTQEARNQDSDNTQSE	+	-
676-692	VVFSTSDGKEYTYPDSL	+	675-692
681-697	SDGKEYTYPDSLEEEYP	-	+

Table S10. Ebola virus RNA-directed RNA polymerase L epitopes. The identified IgG bound epitopes of the Ebola virus RNA-directed RNA polymerase L for the synthesized 4444 spots/cm^2 and 10000 spots/cm^2 microarrays of the Ebola virus disease survivor are shown (Figure S42). Here, an epitope is defined by at least three consecutive peptides with fluorescence intensities above the limit of detection (1110 a. u. and 740 a. u. for the 4444 spots/cm^2 and 10000 spots/cm^2 microarrays). This equals 15 and 10 times the limit of blank (74 a. u. = mean + 3.2 standard deviation; measured from the fluorescence intensity of the secondary antibodies).

Position	Sequence	4444	10000
828-845	AIFDDLQGTLASIGTAFE	+	+
1224-1244	SRLTWVTQGSSNSDLLIKPFL	+	1224-1230
1282-1208	ANRMSNSATRLIVSTNTLGEFSGGGQS	+	1283-1208
1424-1440	LAKTIMQSIISDSNNSS	+	1424-1441
1652-1671	RKYLARDSSTGSSTNNSDGH	+	1652-1670
1769-1790	SQGTRQLTSSNESQTQDEISKY	+	1768-1787

Table S11. Ebola virus transcriptional activator VP30 epitopes. The identified IgG bound epitopes of the Ebola virus transcriptional activator VP30 for the synthesized 4444 spots/cm^2 and 10000 spots/cm^2 microarrays of the Ebola virus disease survivor are shown (Figure S43). Here, an epitope is defined by at least three consecutive peptides with fluorescence intensities above the limit of detection (1110 a. u. and 740 a. u. for the 4444 spots/cm^2 and 10000 spots/cm^2 microarrays). This equals 15 and 10 times the limit of blank (74 a. u. = mean + 3.2 standard deviation; measured from the fluorescence intensity of the secondary antibodies).

Position	Sequence	4444	10000
130-146	TADDFQQEEGPKITLLT	+	-
134-151	FQQEEGPKITLLTLIKTA	+	+
161-177	TIEDSKLRALLTLCAVM	+	-
262-278	RTLVPQSDNEEASTNPG	+	262-281
266-284	PQSDNEEASTNPGTCSWSD	+	-

Table S12. Ebola virus small secreted glycoprotein epitopes. The identified IgG bound epitopes of the Ebola virus small secreted glycoprotein from the synthesized 4444 spots/cm^2 and 10000 spots/cm^2 microarrays of the Ebola virus disease survivor are shown (Figure S44). Here, an epitope is defined by at least three consecutive peptides with fluorescence intensities above the limit of detection (1110 a. u. and 740 a. u. for the 4444 spots/cm^2 and 10000 spots/cm^2 microarrays). This equals 15 and 10 times the limit of blank (74 a. u. = mean + 3.2 standard deviation; measured from the fluorescence intensity of the secondary antibodies).

Position	Sequence	4444	10000
36-52	GVIHNSTLQVSDVDKLV	+	+
40-57	NSTLQVSDVDKLVCRDKL	+	-
51-68	LVCRDKLSSTNQLRSVGL	+	-
113-129	IKKPDGSECLPAAPDGI	+	-
178-199	EGVVAFLILPQAKKDFFSSHPL	+	178-196
223-242	TGFGTNETEYLFEVDNLTYV	+	220-238
231-256	EYLFEVDNLTYVQLESRFTPQFLLQL	+	231-252

Table S13. Ebola virus secreted glycoprotein epitopes. The identified IgG bound epitopes of the Ebola virus secreted glycoprotein for the synthesized 4444 spots/cm^2 and 10000 spots/cm^2 microarrays of the Ebola virus disease survivor are shown (Figure S45). Here, an epitope is defined by at least three consecutive peptides with fluorescence intensities above the limit of detection (1110 a. u. and 740 a. u. for the 4444 spots/cm^2 and 10000 spots/cm^2 microarrays). This equals 15 and 10 times the limit of blank (74 a. u. = mean + 3.2 standard deviation; measured from the fluorescence intensity of the secondary antibodies).

Position	Sequence	4444	10000
36-52	GVIHNSTLQVSDVDKLV	+	+
40-57	NSTLQVSDVDKLVCRDKL	+	-
51-68	LVCRDKLSSTNQLRSVGL	+	-
113-129	IKKPDGSECLPAAPDGI	+	-
178-199	EGVVAFLILPQAKKDFFSSHPL	+	178-196
223-242	TGFGTNETEYLFEVDNLTYV	+	220-238
231-256	EYLFEVDNLTYVQLESRFTPQFLLQL	+	231-252
285-305	IGEWAFWETKKTSLEKFAVKS	+	-

Table S14. Ebola virus matrix protein VP40 epitopes. The identified IgG bound epitopes of the Ebola virus matrix protein VP40 from the synthesized 4444 spots/cm^2 and 10000 spots/cm^2 microarrays of the Ebola virus disease survivor are shown (Figure S46). Here, an epitope is defined by at least three consecutive peptides with fluorescence intensities above the limit of detection (1110 a. u. and 740 a. u. for the 4444 spots/cm^2 and 10000 spots/cm^2 microarrays). This equals 15 and 10 times the limit of blank (74 a. u. = mean + 3.2 standard deviation; measured from the fluorescence intensity of the secondary antibodies).

Position	Sequence	4444	10000
3-25	RVILPTAPPEYMEAIYPVRSNST	+	3-20
22-38	SNSTIARGGNSNTGFLT	+	-
26-45	IARGGNSNTGFLTPESVNGD	+	-
40-60	ESVNGDTPSNPLRPIADDTID	+	40-56
99-115	GVADQKTYSFDSTTAAI	+	-
143-160	PDHPLRLLRIGNQAFLQE	+	-
216-234[4]	ILLPNKSGKKGNSADLTSP	+	-
242-258	TSLQDFKIVPIDPTKNI	+	-
246-265[4]	DFKIVPIDPTKNIMGIEVPE	+	-
275-294[4]	KVTSKNGQPIIPVLLPKYIG	+	-
286-311[4]	PVLLPKYIGLDPVAPGDLTMVITQDC	+	286-309

Table S15. Ebola virus polymerase cofactor VP35 epitopes. The identified IgG bound epitopes of the Ebola virus polymerase cofactor VP35 for the synthesized 4444 spots/cm^2 and 10000 spots/cm^2 microarrays of the Ebola virus disease survivor are shown (Figure S47). Here, an epitope is defined by at least three consecutive peptides with fluorescence intensities above the limit of detection (1110 a. u. and 740 a. u. for the 4444 spots/cm^2 and 10000 spots/cm^2 microarrays). This equals 15 and 10 times the limit of blank (74 a. u. = mean + 3.2 standard deviation; measured from the fluorescence intensity of the secondary antibodies).

Position	Sequence	4444	10000
13-36[4]	ATTQNDRMPGPELSGWISEQLMTG	+	15-32
36-52[4]	GRIPVSDIFCDIENNPG	+	-
40-59[4]	VSDIFCDIENNPGLCYASQM	+	-
145-164[4]	LVMTTGRATATAAATEAYWA	+	-
162-189[4]	YWAEHGQPPPGPSLYEESAIRGKIESR DETVPQSVREA	+	165-181
177-193[4]	EESAIRGKIESRDETVP	-	+
194-212[4]	QSVREAFNNLNSTTSLTEE	+	194-211
200-227[4]	FNNLNSTTSLTEENFGKPDISAKDLRNI	+	202-225

Table S16. Polymer and building block concentrations for the preparation of all used donor slides

Building block	Polymer [SLEC]
3 mg Fmoc-protected and OPfp-activated L-amino acid	27 mg
6 mg Fmoc-protected and OPfp-activated L-amino acid	24 mg
2-aminobenzoic acid **1** (10.00 mg, 72.92 µmol) in 500 µL acetone (no DMF)	27 mg
2-(3-formylphenoxy)acetic acid **2** (4.00 mg, 22.00 µmol, 1.00 equiv.),	27 mg
DIC (2.78 mg, 22.00 µmol, 1.00 equiv.), PfpOH (7.00 mg, 38.04 µmol, 1.73 equiv.)	
50 µL DMF containing 10 µg/mL Rhodamine 6G (Chemodex Ltd.)	20 mg
50 µL DMF containing 100 µg/mL Nile Blue A (Sigma-Aldrich Chemie GmbH)	20 mg

Table S17. Spin coating parameters. Approximated value for ρ_{SLEC} through polystyrene[7] polyacrylic acid.[8] The table was previously published in Paris et al.[9]

Parameter	Value	Unit
ρ_{DCM}	1330	kg m^{-3}
ρ_{SLEC}	≈ 1100	kg m^{-3}
$D_{DCM/air}$	$10.37 \cdot 10^{-6}$ [10]	m^2 s^{-1}
P_{DCM}	$47 \cdot 10^3$	Pa
M_{DCM}	$84.9 \cdot 10^{-3}$	kg mol^{-1}
R	8.3145	kg m^2 s^{-2} mol^{-1} K^{-1}
T	296.15	K
f	80	s^{-1}

Table S18. Coating thickness calculation and experimental analysis. Exponential fit of the kinematic viscosity v and the calculated coating thickness h.[11] The viscosity (dissolved in DCM with 3 different concentrations; 70 mg mL^{-1}, 100 mg mL^{-1}, and 135 mg mL^{-1}) was measured with a Shear Rheometer Anton Paar MCR 301 in the cone-plate mode rotating between 1000 and 3000 rounds per minute at 20 °C. The shown coating thickness measurements (mean ± standard deviation) are calculated from a sample size of three taken from different areas of the different donor slides. The was previously published in Paris et al.[9]

$v = 1.62 \cdot 10^{-7} + 1.82 \cdot 10^{-7} \mathrm{e}^{x_0/0.0323}$	
$h \cong 0.85 x_0 \dfrac{\rho_{DCM}}{\rho_{SLEC}} \left(\dfrac{v\sqrt{D_{DCM/air}} P_{DCM} M_{DCM}}{(2\pi f)^{3/2} \rho_{DCM} RT} \right)^{1/3}$	
Mass ratios x_0	**h theorectical [nm]**
0.030	≈ 185
0.038	≈ 246
0.045	≈ 314
0.052	≈ 391

Table S19. Lasing parameters of the used donor slides

Building block	Power [mW]	Duration [ms]
2-aminobenzoic acid **1** (10.00 mg, 72.92 µmol) in 500 µL acetone	190	14
2-(3-formylphenoxy)acetic acid **2** (4.00 mg, 22.00 µmol, 1.00 equiv.),	190	14
DIC (2.78 mg, 22.00 µmol, 1.00 equiv.), PfpOH (7.00 mg, 38.04 µmol,1.73 equiv.)		
50 µL DMF containing 10 µg/mL Rhodamine 6G	Variable	11
50 µL DMF containing 100 µg/mL Nile Blue A	Variable	13

Table S20. Fluorescence imaging scanning parameters

Sample staining	Wavelength [nm]	PMT
DyLight 633	635	600
CF 633 streptavidin	635	600
Control peptide HA Cy5	635	700
Control peptide Flag Cy3	532	460
Anti-Human IgG DyLight 650	635	600
2-((3-(carboxymethoxy)benzylidene)amino)benzoic acid (autofluorescence)	532	600
Rhodamine 6G 160	532	600
Nile blue A	635	500

Movie S1. Automated laser-based material transfer. The acceptor slide is placed into the lasing area and positioned by three positioning bolts. Then, a donor slide containing Rhodamine 6G is placed on top of the acceptor slide, laser-based materials transfer is initiated, and the donor slide is brought back to its original position. Repeating this procedure with a donor slide containing Nile blue A generates a red-green image (e.g., red-green parrot).

Supplementary references:

[1] S. Eickelmann, S. Moon, Y. Liu, B. Bitterer, S. Ronneberger, D. Bierbaum, F. Breitling, F. F. Loeffler, *Langmuir*, **2022**, *38*, 2220.

[2] V. Stadler, T. Felgenhauer, M. Beyer, S. Fernandez, K. Leibe, S. Güttler, M. Gröning, K. König, G. Torralba, M. Hausmann, V. Lindenstruth, A. Nesterov, I. Block, R. Pipkorn, A. Poustka, F. R. Bischoff, F. Breitling, *Angew. Chem. Int. Ed.* **2008**, *47,* 7132.

[3] J. Heidepriem, V. Krähling, C. Dahlke, T. Wolf, F. Klein, M. M. Addo, S. Becker, F. F. Loeffler, *Biotechnol. J.* **2020**, *15,* 2000069.

[4] P. Becquart, T. Mahlakõiv, D. Nkoghe, E. M. Leroy, *Plos One* **2014**, *9,* e96360.

[5] Kjerish,https://commons.wikimedia.org/wiki/File:RG_16bits_palette_sample_image.png, last accessed 01.07.2021.

[6] G. Paris, https://github.com/GrigoriParis/Grigori-Paris-PhD-code (App.py, laserClient.py, robot.py, and SAT in Spots we Trust.py), last accessed: 14.04.2021.

[7] Polystyrol (PS). Available online: https://www.kern.de/cgi-bin/riweta.cgi?nr=2101&lng=1 (accessed on 6 December 2021).

[8] F. Bracher, P. Heisig, P. Langguth, E. Mutschler, G. Rücker, T. Schirmeister, G. K. E. Scriba, E. Stahl-Biskup, R. Troschütz, *Arzneibuch-Kommentar*, Govi-Verlag, Eschborn, Germany **2018**.

[9] G. Paris, D. Bierbaum, M. Paris, D. Mager, F. F. Loeffler, *Appl. Sci.* **2022**, *12*, 1361.

[10] G. A. Lugg, *Anal. Chem.* **1968**, *40*, 1072.

[11] J. Danglad-Flores, S. Eickelmann, H. Riegler, *Eng. Rep.* **2021**, *3*, e12390.

4. Summary, conclusion and outlook

PMAs allow for fast high-throughput screening of many peptide-protein interactions in parallel. They can be used for infectious disease research to detect antibodies, which are specific for linear epitopes. In two projects, PMAs were combined with ELISA to analyze antibody responses to antigens of an infection or vaccination and detect linear peptide epitopes.

In *Epitopes of Naturally Acquired and Vaccine-Induced Anti-Ebola Virus Glycoprotein Antibodies in Single Amino Acid Resolution,* we analyzed the antibody response of rVSV-ZEBOV vaccine recipients and an EVD survivor in an ELISA for EBOV-specific IgG and on PMAs carrying overlapping peptides of the EBOV GP with one AA offset. The vaccine dose did not correlate with the measured EBOV-specific IgG or the detected number of epitopes. For the vaccine recipients, we detected more IgM than IgG reactive epitopes overlapping in the same peptide position for several vaccine recipients. The EVD survivor showed overall a broader epitope recognition than the vaccine recipients. Furthermore, some vaccine-induced and naturally acquired epitopes were detected in the same protein position and similar epitopes have been described earlier in the literature [119, 120]. With more sera of vaccine recipients, a possible correlation of vaccine dose and antibody response could have been analyzed with greater statistical confidence. Additionally, more sera of EVD (Zaire) survivors could have supported the significance of the analysis.

In *Longitudinal Development of Antibody Responses in COVID-19 Patients of Different Severity with ELISA, Peptide, and Glycan Arrays: An Immunological Case Series*, we analyzed antibody responses of COVID-19 patients during disease progression with three different assays. First, the sera of patients were analyzed with spike glycoprotein subunit 1 ELISA for IgA, IgG and IgM. Second, the sera were screened on MAs carrying overlapping peptides of the whole SARS-CoV-2 proteome and MAs with different immobilized glycans. In patient #1 with moderate symptoms, the level of antibodies detected in the ELISA and the number of peptide epitopes increased over time of the disease. For patient #2 and #3 with mild symptoms, the IgA level measured with ELISA, whereas the IgG level increased over time. The number of detected IgA and IgG peptide epitopes decreased over time for the two patients #2 and #3 with mild symptoms, whereas it increased for patient #1 with moderate symptoms. For all patients, IgA and IgG reactive peptide epitopes in the S GP were identified. The number of detected S GP epitopes followed the same trend over time as the sum of epitopes against the whole SARS-CoV-2 proteome in the patients. A changing antibody binding to a few glycans over time was observed. The IgM response of patient #1 showed the highest increase in glycan binding over time. However, the antibody response to the immobilized glycans was less specific for the other patients. The antibody response of patients with different severity of symptoms could be followed over time with ELISA and PMAs and revealed clearly

recognizable differences. Therefore, a link between the severity of symptoms and the time, for which the number of detected epitopes peaked, was assumed. With more patient sera, this hypothetical link could have been analyzed with statistical confidence. In the future, a more suitable collection of glycans or even glycopeptides could be screened for their recognition by antibodies.

The two projects proved the versatility of peptide microarrays in the field of vaccine development and infectious disease analysis. The detection of linear epitopes is fast and can support the investigation of antibody responses to antigens of pathogens or vaccine-related antigens [59, 62, 63, 129]. The epitope mapping with PMAs can shed light on the question, if humans respond individually to antigens or if they share the same reactive epitopes. This can be important for modern vaccine development, where only specific antigens are targeted instead of using the whole attenuated or inactivated pathogen. The first project showed that the use of ELISA and PMAs could help determining dose-dependent efficacy of a vaccine or the influence of boost vaccinations, because of their ability to compare antibody levels on different time points. Recurring linear epitopes in several individuals could indicate immunogenic parts of an antigen and could be targets for neutralizing antibodies.

With proteome-wide epitope mapping, disease associated biomarkers can be identified. The selected biomarkers can then facilitate the analysis of many samples with less synthetic effort than producing full-proteome PMAs or the entire antigen. Biomarkers could be used to distinguish diseases or to monitor immune responses of a patient over time.

In general, PMAs can only identify linear continuous epitopes, which make up about 10% of all recognized epitopes [40-42]. Especially linear B cell epitopes are interesting, because they can still be recognized by T helper cells after antigen digestion and presentation. Furthermore, they have the potential to replace a whole antigen, what is needed for the development of peptide-based vaccines. It is also possible to produce cyclic peptides in the MA format and therefore, get evidence for the importance of folded structures. It could be interesting to include these in further studies. Nevertheless, for the detection of discontinuous conformational epitopes, the current PMA technology is not suitable and ELISA can only determine the relative amount of antigen-binding antibodies.

For the herein used commercial PMAs, the cost per analysis is relatively high (~ 1000 € per sample with proteome array; ~200 € per sample with one protein). Moreover, only two peptide replicates are available per array. More peptide spots would be necessary to calculate reliable mean and standard deviation.

Both projects applying PMA would have benefited from a higher number of samples to confirm the observed trends. As the costs for commercial PMAs limit the number of analyzed samples, the projects could have also benefited from a higher peptide density for more throughput per array. The particle-based printing technology (commercialized by PEPperPRINT) allows for a flexible in situ

synthesis of PMAs, but is limited to relatively low spot densities in comparison to for example the photolithographic synthesis. In contrast, technologies for PMA production relying on the SPOT synthesis are restricted to the possible number of different peptide sequences synthesized in parallel.

In *Automated Laser-Transfer Synthesis of High-Density Microarrays for Infectious Disease Screening,* we developed a laser-based in situ synthesis method for MAs to screen thousands of peptides, which is required for proteome-wide analyses. We engineered an automated synthesizer for slide transport and spot deposition by laser transfer. This reduced manual handling and positioning errors and significantly sped up the synthesis duration. Furthermore, we implemented an optimization pipeline for the in situ synthesis of peptides, which could also be adapted for other molecules, such as fluorophores. The pipeline included the optimization of various synthesis parameters, such as lasing power and duration, coupling cycles, donor slide stability, and reusability. Additionally, automated spot detection assisted the quantification of spot width and fluorescence intensity of the coupled and stained AAs. We performed multiple test syntheses to evaluate the influence of the optimized parameters on the peptide synthesis yield and to identify shortcomings. We accomplished important milestones, e.g., equal spot width, increase of coupling yield for demanding AAs (His, Arg, Pro, Trp), and the synthesis of long peptides (up to 20 residues). Finally, we synthesized full combinatorial PMAs carrying the EBOV proteome as overlapping 15-mer peptides. We validated our array quality by comparing the antibody binding to an identical commercial PMA. Furthermore, we identified that the 150 µm spot pitch (4444 peptides per cm^2) is the smallest spot pitch resulting in high peptide yield. Our cLIFT-arrays allowed for enhanced epitope detection and higher peptide density compared the commercial PMA of PEPperPRINT.

Due to the excellent results and the small spot width, the parameters used for the 150 µm spot pitch synthesis could be applied for a 140 µm spot pitch without the need for further optimizations, resulting in > 5000 peptides per cm^2. For higher densities, more coupling cycles or material transfer optimization might be required to increase the coupling yield. However, more cycles would result in a more time-consuming and material-intensive process. Therefore, it should be investigated, if the stacking of multiple spots on top of each other could increase the amount of coupled building block. Since our investigations revealed that the spot is only nanometers high, repetitive transfers could be applicable to increase the volume by raising the spot height without increasing the spot width during the melting process. The material deposition could be further modified by changing the properties of the acceptor slide and the polymer of the donor slide film, as shown recently [130]. In another approach, the acceptor slide wettability could be decreased, causing an increased spot contact angle. Consequently, this could lead to a smaller spot size with higher spot volume, resulting in more deposited building block per area.

To this day, the cLIFT process is well-studied, allowing for precise patterning [108]. The now automated laser-transfer and the accelerated process (e.g., automated slide transport and shortened coupling duration) enable a reproducible and faster PMA synthesis. However, the required time for manual work is still the largest cost factor and could be reduced by further automation. The donor slide preparation has the greatest potential for further saving. The high amount of donor slides needed for a synthesis is the most time-consuming factor. In the future, it should be investigated, if the material film can be modified to increase the reusability for higher production throughput with a lower number of donor slides. Moreover, the spin coating process is inefficient, because only a small portion of the solution is adhering to the blank donor slide to create the material film. Other methods, like spray-coating or blade-coating should be investigated for a faster and material-saving donor slide preparation. This would reduce the production cost and allow for syntheses using building blocks, which are more expensive. Next to the improvements of the donor slide film preparation, also the washing, deprotection and capping steps of slides should be automated to further reduce the manual work. Systems for this purpose are already available. For further cost reduction, a device for laser-based transfer can be even constructed from cheap components [131].

PMAs are not only useful for the analysis of antibody binding. They can be applied for the determination of peptide substrates for enzymes [64]. Furthermore, PMAs could be used to test the catalytic activity of enzyme-derived peptides, if the reaction can be visualized with a dye for detection. In general, the strength of the cLIFT method is the flexible exchange of donor slides and therefore the use of different building blocks for broad applications. Monomers, such as D-AAs, modified AAs, or non-natural AAs could be employed in the future. Today, glycosylated AAs can be used for the synthesis of glycopepides, but these building blocks are very expensive. For parallel glycopeptide synthesis, SPOT synthesis on cellulose membranes can be applied [133]. The use of glycosylated AAs could also be a promising application for synthesis with cLIFT. Multivalent glycan structures for lectin-binding studies have been produced by synthesizing non-natural peptide scaffolds with cLIFT for functionalization from solution with sugar azides using CuAAC [134, 135]. Apart from biomolecule synthesis, potentially any molecule with a suitable functional moiety could be attached to the surface of a MA. Usually, well-defined reactions with high yield (e.g., amide bond formation) are performed for the attachment to the surface. Other reactions are also possible, such as shown with the Schiff base formation for fluorescence dye synthesis. However, for the detection of in situ synthesized molecules, we have manly relied on fluorescence imaging, which is limiting the scope of molecules. A great challenge of the small-scale synthesis is the very limited possibility for chemical analysis of the synthesized molecules. Matrix-assisted laser desorption/ionization mass spectrometry (MALDI-MS) imaging for single spot analysis typically requires a conductive surface or a special MALDI-MS setup, and is not yet applied on a regular basis [107].

Next to normalized fluorescence detection (e.g., using antibody staining) that can be used to analyze many peptides in parallel, a chemical analysis method should be considered to obtain more in-depth understanding of the coupling yield during each step. To calculate the coupling of the AAs, we measured the 9-methylene-9H-fluorene-piperidine or dibenzofulvene-piperidine absorbance. Due to the low acceptor slide loading (1-2 nmol/cm^2), the absorbance after AA coupling was below a reliable measuring range and the values strongly varied. Therefore, an adaptation of this method or a different technique could be proposed in the future. This would reveal weak points in the process, which can then be specifically optimized.

5. References

[1]   Williams, M. A. (2013). Protein-ligand interactions: Fundamentals. In: Williams, M., Daviter, T. Protein-Ligand Interactions. *Methods in Molecular Biology*, 1008, 3-34.

[2]   Fan, Y., Li, X., Zhang, L., Wan, S., Zhang, L., Zhou, F. (2022). SARS-CoV-2 Omicron variant: recent progress and future perspectives. *Signal Transduction and Targeted Therapy*, 7.141.

[3]   Böck, A., Forchhammer, K., Heider, J., Leinfelder, W., Sawers, G., Veprek, B., Zinoni, F. (1991). Selenocysteine: the 21st amino acid. Molecular Microbiology, 5(3), 515-520.

[4]   J. M. Berg, J. M., Tymoczko, J. L., Stryer, L. (2002). Biochemistry. 5th Edition. *W. H. Freeman & Company Publishing*.

[5]   Pauling, L., & Corey, R. B. (1951). Configurations of Polypeptide Chains with Favored Orientations Around Single Bonds: Two New Pleated Sheets. *Proceedings of the National Academy of Sciences of the United States of America*, 37(11), 729-740.

[6]   Harata K, Muraki M, Jigami Y. (1993) Role of Arg115 in the catalytic action of human lysozyme. X-ray structure of His115 and Glu115 mutants. *Journal of molecular biology,* 233(3) 524-535.

[7]   Di Lullo, G. A., Sweeney, S. M., Körkkö, J., Ala-Kokko, L., & San Antonio, J. D. (2002). Mapping the ligand-binding sites and disease-associated mutations on the most abundant protein in the human, type I collagen. *The Journal of biological chemistry*, 277(6), 4223-4231.

[8]   Varki, A., Cummings, R. D., Esko, J. D., Stanley, P., Hart, G. W., Aebi, M., Mohnen, D., Kinoshita, T., Packer, N. H., Prestegard, J. J., Schnaar, R. L., Seeberger, P. H. (2022) Essentials of Glycobiology. 4th edition. *Cold Spring Harbor (NY).*

[9]   Murphy, K., Travers, P., Walport, M. (2011). Janeway´s Immunobiology, 8th edition. *Garland Science.*

[10]   Yuseff, M. I., Pierobon, P., Reversat, A., & Lennon-Duménil, A. M. (2013). How B cells capture, process and present antigens: a crucial role for cell polarity. *Nature reviews Immunology*, 13(7), 475-486.

[11]   Harvey, B. P., Gee, R. J., Haberman, A. M., Shlomchik, M. J., & Mamula, M. J. (2007). Antigen presentation and transfer between B cells and macrophages. *European journal of immunology*, 37(7), 1739-1751.

[12]   Heesters, B. A., van der Poel, C. E., Das, A., & Carroll, M. C. (2016). Antigen Presentation to B Cells. *Trends in immunology*, 37(12), 844–854.

[13]   McShane, A. N., & Malinova, D. (2022). The Ins and Outs of Antigen Uptake in B cells. *Frontiers in immunology*, 13, 892169.

[14]   Zhu, Q., Zhang, M., Shi, M., Liu, Y., Zhao, Q., Wang, W., Zhang, G., Yang, L., Zhi, J., Zhang, L., Hu, G., Chen, P., Yang, Y., Dai, W., Liu, T., He, Y., Feng, G., & Zhao, G. (2016). Human B cells have an active phagocytic capability and undergo immune activation upon phagocytosis of Mycobacterium tuberculosis. *Immunobiology*, 221(4), 558-567.

[15]   Hoogeboom, R., Tolar, P. (2015). Molecular Mechanisms of B Cell Antigen Gathering and Endocytosis. In: Kurosaki, T., Wienands, J. B Cell Receptor Signaling. *Current Topics in Microbiology and Immunology*, 393, 45-63.

[16]   Crotty S. (2015). A brief history of T cell help to B cells. *Nature reviews Immunology*, 15(3), 185-189.

[17]   McHeyzer-Williams, M., Okitsu, S., Wang, N., McHeyzer-Williams, L. (2011). Molecular programming of B cell memory. *Nature reviews Immunology*, 12(1), 24-34.

[18]   Kambayashi, T., & Laufer, T. M. (2014). Atypical MHC class II-expressing antigen-presenting cells: Can anything replace a dendritic cell?. *Nature reviews Immunology*, 14(11), 719-730.

[19]   Nutt, S. L., Hodgkin, P. D., Tarlinton, D. M., & Corcoran, L. M. (2015). The generation of antibody-secreting plasma cells. *Nature reviews Immunology*, 15(3), 160-171.

[20]   Wieczorek, M., Abualrous, E. T., Sticht, J., Álvaro-Benito, M., Stolzenberg, S., Noé, F., & Freund, C. (2017). Major Histocompatibility Complex (MHC) Class I and MHC Class II Proteins: Conformational Plasticity in Antigen Presentation. *Frontiers in immunology*, 8, 292.

[21]   Huppa, J. B., & Davis, M. M. (2003). T-cell-antigen recognition and the immunological synapse. *Nature reviews Immunology*, 3(12), 973-983.

[22]   Kumar, B. V., Connors, T. J., & Farber, D. L. (2018). Human T Cell Development, Localization, and Function throughout Life. *Immunity*, 48(2), 202-213.

[23]   Gourley, T. S., Wherry, E. J., Masopust, D., & Ahmed, R. (2004). Generation and maintenance of immunological memory. *Seminars in immunology*, 16(5), 323-333.

[24]   Kaech, S. M., & Wherry, E. J. (2007). Heterogeneity and cell-fate decisions in effector and memory CD8+ T cell differentiation during viral infection. *Immunity*, 27(3), 393-405.

[25]   Stern, L. J., & Wiley, D. C. (1994). Antigenic peptide binding by class I and class II histocompatibility proteins. *Behring Institute Mitteilungen*, 94, 1-10.

[26]   Madden D. R. (1995). The three-dimensional structure of peptide-MHC complexes. *Annual review of immunology*, 13, 587-622.

[27]   Sanchez-Trincado, J. L., Gomez-Perosanz, M., & Reche, P. A. (2017). Fundamentals and Methods for T- and B-Cell Epitope Prediction. *Journal of immunology research*, 2017, 2680160.

[28]   Kloypan, C., Koomdee, N., Satapornpong, P., Tempark, T., Biswas, M., & Sukasem, C. (2021). A Comprehensive Review of *HLA* and Severe Cutaneous Adverse Drug Reactions: Implication for Clinical Pharmacogenomics and Precision Medicine. *Pharmaceuticals*, 14(11), 1077.

[29]   Webster, D. M., Henry, A. H., & Rees, A. R. (1994). Antibody-antigen interactions. *Current Opinion in Structural Biology*, 4 (1), 123-129.

[30]   Al Qaraghuli, M. M., Palliyil, S., Broadbent, G., Cullen, D. C., Charlton, K. A., & Porter, A. J. (2015). Defining the complementarities between antibodies and haptens to refine our understanding and aid the prediction of a successful binding interaction. *BMC Biotechnology*, 15, 99.

[31]   Brandtzaeg P. (2013). Secretory IgA: Designed for Anti-Microbial Defense. *Frontiers in Immunology*, 4, 222.

[32]   Lu, L., Suscovich, T., Fortune, S., Alter, G. (2018). Beyond binding: antibody effector functions in infectious diseases. *Nature Reviews Immunology*, 18(1), 46-61.

[33]   Tonegawa S. (1983). Somatic generation of antibody diversity. *Nature*, 302(5909), 575-581.

[34]   Komori, T., Okada, A., Stewart, V., & Alt, F. W. (1993). Lack of N regions in antigen receptor variable region genes of TdT-deficient lymphocytes. *Science*, 261(5125), 1171-1175.

[35]   Alt, F. W., Yancopoulos, G. D., Blackwell, T. K., Wood, C., Thomas, E., Boss, M., Coffman, R., Rosenberg, N., Tonegawa, S., & Baltimore, D. (1984). Ordered rearrangement of immunoglobulin heavy chain variable region segments. *The EMBO Journal*, 3(6), 1209-1219.

[36]   Shlomchik, M. J., & Weisel, F. (2012). Germinal center selection and the development of memory B and plasma cells. *Immunological Reviews*, 247(1), 52-63.

[37]   Larson, E. D., & Maizels, N. (2004). Transcription-coupled mutagenesis by the DNA deaminase AID. *Genome Biology*, 5(3), 211.

[38]   Stavnezer, J., & Amemiya, C. T. (2004). Evolution of isotype switching. *Seminars in Immunology*, 16(4), 257-275.

[39]   Kéri, G. & Toth, I. (2003) Molecular Pathomechanisms and New Trends in Drug Research. 1st edition. *Imprint CRC Press*.

[40]   Barlow, D. J., Edwards, M. S., & Thornton, J. M. (1986). Continuous and discontinuous protein antigenic determinants. *Nature*, 322(6081), 747-748.

[41]   Van Regenmortel, M. H. V. (1996). Mapping Epitope Structure and Activity: From One-Dimensional Prediction to Four-Dimensional Description of Antigenic Specificity. *Methods*, 9(3), 465-472.

[42]   Andersen, P.H., Nielsen, M., & Lund, O. (2006). Prediction of residues in discontinuous B-cell epitopes using protein 3D structures. *Protein Science*, 15(11), 2558-2567.

[43]   Atsmon, J., Caraco, Y., Ziv-Sefer, S., Shaikevich, D., Abramov, E., Volokhov, I., Bruzil, S., Haima, K. Y., Gottlieb, T., & Ben-Yedidia, T. (2014). Priming by a novel universal influenza vaccine (Multimeric-001)-a gateway for improving immune response in the elderly population. *Vaccine*, 32(44), 5816-5823.

[44]   Nilvebrant, J., & Rockberg, J. (2018). An Introduction to Epitope Mapping. *Methods in Molecular Biology*, 1785, 1-10.

[45]   Cunningham, B. C., & Wells, J. A. (1989). High-resolution epitope mapping of hGH-receptor interactions by alanine-scanning mutagenesis. *Science*, 244(4908), 1081-1085.

[46]   Ahmad, T. A., Eweida, A. E., & Sheweita, S. A. (2016). B-cell epitope mapping for the design of vaccines and effective diagnostics. *Trials in Vaccinology*, 5, 71-83.

[47]   Ledsgaard, L., Kilstrup, M., Karatt-Vellatt, A., McCafferty, J., & Laustsen, A. H. (2018). Basics of Antibody Phage Display Technology. *Toxins*, 10(6), 236.

[48]   Bartling, C., Jensen, T., Henry, S. M., Colliander, A. L., Sereikaite, V., Wenzler, M., Jain, P., Maric, H. M., Harpsøe, K., Pedersen, S. W., Clemmensen, L. S., Haugaard-Kedström, L. M., Gloriam, D. E., Ho, A., & Strømgaard, K. (2021). Targeting the APP-Mint2 Protein-Protein Interaction with a Peptide-Based Inhibitor Reduces Amyloid-β Formation. *Journal of the American Chemical Society*, 143(2), 891-901.

[49]   Weber, L. K., Palermo, A., Kügler, J., Armant, O., Isse, A., Rentschler, S., Jaenisch, T., Hubbuch, J., Dübel, S., Nesterov-Mueller, A., Breitling, F., Loeffler, F. F. (2017). Single amino acid fingerprinting of the human antibody repertoire with high density peptide arrays, *Journal of Immunological Methods*, 443, 45-54.

[50]   Palermo, A., Weber, L. K., Rentschler, S., Isse, A., Sedlmayr, M., Herbster, K., List, V., Hubbuch, J., Löffler, F. F., Nesterov-Müller, A., & Breitling, F. (2017). Identification of a Tetanus Toxin Specific Epitope in Single Amino Acid Resolution. *Biotechnology Journal*, 12(10).

[51]   Liu, Y., Childs, R. A., Palma, A. S., Campanero-Rhodes, M. A., Stoll, M. S., Chai, W., & Feizi, T. (2012). Neoglycolipid-based oligosaccharide microarray system: preparation of NGLs and their noncovalent immobilization on nitrocellulose-coated glass slides for microarray analyses. *Methods in Molecular Biology*, 808, 117-136.

[52]   Heo, H. R., Joo, K. I., Seo, J. H., Kim, C. S., & Cha, H. J. (2021). Glycan chip based on structure-switchable DNA linker for on-chip biosynthesis of cancer-associated complex glycans. *Nature Communications*, 12(1), 1395.

[53]   Bumgarner, R. (2013). Overview of DNA microarrays: types, applications, and their future. *Current Protocols in Molecular Biology*, 22.1.

[54]   Chen, Z., Dodig-Crnković, T., Schwenk, J. M., & Tao, S. C. (2018). Current applications of antibody microarrays. *Clinical proteomics*, 15, 7.

[55]   Sutandy, F. X., Qian, J., Chen, C. S., & Zhu, H. (2013). Overview of protein microarrays. *Current protocols in protein science*, Chapter 27(1), 2711-27.1.

[56]   Spurrier, B., Ramalingam, S. & Nishizuka, S. (2008). Reverse-phase protein lysate microarrays for cell signaling analysis. *Nature Protocols,* 3, 1796-1808.

[57]   Mueller, C., Liotta, L. A., & Espina, V. (2010). Reverse phase protein microarrays advance to use in clinical trials. *Molecular oncology*, 4(6), 461-481.

[58]   Kornblau, S. M., & Coombes, K. R. (2011). Use of reverse phase protein microarrays to study protein expression in leukemia: technical and methodological lessons learned. *Methods in Molecular Biology*, 785, 141-155.

[59]   Loeffler, F. F., Viana, I. F. T., Fischer, N., Coêlho, D. F., Silva, C. S., Purificação Jr., A. F., Araújo, C. M. C. S., Leite, B. H. S., Durães-Carvalho, R., Magalhães, T., Morais, C. N. L., Cordeiro, M. T., Lins, R. D., Marques, E. T. A., Jaenisch, T. (2021). Identification of a Zika NS2B epitope as a biomarker for severe clinical phenotypes. *RSC Medicinal Chemistry*, 12(9), 1525-1539.

[60]   Seco, B. M. S., Xu, F. F., Grafmüller, A., Kottari, N., Pereira, C. L., & Seeberger, P. H. (2020). Sequential Linkage of Carbohydrate Antigens to Mimic Capsular Polysaccharides: Toward Semisynthetic Glycoconjugate Vaccine Candidates against *Streptococcus pneumoniae* Serotype 14. *ACS Chemical Biology*, 15(9), 2395-2405.

[61] Geysen, H. M., Meloen, R. H., & Barteling, S. J. (1984). Use of peptide synthesis to probe viral antigens for epitopes to a resolution of a single amino acid. *Proceedings of the National Academy of Sciences of the United States of America*, 81(13), 3998-4002.

[62] Jaenisch, T., Heiss, K., Fischer, N., Geiger, C., Bischoff, F. R., Moldenhauer, G., Rychlewski, L., Sié, A., Coulibaly, B., Seeberger, P. H., Wyrwicz, L. S., Breitling, F., & Loeffler, F. F. (2019). High-density Peptide Arrays Help to Identify Linear Immunogenic B-cell Epitopes in Individuals Naturally Exposed to Malaria Infection. *Molecular & Cellular Proteomics*, 18(4), 642–656.

[63] Fathi, A., Dahlke, C., Krähling, V., Kupke, A., Okba, N., Raadsen, M. P., Heidepriem, J., Müller, M. A., Paris, G., Lassen, S., Klüver, M., Volz, A., Koch, T., Ly, M. L., Friedrich, M., Fux, R., Tscherne, A., Kalodimou, G., Schmiedel, S., Corman, V. M., Hesterkamp, T., Drosten, C., Loeffler, F. F., Haagmans, B. L., Sutter, G., Becker, S., Addo, M. M. (2022). Increased neutralization and IgG epitope identification after MVA-MERS-S booster vaccination against Middle East respiratory syndrome. *Nature Communications*, 13(1), 4182.

[64] Shi, J., Sharif, S., Ruijtenbeek, R., & Pieters, R. J. (2016). Activity Based High-Throughput Screening for Novel O-GlcNAc Transferase Substrates Using a Dynamic Peptide Microarray. *PloS One*, 11(3), e0151085.

[65] Merrifield, R.B. (1963). Solid Phase Peptide Synthesis. I. Synthesis of a Tetrapeptide. *Journal of the American Chemical Society*, 85(14), 2149-2154.

[66] Merrifield, R.B. (1965). Automated Synthesis of Peptides. *Science*, 150(3693), 178-185.

[67] Marglin, A. and Merrifield, R. B. (1966) The synthesis of bovine insulin by the solid phase method. *Journal of the American Chemical Society*, 88(21), 5051-5052.

[68] Caruthers M. H. (1985). Gene synthesis machines: DNA chemistry and its uses. *Science*, 230(4723), 281-285.

[69] Plante, O. J., Palmacci, E. R., & Seeberger, P. H. (2001). Automated solid-phase synthesis of oligosaccharides. *Science*, 291(5508), 1523-1527.

[70] Jensen K. J. (2013). Solid-phase peptide synthesis: an introduction. *Methods in Molecular Biology*, 1047, 1–21.

[71] Carpino, L. A. & Han, G.Y. (1972). 9-Fluorenylmethoxycarbonyl Amino-Protecting Group. *Journal of Organic Chemistry*, 37(22), 3404-3409.

[72] Chan, W. C. & White, P.D. (1999) Fmoc solid phase peptide synthesis: A practical approach. *Oxford University Press.*

[73] Behrendt, R., White, P., & Offer, J. (2016). Advances in Fmoc solid-phase peptide synthesis. *Journal of Peptide Science*, 22(1), 4-27.

[74] Frank, R. (1992). Spot-Synthesis -An Easy Technique for the Positionally Addressable, Parallel Chemical Synthesis on a Membrane Support. *Tetrahedron*, 48(42), 9217-9232.

[75] Frank R. (2002). The SPOT-synthesis technique. Synthetic peptide arrays on membrane supports--principles and applications. *Journal of Immunological Methods*, 267(1), 13-26.

[76] Dikmans, A., Beutling, U., Schmeisser, E., Thiele, S., Frank, R. (2006). SC2: A novel process for manufacturing multipurpose high-density chemical microarrays. *QSAR & Combinatorial Science*, 25(11), 1069-1080.

[77] Benz, M., Molla, M. R., Böser, A., Rosenfeld, A., & Levkin, P. A. (2019). Marrying chemistry with biology by combining on-chip solution-based combinatorial synthesis and cellular screening. *Nature Communications*, 10(1), 2879.

[78] Lin, W., Gandhi, S., Oviedo Lara, A. R., Thomas, A. K., Helbig, R., & Zhang, Y. (2021). Controlling Surface Wettability for Automated In Situ Array Synthesis and Direct Bioscreening. *Advanced Materials*, 33(36), e2102349.

[79] Hirtz, M., Varey, S., Fuchs, H., & Vijayaraghavan, A. (2016). Attoliter Chemistry for Nanoscale Functionalization of Graphene. *ACS Applied Materials & Interfaces*, 8(49), 33371-33376.

[80] Atwater, J., Mattes, D. S., Streit, B., von Bojničić-Kninski, C., Loeffler, F. F., Breitling, F., Fuchs, H., & Hirtz, M. (2018). Combinatorial Synthesis of Macromolecular Arrays by Microchannel Cantilever Spotting (µCS). *Advanced Materials*, 30(31), e1801632.

[81] Fodor, S. P., Read, J. L., Pirrung, M. C., Stryer, L., Lu, A. T., & Solas, D. (1991). Light-directed, spatially addressable parallel chemical synthesis. *Science*, 251(4995), 767-773.

[82] Singh-Gasson, S., Green, R. D., Yue, Y., Nelson, C., Blattner, F., Sussman, M. R., & Cerrina, F. (1999). Maskless fabrication of light-directed oligonucleotide microarrays using a digital micromirror array. *Nature Biotechnology*, 17(10), 974-978.

[83] Hansen, L. B., Buus, S., & Schafer-Nielsen, C. (2013). Identification and Mapping of Linear Antibody Epitopes in Human Serum Albumin Using High-Density Peptide Arrays. *Plos One*, 8(7), e68902.

[84] Buus, S., Rockberg, J., Forsström, B., Nilsson, P., Uhlen, M., & Schafer-Nielsen, C. (2012). High-resolution mapping of linear antibody epitopes using ultrahigh-density peptide microarrays. *Molecular & Cellular Proteomics*, 11(12), 1790-1800.

[85] Shin, D. S., Lee, K. N., Yoo, B. W., Kim, J., Kim, M., Kim, Y. K., & Lee, Y. S. (2010). Automated maskless photolithography system for peptide microarray synthesis on a chip. *Journal of Combinatorial Chemistry*, 12(4), 463-471.

[86] Heiss, K., Heidepriem, J., Fischer, N., Weber, L. K., Dahlke, C., Jaenisch, T., & Loeffler, F. F. (2020). Rapid Response to Pandemic Threats: Immunogenic Epitope Detection of Pandemic Pathogens for Diagnostics and Vaccine Development Using Peptide Microarrays. *Journal of Proteome Research*, 19(11), 4339-4354.

[87] Bhushan, K. R., DeLisi, C., & Laursen, R. A. (2003). Synthesis of photolabile 2-(2-nitrophenyl)propyloxycarbonyl protected amino acids. *Tetrahedron Letters*, 44(47), 8585-8588.

[88] Kretschy, N., Holik, A. K., Somoza, V., Stengele, K. P., & Somoza, M. M. (2015). Next-Generation o-Nitrobenzyl Photolabile Groups for Light-Directed Chemistry and Microarray Synthesis. *Angewandte Chemie (International Edition in English)*, 54(29), 8555-8559.

[89] Pellois, J. P., Zhou, X., Srivannavit, O., Zhou, T., Gulari, E., & Gao, X. (2002). Individually addressable parallel peptide synthesis on microchips. *Nature Biotechnology*, 20(9), 922-926.

[90] Legutki, J. B., Zhao, Z.-G., Greving, M., Woodbury, N., Johnston, S. A., & Stafford, P. (2014). Scalable high-density peptide arrays for comprehensive health monitoring. *Nature Communications*, 5, 4785.

[91] Beyer, M., Nesterov, A., Block, I., König, K., Felgenhauer, T., Fernandez, S., Leibe, K., Torralba, G., Hausmann, M., Trunk, U., Lindenstruth, V., Bischoff, F. R., Stadler, V., & Breitling, F. (2007). Combinatorial synthesis of peptide arrays onto a microchip. *Science*, 318(5858), 1888.

[92] Loeffler, F., Schirwitz, C., Wagner, J., Koenig, K., Maerkle, F., Torralba, G., Hausmann, M., Bischoff, F. R., Nesterov-Mueller, A., & Breitling, F. (2012). Biomolecule Arrays Using Functional Combinatorial Particle Patterning on Microchips. *Advanced Functional Materials*, 22(12), 2503-2508.

[93] Stadler, V., Felgenhauer, T., Beyer, M., Fernandez, S., Leibe, K., Güttler, S., Gröning, M., König, K., Torralba, G., Hausmann, M., Lindenstruth, V., Nesterov, A., Block, I., Pipkorn, R., Poustka, A., Bischoff, F. R., & Breitling, F. (2008). Combinatorial synthesis of peptide arrays with a laser printer. *Angewandte Chemie (International Edition in English)*, 47(37), 7132-7135.

[94] Maerkle, F., Loeffler, F. F., Schillo, S., Foertsch, T., Muenster, B., Striffler, J., Schirwitz, C., Bischoff, F. R., Breitling, F., & Nesterov-Mueller, A. (2014). High-density peptide arrays with combinatorial laser fusing. *Advanced Materials*, 26(22), 3730-3734.

[95] Serra, P., & Pique, A. (2019). Laser-Induced Forward Transfer: Fundamentals and Applications. *Advanced Materials Technologies*, 4(1), 1800099.

[96] Bohandy, J., Kim, B. F., & Adrian, F. J. (1986). Metal-Deposition from a Supported Metal-Film Using an Excimer Laser. *Journal of Applied Physics*, 60(4), 1538-1539.

[97] Bohandy, J., Kim, B. F., Adrian, F. J., & Jette, A. N. (1988). Metal-Deposition at 532 nm using a Laser Transfer Technique. *Journal of Applied Physics*, 63(4), 1158-1162.

[98] Piqué, A., Chrisey, D. B., Auyeung, R. C. Y., Fitz-Gerald, J., Wu, H. D., McGill, R. A., Lakeou, S., Wu, P. K., Nguyen, V., & Duignan, M. (1999) A novel laser transfer process for direct writing of electronic and sensor materials. *Applied Physics A: Materials Science and Processing,* 69, 79-284.

[99] Duocastella, M., Fernández-Pradas, J. M., Serra, P., Morenza, J. L. (2008). Jet formation in the laser forward transfer of liquids. *Applied Physics A: Materials Science and Processing*, 93(2), 453-456.

[100] Duocastella, M., Fernández-Pradas, J. M., Morenza, J. L., & Serra, P. (2009). Time-resolved imaging of the laser forward transfer of liquids. *Journal of Applied Physics*, 106(8), 084907.

[101] Wu, P. K., Ringeisen, B. R., Callahan, J., Brooks, M., Bubb, D. M., Wu, H. D., Piqué, A., Spargo, B., McGill, R. A., & Chrisey, D. B. (2001). The deposition, structure, pattern deposition, and activity of biomaterial thin-films by matrix-assisted pulsed-laser evaporation (MAPLE) and MAPLE direct write. *Thin Solid Films*, 398, 607-614.

[102] Barron, J. A., Wu, P., Ladouceur, H. D., & Ringeisen, B. R. (2004). Biological laser printing: A novel technique for creating heterogeneous 3-dimensional cell patterns. *Biomedical Microdevices*, 6, 139-147.

[103] Tolbert, W. A., Lee, I. Y. S., Doxtader, M. M., Ellis, E. W., & Dlott, D. D. (1993). High-speed color imaging by laser-ablation transfer with a dynamic release layer: fundamental mechanisms. *Journal of Imaging Science and Technology*, 37(4), 411-422.

[104] Fitz-Gerald, J. M., Piqué, A., Chrisey, D. B., Rack, P. D., Zeleznik, M., Auyeung, R. C. Y., & Lakeou, S. (2000). Laser direct writing of phosphor screens for high-definition displays. *Applied Physics Letters*, 76(11), 1386-1388.

[105] Lippert, T., Wokaun, A., Stebani, J., Nuyken, O., & Ihlemann, J. (1993). Triazene Polymers Designed for Excimer Laser Ablation. *Angewandte Makromolekulare Chemie*, 206(1), 97-110.

[106] Loeffler, F. F., Foertsch, T. C., Popov, R., Mattes, D. S., Schlageter, M., Sedlmayr, M., Ridder, B., Dang, F.-D., von Bojničić-Kninski, C., Weber, L. K., Fischer, A., Greifenstein, J., Bykovskaya,V., Buliev, I., Bischoff, F. R., Hahn, L., Meier, M. A. R., Bräse, S., Powell, A. K., Balaban, T. S., Breitling, F., & Nesterov-Mueller, A. (2016). High-flexibility combinatorial peptide synthesis with laser-based transfer of monomers in solid matrix material. *Nature Communications*, 7, 11844.

[107] Mattes, D. S., Streit, B., Bhandari, D. R., Greifenstein, J., Foertsch, T. C., Münch, S. W., Ridder, B., von Bojničić-Kninski, C., Nesterov-Mueller, A., Spengler, B., Schepers, U., Bräse, S., Loeffler, F. F., & Breitling, F. (2019). Combinatorial Synthesis of Peptoid Arrays via Laser-Based Stacking of Multiple Polymer Nanolayers. *Macromolecular Rapid Communication*, 40(6), e1800533.

[108] Paris, G., Klinkusch, A., Heidepriem, J., Tsouka, A., Zhang, J., Mende, M., Mattes, D. S., Mager, D., Riegler, H., Eickelmann, S., & Loeffler, F. F. (2020). Laser-induced forward transfer of soft material nanolayers with millisecond pulses shows contact-based material deposition. *Applied Surface Science*, 508, 144973.

[109] Paris, G., Bierbaum, D., Paris, M., Mager, D., & Loeffler, F. F. (2022). Development and Experimental Assessment of a Model for the Material Deposition by Laser-Induced Forward Transfer. *Applied Sciences*, 12(3), 1361.

[110] Eickelmann, S., Moon, S., Liu Y., Bitterer, B., Ronneberger, S., Bierbaum, D., Breitling, F., & Loeffler, F. F. (2022). Assessing Polymer-Surface Adhesion with a Polymer Collection. *Langmuir*, 38(7), 2220-2226.

[111] Website of the World Health Organization.
https://www.who.int/news-room/fact-sheets/detail/ebola-virus-disease

[112] Jain, S., Martynova, E., Rizvanov, A., Khaiboullina, S., & Baranwal, M. (2021). Structural and Functional Aspects of Ebola Virus Proteins. *Pathogens*, 10(10), 1330.

[113] Henao-Restrepo, A. M., Longini, I. M., Egger, M., Dean, N. E., Edmunds, W. J., Camacho, A., Carroll, M. W., Doumbia, M., Draguez, B., Duraffour, S., Enwere, G., Grais, R., Gunther, S., Hossmann, S., Kondé, M. K., Kone, S., Kuisma, E., Levine, M. M., Mandal, S., Norheim, G., Riveros, X., Soumah, A., Trelle, S., Vicari, A. S., Watson, C. H., Kéïta, S., Kieny, M. P., Røttingen, J.-A. (2015). Efficacy and effectiveness of an rVSV-vectored vaccine expressing Ebola surface glycoprotein: interim results from the Guinea ring vaccination cluster-randomised trial. *Lancet*, 386(9996), 857-866.

[114] Henao-Restrepo, A. M., Camacho, A., Longini, I. M., Watson, C. H., Edmunds, W. J., Egger, M., Carroll, M. W., Dean, N. E., Diatta, I., Doumbia, M., Draguez, B., Duraffour, S., Enwere, G., Grais, R., Gunther, S., Gsell, P. S., Hossmann, S., Watle, S. V., Kondé, M. K., Kéïta, S., Kone, S., Kuisma, E., Levine, M. M., Mandal, S., Mauget, T., Norheim, G., Riveros, X., Soumah, A., Trelle, S., Vicari, A. S., Røttingen, J.-A., Kieny, M.-P. Kieny, (2017). Efficacy and effectiveness of an rVSV-vectored vaccine in preventing Ebola virus disease: final results from the Guinea ring vaccination, open-label, cluster-randomised trial (Ebola Ça Suffit!). *Lancet*, 389(10068), 505-518.

[115] Website of the U.S. Food & Drug Administration.
https://www.fda.gov/news-events/press-announcements/first-fda-approved-vaccine-prevention-ebola-virus-disease-marking-critical-milestone-public-health

[116] Krähling, V., Becker, D., Rohde, C., Eickmann, M., Eroğlu, Y., Herwig, A., Kerber, R., Kowalski, K., Vergara-Alert, J., Becker, S., & the European Mobile Laboratory consortium (2016). Development of an antibody capture ELISA using inactivated Ebola Zaire Makona virus. *Medical Microbiology and Immunology*, 205(2), 173-183.

[117] Heidepriem, J., Krähling, V., Dahlke, C., Wolf, T., Klein, F., Addo, M. M., Becker, S., & Loeffler, F. F. (2020). Epitopes of Naturally Acquired and Vaccine-Induced Anti-Ebola Virus Glycoprotein Antibodies in Single Amino Acid Resolution. *Biotechnology Journal*, *15*(9), e2000069.

[118] Ehrhardt, S. A., Zehner, M., Krähling, V., Cohen-Dvashi, H., Kreer, C., Elad, N., Gruell, H., Ercanoglu, M. S., Schommers, P., Gieselmann, L., Eggeling, R., Dahlke, C., Wolf, T., Pfeifer, N., Addo, M. M., Diskin, R., Becker, S., & Klein, F. (2019). Polyclonal and convergent antibody response to Ebola virus vaccine rVSV-ZEBOV. *Nature Medicine*, 25(10), 1589-1600.

[119] Becquart, P., Mahlakõiv, T., Nkoghe, D., & Leroy, E. M. (2014). Identification of continuous human B-cell epitopes in the VP35, VP40, nucleoprotein and glycoprotein of Ebola virus. *PloS One*, 9(6), e96360.

[120] Rijal, P., Elias, S. C., Machado, S. R., Xiao, J., Schimanski, L., O'Dowd, V., Baker, T., Barry, E., Mendelsohn, S. C., Cherry, C. J., Jin, J., Labbé, G. M., Donnellan, F. R., Rampling, T., Dowall, S., Rayner, E., Findlay-Wilson, S., Carroll, M., Guo, J., Xu, X.-N., Huang, K.-J. A., Takada, A., Burgess, B., McMillan, D. Popplewell, A., Lightwood, D. J., Draper, S. J., Townsend, A. R. (2019). Therapeutic Monoclonal Antibodies for Ebola Virus Infection Derived from Vaccinated Humans. *Cell Reports*, 27(1), 172-186.

[121] Chertow, D., Stein, S., Ramelli, S., Grazioli, A., Chung, J., Singh, M., Yinda, C. K., Winkler C., Dickey J., Ylaya, K., Ko, S. H., Platt, A., Burbelo, P., Quezado,M., Pittaluga, S., Purcell, M., Munster, V., Belinky, F., Ramos-Benitez, M., Boritz, E., Herr, D., Rabin, J., Saharia, K., Madathil, R., Tabatabai, A. Soherwardi S., McCurdy, M., Peterson, K., Cohen, J., de Wit, E., Vannella, K., Hewitt, S., Kleiner, D., (2021). SARS-CoV-2 infection and persistence throughout the human body and brain. *Research Square*.

[122] Puelles, V. G., Lütgehetmann, M., Lindenmeyer, M. T., Sperhake, J. P., Wong, M. N., Allweiss, L., Chilla, S., Heinemann, A., Wanner, N., Liu, S., Braun, F., Lu, S., Pfefferle, S., Schröder, A. S., Edler, C., Gross, O., Glatzel, M., Wichmann, D., Wiech, T., Kluge, S., Pueschel, K., Aepfelbacher, M., Huber, T. B. (2020). Multiorgan and Renal Tropism of SARS-CoV-2. *The New England Journal of Medicine*, 383(6), 590-592.

[123] Heidepriem, J., Dahlke, C., Kobbe, R., Santer, R., Koch, T., Fathi, A., Seco, B. M. S., Ly, M. L., Schmiedel, S., Schwinge, D., Serna, S., Sellrie, K., Reichardt, N. C., Seeberger, P. H., Addo, M. M., Loeffler, F. F., & On Behalf Of The Id-Uke Covid-Study Group (2021). Longitudinal Development of Antibody Responses in COVID-19 Patients of Different Severity with ELISA, Peptide, and Glycan Arrays: An Immunological Case Series. *Pathogens*, 10(4), 438.

[124] Ma, H., Zeng, W., He, H., Zhao, D., Jiang, D., Zhou, P., Cheng, L., Li, Y., Ma, X., & Jin, T. (2020). Serum IgA, IgM, and IgG responses in COVID-19. *Cellular & Molecular Immunology,* 17, 773-775.

[125] Shrock, E., Fujimura, E., Kula, T., Timms, R. T., Lee, I. H., Leng, Y., Robinson, M. L., Sie, B. M., Li, M. Z., Chen, Y., Logue, J., Zuiani, A., McCulloch, D., Lelis, F., Henson, S., Monaco, D. R., Travers, M., Habibi, S., Clarke, W. A., Caturegli, P., Laeyendecker, O., Piechocka-Trocha, A., Li, J. Z., Khatri, A., Chu, H. Y., MGH COVID-19 Collection & Processing Team, Villani, A.-C., Kays, K., Goldberg, M. B., Hacohen, N., Filbin, M. R., Yu, X. G., Walker, B. D., Wesemann, D. R., Larman, H. B., Lederer, J. A., Elledge, S. J. (2020). Viral epitope profiling of COVID-19 patients reveals cross-reactivity and correlates of severity. *Science*, 370(6520), eabd4250.

[126] Yuan, M., Wu, N. C., Zhu, X., Lee, C. D., So, R., Lv, H., Mok, C., & Wilson, I. A. (2020). A highly conserved cryptic epitope in the receptor binding domains of SARS-CoV-2 and SARS-CoV. *Science*, 368(6491), 630-633.

[127] Wang, H., Wu, X., Zhang, X., Hou, X., Liang, T., Wang, D., Teng, F., Dai, J., Duan, H., Guo, S., Li, Y., & Yu, X. (2020). SARS-CoV-2 Proteome Microarray for Mapping COVID-19 Antibody Interactions at Amino Acid Resolution. *ACS Central Science*, 6(12), 2238-2249.

[128] Paris, G., Heidepriem, J., Tsouka, A., Liu, Y., Mattes, D. S., Pinzón Martín, S., Dallabernardina, P., Mende, M., Lindner, C., Wawrzinek, R., Rademacher, C., Seeberger, P. H., Breitling, F., Bischoff, F. R., Wolf, T., & Loeffler, F. F. (2022). Automated Laser-Transfer Synthesis of High-Density Microarrays for Infectious Disease Screening. *Advanced Materials*, 34(23), e2200359.

[129] Freire, M., Pol-Fachin, L., Coêlho, D. F., Viana, I., Magalhães, T., Cordeiro, M. T., Fischer, N., Loeffler, F. F., Jaenisch, T., Franca, R. F., Marques, E., & Lins, R. D. (2017). Mapping Putative B-Cell Zika Virus NS1 Epitopes Provides Molecular Basis for Anti-NS1 Antibody Discrimination between Zika and Dengue Viruses. *ACS Omega*, 2(7), 3913-3920.

[130] Zhang, J., Liu, Y., Ronneberger, S., Tarakina, N. V., Merbouh, N., & Loeffler, F. F. (2022) Nanolayer Laser Absorber for Femtoliter Chemistry in Polymer Reactors. *Advanced Materials*, 34(8), 2108493.

[131] Eickelmann, S., Tsouka, A., Heidepriem, J., Paris, G., Zhang, J., Molinari, V., Mende, M., & Loeffler, F. F. (2019). A Low-Cost Laser-Based Nano-3D Polymer Printer for Rapid Surface Patterning and Chemical Synthesis of Peptide and Glycan Microarrays. *Advanced Materials Technologies*, 4(11), 1900503.

[133] Mehta, A. Y., Veeraiah, R., Dutta, S., Goth, C. K., Hanes, M. S., Gao, C., Stavenhagen, K., Kardish, R., Matsumoto, Y., Heimburg-Molinaro, J., Boyce, M., Pohl, N., & Cummings, R. D. (2020). Parallel Glyco-SPOT Synthesis of Glycopeptide Libraries. *Cell Chemical Biology*, 27(9), 1207-1219.e9.

[134] Mende, M., Tsouka, A., Heidepriem, J., Paris, G., Mattes, D. S., Eickelmann, S., Bordoni, V., Wawrzinek, R., Fuchsberger, F. F., Seeberger, P. H., Rademacher, C., Delbianco, M., Mallagaray, A., & Loeffler, F. F. (2020). On-Chip Neo-Glycopeptide Synthesis for Multivalent Glycan Presentation. *Chemistry - A European Journal*, 26(44), 9954-9963.

[135] Tsouka, A., Hoetzel, K., Mende, M., Heidepriem, J., Paris, G., Eickelmann, S., Seeberger, P. H., Lepenies, B., & Loeffler, F. F. (2021). Probing Multivalent Carbohydrate-Protein Interactions With On-Chip Synthesized Glycopeptides Using Different Functionalized Surfaces. *Frontiers in Chemistry*, 9, 766932.